COMPETITIVE ADSORPTION OF FURFURAL AND PHENOLIC COMPOUNDS ONTO ACTIVATED CARBON IN FIXED BED COLUMN

PROF. DR. ABBAS H. SULAYMON
DR.KAWTHER W. AHMED
Environmental Engineering Department-college of Engineering-University of Baghdad, Iraq

ABSTRACT

For a multicomponent competitive adsorption of furfural and phenolic compounds, a mathematical model was built to describe the mass transfer kinetics in a fixed bed column with activated carbon. The effects of competitive adsorption equilibrium constant, axial dispersion, external mass transfer and intraparticle diffusion resistance on the breakthrough curve were studied for weakly adsorbed compound (furfural) and strongly compounds (parachlorophenol and phenol). Experiments were carried out to remove the furfural and phenolic compound from aqueous solution. The equilibrium data and intraparticle diffusion coefficients obtained from separate experiments in a batch absorber, by fitting the experimental data with theoretical model. The results show that the mathematical model includes external mass transfer and pore diffusion using nonlinear isotherms, provides a good description of the adsorption process for furfural and phenolic compounds in fixed bed adsorber.

KEY WORDS: Competitive, Adsorption, Fixed-Bed, Activated-Carbon, Multi-component, Mathematical Model, Mass Transfer Coefficient.

INTRODUCTION

Furfural and phenolic compounds are organic compounds that enter the aquatic environment through direct discharge from oil refineries. The content of these pollutants in the industrial wastewater are usually higher than the standard limit (less than 5 ppm for furfural and less than 0.5 ppm for phenolic compounds).

Activated carbon adsorption is one of the important unit processes that is used in the treatment of drinking waters and renovation of wastewaters (Alexander, 1989).

Understanding of the dynamics of fixed bed adsorption column for modeling is a demanding task due to the strong nonlinearities in the equilibrium isotherms, interference effects of competition of solute for adsorbent sites, mass transfer resistance between fluid phase and solid phase and fluid-dynamics dispersion phenomena. The interplay of these effects produces steep concentration fronts, which moves along the column during the adsorption process, which has to be accounted for in modeling (Babu, 2004).

Several rate models have been developed that take into account an external film transfer rate step, unsteady state transport in the solid phase and nonlinear equilibrium isotherm to predict adsorption rates in batch reactor and fixed bed (Crittenden and Weber, 1978).

The key parameters for design of the adsorption system are the process parameters that are used for modeling the system for predicting the quality of effluent under a wide range of operating conditions. The key process parameters in adsorption such as isotherm constants and mass transfer coefficients are established by conducting batch studies of adsorption. Established isotherm models such as Langmuir and Freundlich are used for assessing the suitability of an adsorbent in adsorption system, where the experimental data are fitted to any one of these models.

The parameters that are responsible for mass transfer operation are the external mass transfer coefficient and intraparticle diffusivity or surface diffusion coefficient in the case of the homogeneous solid phase diffusion model.

The objective of the present research are to conduct experiments on the competitive adsorption equilibrium and adsorption kinetics in a fixed bed for removal of furfural (Fu) in the presence of phenolic compounds (Ph, PCP) from aqueous solution and to compare the experimental results with that simulated by the numerical solution of the general rate model which include axial dispersion, film mass transfer, pore diffusion resistance and nonlinear isotherms.

MODELING OF MULTICOMPONENT FIXED-BED ADSORBER

The dynamics of a fixed bed is described by a set of convection diffusion equations, coupled with source terms due to adsorption and diffusion inside the adsorbent particles.

The adsorption column is subjected to axial dispersion, external film resistance and intraparticle diffusion resistance.

A rate model which considers axial dispersion, external mass transfer, intraparticle diffusion and nonlinear isotherms is called a general multicomponent rate model. Such a model is adequate in many cases to describe the adsorption and mass transfer processes in multicomponent adsorption (Eggers, 2000; Volker, 1999).

The following equations are based on the hypothesis of an intraparticular mass transfer controlled by diffusion into macropores (pore diffusion model). This approach considers three phases:

a. The mobile phase flowing in the space between particles.
b. The stagnant film of mobile phase immobilized in the macropores.
c. The stationary phase where adsorption occurs.

The following basic assumptions are made in order to formulate a general rate model (Eggers, 2000):

- Adsorption process is isothermal.
- The adsorbent particles in the column are spherical and uniform in diameter.
- The concentration gradients in the radial direction are negligible.
- An instantaneous local equilibrium exists between the macropore surface and the stagnant fluid inside macropores of the particles.
- The film mass transfer mechanism can be used to describe the interfacial mass transfer between the bulk-fluid and particle phases.
- The diffusional and mass transfer parameters are constant and independent of the mixing effects of the components involved.

Continuity equation in the bulk-fluid phase:

$$-D_{bi}\frac{\partial^2 C_{bi}}{\partial Z^2}+v\frac{\partial C_{bi}}{\partial Z}+\frac{\partial C_{bi}}{\partial t}+\frac{1-\varepsilon_b}{\varepsilon_b}\frac{\partial q_i}{\partial t}=0 \qquad \ldots 1$$

Using C_{pi}, the concentration in the stagnant fluid-phase (in the macropores), and writing the expression of interfacial flux leads to:

$$\frac{\partial q_i}{\partial t} = \frac{3k_{fi}}{R_p}\left(C_{bi} - C_{pi,R=R_p}\right) \qquad \ldots 2$$

Substitution of equation 2 into equation 1 gives:

$$-D_{bi}\frac{\partial^2 C_{bi}}{\partial Z^2} + \nu\frac{\partial C_{bi}}{\partial Z} + \frac{\partial C_{bi}}{\partial t} + \frac{3k_f(1-\varepsilon_b)}{\varepsilon_b R_p}\left[C_{bi} - C_{pi,R=R_p}\right] = 0 \qquad \ldots 3$$

The particle phase continuity equation in spherical coordinates is:

$$(1-\varepsilon_p)\frac{\partial C^*_{pi}}{\partial t} + \varepsilon_p\frac{\partial C_{pi}}{\partial t} + \varepsilon_p D_{pi}\left[\frac{1}{R^2}\frac{\partial}{\partial R}\left(R^2\frac{\partial C_{pi}}{\partial R}\right)\right] = 0 \qquad \ldots 4$$

Initial and boundary conditions

$$C_{bi} = C_{bi}(0,Z) = 0 \qquad \ldots 5$$

$$C_{pi} = C_{pi}(0,R,Z) = 0 \qquad \ldots 6$$

$$Z = 0: \quad \frac{\partial C_{bi}}{\partial Z} = \frac{\nu}{D_{bi}}\left(C_{bi} - C_{oi}\right) \qquad \ldots 7$$

$$Z = L: \quad \frac{\partial C_{bi}}{\partial Z} = 0 \qquad \ldots 8$$

$$R = 0: \quad \frac{\partial C_{pi}}{\partial R} = 0 \qquad \ldots 9$$

$$R = R_p: \quad \frac{\partial C_{pi}}{\partial R} = \frac{k_{fi}}{\varepsilon_p D_{pi}}\left(C_{bi} - C_{pi,R=R_p}\right) \qquad \ldots 10$$

Defining the following dimensionless variables;

$$c_{bi} = \frac{C_{bi}}{C_{oi}},\ c_{pi} = \frac{C_{pi}}{C_{oi}},\ c^*_{pi} = \frac{C^*_{pi}}{C_{oi}},\ \tau = \frac{\nu t}{L},\ r = \frac{R}{R_p},\ z = \frac{Z}{L}$$

$$Pe_{Li} = \frac{\nu L}{D_{bi}},\ Bi_i = \frac{k_{fi}R_p}{\varepsilon_p D_{pi}},\ \eta_i = \frac{\varepsilon_p D_{pi} L}{R_p^2 \nu},\ \zeta_i = \frac{3Bi_i\eta_i(1-\varepsilon_b)}{\varepsilon_b}$$

The model equations can be transformed into the following dimensionless equations:

$$-\frac{1}{Pe_{Li}}\frac{\partial^2 c_{bi}}{\partial z^2} + \frac{\partial c_{bi}}{\partial z} + \frac{\partial c_{bi}}{\partial \tau} + \zeta_i\left(c_{bi} - c_{pi,r=1}\right) = 0 \qquad \ldots 11$$

$$\frac{\partial}{\partial \tau}\left[(1-\varepsilon_p)c^*_{pi} + \varepsilon_p c_{pi}\right] - \eta_i\left[\frac{1}{r^2}\frac{\partial}{\partial r}\left(r^2\frac{\partial c_{pi}}{\partial r}\right)\right] = 0 \qquad \ldots 12$$

Initial condition becomes ($\tau = 0$):

$$c_{bi} = c_{bi}(0, z) = 0 \qquad \ldots 13$$
$$c_{pi} = c_{pi}(0, r, z) = 0 \qquad \ldots 14$$

And boundary conditions become;

$$z = 0: \quad \frac{\partial c_{bi}}{\partial z} = Pe_{Li}\left(c_{bi} - 1\right) \qquad \ldots 15$$

$$z = 1: \quad \frac{\partial c_{bi}}{\partial z} = 0 \qquad \ldots 16$$

$$r = 0: \quad \frac{\partial c_{pi}}{\partial r} = 0 \qquad \ldots 17$$

$$r = 1: \quad \frac{\partial c_{pi}}{\partial r} = Bi_i\left(c_{bi} - c_{pi,r=1}\right) \qquad \ldots 18$$

The concentration c_{pi}* in equation 12 is the dimensionless concentration of component *i* in the solid phase of the particles. It is directly linked to a multicomponent Langmuir isotherm:

$$q_{e,i} = C^*_{pi} = \frac{q_i b_i C_{pi}}{1 + \sum_{j=1}^{N_s} b_j C_{pj}} = \frac{a_i C_{pi}}{1 + \sum_{j=1}^{N_s} b_j C_{pj}} \qquad \ldots 19$$

And in dimensionless form:

$$c^*_{pi} = \frac{a_i c_{pi}}{1 + \sum_{j=1}^{N_s} \left(b_j C_{oj}\right) c_{pj}} \qquad \ldots 20$$

Finite element method is used for the discretization of the bulk-fluid phase partial differential equation and the orthogonal collocation method for the particle phase equations an ordinary differential equation system is produced. The ordinary differential equation system with initial values can be readily solved using an ordinary differential equation solver such as the subroutine "ODE15S" of MATLAB which is a variable order solver based on the numerical differentiation formulas (NDFs). Optionally it uses the backward differentiation formulas (BDFs), which is also known as Gear's method.

EXPERIMENTAL WORK AND PROCEDURE

The granulated activated carbon (GAC) used in the experiments was supplied by Unicarbon, Italian. Its physical properties are listed in table 1.

The GAC was sieved into 28/32 mesh with geometric mean diameter of 0.5 mm. The GAC was boiled, washed three times in distilled water and dried at 110^o C for 24 hours, before being used as adsorbent.

The aqueous solutions of furfural, phenol and parachlorophenol where prepared using reagent grades. Their properties are listed in table 2.

The experiments were adjusted at the initial pH of 5.7 for phenolic compounds (Ping and Guohua (I), 2001) and 8.1 for furfural, with 0.01 mol/l NaOH and 0.01 mol/l HCl. This is for single component experiments, while for multicomponent systems, the pH were adjusted at 7. Solutions were not buffered to avoid adsorption competition between organic and buffer (Monneyron and Faur-Brasqet, 2002).

The experiments were carried out in Q.V.F. glass column of 50 mm (I.D.) and 50 cm in height. The GAC was confined in the column by fine stainless steel screen, at the bottom and glass packing at the top of the bed to ensure a uniform distribution of influent through the carbon bed. The influent solutions were introduced to the column through a perforated plate, fixed at the top of the column. Feed solutions were prepared in Q.V.F. vessel supplied with immersed heater with a thermocouple to adjust the temperature of the solution.

For the determination of adsorption isotherms, 250 ml flasks were filled with 100 ml of known concentration of solutes and a known weight of GAC. The flasks were then placed on a shaker and agitated continuously for 30 hours at 30^o C. The concentration of furfural, phenol and parachlorophenol in the solutions were determined by a UV-160A spectrophotometer at 254, 270 and 300 nm, respectively.

The adsorbed amount is calculated by the following equations:

$$q_e = \frac{V(C_o - C_e)}{W_A} \qquad \ldots 21$$

The intraparticle diffusion coefficient for each solute was obtained by 2 liter Pyrex beaker fitted with a variable speed mixer. The beaker was filled with 1 liter of known concentration solution and the agitation started before adding the GAC. At time zero, the accurate weight of GAC where added. Samples were taken every 5 minutes.

The necessary dosage of GAC, to reach equilibrium related concentration of C_e/C_o equal 0.05, were calculated from isotherms model and mass balance equation as follow:

$$W_A = \frac{V(C_o - C_e)}{q_e} \qquad \ldots 22$$

Where:

$$q_e = f(C_e) \qquad \ldots 23$$

RESULTS AND DISCUSSION

Adsorption isotherm

The equilibrium isotherms for the investigated solutes onto GAC are presented in figure 1 .All the adsorption isotherm display a nonlinear dependence on the equilibrium concentration.

The adsorption data for all the system fitted by Langmuir (Lucas and Cocero, 2004), Freundlich (Weber and Walter, 1972), Radke-Prausnitz (Radke and Prausnitz, 1972), Dubinin-Radushkevich (Monneyron and Faur-Brasqet, 2002), Reddlich-Peterson (Jossens et al., 1972) and combination of Langmuir-Freundlich models (Sips, 1984).

The correlation between experimental data and the theoretical models was very good for all systems. The Langmuir adsorption model was selected to be introduced in the fixed bed model, where:

$$q_e = \frac{q_m b C_e}{1 + b C_e} \qquad \ldots 24$$

The equilibrium data for furfural, phenol and parachlorophenol (multicomponent system) aqueous solution in GAC is adapted as the competitive Langmuir isotherm model (Fahmi and Munther, 2003):

$$q_{e,i} = \frac{q_{m,i} b_i C_{e,i}}{1 + \sum_{j=1}^{N_s} b_j C_{e,j}} \qquad \ldots 19$$

In which the parameters $q_{m,i}$, b_i are the coefficient of the single component. The parameters are evaluated to be:

$q_{m,\,Fu}$= 0.3744 kg/kg $\qquad$ b_{Fu}=18.42 m^3/kg
$q_{m,\,Ph}$= 0.3500 kg/kg $\qquad$ b_{Ph}=34.6 m^3/kg
$q_{m,\,PCP}$= 0.3199 kg/kg $\qquad$ b_{PCP}=49.6 m^3/kg

INTRAPARTICLE DIFFUSION COEFFICIENT

There were a good matching between batch experimental results and predicted data using pore diffusion model for batch operation (Ping and Guohua (II), 2001) as shown in figure 2.

The pore diffusion coefficient for each solute are evaluated form the batch experiments to be $D_{p,\,Fu}$ = 9.870×10^{-10} m^2/s, $D_{p,\,Ph}$ = 8.251×10^{-10} m^2/s and $D_{p,\,PCP}$ =7.657×10^{-10} m^2/s.

The external mass transfer coefficients in packed bed model for each solute were evaluated by the correlation of Wilson and Gearkoplis (Ping and Guohua (I), 2001).

$$Sh_i = \frac{1.09}{\varepsilon_b} Sc_i^{1/3} \mathrm{Re}^{1/3} \quad \text{for } Re\text{=0.0015-55} \qquad \ldots 25$$

Where: $Sh_i = \frac{K_{f,i} d_p}{D_{m,i}}$, $Sc_i = \frac{\mu_w}{\rho_w D_{m,i}}$ and $\mathrm{Re} = \frac{\rho_w u d_p}{\mu_w}$.

In which the molecular diffusion coefficient $D_{m,i}$ of furfural, phenol and parachlorophenol in aqueous solution are listed in table 2.

These values substitutes in equation 25 to evaluate $K_{f,i}$ at different interstitial velocity in the mathematical mode.

The axial dispersion coefficient calculated form Chung and Wen equation (Gupta et al., 2001):

$$\frac{D_b \rho_w}{\mu_w} = \frac{\mathrm{Re}}{0.2 + 0.011\mathrm{Re}^{0.48}} \qquad \ldots 26$$

BREAKTHROUGH CURVE

Figures 3 to 10 show that the experimental and predicted breakthrough curves for multicomponent system at different flow rate, bed depth and initial concentration of solutes at constant temperature of 30^o C. It is clear from these figures that:

1. The adsorption capacity order for the ternary system onto GAC as follow:

$$PCP > Ph > Fu$$

In this case, the capacity of the adsorbate seems to influence the adsorption energy greatly. The octanol-water partition coefficient K_{ow} given in table 2, shows that the parachlorophenol is more hydrophobic than phenol and furfural.

It has been clearly demonstrated that adsorption of phenolic compounds onto activated carbon induces the formation of π-π bond, where activated carbon act as an electron donor and the solute benzene ring has an electron-withdrawing character (Monneyron and Faur-Brasqet, 2002). The mesomeric and/or inductive character of the substitutent of the aromatic compound influences this formation and thus the molecule's adsorption energy. This interpretation is supported by experimental results: the withdrawing inductive character of chloride substitutents (Gupta, 1946) decreases the electron density of the parachlorophenol-benzene ring compared with that of phenol-benzene ring (Wheeler and Levy, 1959). The adsorption energy of parachlorophenol is higher than that of Ph. These results agree with Ping and Guohua (I) (2001).

The adverse effect of the OH group (Bartell and Miller, 1923) on adsorption of phenol may be attributed to the capability of this group to form hydrogen bonding with the water which renders the compound less liable to be adsorbed in compared with parachlorophenol.

The lower adsorption capacity of furfural may be explained by its higher solubility, low molecular weight and low octanol-water coefficient in compared with parachlorophenol or phenol.

Furfural is a polar solvent and activated carbon is generally regarded to favor the adsorption of non-polar compound rather than polar compounds. Since pure carbon surface is considered to be non-polar, but in actual practice, some carbon-oxygen complexes are present which render the surface slightly polar (Al-Bahrani and Martin, 1977).

2. In case of multicomponent systems, at the initial stage, there are a lot of active sites of GAC, the strongly and weakly adsorbed components take the active sites freely. With increasing time, the weakly adsorbed component is not easily adsorbed but moves a head with the bulk fluid and takes the active sites first in the front part of the fixed bed. Because the strongly adsorbed component tends to take the active sites instead of the weakly adsorbed component, it will displace the sites that had been taken by the weakly adsorbed components. The result is that the local concentration of the weakly adsorbed component within the fixed bed adsorber is higher (Ping and Guohua (I), 2001).

3. The frontal concentration profile of the breakthrough curves, in a fixed bed adsorber, is related to the initial solutes concentration, Biot number (Bi) and Peclet number (Pe).

4. An increase in the flow rate at constant bed depth will increase the Biot number with slight increase in Peclet number, Biot is the ratio of external mass transfer rate to the intraparticle mass transfer rate.

When Biot number is large (that is, the intraparticle mass transfer is the controlled step (Ping and Guohua (I), 2001)), the break point will appear early, this is due to the decrease in contact time between the solute and the adsorbent at higher flow rate.

5. An increase in bed depth at constant flow rate will increase the Peclet number at constant Biot number, where Peclet number is the ratio of axial convection rate to the axial dispersion rate.

When Peclet number is small (that is, the effect of axial dispersion is not negligible (Ping and Guohua (I), 2001)), the breakthrough curve become flat and the break point appear early.

6. The simulated breakthrough curves for adsorption of ternary system (furfural, phenol, and parachlorophenol) onto activated carbon are in a close agreement with the experimental results. Thus, the mathematical model which includes axial dispersion, film mass transfer, pore diffusion resistance and nonlinear isotherms provides a good description of the competitive adsorption process in fixed bed adsorber.

CONCLUSIONS

This work has studied the characteristics of the competitive adsorption of furfural in the presence of phenolic compounds in aqueous solution in a fixed bed adsorber. A mathematical model which includes external mass transfer and pore diffusion using non-linear isotherm was investigated.

The results show that the solubility and hydrophobicity has a large influence on adsorption capacity and energy respectively. These influences were confirmed by ternary adsorption.

The general rate model provides a good description of the adsorption process of furfural and phenolic compounds in fixed bed adsorber onto activated carbon.

REFERENCES

Alexander, P. M. and Zayas, I.,(1989), "*Particle size and shape effects on adsorption rate parameters*", J. Environmental Engineering, **115** (1), Feb., p 41-55.

Al-Bahrani, K. S. and Martin, R. J., (1977), Water Res., **11**, pp 991-999.

Babu, B. V. and Gupta, S., (2004), "*Modeling and simulation for dynamics of packed bed adsorption*", Chem. Conf., Mumbai.

Bartell, F. E. and Miller, E. J., (1923), J. Amer. Chem. Soc., **45**, pp 1106-1110.

Crittenden, J. C. and Weber, I. R., (1978), "*Predictive model for design of fixed-bed adsorbers, single component model verification*", Environmental Engineering Division, **104** (EE3), June, pp 433-443.

Eggers, R., (2000), "*Simulation of frontal adsorption*", HIWI report by Hamburg-Hamburg University.

Fahmi, A. and Munther, K., (2003), "*Competitive adsorption of Nickel and cadmium on sheep monure waste, experimental and prediction studies*", Separation Science and Technology, **38** (2), pp 483-497.

Gu, T. and Zheng, Y., (1999), "*A study of the scale-up of reversal-phase liquid chromatography*", Separation and Purification technology, **15**, pp 41-58.

Gupta, A., Nanoti, O. and Goswami, A. N., (2001), "*The removal of furfural from water by adsorption with polymeric resin*", Separation Science and Technology, **36** (13), pp 2835-2844.

Gupta, P., (1946), "*Polarity of molecules in relation to their adsorption by charcoal*", J. Indian Chem. Soc., **23**, pp 353-360.

Jossens, L., Prausnitz, J. M. and Frits, W., (1978), "*Thermodynamic of multi-solute adsorption from dilute aqueous solutions*", Chem. Eng. Sci., **33**, pp 1097-1106.

Lucas, S. and Cocero, M. J., (2004), "*Adsorption isotherms for ethylacetate and furfural on activated carbon from supercritical carbon dioxide*", Fluid Phase Equilibria, **219**, pp 171-179.

Monneyron, P. and Faur-Brasqet, C., (2002), "*Competitive adsorption of organic micropollutant in the aqueous phase onto activated carbon cloth*", Langmuir, **18**, pp 5163-5168.

Ping L. and Guohua, X. (I), (2001), "*Competitive adsorption of phenolic compounds onto activated carbon fibers in fixed bed*", J. Environmental Engineering, August, pp 730-734.

Ping L. and Guohua, X. (II), (2001), "*Adsorption and desorption of phenol on activated carbon fibers in fixed bed*", Separation Sience and Technology, **36** (10), pp 2147-2163., August, pp 730-734.

Radke, C. J. and Prausnitz, J. M., (1972), "*Adsorption of organic compounds from dilute aqueous solution on activated carbon*", Ind. Eng. Chem. Fund., **11**, pp 445-451.

Sips, R., (1948), J. Chem. Phys., **16**, pp 490-495.

Volker, K., (1999), "*Simulation of liquid chromatography and simulated moving bed system*", Technical report by Hamburg-Hamburg University (TUHH).

Weber, J. R. and Walter, J., (1972), "*Physicochemical processes for water quality control*", Wiley Inter. Science, New York.

Wheeler, O. H. and Levy, E. M., (1959), Can. J. Chem., **37**, pp 1235-1240.

NOTATION

Symbols	
b	Langmuir constant, m^3/kg
Bi	Biot number $\left(\dfrac{K_f R_p}{\varepsilon_p D_{pi}}\right)$, -
C	Concentration in fluid, kg/m^3
C_o	Initial concentration, kg/m^3
D_b	Axial dispersion coefficient, m^2/s
D_m	Molecular diffusion coefficient, m^2/s
D_p	Pore diffusion coefficient, m^2/s
d_p	Particle diameter, m
K_f	Fluid to particle mass transfer coefficient, m/s
L	Length of column, m
Pe	Peclet number $\left(\dfrac{uL}{D_b}\right)$, -
Q	Fluid flow rate, m^3/s
q_e	Internal concentration of solute in particle, kg/kg
q_m	Adsorption equilibrium constant defined by Langmuir equation, kg./kg
Re	Reynolds number $\left(\dfrac{\rho_w u d_p}{\mu_w}\right)$, -
R_p	Radius of particle, m
Sc	Schmidt number $\left(\dfrac{\mu_w}{\rho_w D_{m,i}}\right)$, -
Sh	Sherwood number $\left(\dfrac{K_{f,i} d_p}{D_{m,i}}\right)$, -
t	Time, s

Symbols

u	Interstitial velocity $\left(\dfrac{Q}{\pi R_p^2 \varepsilon_b}\right)$, m/s
V	Volume of solution, m^3
W_A	Mass of activated carbon, kg
Z	Axial distance, m

Greek symbols

ε_b	Bed porosity, -
ε_p	Porosity of adsorbent, -
μ_w	Viscosity of water, Pa.s
ρ_w	Density of water, kg/m^3

Subscript

b	Bulk fluid phase
e	Equilibrium
Fu	Furfural
i	Component number (1, 2, 3 …)
L	Liquid phase
o	Initial
p	Particle phase
PCP	Parachlorophenol
Ph	Phenol

TABLES AND FIGURES

Table 1, Physical properties of activated carbon

Raw material	Coconut shell
Apparent density, kg/m^3	480 - 490
Bulk density, kg/m^3	770
BET surface area, m^2/g	1100
Particle porosity	0.5
Bed porosity	0.41
Iodine number, mg/g	1100 - 1130
pH	10.2 - 10.6
Ash content, %	5 (max)
Particle size, %	
Mesh +12	0.2
12 – 16	20.67
16 – 20	25.05
20 – 30	34.18
30 – 40	18.83
40 -	1.08

Table 2, Main properties of adsorbates

Property	Furfural	Phenol	Parachlorophenol
Symbol	Fu	Ph	PCP
Formula	$C_5H_4O_2$	C_6H_5OH	C_6H_5OCl
Structure	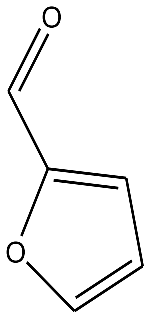	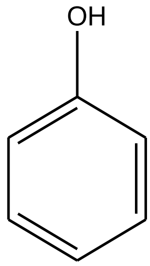	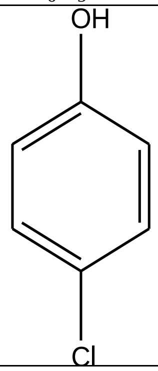
Molecular weight, g/mole	96.08	94.11	129
Solubility in water (at 20^o C), g/l	83	66.7	28
Log (K_{ow})	1.58	1.50	2.35
Molecular diffusion (at 20^o C), m^2/s	1.04×10^{-8}	9.6×10^{-9}	8.82×10^{-9}

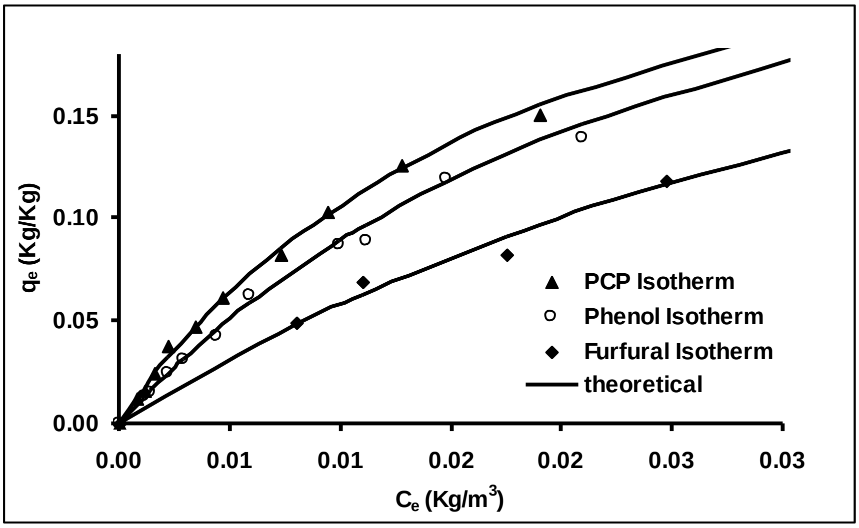

Fig (1) Adsorption isotherm for PCP,Phenol and Furfural onto activated carbon at 303 K.

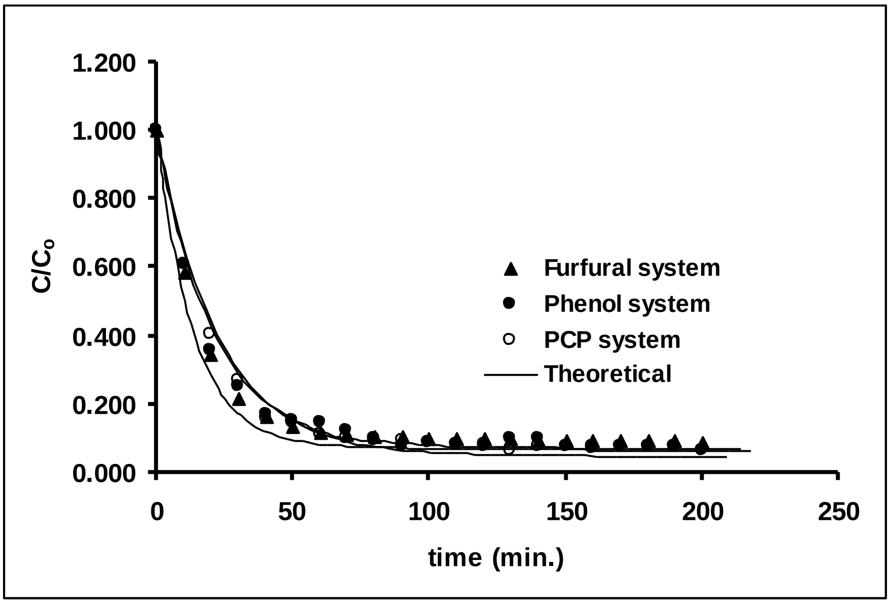

Fig (2) Comparison of the measured concentration-time data with that predicted by pore diffusion model in batch adsorber for Furfural ,Phenol and PCP systems.

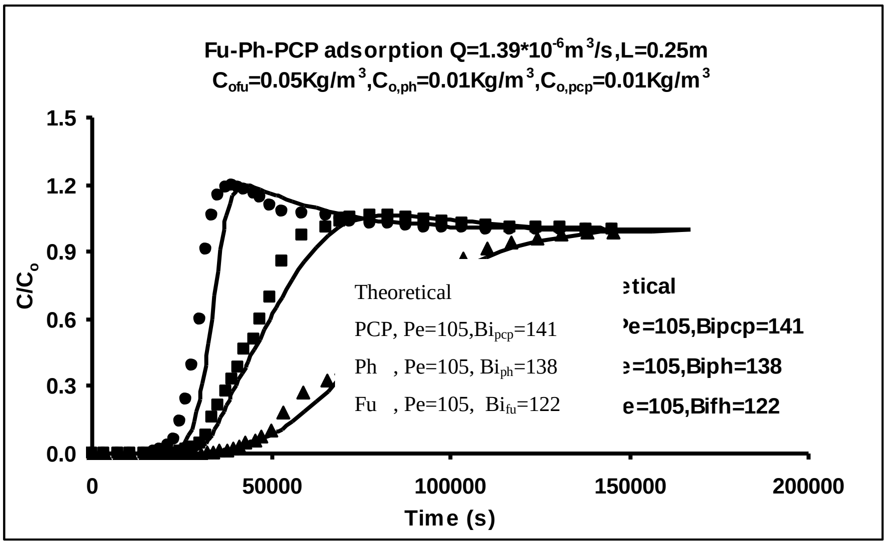

Fig (3) The experimental and predicted breakthrough curves for adsorption of Fu-Ph-PCP system onto activated carbon at $C_{o,pcp}$=0.01 kg/m^3.

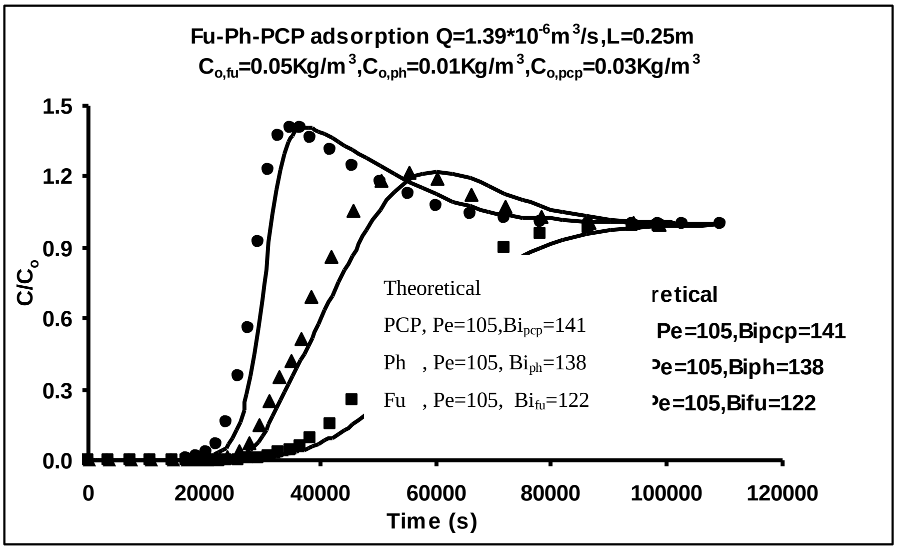

Fig (4) The experimental and predicted breakthrough curves for adsorption of Fu-Ph-PCP system onto activated carbon at $C_{o,pcp}$=0.03 kg/m^3.

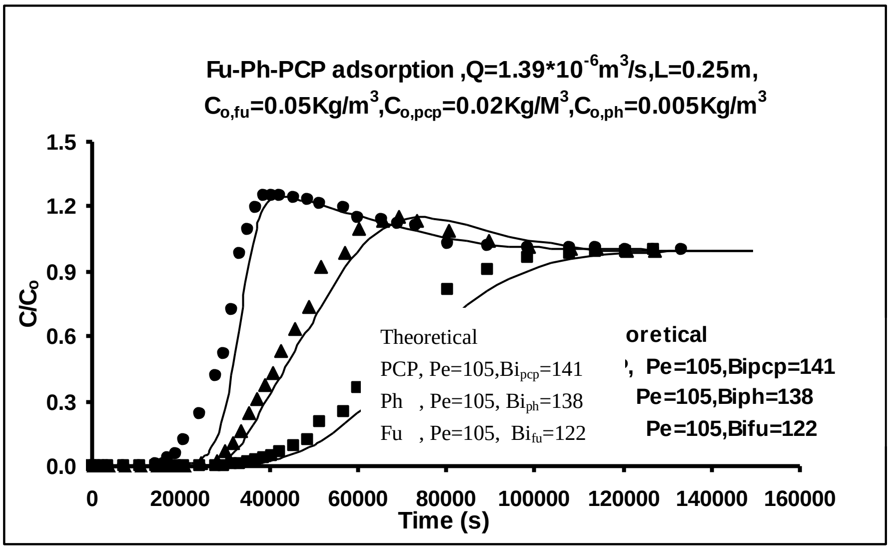

Fig (5) The experimental and predicted breakthrough curves for adsorption of Fu-Ph-PCP system onto activated carbon at $C_{o,ph}$=0.005 kg/m^3.

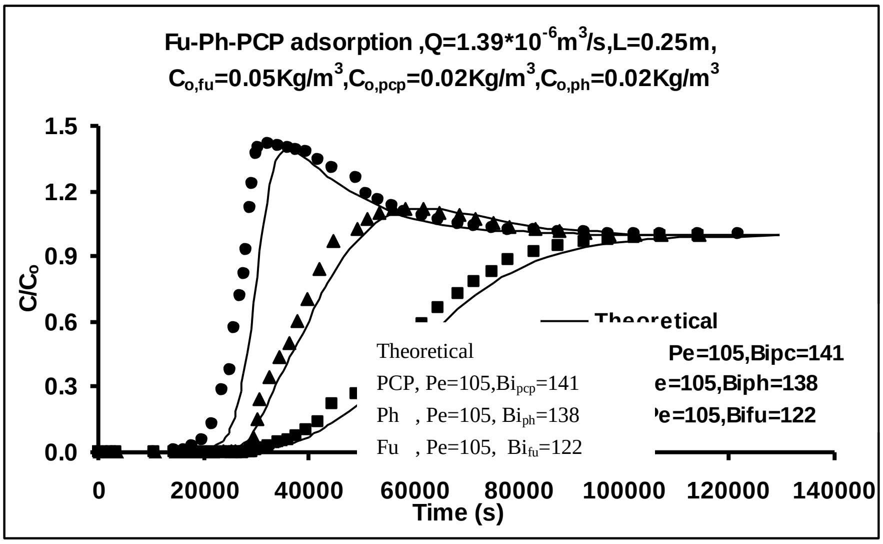

Fig (6) The experimental and predicted breakthrough curves for adsorption of Fu-Ph-PCP system onto activated carbon at $C_{o,ph}$=0.02 kg/m^3.

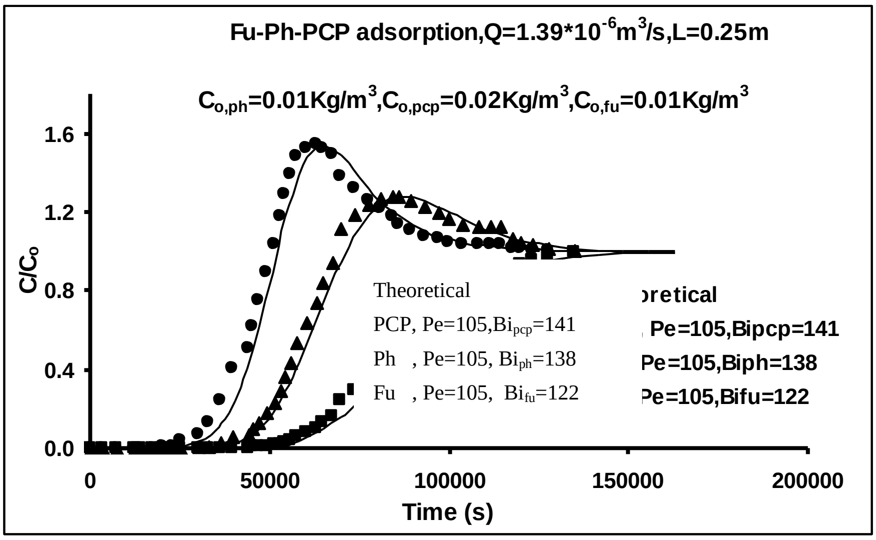

Fig (7) The experimental and predicted breakthrough curves for adsorption of Fu-Ph-PCP system onto activated carbon at $C_{o,fu}$=0.01 kg/m^3.

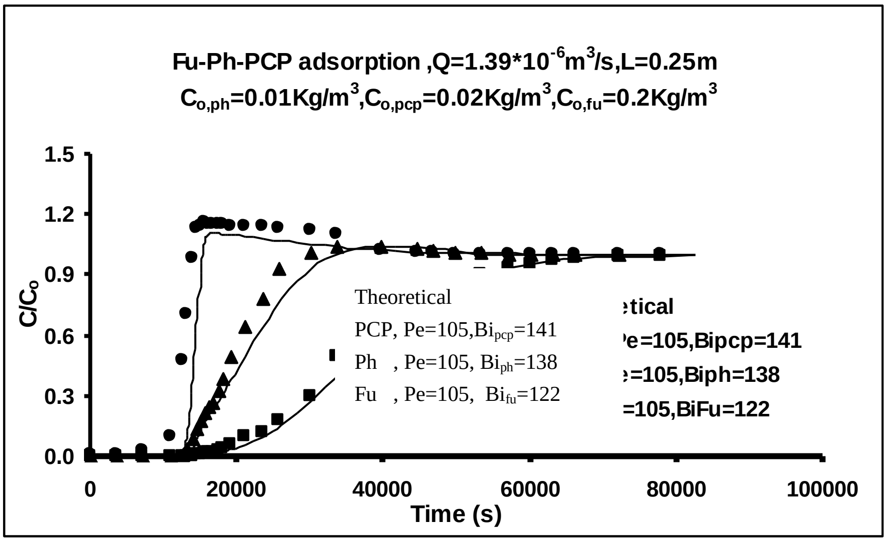

Fig (8) The experimental and predicted breakthrough curves for adsorption of Fu-Ph-PCP system onto activated carbon at $C_{o,fu}$=0.2 kg/m^3.

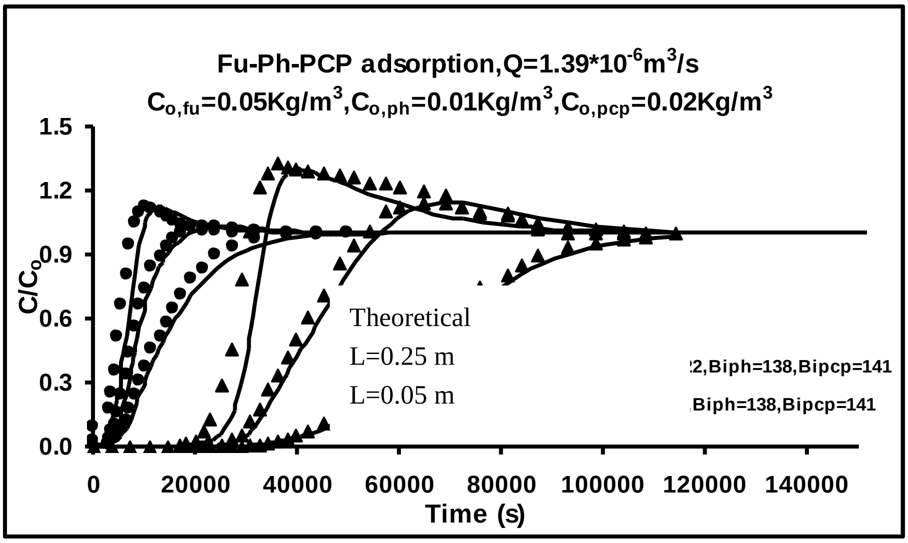

Fig (9) The experimental and predicted breakthrough curves for adsorption of Fu-Ph-PCP system onto activated carbon at different bed depth.

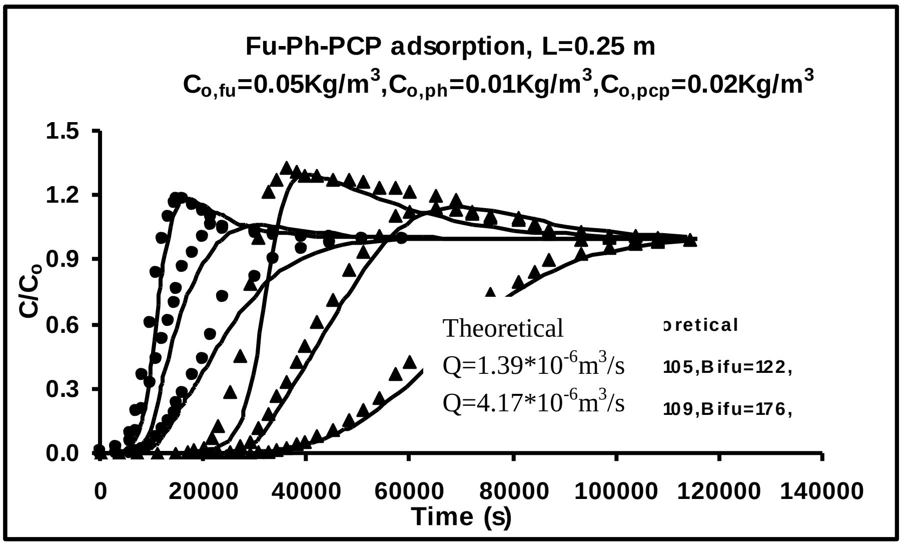

Fig (10) The experimental and predicted breakthrough curves for adsorption of Fu-Ph-PCP system onto activated carbon at different flow rate.

ANALYSIS OF GALVANIC CORROSION UNDER MASS TRANSFER CONTROLLED CONDITIONS

Qasim. J.M Slaiman	Basim O. Hasan	Baker M. Al-Zaidy
Chemical Eng. Dept.- Nahrain University-Baghdad -Iraq		

ABSTRACT

Because of practical importance of protecting industrial equipments from galvanic corrosion, the need arises to analyze the effects of variables, such as temperature, velocity, and area fraction of metals on galvanic corrosion in systems under mass transfer control as in seawater (pH=7). For these reasons the galvanic corrosion of Fe-Zn is analyzed to study the influence of Reynolds number, temperature, and area fraction on the galvanic corrosion rates and galvanic corrosion potential under mass transfer control.

It is found that galvanic corrosion rate of more active metal (Zn) is increased with Reynolds number while the corrosion rate of more noble metal (Fe) is slightly increased with Re depending on the galvanic potential that depends on the area fraction. Increasing Reynolds number shifts the galvanic potential to more positive values. Also increasing temperature leads to shift the corrosion potential to more negative values and to change the corrosion rate of more active metal (Zn) depending on two parameters oxygen solubility and oxygen diffusivity. As area fraction of more active metal (Zn) increased the galvanic potential is shifted to the negative anodic direction while the corrosion rate for more noble metal is decreased.

KEY WORDS: Galvanic corrosion, mass transfer control, Fe-Zn couple, temperature, area fraction

االخلاصة

بسبب الاهمية التطبيقية لحماية المعدات الصناعية من التاكل الغلفاني ظهرت الحاجة لدراسة وتحليل تأثير بعض العوامل مثل درجة الحرارة وسرعة السائل ومساحة الكاثود والانود على التاكل الغلفاني في الانظمة التي تكون تحت سيطرة انتقال الكتلة(pH=7) كما في ماء البحر.

تمت دراسة التاكل الغلفاني لمعدني الحديد والخارصين لمعرفة تاثير عدد رينولد (او السرعة) ودرجة الحرارة ونسبة المساحة في ظروف سيطرة انتقال الكتلة. أظهرت النتائج ان زيادة عدد رينولد يؤدي الى زيادة تأكل المعدن الفعال الانود (Zn) بصورة رئيسية ويؤثر قليلا على المعدن الاقل فعالية (الكاثودFe) وحسب جهد التاكل الذي يعتمد على نسبة المساحة بين المعدنين. زيادة عدد رينولد يؤدي الى زيادة جهد التاكل الغلفاني بالاتجاه الموجب و زيادة درجة الحرارة تؤدي الى تقليل معدل التاكل الغلفاني وتقليل جهد التاكل الغلفاني(ازاحته بالاتجاه السالب) وازاحته بالاتجاه السالب اما زيادة مساحة المعدن الفعال (Zn) تؤدي الى تقليل الجهد الغلفاني وتقليل تاكل المعدن الاقل فعالية (Fe).

INTRODUCTION

Corrosion is the deterioration of materials by chemical interaction with their environment. The term corrosion is some times also applied to the degradation of plastics, concrete, and wood but generally refers to metals. The consequences of corrosion are many and varied and the effect of these on the safe, reliable, and efficient operation of equipment or structures are often more serious than the simple loss of a mass of metal. Failures of various kinds and the need for expensive replacements may occur even though the amount of metal destroyed is quite small. Some of the major harmful effects of corrosion are [Shreir 2000]: reduction of metal thickness, hazards or injuries to people arising from structural failure, loss of time, reduced value of goods, contamination of fluids in vessels and pipes, perforation of vessels and pipes, loss of technically important surface properties of a metallic component, and mechanical damage to valves, pumps, etc. Galvanic corrosion, often misnamed "electrolysis," is one common form of corrosion in marine environments. It occurs when two (or more) dissimilar metals are brought into electrical contact under corrosive environment. When a galvanic couple forms, one of the metals in the couple becomes the anode and corrodes faster than it would all by itself, while the other becomes the cathode and corrodes slower than it would alone. Either (or both) metal in the couple may or may not corrode by itself (themselves) in seawater. When contact with a dissimilar metal is made, however, the self-corrosion rates will cause the corrosion of the anode to accelerate and corrosion of the cathode to decelerate or even stop. If any two metals are coupled together, the one closer to the anodic (or active) end of the series, will be the anode and thus will corrode faster, while the one toward the cathodic (or noble) end will corrode slower. The two major factors affecting the severity of galvanic corrosion are, (i) the voltage difference between the two metals on the galvanic series, (ii) the size of the exposed area of cathodic metal relative to that of the anodic metal.

Corrosion of the anodic metal is more rapid and more damaging as the voltage difference increases. It is well known that the rate-controlling step in most aerated water corrosion processes is the cathodic half reaction. The most important cathodic process in aerated waters is oxygen reduction. The rate of this half reaction is generally limited by the speed at which oxygen can reach the surface of the metal. This oxygen is transported from the bulk water to the surface across the boundary layer by diffusion [Smith et. al. 1989, Cheng and Steward 2004].

Many investigations were carried out to study the galvanic corrosion. Copson [1945] studied the galvanic action between steel coupled to nickel in tap water with 3 to 1 area ratio of Ni/ Fe and found that the galvanic corrosion of steel was appreciable. Pryor [1946] investigated the galvanic corrosion of Al/steel couple in chloride containing solution and found that aluminum completely protects steel cathodically within the pH range 0-14, and the galvanic current and the corrosion rate of aluminum are at a minimum in the nearly neutral pH range. Wranglen et al. [1969] studied the difference between the galvanic corrosion rates of high and low carbon steel in acid solutions and concluded that the engineers should not depend only on the galvanic series in the selection of their materials of construction. Mansffeld et al [1971, 1973a, 1973b, 1973c,1973d] investigated experimentally many factors that affect the galvanic interaction of various metals and alloys (as Al and Ti) in 3.5% NaCl solution and in HCl and gave a detailed explanations. Tsujino et al.[1982] studied the galvanic corrosion of steel coupled to noble metals (Pt, Cu, 304 stainless steel) in sodium chloride solution and found that the local currents on the steel depend on the area ratio of the steel to the cathodic metal and these currents are not related to the concentration of sodium chloride in neutral solutions. Bardal et al.[1984] predicted galvanic corrosion rates by means of numerical calculation and experimental models based on boundary element method. Glass and Ashworth [1985] perform experimental study to determine the corrosion rates of zinc- mild steel couple at 65 ^{o}C in pH of 8. They determined and discussed the variation of corrosion potential and corrosion rate with time. Fangteng et al.[1988] presented a theoretical approach for galvanic corrosion allowing for cathode dissolution, and found that the cathode of the couple is also corroded at the galvanic corrosion potential where the corrosion is controlled by the rate of oxygen diffusion to the electrode surfaces and the cathode dissolution in a galvanic system leads to a decrease in the galvanic current and it has been shown that the current density through the anode is independent of the area ratio of the electrodes. Jones and Paul [1988] stated that many semi conducting minerals have sufficient conductivity to permit electrochemical reactions on their surfaces and consequently, galvanic interactions will occur when such minerals are coupled to metals or other conducting minerals. Morris and Smyrl [1989] calculated galvanic currents and potentials on heterogeneous electrode surfaces comprised of random configurations of coplanar anodes and cathodes, for the purpose of investigating system behavior on different electrode geometries. Symniotis [1990] investigated the active dissolution of a duplex stainless steel in two different acidic solutions together with a comparison of the active dissolution of the corresponding γ and α phases and found that the galvanic action takes place between the two phses. Also he studied the influence of dependence of anodic currents on time, surface morphology, and surface area. Chang et al [1997] studied the galvanic corrosion behavior of tungsten coupled with several selected metals/alloys. They stated that from an environmental perspective, tungsten is a more desirable material than depleted uranium (DU) for penetration applications. Lee et al [2000] investigated the corrosion behavior of an as-cast magnesium alloy focusing on the galvanic corrosion between a precipitate and Mg-rich matrix. Al-Hadithi [2002] investigated experimentally the effects of temperature, pH, and area fraction on the galvanic corrosion rate of binary galvanic system by coupling carbon steel, zinc, copper, and brass under activation control conditions. He studied the coupling of each pair of these metals individually. Song et al [2004] investigated experimentally the galvanic corrosion of megnisium alloy AZ9ID in contact with zinc, aluminum, and steel alloys. AL-Maypof [2006] studied the galvanic coupling between magnetite and iron in acidic solution.

The present study aims to analyze the galvanic corrosion behavior of binary metals (Fe-Zn) under mass transfer control to investigate the influence of temperature, Reynolds number, and area fraction, on the free corrosion rate and galvanic corrosion rate for binary galvanic system under mass transfer (diffusion) control.

ANALYSIS

When two different metals are in a corrosive environment, they corrode at different rates according to their specific corrosion resistances to that environment, however, if the two metals are in contact, the more corrosion prone (metal 1) corrodes faster and the less corrosion prone (metal 2 the more noble one) corrodes slower than originally, i.e. when no contact existed. The accelerated damage to the less resistant metal is called galvanic corrosion, and is heavily dependent on the relative surface areas of the metals

To determine the potential of a system in which the reduced and oxidized species are not at unit activity, the familiar Nernest equation can be employed:

$$E = E_o - \frac{RT}{nF} \ln \frac{a_{red}}{a_{oxd}} \tag{1}$$

Tafel slopes (Tafel constants) are determined from the following equation [Shreir 2000]

$$\beta_a = \frac{RT}{\alpha_a nF} \tag{2}$$

$$\beta_c = -\frac{RT}{\alpha_c nF} \tag{3}$$

The relationship between reaction rate and overvoltage for activation polarization is

$$\eta^A = \pm \beta \log \frac{i}{i_o} \tag{4}$$

The reaction rate is given by the reaction current or current density [David and James 1998]:

$$i_a = i_{o,a} e^{(Ea - E_{ea}/\beta_a)} \tag{5}$$

and

$$i_c = i_{o,c} e^{(E_c - E_{ec}/\beta_c)} \tag{6}$$

The effect of temperature is to change the value of exchange current density i_o as follows [Nesic et al 1996]:

$$i_{o,T} = i_{o,298}\exp[\frac{E_{act}}{R}(\frac{1}{298} - \frac{1}{T})] \quad (7)$$

The anodic current is given by [West 1965]

$$I_a = i_{o,a}A_a\exp[\frac{\alpha_a n_a F}{RT}(E_a - E_{e,a})] \quad (8)$$

or

$$i_a = i_{o,a}f_a\exp[\frac{\alpha_a n_a F}{RT}(E_a - E_{e,a})] \quad (9)$$

and cathodic one

$$I_c = i_{o,c}A_c\exp[-\frac{\alpha_c n_c F}{RT}(E_c - E_{e,c})] \quad (10)$$

$$i_c = i_{o,c}f_c\exp[-\frac{\alpha_c n_c F}{RT}(E_c - E_{e,c})] \quad (11)$$

For diffusion (mass transfer) controlled corrosion systems the reaction current is given by Fick's law [Shreir 2000]

$$\frac{I}{z_c FA} = D\frac{dC}{dx} = k(C_b - C_s) \quad (12)$$

The limiting current, i.e., the maximum current under diffusion control is obtained when C_s=0, so

$$I_L = z_c FAkC_b \quad (13)$$

Where the mass transfer coefficient, k, is defined by, k=D/δ. The corrosion current is then

$$I_{corr} = I_L = z_c FAkC_b$$

or $$i_L = z_c FkC_b \quad (14)$$

z_C is used because in the corrosion processes the cathodic reaction is the one likely to be controlled by diffusion. The bulk concentration of oxygen in the solution changes with temperature as shown in Table 1.

The mass transfer coefficient (k) varies with flow or relative speed between metal and environment, the geometry of system, and the physical properties of the liquid. To calculate k in dynamic environment, the dimensionless groups are often used. Over the years there were many correlations proposed for predicting k for systems under mass transfer control. The well known correlation is that of Poulson and Robinson [1986] under turbulent flow conditions:

$$Sh=0.026Re^{0.82}Sc^{0.35} \quad (15)$$

Hence the expression of k is

$$k=(D/d)\ 0.026Re^{0.82}Sc^{0.35} \quad (16)$$

The effect of temperature and pressure on the diffusion coefficient is given by [Brodkey and Hershey 1989]

$$D_{P,T} = D_o \frac{P_o}{P}(\frac{T}{T_o})^n \qquad (17)$$

where the exponent n varies from 1.75 to 2.

For galvanic corrosion under mass transfer or activation control at galvanic potential (E_g):

$$I_{corr} = I_a = |I_c| \qquad (18)$$

and

$$\Sigma I_a = \Sigma I_c \qquad (19)$$

For two metal galvanic corrosion

$$i_{a,1}A_1+i_{a,2}A_2= i_{c,1}A_1+i_{c,2}A_2 \qquad (20)$$

or $$i_{a,1}f_1+i_{a,2}f_2= i_{c,1}f_1+i_{c,2}f_2 \qquad (21)$$

Where f_1 and f_2 are the area fractions (individual metal area/total metals area) of metals 1 and 2 respectively. At galvanic corrosion potential, $E_a= E_c= E_g$, hence at E_g

$$i_{a1} = i_{o,a_1}\exp[\frac{\alpha_a n_a F}{RT}(E_g - E_{e,a1})] \qquad (22)$$

$$i_{a2} = i_{o,a_2}\exp[\frac{\alpha_a n_a F}{RT}(E_g - E_{e,a2})] \qquad (23)$$

$$i_{c1} = i_{o,c1}\exp[-\frac{\alpha_c n_c F}{RT}(E_g - E_{e,c1})] \qquad (24)$$

$$i_{c2} = i_{o,c2}\exp[-\frac{\alpha_c n_c F}{RT}(E_g - E_{e,c2})] \qquad (25)$$

For mass transfer control the summation of cathodic currents equal the oxygen limiting diffusion currents on both metals since the hydrogen evolution currents are negligible (pH=7). Hence

$$\Sigma I_a = \Sigma I_L \qquad (26)$$

$$i_{a,1}f_1+i_{a,2}f_2= i_L f_1+i_L f_2 \qquad (27)$$

since $f_1+f_2=1$, hence

$$i_{a,1}f_1+i_{a,2}f_2= i_L \qquad (28)$$

Insertion of Eqs. (22) and (23) in Eq.(28) with i_L from Eqs. (14) and (16), E_g can be obtained by iteration method.

Simplifications leading to analytic solutions of the above equations are so complex, so numerical solutions must be attempted. As an example, a numerical method implemented on a microcomputer. The sweeping method is as follows:

a. Estimate equilibrium potentials for metals using equation (1) at a particular temperature for pH of 7. The calculations are performed for the activity of oxidized species (F^{2+} and Zn^{2+}) of 10^{-6} molar.

b. Tafel slopes for anodic and cathodic reactions are established from equations (2) and (3) with $\alpha_a = \alpha_c = 0.5$.
c. The exchange current density is calculated from equation (7) for three values of temperatures 25, 40 and 60 ^oC with E_{act} from Table 2. Table 3 gives values of i_o at 25 ^oC.
d. Bulk concentration of oxygen in water at any temperature is from Table (1).
e. The value of oxygen diffusivity is estimated from Eq. (17) at different temperatures 25, 40 and 60 ^oC with oxygen diffusivity at 25 ^oC (D^o) of 2.04×10^{-9} m^2/s [Perry and Green 1997].
f. The mass transfer coefficient k is calculated by using Eq. (16) with d=5 cm.
g. The limiting current is estimated of from Eqs. (14) and (16) at a particular Re at each temperature. To calculate Schmidt number ($Sc=\nu/D$) the physical properties of water are taken from Perry and Green [1997].
h. E_g is assumed to start the iteration. It is necessary to realize that the galvanic corrosion potentials (Eg) of the reactions involved are chosen between the more negative equilibrium potential and the less negative one.
i. The values of E_e, i_a, and E_g are substituted in Eqs.(22) and (23) to determine anodic currents.
j. The summations of the anodic and limiting currents (cathodic currents) are compared to determine the absolute value of their difference.
k. A new value of E_g is assumed as in h until the difference between the summation of the anodic and cathodic (limiting) currents becomes very small to obtain the galvanic corrosion potential.

RESULTS AND DISCUSSION

Free Corrosion

Fig. 1 shows the variation of free corrosion potential with Re for the two metals Fe and Zn at 25 ^oC. The Fig. indicates that increasing Re shifts the corrosion potential to more positive direction for both metals. Fig. 2 shows the variation of Fe free corrosion potential with Re at different temperatures. The Fig. reveals that increasing Re shifts the free corrosion potential to more positive values. This can be ascribed to the increased oxygen transport to the metal surface. Also the Fig. indicates that increasing temperature shifts the free corrosion potential to more negative due to the decreased oxygen solubility. Fig.3 shows the variation of oxygen limiting current density with Re at various temperatures. The oxygen limiting diffusion current equals the total cathodic currents since the hydrogen evolution current is negligible in systems of PH=7. Increasing Re increases the limiting current density via increasing oxygen supply to the metal surface by eddy diffusion [Fontana and Green 1984, Poulson and Robinson 1986]. Also the figure reveals that the higher the temperature is the lower the i_L because the O_2 solubility in the bulk of the solution decreases with temperature.

Galvanic Corrosion

Fig. 4 shows the variation of galvanic corrosion potential with Re at various area fraction values. The Fig. shows that increasing Re leads to increase the galvanic potential to more positive direction for the whole range of area fractions. This is ascribed to the fact that increasing Re leads to increase the supply of cathodic species (oxygen) and hence increase the oxygen limiting diffusion current density shifting the corrosion potential to more positive. Also at a particular Re the higher the area fraction of Fe is the more positive value of galvanic corrosion potential. This trend holds for the whole range of temperature. Fig. 5 for area fraction of Fe of 0.1 and Zn of 0.9 shows the variation of current density with Re. It is evident that the Zn corrosion current density is equal to the oxygen limiting current density while the Fe corrosion current density is very low or negligible indicating that at coupling Fe with Zn, the Fe is totally protected because the equilibrium potential of Fe is higher than the galvanic potential of Fe= Zn couple. Also the galvanic corrosion current density of Zn increases appreciably with Re while that of Fe is not affected with Re since it is galvanically protected with Zn because coupling Zn with Fe shifts the galvanic potential below the equilibrium potential of Fe stopping its corrosion . Mansfeld [1971] stated that the corrosion rate of more active metal in aerated neutral solutions is controlled by the diffusion rate of the oxidizer (oxygen) to the metal surface. Fig. 6 for area fraction of Fe and Zn of 0.5 exhibits the same trend. Fig. 7 shows that decreasing area fraction of Fe (or increasing area fraction of Zn) leads to decrease the Fe galvanic corrosion current density indicating that increasing the area fraction of more active metal leads to decrease the corrosion rate of more noble metal. Also at high Fe area fraction, increasing Re increases the corrosion current density of Fe. Fig. 8 indicates that the Zn corrosion current density increases with Re and slightly affected with the area fraction.

Figs. 9 and 10 for Re=10000 and 60000 respectively show the variation of galvanic corrosion potential with temperature at various area fractions. The figures reveal that increasing the temperature shifts the corrosion potential to more negative values. This behavior is attributed to certain solubility considerations. Many gases such as oxygen have lower solubility in open systems at higher temperatures. As temperature increases, the resulting decrease in solubility of gas causes corrosion potential and corrosion rate to go down [Nesic et al. 1996, Shreir 2000]. The effect of Re on the Fe galvanic corrosion current density in galvanic coupling with Zn at various temperatures is shown in Figs. 11 and 12 for different area fractions. The figures reveal also that the Fe galvanic current density varies with temperature where the highest corrosion current occurs at 40 ^oC and the lowest at 60 ^oC depending on two parameters, oxygen solubility and oxygen diffusivity.

Practically Zn in certain environmental conditions may exhibits a passivity or polarity reversal when coupled with Fe as noticed by Glass and Ashworth [1985] in 0.01 M $NaHCO_3$ at 65 ^oC.

CONCLUIONS

1- At coupling two metals in systems under mass transfer control, the galvanic corrosion rate of more active metal increases with increasing Re. The galvanic corrosion rate of more noble metal is slightly affected by Re. The effect of Re on both metal is depending on area fraction of both metals.
2- Increasing temperature shifts the galvanic corrosion potential to more negative while the effect of temperature on the corrosion rate is unstable.
3- Increasing area fraction of more active metal has negligible effect on the corrosion rate of this metal and decreases the corrosion rate for more noble metal via shifting the corrosion potential to more negative.

Table 1 Solubility of Oxygen in Sea Water at 1 atm [Perry and Green 1997]

Temperature, ^oC	Solubility of oxygen mg/l
25	7.8
40	6.0
60	3.1

Table 2: Activation Energy of Metals [West 1965]

Metal	Activation Energy (J/mol)
Fe	2625
Zn	13609

Table 3: Values of Exchange Current Density at 25 ^oC and pH=7 [West 1965]

Metal	E_o, V	i_o, A/cm^2
Fe	-0.44	10^{-6}
Zn	-0.76	10^{-9}

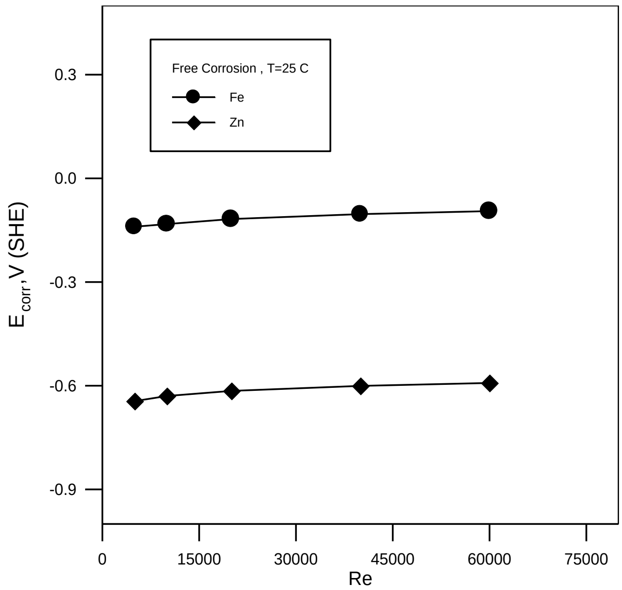

Fig.1: Variation of Free Corrosion Potential with Re.

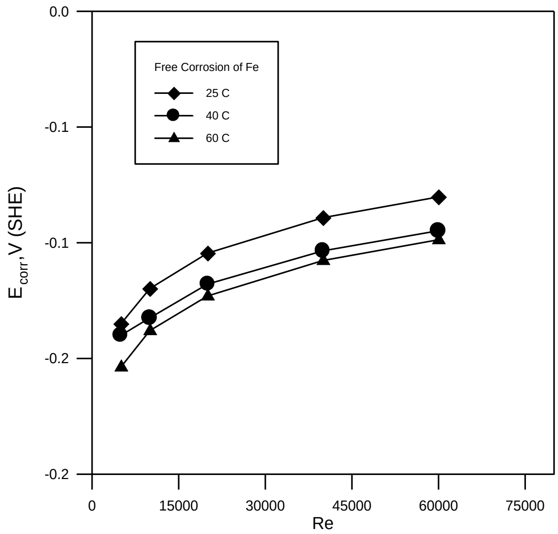

Fig.2: Variation of Free Corrosion Potential of Fe with Re

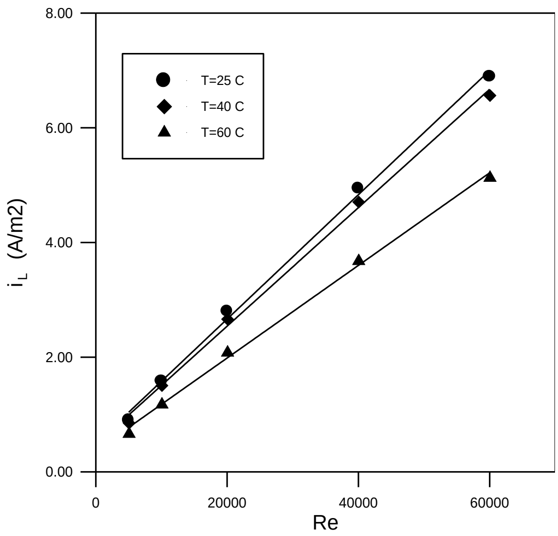

Fig.3: Variation of Limiting Current Density with Re.

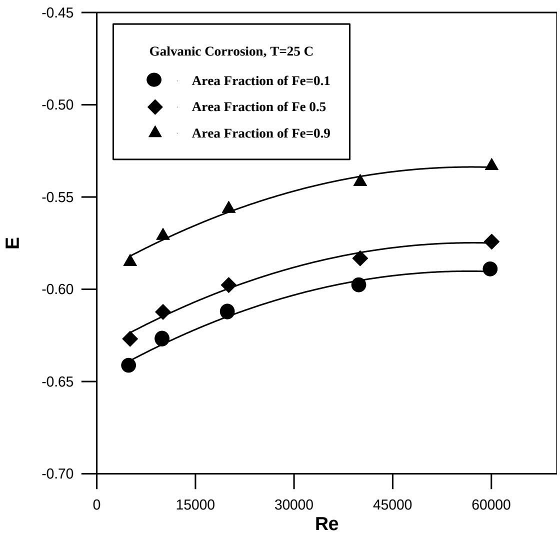

Fig. 4: Variation of Galvanic Potential with Re for Fe-Zn Couple at T=25 C.

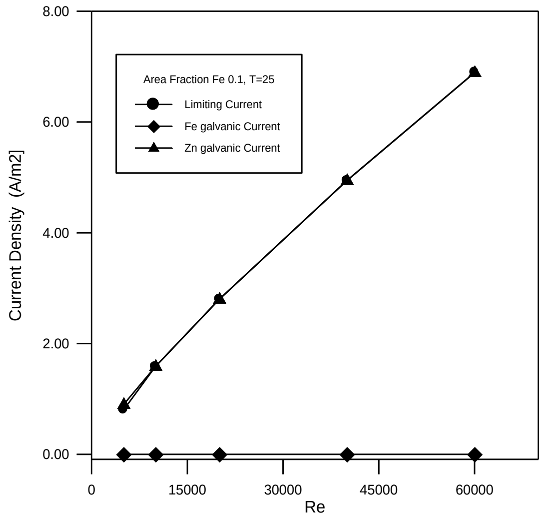

Fig. 5: Variation of Current Density with Re for Fe-Zn Couple at T=25 C.

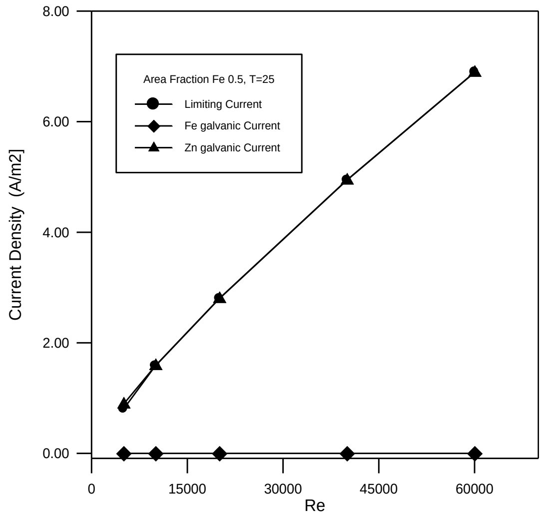

Fig. 6: Variation of Current Density with Re for Fe-Zn Couple at T=25 C.

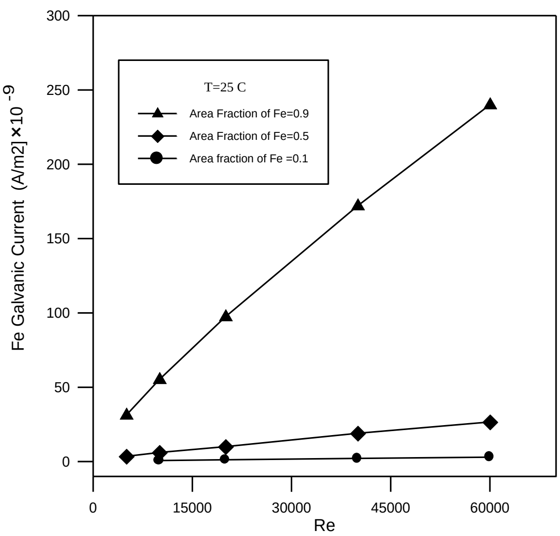

Fig. 7: Variation of Current Density of Fe with Re at Various Area Fractions at T=25 ^{o}C.

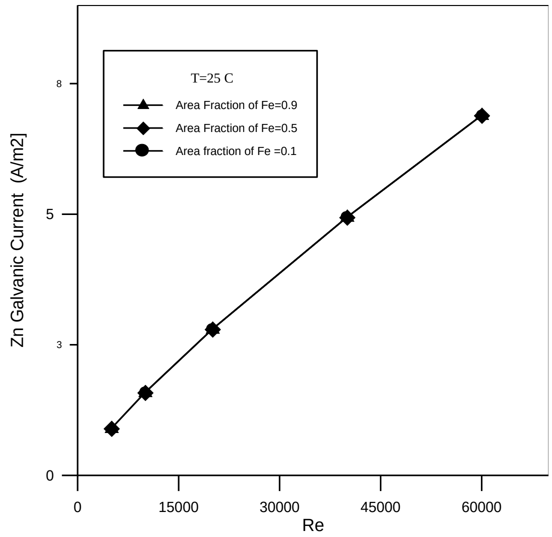

Fig. 8: Variation of Current Density of Fe with Re for Various Area Fractions at T=25 ^{o}C.

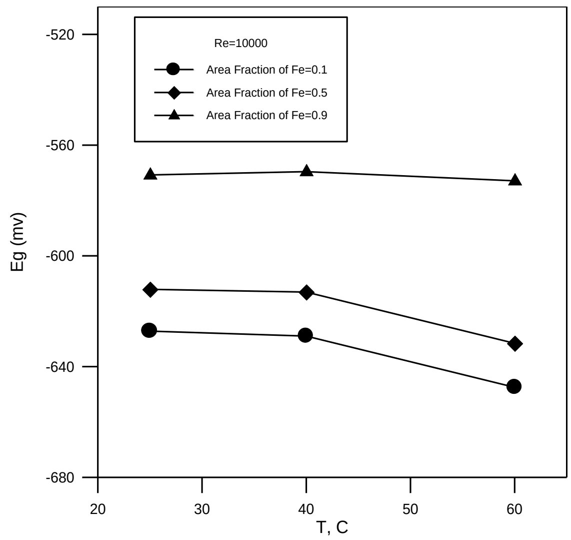

Fig. 9: Variation of Galvanic Corrosion Potential with Temperature at Re=10000.

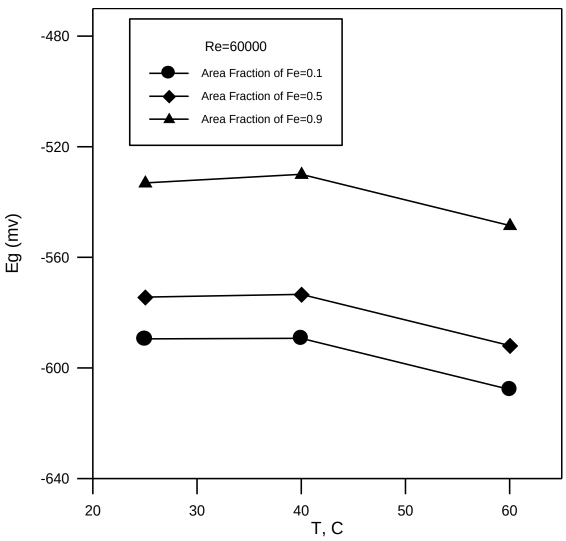

Fig.10: Variation of Galvanic Corrosion Potential with Temperature at Re=6000.

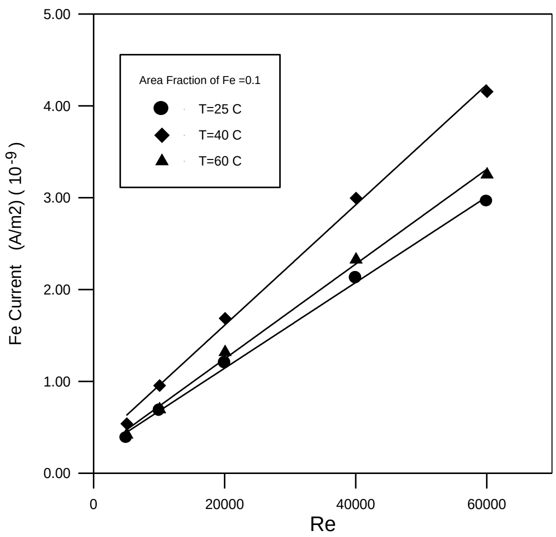

Fig. 11: Variation of Fe Corrosion Current with Re at Various Temperatures for Fe Area Fraction of 0.1.

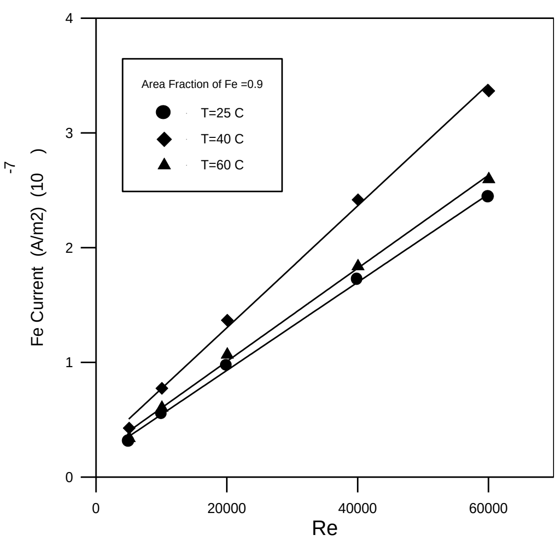

Fig. 12: Variation of Fe Corrosion Current with Re at Various Temperatures for Fe Area Fraction of 0.9.

NOMENCLATURE

A	Surface area of specimen	m^2
a	Activities (concentration) of reduced and oxidized species	Mol/liter
C	Bulk concentration	mole/m^3
D	Diffusion coefficient of reacting ion	m^2/s
d	Diameter	m
E	Electrode potential	V
F	Faradays constant	96487 Coulomb/g.equivalent
i	Current density	μA/cm^2
I	Total corrosion	μA
i_o	Exchange current density at concentration	μA/cm^2
k	Mass Transfer Coefficient	m/s
L	Distance between the pressure taps	m
n	Number of electrons transfer	
R	Gas constant	8.314 J/mol.K
Re	Reynolds number	
Sc	Schmidt number.	
T	Temperature	^{o}C or K
u	Velocity	m/s
z	Number of electrons Transferred	

Greek Letters

α	Symmetry factor	
β	Tafel slope	V
δ	Thickness of diffusion layer	m
η	overpotential	V
μ	Viscosity	Kg/m.sec^2
ν	Kinematic viscosity	m^2/s
ρ	Density	Kg/m^3

Subscripts

a	anode
b	bulk
c	cathode
e	equilibrium
g	galvanic
L	limiting
s	surface

Abbreviations

corr	corrosion
oxid	oxidation
red	reduction

REFERENCE

Al- Hadithi F. F. (2002), " Computer Aided Simulation and Laboratory Investigation of Glavanic Corrosion", Ph.D Theisis, Nahrain University, Baghdad, Iraq.

AL-Mayouf A.M., (2006)," Dissolution of megnettite coupled galvanically with iron in environmentally friendly chelant solution, Corrosion Scince, 48, 898-912.

Bardal E., Johnson R., and Gastland P., Corrosion J., 12 40 (1984), P.628-P.633

Brodkey R. S. and H. C. Hershey, Transport Pkenomena, 2nd Printing Mc Graw Hill, New York, 1989.

Chang, Beatty, Kane and Beck,, Tri-Service Conference on Corrosion. I; Naval Surface Warfare Center-Carderock Division 1997, pp. 6.33-6.45.

Copson H.R., (1945) Ind. Eng. Chem. J., 8, 37, P.721-723.

David Tabolt and James Tabolt, 1998, "Corrosion Science and Technology", CRC series, Library of Congress, 1st Edition, New York.

Fangteng, S., (1988) Corrosion Science Jounal, 6, 25, ,P.649-P.655.

M. G. Fontana, N. D. Green, 1984, Corrosion Engineering, 2nd Edition.,London.

Glass G. K., and Y. Ashworth (19985), “The Behavior of the Zinc-Mild steel Galvanic Cell In Hot Sodium Bicarbonate Solution”, Corrsion Science, Vol. 25, No. 11, pp. 971-983.

Jones D. A. and A. J. P. Paul, (1988) Corrosion 88/245. NACE, Houston, TX.

Lee , Kang , Shin, (2000) Metals and Materiald, Vol. 6, No. 4, pp. 351-358, Aug.

Mansfeld F., 1971, Corrosion Journal, 10, 27, pp. 436-442.

Mansfeld F., 1973a, Corrosion Journal, 7, 29, pp. 276-281.

Mansfeld F., 1973b, Corrosion Journal, 2, 29, pp. 56-58.

Mansfeld F., and Parry E. P., 1973c, Corrosion Journal, 4,13, pp. 397-402.

Mansfeld F., and Parry E. P., 1973d, Corrosion Journal, 10,30, pp. 343-353.

Morris, W. Smyrl, (1989) J. Electrochem. Soc., Vol. 136, No. 11, November, p. 3237-3248.

Nesic S., J. Postlethwaite , and S. Olsen, (1996) "An Electrochemical Model for Prediction of Corrosion of Mild Steel in Aqueous Carbon Dioxide Solution", Corrosion J., April, Vol.52, No.4, P.280.

Perry, R. H ,and Green ,D. W , 1997, Perry Chemical Engineers Handbook, 7th ed, Mc Graw Hill ,United states ,

Poulson B. and R. Robinson (1986), "The Use of Corrosion Process to Obtain Mass Transfer Correlations", Corr. Sci. Vol, 26, No.4, P.265.

Pryor, M.J., (1946) Corrosion Journal , Vol.1, P.14.

Shreir L.L, (2000), Corrosion, Vol. 1, Metal Environment Reactions, 3rd Edition, Butterworth-Heinemann.

Smith S. W., K. McCabe, and D.W. Black, 1989 Corrosion-NACE, 45, 790-793.

Song G., B. Johannesson, S. Hapugoda, and D. Stjohn, 2004," Galvanic Corrosion of Magnesium Alloy in Contact with aluminum, Steel, and Zinc, Corr. Sci., 46, 995-977.

Symniotis E., (1990), "Galvanic Effects on the Active Dissolution of Duplex Stainless Steels", Corrosion J., January, No.1, 46, P.2.

Tsujino, B .and Miyase S., (1982), Corrosion Journal, 4, 38, P.226-230.

West J. M. , (1965.), Electrodeposition and Corrosion Processes, Van Nostrand Co. LTD, London.

Wranglen G. and Khokhar , (1969), Corrosion Science Journal , 8, 9, P. 439-449.

SLANTLET TRANSFORM-BASED OFDM SCHEME

Sulaiman M.Abbas
Ass.Prof Department of Electrical Engineering

Mohammed Nadhim Abbas
Department of Electrical Engineering

Saifuldeen A.Mohammed
University of Baghdad, Baghdad,Iraq

الخلاصة

إن الاتصالات الرقمية اللاسلكية في توسع مستمر مما يستدعي الحاجة إلى أنظمة موثوقة وذات كفاءة طيفية عالية و لتحقيق هذه الحاجة فأن تقنية مزج الترددات المتعامدة (OFDM) استحوذت على الكثير من الاهتمام. في هذا البحث اقترحت طريقة جديدة لتحسين اداء ال(OFDM). ان الطريقة الجديدة في هذا البحث هو تقليل مستوى التداخل وازالة الحاجة الى استعمال الفترة الفاصلة وبهذا تم تحسين كفاءة النطاق (Bandwidth) في منضومة ال(OFDM)، هذا يتم عن طريق تبديل تحويل الفوريير بطريقة الأنحدار المائل(Slantlet). وان ال (Slantlet) هو تطويرحصل في المويجات (Wavelet) فقد لوحظ ان (SLT-OFDM) افضل من (WP-OFDM) في حالة القناة الوهن الانتقائي للتردد و كذلك ان خوارزمية (Slantlet) اسرع بكثير من خوارزمية (Wavelet). في هذا البحث تم التركيز على المقارنة بين (FFT-OFDM) و (SLT-OFDM) من اهم النتائج التي تم الحصول عليها هو ان اداء (SLT-OFDM) يكون افضل بحدود18 dBعن اداء (FFT-OFDM) في قناة الوهن المستوي. بينما اداء نظام(SLT-OFDM) يكون افضل فقط في منطقة SNR الواطئة وسوف ينعكس الاداء مع زيادة SNR في حالة القناة الوهن الانتقائي للتردد.

ABSTRACT

Wireless digital communication is rapidly expanding resulting in a demand for systems that are reliable and have a high spectral efficiency. To fulfill these demands OFDM technology has drawn a lot of attention.

In this paper a new technique is proposed to improve the performance of OFDM. The new technique is use the slantlet transform (SLT) instead Fast Fourier transform (FFT) in order to reduce the level of interference. This also will remove the need for Guard interval (GI) in the case of the FFT-OFDM and therefore improve the bandwidth efficiency of the OFDM. The SLT-OFDM is also better than wavelet packet (WP)-OFDM in the selective channel because the slantlet filter bank is less frequency selective than the traditional DWT filter bank, due to the shorter length of the filters and SLT algorithm is faster than WP algorithm. The main results obtained indicate that the performance of SLT-OFDM is better on average by 18dB in comparison with that of FFT-OFDM flat fading channels. For frequency selective fading channel the SLT-OFDM performs is better than the FFT-OFDM on the lower SNR region, while the situation will reverse with increase SNR values.

WORD KEY

slant let transform - OFDM- Guard interval

INTRODUCTION

Orthogonal Frequency Division Multiplexing (OFDM) is very similar to the well known and used technique of Frequency Division Multiplexing (FDM). OFDM uses the principles of FDM to allow multiple messages to be sent over a single radio channel. It is however in a much more controlled manner, allowing an improved spectral efficiency.

The Fourier transform (or other transform) data communication system is a realization of FDM in which discrete Fourier transform are computed as part of modulation and demodulation process. In addition to eliminating the banks of subcarrier oscillators and coherent demodulators usually required in FDM system, a completely digital implementation can be built around a special-purpose computer performing the fast Fourier transform [1]. OFDM has recently been applied widely in wireless communication systems due to its high data rate transmission capability with high bandwidth efficiency and its robustness to multi-path delay. It has been used in wireless LAN standards such as American IEEE802.11a and the European equivalent HIPERLAN/2 and in multimedia wireless services such as Japanese Multimedia Mobile Access Communications. A dynamic estimation of channel is necessary before the demodulation of OFDM signals since the radio channel is frequency selective and time-varying for wideband mobile communication systems [2].

Recently, Selesnick has constructed the new orthogonal discrete wavelet transform, called the slantlet wavelet, with two zero moments and with improved time localization [3]. This Transform method have played an important role in signal and image processing applications. The slantlet has been successfully applied in compression and denoising. It also retains the basic characteristic of the usual filterbank such as octave band characteristic, a scale dilation factor of two and efficient implementation. However, the SLT is based on the principle of designing different filters for different scales unlike iterated filterbank approaches for the DWT [4].

SLANT LET FILTER BANK [5]

It is useful to consider first the usual iterated DWT filter bank and an equivalent form, shown in Figure 1. The symbol a_1 is the symbol with the highest frequency, while symbol a_4 is the symbol with the lowest frequency. The 'slantlet' filter bank described here is based on the second structure in figure (1.b), but it will be occupied by different filters, that are not products. With the extra degrees of freedom obtained by giving up the product form, it is possible to design filters of shorter length, while satisfying orthogonality and zero moment conditions, as will be shown. For the two-channel case, the shortest filters for which the filter bank is orthogonal and having K zero moments, are the well known filters described by Daubechies [6]. For K = 2 zero moments, those filters H (z) and F (z) are of length 4. For this system, designated D2,the iterated filters in Figure 1 are of length 10 and 4. Without the constraint that the filters are products, an orthogonal filter bank with K = 2 zero moments can be obtained where the filter lengths are 8 and 4, as shown in Figure 2, side by side with the iterated D2 system. That reduction of two samples grows with the number of stages, as in Figure 3. We make several comments regarding Figures 2 and 3.

- Each filter bank (equivalently, discrete-time basis) is orthogonal. The filters in the synthesis filter bank are obtained by time-reversal of the analysis filters.
- Each filter bank has 2 zero moments. The filters (except for the lowpass ones) annihilate discrete-time polynomials of degree less than 2.
- Each filter bank has an octave-band characteristic.
- The scale-dilation factor is 2 for each filter bank. Between scales, the filters dilate by roughly a factor of 2. (In the slantlet filter banks, by exactly a factor of 2.)
- Each filter bank provides a multiresolution decomposition. By discarding the highpass channels, and passing only the lowpass channel outputs through the synthesis filter bank, a lower resolution version of the original signal is obtained.

- The slantlet filter bank is less frequency selective than the traditional DWT filter bank, due to the shorter length of the filters. The time-localization is improved with a degradation of frequency selectivity.
- The slantlet filters are piecewise linear.
- In figure 1 it is clear that DWT needs two stages while Slantlet needs one stage only.

It must be admitted that, although both types of filter banks posses the same number of zero moments, the smoothness properties of the filters are somewhat different. In Figures 2 and 3, the slantlet filters have greater "jumps" than do the iterated D2 filters.
However, the Haar basis, with its discontinuities, is suitable for analyzing piecewise constant functions that have jumps. Likewise, the slantlet filter bank appears appropriate for the analysis of piecewise linear functions, as illustrated in the denoising example below.

The ability to model jumps is also relevant for other applications, like edge detection and change point analysis, in which the detection of abrupt changes in an otherwise relatively smooth but unknown function is considered [7]. In figure(2) the S1 is frequency response of F(z) and S2 is frequency response of $H(z)F(z^2)$ and S3 is frequency response of $H(z)H(z^2)$ and V1 is frequency response of $G_1(z)$ and V2 is frequency response of $F_2(Z)$ and V3 is frequency response of $H_2(Z)$ and also in figure(3) the S1 is frequency response of F(z) and S2 is frequency response of $H(z)F(z^2)$ and S3 is frequency response of $H(z)H(z^2)F(z^4)$ and S4 is frequency response of $H(z)H(z^2)H(z^4)$ and V1 is frequency response of $G_1(z)$ and V2 is frequency response of $G_2(z)$ and V3 is frequency response of $F_3(z)$ and V4 is frequency response of $H_3(z)$.

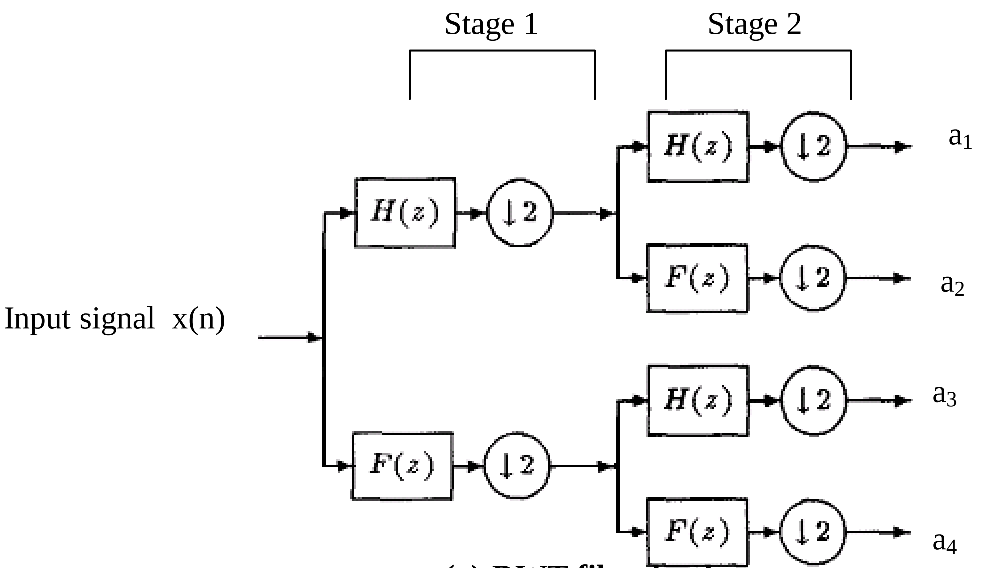

(a) DWT filter bank

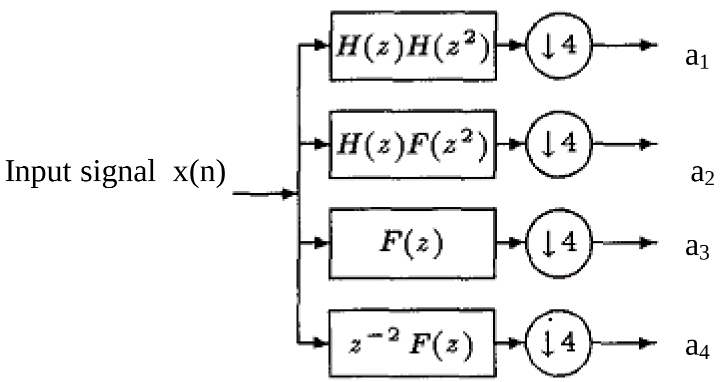

(b) slantlet filter bank

Fig. 1: Iterated filter bank and an equivalent structure.

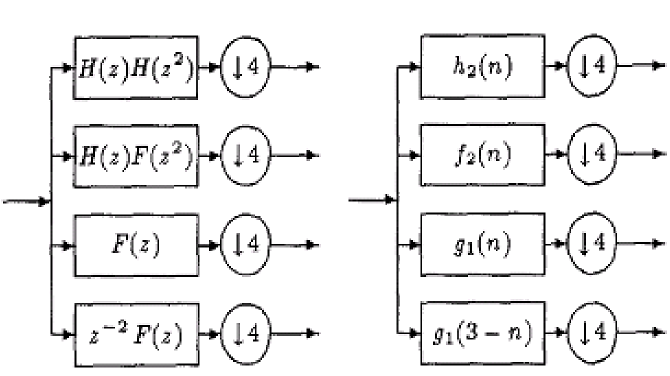

(a) Block diagram

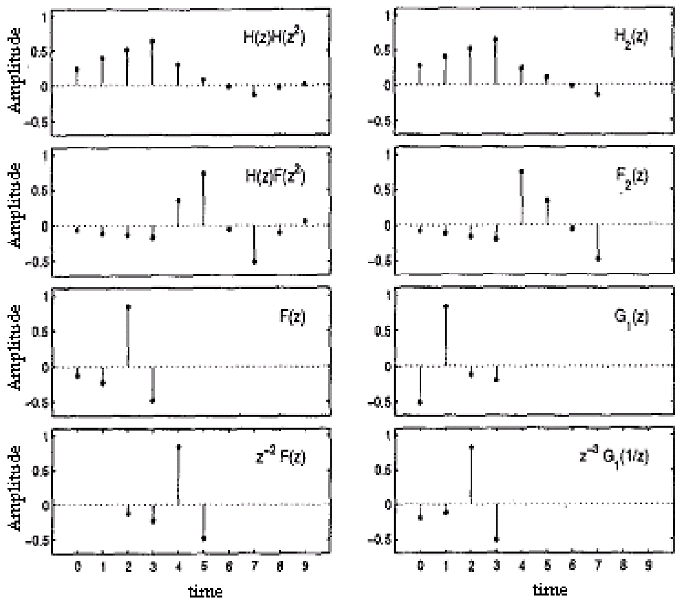

(b) Impulse response of filter bank.

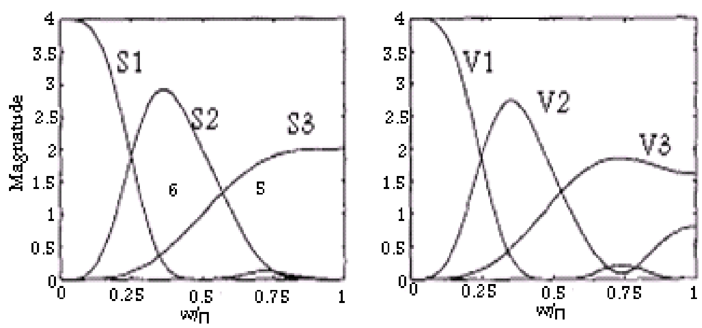

(c) Frequency response.

Fig. 2: Comparison of iterated D2 filter bank (left-hand side) and slantlet filter bank (right-hand side).

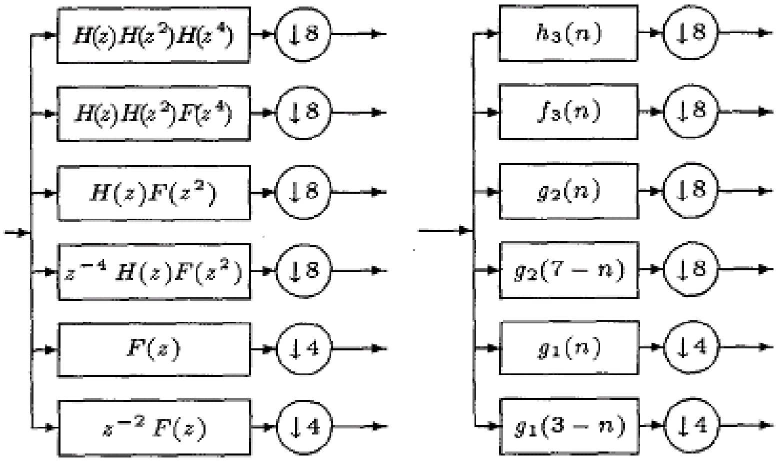

(a) Block diagram

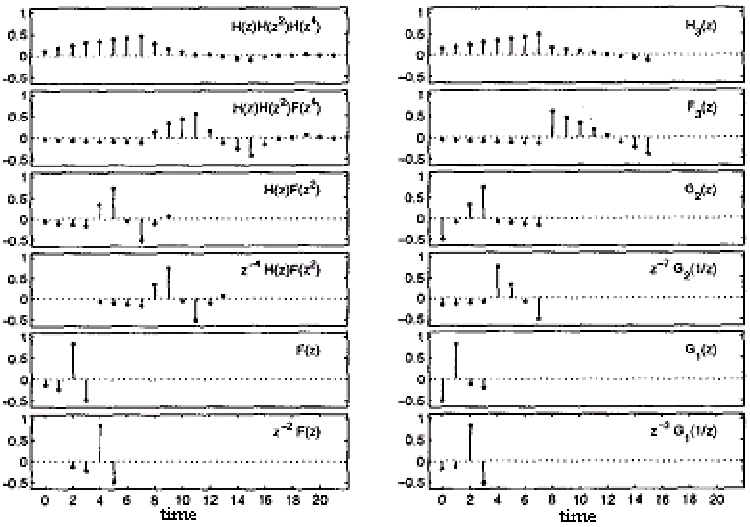

(b) Impulse response of filter bank .

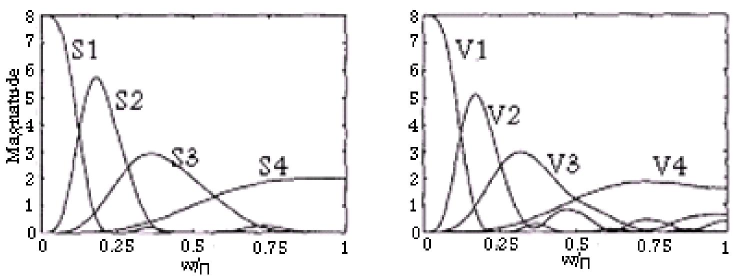

(c) Frequency response.

Fig. 3: Comparison of iterated D2 filter bank (left-hand side) and slantlet filter bank (right-hand side).

A SYSTEM FOR FFT-BASED OFDM

The block diagram of the system for OFDM is depicted in figure (4).

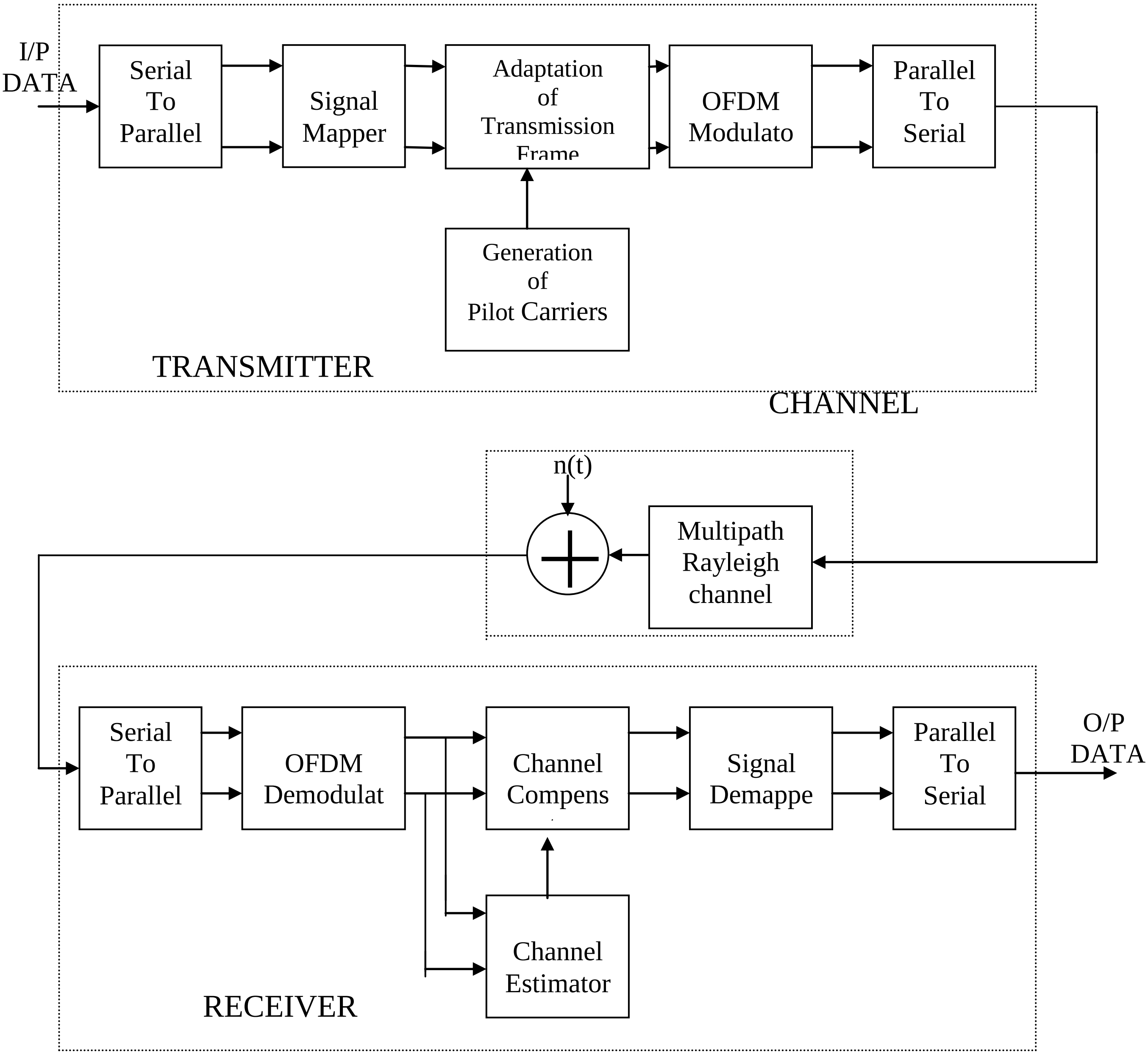

Fig. 4: Block Diagram of OFDM System.

The OFDM modulator and demodulator of FFT-based OFDM is shown in figure (5).

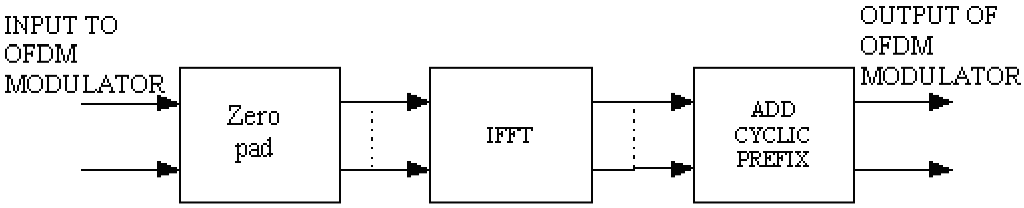

(a) OFDM Modulator.

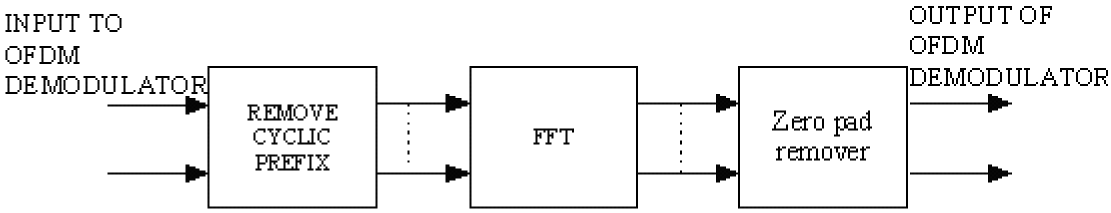

(b) OFDM Demodulator.

Fig. 5: The OFDM modem system.

First of all, the input serial data stream is formatted into the word size required for transmission e.g. 2 bit/word for QPSK and 4 bit/word for 16-QAM, and shift into a parallel format. The data is then transmitted in parallel by assigning each word to one sub-carrier in the transmission. After that, the data to be transmitted on each sub-carrier is then mapped into QPSK or 16-QAM constellation format. This process will convert data to corresponding value of M-ary constellation which is complex word, i.e. real and imaginary part. The training frame (pilot sub-carriers frame) will be inserted and sent prior to information frame. This pilot frame will be used for channel estimation that's used to compensate the channel effects on the signal. After that, the complex words frame and pilots frame will pass to IFFT to generate an OFDM symbol. Zeros will be inserted in some bins of the IFFT in order to make the transmitted spectrum compacts and reduce the adjacent carriers interference.

PROPOSED SYSTEM FOR SLANTLET TRANSFORM -OFDM

The overall system of OFDM is the same as in figure (4). The only difference is the OFDM modulator and demodulator. The slantlet transform SLT-OFDM modulator and demodulator that used are shown in the figure below:

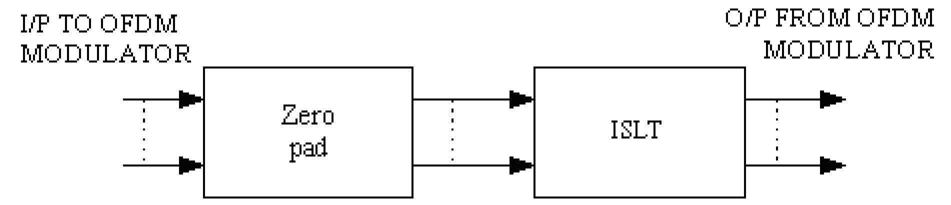

(a) SLT-OFDM modulator.

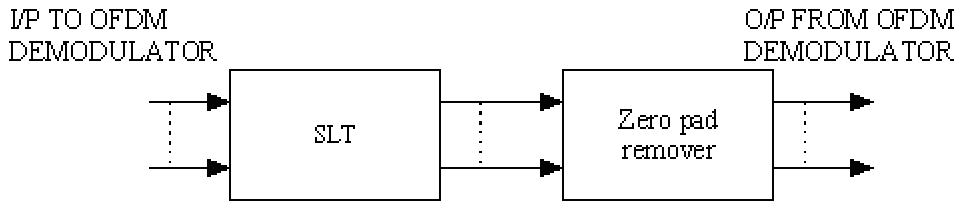

(b)ISLT-OFDM demodulator.

Fig. 6: SLT-OFDM modem system

The processes of the S/P converter, the signal demapper and the insertion of training sequence are the same as in the system of FFT-OFDM. Also the zeros will be added as in the FFT based case and for the same reasons. After that the inverse slantlet transform (ISLT) will be applied to the signal.

The main and important difference between FFT based OFDM and SLT based OFDM is that the SLT based OFDM will not add a cyclic prefix to OFDM symbol. Therefore the data rates in SLT based OFDM can surpass those of the FFT implementation. After that the P/S converter will convert the OFDM symbol to its serial version and will be sent through the channel.

At the receiver, also assuming synchronization conditions are satisfied, first S/P converts the OFDM symbol to parallel version. After that the SLT will be done. Also the zero pad will remove and the other operations of the channel estimation, channel compensation, signal demapper and P/S will be performed in a similar manner to that of the FFT based OFDM.

PERFORMANCE OF THE OFDM SYSTEMS IN THE FLAT FADING CHANNEL:

In this type of channel, the signal will be affected by the flat fading with addition to AWGN (Additive White Gaussian Noise), in this case all the frequency components in the signal will be affected by a constant attenuation and linear phase distortion of the channel, which has been chosen to have a Rayleigh's distribution. A Doppler frequency (Doppler Shift) of 50 & 100 Hz is used in this simulation and the table (1) explains the simulation parameters. Figure (7) show the BER performance of SLT-OFDM and FFT-OFDM in flat fading channel for QPSK modulation type.

Table (1): Simulation Parameters.

Number of sub-carriers	64
Number of SLT points	64
Number of FFT points	64
Channel model	Flat fading+AWGN
	Frequency selective fading+AWGN

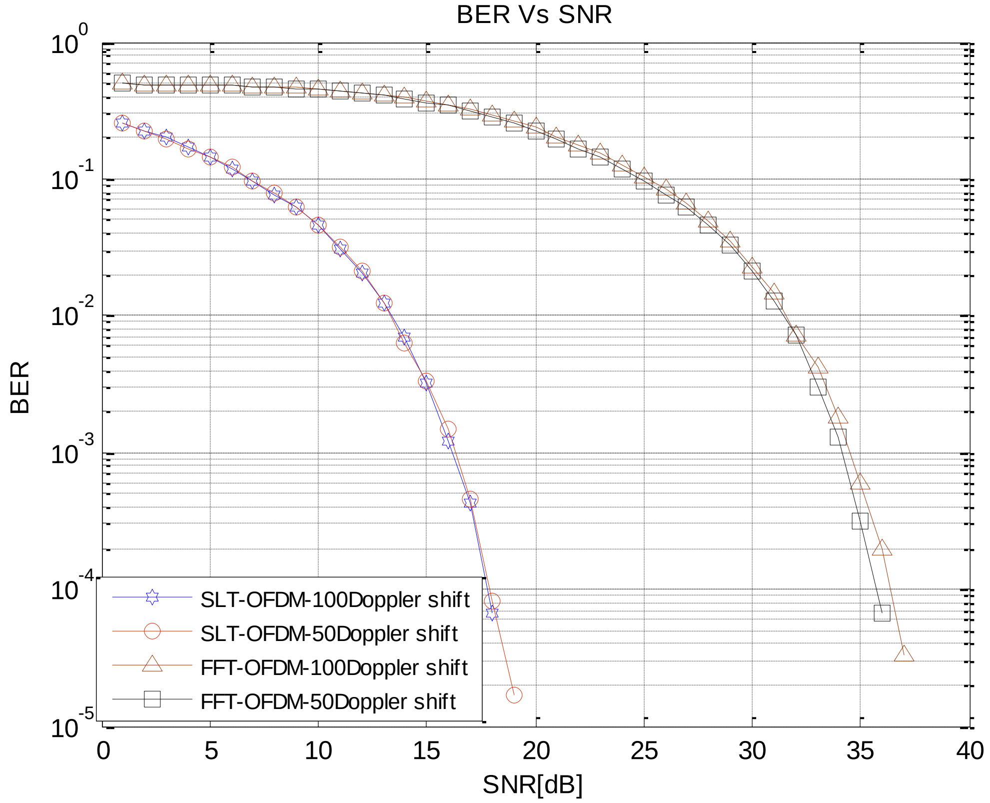

Fig. 7: BER performance of SLT and FFT- OFDM for QPSK modulation in flat fading channel.

The Performance of OFDM Systems in Frequency Selective Fading Channel (multipart's-channel).

The BER performance of SLT and FFT-OFDM systems in frequency selective fading channel are shown in figure (8). This case corresponding to multipaths where two paths are chosen and the attenuation and delay of the second path are -8dB and 8 samples respectively. From the figure (8), it is clear that the BER performance of SLT-OFDM will become constant after a certain SNR. From the same figure, one can see that the BER curves of FFT-OFDM will decrease with the increase of the SNR. In the frequency selective fading the SLT-OFDM is not better than the FFT-OFDM for all the SNR.

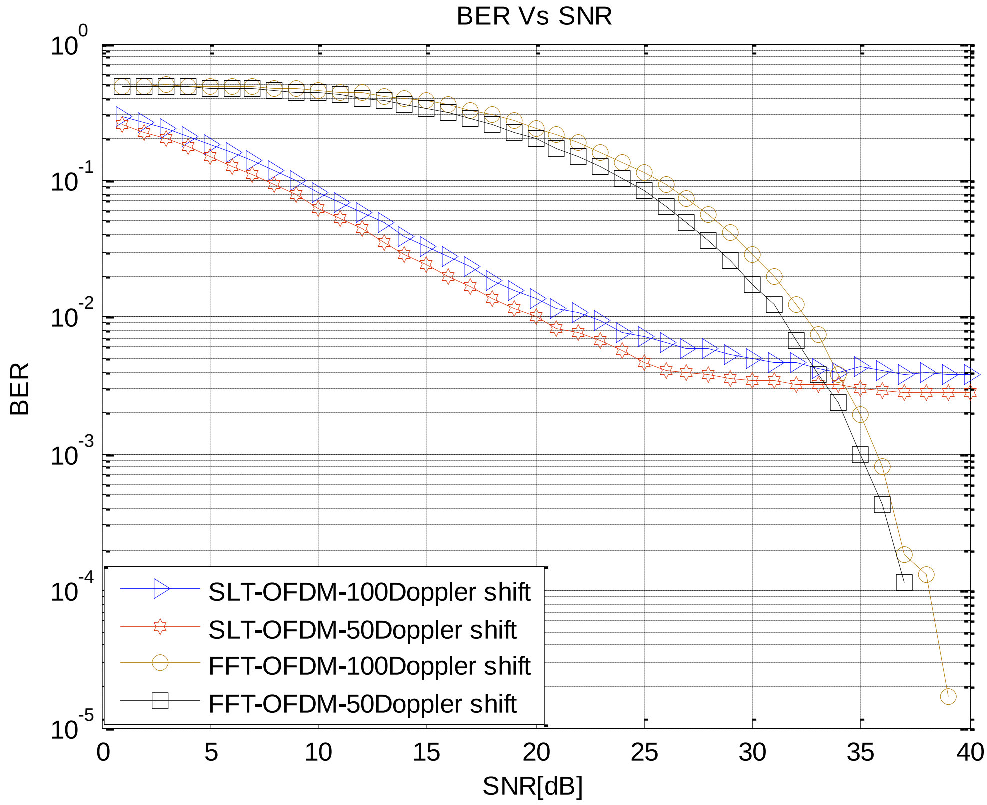

Fig. 8: BER performance of SLT and FFT-OFDM for QPSK modulation in selective fading channel.

The above results can be interpret as follows. The FFT-OFDM has a guard interval(cyclic prefix) of 25% this mean that a cyclic prefix is equivalent to 16-samples, therefore no ISI will effect on the FFT-OFDM until the delay of the second path exceed 16 samples. Since the delay of the second path is equal to 8-samples as assumed above, no ISI will effect on it, while in SLT-OFDM there's no cyclic prefix this mean that ISI will occur in SLT-OFDM. Also due to high spectral containment between the sub-channels in SLT,SLT-OFDM will robust again ISI and ICI until a certain SNR value, after this value , the SLT-OFDM performance will be constant approximately with the increasing of SNR and the FFT-OFDM performance will become better than it.

CONCLUSION

In flat fading channel, it was found that the SLT-OFDM performance was better than that of the FFT-OFDM. A gain of about 18dB was obtained in SLT-OFDM over that for the FFT-OFDM and also the effect of Doppler Shift is very slightly in SLT-OFDM. But in frequency selective fading channel (multipaths case), the situation will be changed. Since the Cyclic Prefix (CP) which is already exists in the FFT-OFDM will eliminate the ISI, therefore no ISI will occurred in FFT-OFDM if the CP is greater than the delay spread of multipaths (in this case we considered that this condition is satisfied). In the case of WP-OFDM there's no CP therefore ISI will occurred. Therefore the BER performance of SLT-OFDM was better than the FFT-OFDM case until a certain value of SNR. After this value the FFT-OFDM was better than SLT-OFDM. It was noticed that the BER curves of SLT-OFDM will become flat (constant with the increase of SNR).

REFERENCES

[1] S. B. Weinstein and Paul M. Ebert, "Data Transmission by Frequency-Division Multiplexing Using the Discrete Fourier Transform", IEEE Transactions on Communication Technology, Vol. COM-19, No. 5, October 1971, pp. 628 – 634

[2] A.Bahai, S.Coleri, M.Ergen, A.Puri"Channel Estimation Techniques Based on Pilot Arrangement in OFDM systems ", IEEE Trans. on Broadcasting, Vol.48, No.3, pp 223-229, September 2002.

[3] Edward R. Dougherty, Jaakko T. Astola, Karen O. Egiazarian "The fast parametric slantlet transform with applications" Proceedings of SPIE -- Volume 5298, May 2004, pp. 1-12.

[4] G. Panda, P. K. Dash, A. K. Pradhan, and S. K. Meher "Data Compression of Power Quality Events Using the Slantlet Transform" IEEE TRANSACTIONS ON POWER DELIVERY, VOL. 17, NO. 2, APRIL 2002.

[5] Ivan W. Selesnick" THE SLANTLET TRANSFORM" Polytechnic University Electrical Engineering 6 Metrotech Center, Brooklyn, 0-7803-5073 ©1998 IEEE

[6] I. Daubechies. Ten Lectures on Wavelets. SIAM, Philadelphia, PA, first edition, 1992.

[7] T. Ogden and E. Parzen. Data dependent wavelet thresholding in nonparametric regression with change-point applications. Computational Statistics and Data Analysis, 2253-70, 1996.

طرائق الازالة في تقليل اعداد الطحالب في مياه الاحواض المكشوفة

Removal Method Assessment Through Reduction Algae Count in Uncovered water Reservoir

د. ثائر ابراهيم قاسم
Dr. Thaer I. Kassim
جامعة بغداد– معهد الهندسة الوراثية

أ.د رافع هاشم السهيلي
Prof. Dr. Rafa H. Suhaili
جامعة بغداد – كلية الهندسة

م . م محمد صادق سلمان
Mohammed S. Salman
جامعة بغداد– كلية الهندسة

الخلاصة

تعد الطحالب من المسببات الرئيسية في مشاكل واسعة في محطات المياه والانهار والبحيرات والقنوات الاروائية ، وما تسببه من مشاكل في الطعم والرائحة وأنسداد القنوات وتغير خصائص قاعدية المياه نتيجة لتواجدها بكثرة حيث أعتبرت الطحالب معياراً لتلوث المياه السطحية. تم في هذا البحث اعتماد طرائق السيطرة الكيميائية مختبريا باستخدام جهاز فحص الجرة (Jar Test) وذلك من خلال استخدام مركبات كيميائية مثل الشب بتراكيز (10 - 50) ملغم/لتر وتم الحصول على نسبة تقليل العكورة بمقدار (94%) وبالتالي تقليل اعداد الطحالب بنسبة(95%). اضافة الى ذلك تم استخدام مركبات كيميائية مثل برمنكنات البوتاسيوم وكبريتات النحاس ومادة الهايبوكلوراين (كلور) بتراكيز من (1 - 5) ملغم/لتر بعد اضافة التركيز الامثل للشب وكانت نتائج نسب تقليل العكورة 95% و 79.3% و و95% على التوالي ونسب أزالة الطحالب 99.2% و 100% و 99% على التوالي.

Abstract

The Algae is considered as one of the major causes of some serious problems that occur in water plants, rivers, lakes and irrigation channels. Those problems are the unpleasant taste and odor, the clogging of waterways, and others. Hence, the algae existing extensively in any water body is considered as an obvious indication of surface water pollution.

Chemical control methods were used in this research for reducing the turbidity and Algae in the laboratory using the (Jar Test). This was done by using chemical materials like Alum with concentration (10 - 50 mg/l). The percentage of the reduction in the algae was (95%) and in turbidity (94%). It is shown also that when using $KMnO_4$, $CuSO_4$ and Cl, each separately after adding the ideal dose of alum found before, will reduce the turbidity with (95% ,79.3% .95%) and algae removal of (99.2%, 100%, 99%) respectively

الكلمات الرئيسية: الطحالب ، الازالة ، تقليل ، العكورة ، سيطرة ، معالجة ، كيميائية ، فيزيائية ، اثراء غذائي ، بايولوجية.

المقدمة

تسبب الطحالب ظهور عدد من المشاكل في المياه حيث تعيق حركة الماء في أنظمة التفريغ Drainage System والإنسداد بالمضخات والصمامات ، وتؤثر على نمو الاسماك وحركتها وبقية الاشكال الحياتية في الماء و تسبب كذلك مشكلة الرائحة والطعم في المياه مما يؤدي الى مخاطر صحية على الحياة البشرية والحياة المائية (Rashash *et al*.,1996)

هذه المشاكل تبدو في حالة الازدياد بسبب ارتفاع نسبة المغذيات الناتجة عن النشاط البشري والعمليات الطبيعية ، وبنفس الوقت هناك طلب عالمي واضح حول فحص نوعية الماء المستخدم. ومما ورد ذكره هناك متطلب واضح هو الحد من أو السيطرة على نمو الطحالب لأسباب بيئية وصحية وبشرية.

الطحالب صغيرة الحجم وسريعة النمو بالاضافة إلى أنه من الصعب السيطرة عليها بالطرائق التي تستخدم لبقية النباتات المائية مثل القطع أي بالطرق الميكانيكية التي تساعد في تقليل اثر هذه المشاكل مع الطحالب الخيطية. يتأثر نمو بعض الطحالب بأستخدام المبيدات ولكن هناك تأثيرات جانبية على الصحة العامة والبيئة إضافة الى أن هذه المبيدات تؤثر على جميع انواع الأحياء في المسطحات المائية بالإضافة إلى أن الطحالب تعود مرة اخرى للنمو بعد زوال تأثير المبيدات (إنخفاض تركيزه) وقد يكون النمو بشكل أكثف من السابق .

الطرائق مستخدمة في عملية السيطرةعلى الطحالب منها:-

أ - السيطرة على عملية الاثراء الغذائي

تعد طرائق السيطرة على عملية الاثراء الغذائي هي الأهم ، ويقصد بها السيطرة على مصادر المغذيات حيث يتم السيطرة على المنابع التي يكون الاثراء الغذائي فيها بنسب عالية ، حيث اكد (Kathandaraman and Evans, 1983) ان السيطرة على الطحالب في البحيرات تتم من خلال الادارة الجيدة لمصادر المياه في البحيرات. اشار (Sawyer,1968) الى ضرورة الحاجة الى دقة العمليات الزراعية والسيطرة التامة على عملية معالجة المخلفات المدنية السائلة والمخلفات الصناعية للحد من ظاهرة الاثراء الغذائي. وناقش (Makenthun and kemp,1970) أيضاً عدم مثالية التقنية المستخدمة لأزالة المغذيات بوساطة استخدام اسماك او نمو النباتات أو امكانية تحريك الرواكد القاعية بوساطة مواد غير قابلة للتفاعل.

ب – السيطرة الفيزيائية

تتضمن طرائق السيطرة الفيزيائية على الطحالب الازالة الميكانيكية لها Harvesting أواستخدام اصباغ لغرض تقليل نفوذ الضوء وازالة الرواكد وكذلك استخدام شحنات او أشعة (Ultrasonic) والتي تؤثر على خلخلة الغاز في السائل الخلوي للطحالب وعلى الاحياء الاخرى ايضاً وهذا غير مقبول ، أو السيطرة عليها من خلال التحكم بمستوى الماء وجريانه. كذلك تم استخدام الفحم المنشط ولكن لم يكن هناك اقبال واضح لهذه الطريقة في خزانات تجهيز المياه (Janik,1980). أذ يمكن إستخدام قليل من مسحوق الكاربون المنشط (Powdered activated carbon) للسيطرة على الطحالب في الماء والذي يساعد على تجمع أو تخثر الطحالب وبالتالي يمكن إزالتها (Morris and Riley, 1963) .

جـ – السيطرة الكيميائية

من الطرائق الاخرى في السيطرة على الطحالب هي السيطرة الكيميائية باستخدام المبيدات ومن المركبات الشائعة الاستخدام هي مركبات النحاس مثل كبريتات النحاس (Steel and McGhee , 1979) وبرمنكنات البوتاسيوم الذي استخدم بنجاح في بعض الحالات (Ficek, 1983). أما المبيدات الاخرى فهي محدودة الإستخدام في السيطرة على الطحالب مثل Rosin amines و Triazine derivative وخليط من كبريتات النحاس مع نترات الفضة ومركبات الامونيوم الرباعي وأحماض عضوية وألديهايدات وكيتونات. وبعد أختبار أكثر من 10000 مركب عضوي ثبت بأن P-chlorphenyl-2thienyl iodonium chloride هو أفضل المركبات فعالية في السيطرة على الطحالب (Prows and McIlhenny, 1974).

عمل كثير من الباحثين بأتجاه ايجاد بدائل عن كبريتات النحاس للسيطرة على الطحالب ولكن نظراً للكلفة الاقتصادية الواطئة لكبريتات النحاس جعلتها مفضلة في الاستخدام ، يعتبر الكلور والشب Alum الذي يعتبر مواد مختثرة من أفضل المواد التي تستخدم من اجل السيطرة على الطحالب بالرغم من المشاكل السمية تجاه الحياة المائية التي أخذت بنظر الأعتبارفي إستخدام هذه المواد (Sawyer, 1968).

د – السيطرة البايولوجية

يمكن استخدام فكرة نظام السيطرة البايولوجية مع الأخذ بنظر الاعتبار أنها تسبب ضرر على البيئة بدلاً من السيطرة بالطرائق الكيميائية . فكثير من الطرائق البايولوجية المتنوعة للسيطرة على الطحالب تم ابتكارها وتتضمن إستخدام فايروسات وبكتريا وفطريات وإستخدام مجاميع ناشطة للكشف مثل الابتدائيات والهائمات الحيوانية والأسماك (Dunst, 1974).

الجانب العملي

تم اجراء تجارب لدراسة تأثير بعض المركبات الكيميائية مثل كبريتات النحاس وبرمنكنات البوتاسيوم والكلوراين على الطحالب وعملية إزالتها من مصدر المياه الداخلة للأحواض Raw Water بوجود الشب الذي تم استخدامه كمخثر Coagulant.

تمت التجارب اعلاه باستخدام جهاز Jar Test والغرض من هذه التجارب هو دراسة أثر التركيز الفعال للمواد المضافة في عملية إزالة الطحالب وتقليل العكورة .

تضمن العمل المختبري تحضير المحاليل اللازمة لكل تجربة وكما يلي :

أ- محلول الشب

تم تحضير محلول الشب من خلال اذابة 1 غرام من حبيبات او مسحوق الشب ($Al_2SO_4.18H_2O$) والذي يسمى محلياً بشب المحطة المتوافر في محطات التصفية في 100 مل من الماء المقطر وتمت عملية المزج بوساطة جهاز دوار مغناطيسي Magnetic Stirrer لمدة ساعة حيث يتم الحصول على محلول من الشب تركيزه 1%. ومن هذا المحلول تم تحضير محاليل التجربة لمعاملتها بجهاز Jar Test بالنسبة للحاويات سعة 1 لتر تحتوي على مياه النموذج حيث يتم سحب 1 و 2 و 3 و 4 و 5 مل على التوالي من المحلول ويضاف الى خمس حاويات من اصل ستة لغرض الحصول على تركيز الشب في هذه الحاويات بمقدار (10, 20, 30, 40, 50) ملغم/لتر على التوالي . ويتم أستخدام جهاز Jar Test وفق الخطوات التالية بعد اضافة الشب الى الحاويات الخمسة حيث تترك الحاوية السادسة بلا اضافة.

أ- اجراء مزج سريع لمدة دقيقة واحدة بسرعة 200 دورة بالدقيقة لغرض تجانس المحلول في الحاويات

ب- اجراء مزج بطئ بسرعة 20 دورة بالدقيقة لمدة 20 دقيقة

جـ- ايقاف عملية المزج البطي وترك المحاليل لمدة 30 دقيقة لغرض التركيد

ء- قياس العكورة و pH وأعداد الطحالب لغرض بيان أفضل جرعة للشب والتي تعطي أوطئ قراءة للعكورة.

ب - محلول برمنكنات البوتاسيوم والكلوراين وكبريتات النحاس.

حضر محلول برمنكنات البوتاسيوم $KMnO_4$ ذو نقاوة 99.5 % منشأ أنكليزي من خلال اذابة 1غرام من المادة في 100 مل من الماء المقطر للحصول على محلول بتركيز 1% والذي أخذ منه 0.1 و 0.2 و 0.3 و 0.4 و 0.5 مل على التوالي لكي يتم اضافته الى نماذج الماء والتي تحتوي مسبقا على الجرعة المثالية للشب من الخطوة السابقة لذلك سيكون تراكيز محلول برمنكنات البوتاسيوم في خمس حاويات هي (1 , 2 , 3 ,4 , 5) ملغم /لتر ويتم اعادة الخطوات أ ، ب ، جـ لعملية استخدام جهاز Jar Test ويتم قياس العكورة وpH وأعداد الطحالب. لغرض بيان افضل جرعة لبرمنكنات البوتاسيوم والتي تعطي افضل القراءات .وكذلك الحال في عملية تحضير محلول الكلوراين وكبريتات النحاس.

النتائج والمناقشة

أن من الطرائق التقليدية لتقيم عملية التخثير والازالة هي فحص الجرة (Jar Test) حيث تمتاز هذه الطريقة بالبساطة والمرونة وتعطي صورة واضحة عن التخثير والتلبيد والترسيب ومعلومات مفصلة عن فترة التلبيد وميكانيكية المزج وتأثير بعض العوامل مثل درجة الحرارة وكمية ونوعية المخثر والاس الهيدروجيني ، لذ تعتبر أهم وسيلة مختبرية في أيجاد أنسب جرعة من المخثر ويعتبر أسلوب Jar Test نموذج مصغر لتقييم كل المتغيرات في عملية التخثير وعندما تكون وحدات المعالجة غير موجودة (Hannah *et al.*, 1967).

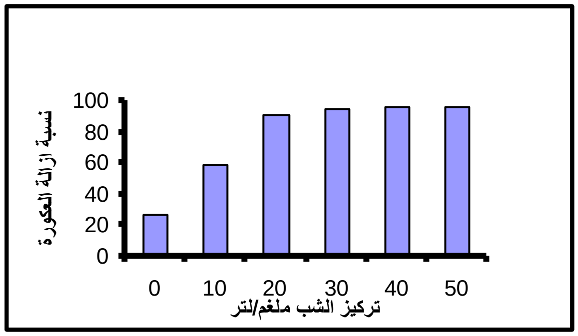

شكل (١) تغيرات نسب الازالة للعكورة مع تراكيز الشب خلال مدة البحث

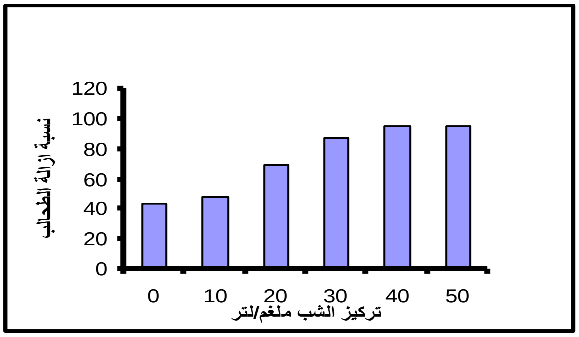

شكل (٢) تغيرات نسب الازالة الطحالب مع تراكيز الشب خلال مدة البحث

استخدام الشب

يتضح من خلال النتائج المستحصلة من التجارب المختبرية (**الشكل ١ والشكل ٢**) بأن مادة الشب لها امكانية ازالة بنسبة تتراوح بين 30.4 – 94.6 % من العكورة الكلية ، وبالتالي تقليل اعداد الطحالب من 2708253فرد/لتر الى 6197 فرد/لتر اي بنسبة ازالة 95% . واغلب تراكيز الادنى للشب أنحصرت بين 40 - 30 ملغم /لتر

أضافة الذلك فأن قيمة الاس الهيدروجيني قد تناقصت بزيادة تركيز الشب والمواد الكيميائية الاخرى من (8.1 – 7.2) وهذا ما يتطابق مع ما لاحظه (Kim ,2000) أذ وجد بأن أفضل قيمة للاس الهيدروجيني لتحقيق عملية التخثير تعتمد على القيمة الاولية للقاعدية، حيث أنه بزيادة قاعدية المحلول فأن مدى الاس الهيدروجيني سوف يقل كما في جدول رقم (١)

جدول (١) **قيم تغير الاس الهيدروجيني مع أختلاف تراكيز المواد الكيمياوية بثبوت الشب**

pH	تراكيز $CuSO_4$ mg/l	pH	تراكيز Cl_2 Mg/l	pH	تراكيز $KMnO_4$ mg/l	pH	تراكيز الشب mg/l

Raw Water	8.1	Raw Water	8.1	Raw Water	8.1	Raw Water	8.1
0	8.1	0	7.3	0	7.9	0	7.7
10	7.7	1	7.3	1	7.6	1	7.2
٢٠	٧,٥	٢	7.3	٢	7.4	٢	7.2
٣٠	٧,٣	٣	7.3	٣	7.3	٣	7.2
٤٠	٧,٣	٤	7.3	٤	7.3	٤	7.2
٥٠	٧,٢	٥	7.3	٥	7.2	٥	7.2

استخدام برمنكنات البوتاسيوم

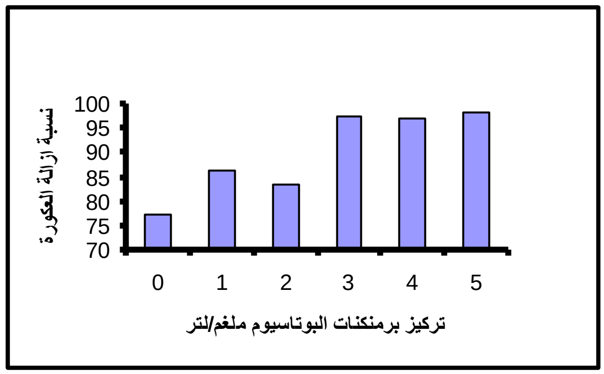

شكل (٣) تغيرات نسب الازالة للعكورة مع تراكيز برمنكنات البوتاسيوم بثبوت الشب خلال مدة البحث

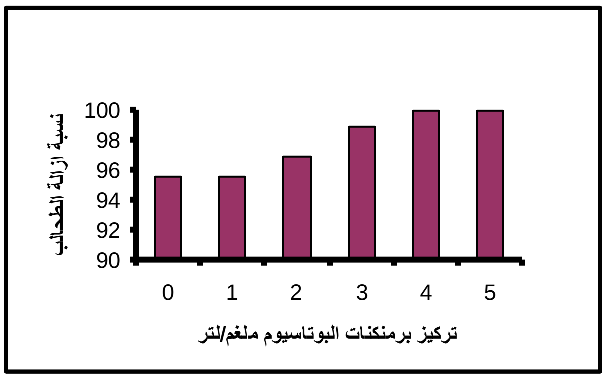

شكل (٤) تغيرات نسب الازالة الطحالب مع تراكيز برمنكنات البوتاسيوم بثبوت الشب خلال مدة البحث

اما عند استخدام برمنكات البوتاسيوم كمؤكسد ابتدائي والكلورة الابتدائية واعتماد التراكيز الادنى للشب حيث أتضح بان استخدام برمنكات البوتاسيوم مع التركيز الادنى للشب (**الشكل ٣ و الشكل ٤**) يحسن كفاءة اداء عملية التخثير في إزالة العكورة بنسبة من 88% الى 98% . وبالتالي تقليل اعداد الطحالب من 2708253 فرد / لتر الى الصفر وبنسبة ازالة قدرها 96.2 – 99.5 %. ويعزى السبب في ذلك الى تكون ثنائي اوكسيد المنغنيز (Manganese dioxide) خلال عملية الاكسدة بالبرمنكات والذي يؤدي الى تحسين كفاءة التخثير وبالتالي تكسير المواد العضوية والغروية من خلال تشكيل ملبدات تؤدي الى الترسيب او قد تعزى ايضا الى قابلية أوكسيد المنغنيز العالية على الامدصاص للمواد العضوية من خلال الاواصر الهيدروجينية وبالتالي تكون ملبدات كبيرة الحجم والتي تزيد من عملية الترسيب بالجاذبية. (Ma *et al*., 1997)

استخدام مادة الكلور

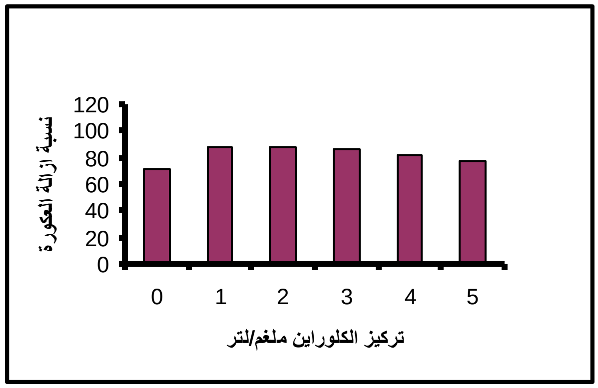

شكل (٥) تغيرات نسب الازالة للعكورة مع تراكيز الكلور بثبوت الشب خلال مدة البحث

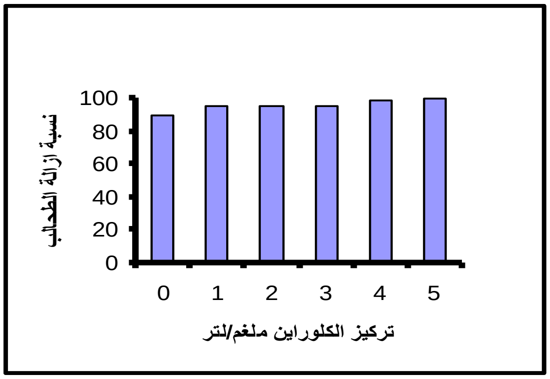

شكل (٦) تغيرات نسب الازالة الطحالب مع تراكيز الكلور بثبوت الشب خلال مدة البحث

اما عند استخدام تراكيز الكلورة الابتدائية وباعتماد التركيز الادنى للشب فقد لوحظ بان التراكيز القليلة للكلور (الشكل ٥ والشكل ٦) تقلل العكورة للمياه المترسبة بنسبة 95 % ولكن عند استخدام التراكيز الأعلى يؤدي الى زيادة العكورة بنسبة 12 % وتذبذب ازالة الطحالب بنسبة من (93 - 99) %.

استخدام مادة كبريتات النحاس

أما عند أستخدام كبريتات النحاس للازالة او السيطرة على الطحالب لاحظ (Steel and McGhee, 1979) أنخفاض نسبة تركيز الاوكسجين في الماء وزيادة نسبة النحاس في الرواسب. وهناك عدة دراسات استخدمت النحاس كمزيل للطحالب في البحيرات والقنوات الاروائية حيث تباينت التراكيز المثلى من 0.5 – 10 ملغم /لتر اعتماداً على عدة عوامل منها شكل البحيرة والصفات الفيزيائية والكيميائية للماء بالاضافة الى الخصائص الهيدروليكية لها (Charles, 1978). و لوحظ عند استخدام النسب العالية من كبريتات النحاس فأنه يؤدي الى قتل الاسماك بالاضافة الى توالد مقاومة للطحالب ضد كبريتات النحاس لذى يتطلب دقة عند احتساب الجرع المثلى لكبريتات النحاس اللازمة لازالة الطحالب اعتماداً على قاعدية الماء حيث تتأثر المركبات المعقدة والسمية الناجمة عن تفاعل كبريتات النحاس مع المواد العضوية المتواجدة في الماء عند اس هيدروجيني 7 فأن 55% من النحاس الذائب يتحول الى ايون النحاس وعند أس هيدروجيني 8 فان 10% من النحاس الذائب يتحول الى ايون النحاس وهو المسؤول عن السمية المتراكمة في الماء (Raman, 1985).

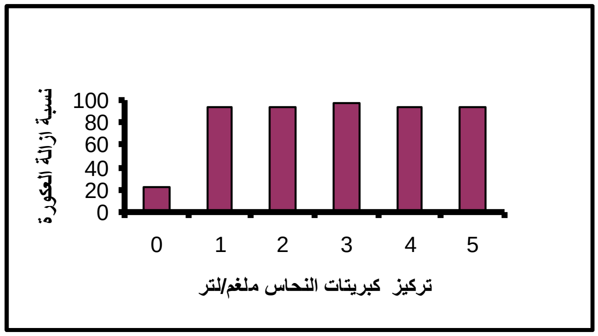

شكل (٧) تغيرات نسب الازالة للعكورة مع تراكيز كبريتات النحاس بثبوت الشب خلال مدة البحث

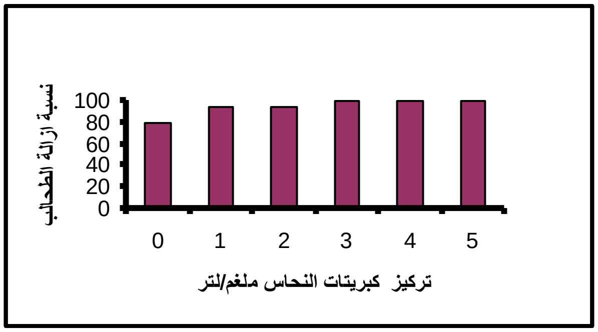

شكل (٨) تغيرات نسب الازالة الطحالب مع تراكيز كبريتات النحاس بثبوت الشب خلال مدة البحث

عند أجراء تجارب مختبرية بأستخدام جهاز Jar Test وبأعتماد جرع مختلفة من كبريتات النحاس تتراوح من 5 – 1 ملغم / لتر وبجرعة ثابتة من الشب بمقدار 30–40 ملغم / لتر لوحظ من (الشكل ٧ والشكل ٨) ان العكورة تقل بمقدار يتراوح من 1.12–14.7 NTU بمعدل ازالة يتراوح من 73.4 – 83.3 % من العكورة الكلية وبالتالي يقلل أعداد الطحالب من 135062 فرد/لتر الى الصفر أي بنسبة أزالة 100%. ويعزى السبب الى تداخل كبريتات النحاس كيميائياً مع المركبات العضوية للطحالب وهذا يتفق مع (Charles,1978) حيث كانت أفضل نسبة أزالة للعكورة والطحالب عند أستخدام جرع كبريتات النحاس بتركيز يتراوح بين 3 – 4 ملغم / لتر و يتفق كذلك مع (Robert *et al.*,1980) وبسببها تأثرت قيمة الحامضية وبالتناقص مع زيادة جرع $CuSO_4$.

الاستنتاجات

١– ان أستخدام برمنكنات البوتاسيوم ذو فعالية أعلى من الكلورة الابتدائية مع استخدام الشب في تحسين كفاءة عملية التخثير لازالة العكورة واعداد الطحالب بنسبة 99% أضافة الى أنة مادة غير سامة وذو تأثير طويل مما يفضل استخدامها على كبريتات النحاس .

٢– أن قيم pH عند استخدام تراكيز برمنكنات البوتاسيوم أقل من قيم pH عند استخدام نفس التراكيز من الكلور.

References

Charles B. Muchmore, (1978) "Algae Control In Water Supply Reservoirs", Jour. AWWA, 70,273-278.

Dunst, R. C. (1974). Survey of Lake Rehabilitation Techniques and Experience Tech. Bull. 75. Dept. Natural Resource, Madison, wis.

Ficek, K. J. (1983). Raw Water Reservoir Treatment with Potassium Permanganate.,74th Ann. Mtg. III. Sec. AWWA. Chicago. III. 3 :3:14490.

Hannah, S. A. , Cohen, J. M. and Robeck, G. G. (1967). Control Techniques for coagulation – Filteration. Jour. AWWA, 59 : 9 : 1149 – 1163.

Janik, J. F. (1980). A Compilation of Common Algal-Control and Management Techniques., Univ. Nev., Las Vegas. Steel, E. W. and Mc Ghee, T. J. (1979). Water Supply and Sewerage. Fifth edition McGraw-Hill Book Company, Japan, 285 pp.

Kim Luu (2000) " Study of Coagulation and Settling Processes for Implementation in Nepal " Submitted To the Department of Civil and Environmental Engineering in Partial Fulfillment of the Requirements for the Degree Of Master of Engineering in Civil and Environmental Engineering

Kothandaraman, V. & Evans, R.L. (1983) Diagnostic-Feasibility Study of Johnson Sank Trail Lake., Contract Rept. 312, State Water Survey, Urbana

Ma, J., Graham, N.J.D., And Li, G.B. (1997) “Effectiveness Of Permanganate Preoxidation In Enhancing The Coagulation Of Surface Waters-Laboratory Studies” Journal Water SRT-Aqua, 46(1), 1-11.

Mackenthun, K. M. & Kemp, L. E. (1970). Biological Problems Encountered in Water Supplies. Jour. AWWA , 62:8:520.

Morris , A.W & Riley, J.P. , 1963 . The determination of nitrate in sea water. Analytica chim. Acta , vol. 29 , pp. 272 – 297

Prows, B. L. & Mcilhenny, W. F. (1974). Research and Development of a Selective Algicide to Control Algal Growth. Ofce.Res. & Devel., USEPA, Washington, D.C.

Raman K. Raman, (1985) “Controlling Algae In Water Supply Impoundments” Jour. AWWA, 77:8:Pp. 41-43

Rashash, D., Hoehn, R., Dietrich, A., Grizzard, T., Parker, B. (1996)"Identification and Control of Odorous Algal Metabolites"J. AWWA Research Foundation and American Water Works Association.

Robert C. Hoehn, Donald B. Barnes, Barbara C. Thompson, Clifford W. Randall, Thomas J. Grizzard, And Peter T.B. Shaffer, (1980). Algae as Sources of Trihalomethane Precursors. Jour. AWWA, 72:6:Pp.344-350.

Sawyer, C. N. (1968). The Need for Nutrient Control., Jour. WPCF, 40:3:363.

Steel, E. W. and Mc Ghee, T. J. (1979). Water Supply and Sewerage. Fifth edition McGraw-Hill Book Company, Japan, 285 pp.

THE MIGRATION OF LIGHT ORGANIC LIGUIDS IN AN UNSATURATED-SATURATED ZONE OF THE SOIL

Prof. Dr. Rafa H. Al-Suhaili* **Lec. Dr. Ayad A. Faisal***
University of Baghdad / College of Engineering.

ABSTRACT

A one-dimensional finite difference model for the simultaneous movement of light non-aqueous phase liquid (LNAPL) and water through unsaturated-saturated zone of the soil in a three fluid phase system with air assumed constant at atmospheric pressure is developed. The flow equations described the motion of light non-aqueous phase liquid and water are cast in terms of the wetting and non-wetting fluid pressure heads respectively. The finite difference equations are solved fully implicitly using Newton-Raphson iteration scheme. The present numerical results are compared with results of Kaluarachchi and Parker (1989) and there is a good agreement between them. The present model can be used to simulate various transport problems in a good manner. Results proved that the maximum LNAPL saturation occurred below the source of the contaminant during LNAPL infiltration. During redistribution, the LNAPL saturation had a maximum value at the advancing of the LNAPL infiltration front.

الخــلاصـــة

في هذه الدراسة تم تطوير نموذج عددي ذو بعد واحد يستخدم الفروقات المحددة لوصف حركة الماء والسائل العضوي الأخف منه خلال التربة المشبعة وغير المشبعة مع ثبوت ضغط الهواء عند الضغط الجوي. أن المعادلات التي تصف حركة الماء والسائل العضوي وضعت بدلالة عمود الضغط لتلك السوائل. أن معادلات الفروقات المحددة حلت (fully implicitly) وباستخدام طريقة (Newton-Raphson). تمت عملية اختبار كفاءة النموذج الحالي من خلال مقارنة نتائجه مع نتائج النموذج المقدم من قبل(Kaluarachchi and Parker (1989. أن النموذج الحالي ممكن آن يستخدم لوصف مختلف المسائل بشكل جيد. أن اكبر تشبع بالملوث يحدث اسفل مصدر التلوث خلال التسرب في حين تكون هذه القيمة في مقدمة جبهة الملوث خلال اعادة التوزيع.

KEYWORDS: Multiphase, Unsaturated, Saturated, Modeling And Contaminant

.

INTRODUCTION

Groundwater contamination due to surface spills or subsurface leakage of Light Non-Aqueous Phase Liquids (LNAPLs) such as hydrocarbon fuels, organic solvents, and other immiscible organic liquids is a widespread problem which poses a serious threat to groundwater resources. These compounds have some acute and long-term toxic effects. As these compounds are migrated through unsaturated-saturated zone, they will pollute great extents of soil and groundwater. This represents a major environmental problem. According to the Environmental Protection Agency (EPA) records, there are 1.8 million underground storage tanks which are in use in the United States. According to EPA estimates 280000 tanks are leaking, from which more than 20% are discharging their contents directly to the groundwater (El-Kadi, 1992). Light Non-Aqueous Phase Liquids (NAPLs) are organic fluids that are only slightly miscible with water where the “L” stands for “lighter” than water, i.e., less denser than water.

As the LNAPL (or oil) migrates, the quantity of mobile oil decreases due to the residual oil left behind. If the amount of oil spilled is small, all of the mobile oil will eventually become exhausted and the oil will percolate no further. The column of oil is immobile and never reaches the capillary fringe unless it is displaced by water from a surface source. However, if the quantity of oil spilled per unit surface area is large, mobile oil will reach the water table. Depending on the nature of the spill, a mound of the oil will develop and spread laterally. Fig.1 is a pictorial conceptualization of a subsurface area to which LNAPL is introduced from an oil source, resulting in contamination of the unsaturated and saturated zones. The LNAPL plume (Fig.1)through the unsaturated zone and it forms a free-product mound floating on the water table. This mound will spread laterally and move in the direction of decreasing hydraulic gradient until it reaches residual and can travel no further (Kim and Corapcioglu, 2003).

Floating LNAPL can partly be removed by using a pumping well. The LNAPL will flow towards the well facilitated by the water table gradient and can be pumped into a recovery tank. The movement of oil through unsaturated and saturated zones will accompanied with leaving the residual droplets (or ganglia) in the pore spaces between the soil particles. This remaining oil may persist for long periods of time, slowly dissolving into the water and moving in the water phase through advection and dispersion. In the unsaturated zone, residual oil as well as oil dissolved in the water phase may also volatilize into the soil gas phase. In the absence of significant pressure and temperature gradients in the soil gas phase, vapors less dense than air may rise to the ground surface, while those more dense than air may sink to the capillary fringe, leading to increased contamination of the saturated zone. Once in the groundwater system, estimates of oil plume migration over time is necessary in order to design an efficient and effective remediation program. Groundwater modeling serves as a quick and efficient tool in setting up the appropriate remediation program. In many regulatory jurisdictions the use of the liquid phase contaminant in an environmental field setting is prohibited, and numerical modeling is therefore often the only practical alternative in studying the field-scale behaviour of these compounds (Kim and Corapcioglu, 2003).

A number of multiphase flow models in the contaminant hydrology literature have been presented. Faust (1985) presented an isothermal two-dimensional finite difference simulator. It describes the simultaneous flow of water and NAPL under saturated and unsaturated conditions. Abriola and Pinder (1985) formulated a one-dimensional finite difference model which included immiscible organic flow, water flow, and equilibrium inter-phase transfer between the immiscible organic phase, the water phase, and a static gas phase as cited by Sleep and Sykes (1989). Faust et al. (1989) developed model that might be used to three-dimensional two-phase transient flow system based on finite difference formulation. The governing equations were cast in terms of non-wetting fluid (NAPL) pressure and water saturation. Similarly, Parker et al. and Kuppusamy et al. as cited by (Suk, 2003) developed a two-dimensional multiphase flow simulator involving three immiscible fluids: namely, air, water and NAPL with the assumption of constant air phase pressure. Kaluarachchi and Parker (1989) applied a two-dimensional finite element model named MOFA-2D for three phases, multicomponent, isothermal flow and transport by allowing for interphase mass exchange but assuming gas phase pressure gradients are negligible.

The present study is aimed to develop a verified multiphase, one-dimensional, finite-difference numerical simulator which tracks the percentage of LNAPL saturation as well as the lateral and vertical position of the LNAPL plume in the subsurface at the specified times with different types of boundary conditions. The present model is formulated in terms of two primary unknowns: wetting phase pressure and non-wetting phase pressure. It is tested on a simple hypothetical problem adopted by Kaluarachchi and Parker (1989).

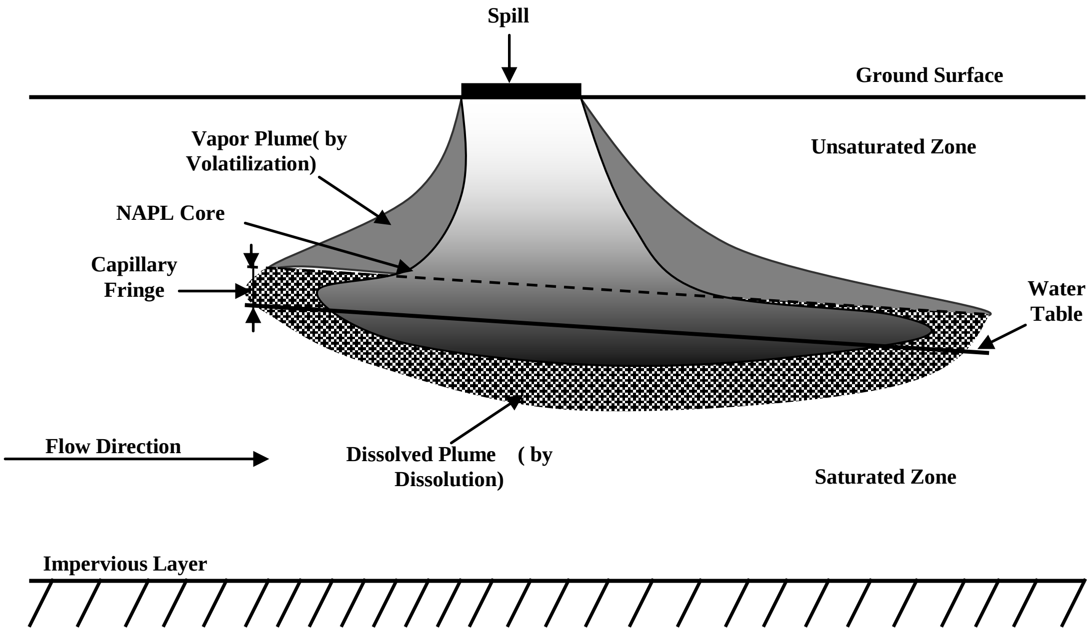

Fig.1: Conceptualization representation of LNAPL migration and contamination of the subsurface.

GOVERNING EQUATIONS

The unsaturated zone is a multiphase system, consisting of at least three phases: a solid phase of the soil matrix, a gaseous phase and the water phase. Additional phase may also be present such as a separate phase organic liquid. In the air/oil/water system of the vadose zone, oil is the wetting phase with respect to air on the surface of the water enveloping the soil grains and the water is the wetting phase with respect to oil on the soil grain surfaces. The movement of a non-aqueous phase liquid through the unsaturated-saturated zone may be represented mathematically as a case of two-phase flow because the air phase equation can be eliminated by the assumption that the air phase remains constant essentially at atmospheric pressure and consequently the pressure gradients in the air phase are negligible (Faust et al., 1989). Also, assuming that there is no component partitioning between liquid phases (Kueper and Frind, 1991).The mass balance equation for each of the fluid phase in cartesian coordinates can be written as (Bear, 1972): -

$$-\frac{\partial}{\partial x_i}\left(\rho_f \cdot q_f\right)+Q_f=\frac{\partial}{\partial t}\left(\phi \cdot \rho_f \cdot S_f\right) \tag{1}$$

Where f Subscript denoting the phase the equation applies. In the present study, f will refer to water and oil unless otherwise noted, ϕ porosity of the medium, ρ_f density of phase f [M][L^{-3}], S_f saturation of phase f [L^3/L^3], q_f volumetric flux (or Darcy flux) of phase f [L][T^{-1}], Q_f source or sink of phase f and t is the time [T]. Darcy's law is an empirical relationship that describes the relation between the flux and the individual phase pressure. Since its discovery last century it has been derived from the momentum balance equations (Kueper and Frind, 1991).

$$q_f = -\frac{k_{ij} \cdot k_{rf}}{\mu_f}\left(\frac{\partial \mathrm{P}_f}{\partial x_j} + \rho_f \cdot g\,\frac{\partial z}{\partial x_j}\right) \tag{2}$$

Where k_{ij} is the intrinsic permeability tensor of the medium [L^2], k_{rf} is the relative permeability of the phase f which is a function to either water (wetting phase) or oil (non-wetting phase). The relative permeability is a non-linear function of saturation. It ranges in value from 0 when the fluid is not present, to 1 when the fluid is presented, μ_f dynamic viscosity of fluid f [M][L^{-1}][T^{-1}], P_f fluid pressure of phase f [M][L^{-1}] [T^{-2}], g acceleration due to gravity vector [L][T^{-2}]. Darcy's law can be written equivalently in the form of the pressure head as below:

$$q_f = -\mathrm{K}_{fij}\left(\frac{\partial h_f}{\partial x_j} + \frac{\rho_f}{\rho_w}\cdot\frac{\partial z}{\partial x_j}\right) \tag{3}$$

With $\frac{\partial z}{\partial x_j}$ is a unit gravitational vector, where z is elevation and t is time. The volumetric flux can be thought of as the volume of fluid f passing through a unit area of porous medium in a unit time. This variable is the natural one when making mass fluid balance arguments. By substituting (eq.(3) into eq.(1)), assuming that the fluid and the porous media are incompressible, ignore the source-sink term, and according to Kaluarachchi and Parker (1989), the coordinate system is oriented with the conductivity tensor, or otherwise that off-diagonal components may be disregarded, so that $\mathrm{K}_{fsij} = 0$ for i$\neq$j. the resulting equation can be represented by: -

$$\frac{\partial}{\partial x}\left[\mathrm{K}_f\left(\frac{\partial h_f}{\partial x} + \frac{\rho_f}{\rho_w}\frac{\partial z}{\partial x}\right)\right] = \phi\frac{\partial S_f}{\partial t} \tag{4}$$

ONE-DIMENSIONAL NUMERICAL SOLUTION

Eq.4 will be re-written as two one-dimensional equations, one for water phase and the other for oil phase. Both of which are expressed in terms of the phase pressure head as below:-

$$\frac{\partial}{\partial z}\left[\mathrm{K}_w\left(\frac{\partial h_w}{\partial z} + 1\right)\right] = C_w\frac{\partial h_w}{\partial t} \tag{5}$$

$$\frac{\partial}{\partial z}\left[\mathrm{K}_o\left(\frac{\partial h_o}{\partial z} + \rho_{ro}\right)\right] = C_o\frac{\partial h_o}{\partial t} \tag{6}$$

Where z is positive upward vertical coordinate [L], $\mathrm{K}_w = \mathrm{K}_{ws}k_{rw}$ and $\mathrm{K}_o = \mathrm{K}_{os}k_{ro} = \frac{\mathrm{K}_{ws}k_{ro}}{\mu_{ro}}$; μ_{ro} is the ratio of oil to water viscosity, ρ_{ro} is the ratio of oil to water density and C is the specific fluid capacity, It is defined by $C_w = \phi\frac{\partial S_w}{\partial h_w}$ & $C_o = \phi\frac{\partial S_o}{\partial h_o}$.

However, in the present study, the two-pressure forms of the flow equations are cast in terms of the two fluid pressure heads. The equations in this form are a direct statement of conservation of mass. There are two principle difficulties associated with solving the governing equations (eqs.(5) &(6)). The first is that these equations are first order partial differential equations with respect to time and second order with space. Further, they are nonlinear differential equations because **C** and **K** are nonlinear functions of capillary pressure heads of two fluids. The second difficulty in solving these equations lies in the linearization procedure and the method for dealing with the coupling between the equations. However, the solution techniques used here consisted of a finite-difference approximation (implicit method) of the differential equations, the Newton-Raphson with a Taylor series expansion to treat the nonlinearities, and direct matrix solution (Gauss-Elimination method). These techniques result in the following equations:-

$$a_{fi}^{k}\delta_{fi-1}^{k+1}+b_{fi}^{k}\delta_{fi}^{k+1}+c_{fi}^{k}\delta_{fi+1}^{k+1}=-r_{fi}^{k} \tag{7}$$

Where:-

$$a_{fi}^{k}=\left[-R1\left(\mathrm{K}_{fi-1}^{k}+h_{fi-1}^{k}\frac{\partial \mathrm{K}_{fi-1}^{k}}{\partial h_{fi-1}^{k}}\right)-R2\rho_{rf}\frac{\partial \mathrm{K}_{fi-1}^{k}}{\partial h_{fi-1}^{k}}\right]$$

$$b_{fi}^{k}=\left[C_{fi,j}^{k}+\left(h_{fi,j}^{k}-h_{fi,j}^{n}\right)\frac{\partial C_{fi,j}^{k}}{\partial h_{fi,j}^{k}}\right]+\left[R1\mathrm{K}_{fi-1,j}^{k}\right]+\left[R11\left(\mathrm{K}_{fi,j}^{k}+h_{fi,j}^{k}\frac{\partial \mathrm{K}_{fi,j}^{k}}{\partial h_{fi,j}^{k}}\right)\right]+\left[R2\rho_{rf}\frac{\partial \mathrm{K}_{fi,j}^{k}}{\partial h_{fi,j}^{k}}\right]$$

$$c_{fi}^{k}=-R11\mathrm{K}_{fi}^{k}$$

$$r_{fi}^{K}=C_{fi}^{k}\left(h_{fi}^{k}-h_{fi}^{n}\right)-R1\mathrm{K}_{fi-1}^{k}h_{fi-1}^{k}+R1\mathrm{K}_{fi-1}^{k}h_{fi}^{k}+R11\mathrm{K}_{fi}^{k}h_{fi}^{k}-R11\mathrm{K}_{fi}^{k}h_{fi+1}^{k}-R2\rho_{rf}\mathrm{K}_{fi-1}^{k}+R2\rho_{rf}\mathrm{K}_{fi}^{k}$$

$$R1=\frac{\Delta t}{\Delta z_i\left(z_{i-1}-z_i\right)}\quad,\quad R11=\frac{\Delta t}{\Delta z_i\left(z_i-z_{i+1}\right)}\quad\&\quad R2=\frac{\Delta t}{\Delta z_i}.$$

Where r_{fi}^{k} is the residual in node (i) at iteration k. At each time step the solution is iterated until the pressure head converges. During each iteration, the equations are solved to find the pressure heads at the new iteration level. Thus, the nonlinear coefficients (i.e. C & K) are evaluated using the pressure heads at the old iteration level thus linearizing the equations. The increment in pressure head at each iteration level must be added to the tried solution at iteration k, this increment is termed as $\delta^{n+1,k+1}$, to produce the solution to the next iteration, $k+1$ and next time step, $n+1$. Fig.2(a) shows unsaturated-saturated zone and Fig.2(b) shows the discretized domain in the z-direction with the time.

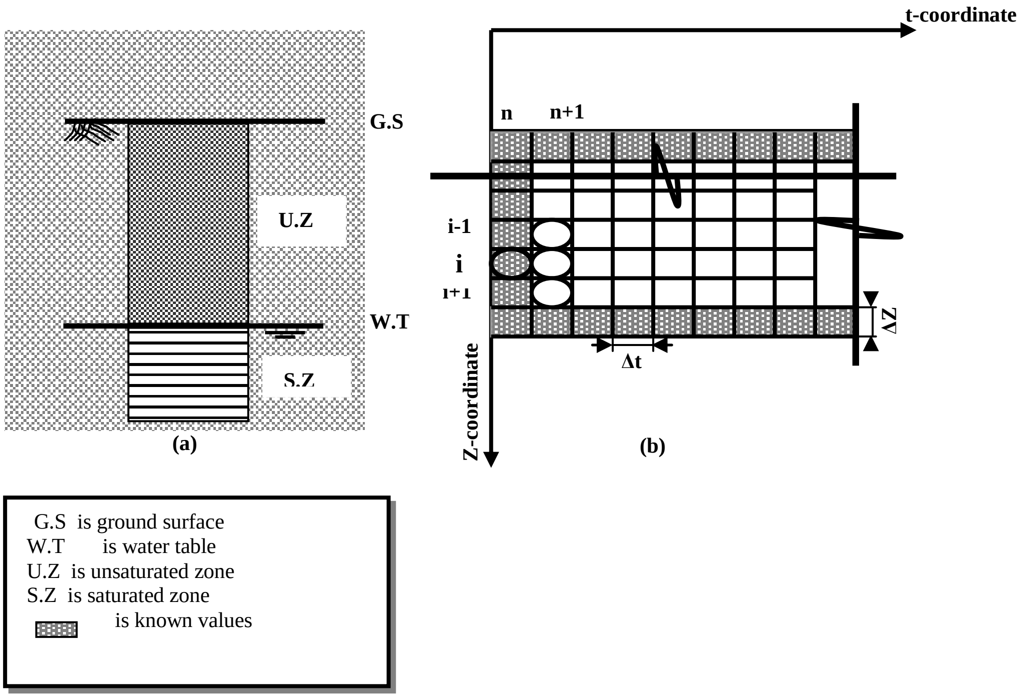

Fig.2: (a) The common situation to the virtual solution column, (b) image to the solution domain.

The coefficients a, b and c in eq. (7) are associated with δ_{i-1}^{k+1} , δ_{i}^{k+1} & δ_{i+1}^{k+1}, respectively, and in general it is formed as:-

$$A^k \delta^{k+1} = -r^k \tag{8}$$

Where A is the coefficient matrix for the linearized system. For each node (i), there is one linear equation in three variables δ_{i-1}^{k+1} , δ_{i}^{k+1} & δ_{i+1}^{k+1}. The collection of equations for each nodal solution leads to have a global tri-diagonal coefficient matrix (its bandwidth equal to three) to whole solution domain. For example, in a ten nodded domain, the soil column is subdivided into ten vertical grids. Thus, there will be ten equations that form the whole grids. These equations can be written, after application of the boundary and initial conditions, in matrix notation as:-

$$\begin{bmatrix} b_1 & c_1 & 0 & 0 & 0 & 0 & 0 & 0 & 0 & 0 \\ a_2 & b_2 & c_2 & 0 & 0 & 0 & 0 & 0 & 0 & 0 \\ 0 & a_3 & b_3 & c_3 & 0 & 0 & 0 & 0 & 0 & 0 \\ 0 & 0 & a_4 & b_4 & c_4 & 0 & 0 & 0 & 0 & 0 \\ 0 & 0 & 0 & a_5 & b_5 & c_5 & 0 & 0 & 0 & 0 \\ 0 & 0 & 0 & 0 & a_6 & b_6 & c_6 & 0 & 0 & 0 \\ 0 & 0 & 0 & 0 & 0 & a_7 & b_7 & c_7 & 0 & 0 \\ 0 & 0 & 0 & 0 & 0 & 0 & a_8 & b_8 & c_8 & 0 \\ 0 & 0 & 0 & 0 & 0 & 0 & 0 & a_9 & b_9 & c_9 \\ 0 & 0 & 0 & 0 & 0 & 0 & 0 & 0 & a_{10} & b_{10} \end{bmatrix}_k \begin{bmatrix} \delta_1 \\ \delta_2 \\ \delta_3 \\ \delta_4 \\ \delta_5 \\ \delta_6 \\ \delta_7 \\ \delta_8 \\ \delta_9 \\ \delta_{10} \end{bmatrix}_{k+1} = -\begin{Bmatrix} r_1 \\ r_2 \\ r_3 \\ r_4 \\ r_5 \\ r_6 \\ r_7 \\ r_8 \\ r_9 \\ r_{10} \end{Bmatrix}_k$$

This system is solved for δ and then the algorithm enters the next iteration with new values of h_f is evaluated as follows:-

$$h_{fi}^{k+1} = h_{fi}^{k} + \omega_f^{k+1} \delta_{fi}^{k+1} \tag{9}$$

Where ω_f^{k+1} is a damping parameter as mentioned by Cooley (1983). During each iteration, nodal pressure heads need to be updated for the next iteration. With highly nonlinear flow problems, the updating method introduced by Cooley (1983) which introduces an optimal relaxation scheme, which accounts for the maximum convergence error for entire mesh, is used in the present study in conjunction with Newton–Raphson scheme. For clarification, this method is briefly described as follows:-

Let e_f^{k+1} be the largest in absolute value of the δ_i^{k+1} values for all i. Then

<u>Step(1):</u>

$$s_f = \frac{e_f^{k+1}}{\omega_f^k e_f^k} \qquad \text{for} \qquad k > 0 \tag{10}$$

$$s_f = 1 \qquad \text{for} \qquad k = 0$$

<u>Step(2):</u>

$$\omega_f^* = \frac{3 + s_f}{3 + |s_f|} \qquad \text{for} \qquad s_f \geq -1 \tag{11}$$

$$\omega_f^* = \frac{1}{2|s_f|} \qquad \text{for} \qquad s_f < -1$$

Step(3):

$$\omega_f^{k+1} = \omega_f^* \qquad \text{for} \qquad \omega_f^* \left| e_f^{k+1} \right| \le e_{f\max} \tag{12}$$

$$\omega_f^{k+1} = \frac{e_{f\max}}{\left| e_f^{k+1} \right|} \qquad \text{for} \qquad \omega_f^* \left| e_f^{k+1} \right| > e_{f\max}$$

Where $e_{f\max}$ is the maximum allowable change in the fluid pressure head, h_f, during any iteration. This value is chosen beforehand. The convergence criterion used in the present study for a given phase f (=o,w) is as follows:-

$$\frac{\max.\left|\delta_{fi}^{k+1}\right|}{\max.\left|h_{fi}^{k} + \delta_{fi}^{k+1}\right|} \le \varepsilon \tag{1٣}$$

Where ε is a small number termed the convergence tolerance. A typical convergence criterion for pressure head is 0.001 or less.

When the Global finite difference approximation is founded by summing the node equations, the boundary terms must be accounted. Two types of boundary condition are considered. For Type-1 (Dirichlet), or fixed head boundary condition, the finite difference equation at boundary node (i) is replaced by $\delta_{fi,j}^{k+1} = zero$ or $h_{fi,j}^{k+1} = given$. The other form of boundary condition is Type-2 (Neumann), or specified fluid flux condition. A flux boundary condition is incorporated into the global approximation at boundary node (i) by using the discretized finite difference form of continuity equation in conjunction with Darcy's law.

CONSTITUTIVE RELATIONSHIPS

Eqs.(5) and (6) describe the flow conditions in the subsurface system. There are several unknowns in these equations. In order to close the system, constitutive relationships that relate the unknowns must be specified. These relationships can be written in a variety of ways that result in different variables becoming the dependent variables for the system.

The most common choices for dependent variables are the individual phase pressures and the phase saturations. The constitutive relationships that will be used in the present study are the pressure–saturation and relative permeability–saturation relationships. The fluid saturation is a function of the difference between the pressure of the two fluids in the porous medium, the pressure difference is called the capillary pressure , $P_{ow} = P_o - P_w$, or capillary pressure head $h_{ow} = h_o - h_w$.

Many different functional forms have been proposed to describe the pressure–saturation and relative permeability–saturation relationships. They are generally empirical relations. However, constitutive relationships used in the present study to describe three phase fluid relative permeabilities and saturations as functions of fluid heads described by (Parker et. al., 1987) which is based on (Van Genuchten's model, 1980).The following relationships will be needed to complete the description of a multiphase flow through the porous media: -

$$S_w + S_o + S_a = 1 \tag{14}$$

$$S_t = S_w + S_o \tag{15}$$

$$\bar{S}_w = \frac{S_w - S_r}{1 - S_r} \quad (16)$$

$$\bar{S}_t = \frac{S_t - S_r}{1 - S_r} \quad (17)$$

$$\bar{S}_w = \left[1 + \left(\alpha \cdot \beta_{ow} \cdot h_{ow}\right)^n\right]^{-m} \qquad h_o > h_o^{cr.} \quad (18)$$

$$\bar{S}_w = \left[1 + \left(\alpha \cdot h_{aw}\right)^n\right]^{-m} \qquad h_o \le h_o^{cr.} \quad (19)$$

$$h_o^{cr.} = \beta_{ow} h_w \Big/ \left(\beta_{ao} + \beta_{ow}\right) \quad (20)$$

$$\bar{S}_t = \left[1 + \left(\alpha \cdot \beta_{ao} \cdot h_{ao}\right)^n\right]^{-m} \quad (21)$$

$$k_{rw} = \bar{S}_w^{1/2}\left[1 - \left(1 - \bar{S}_w^{1/m}\right)^m\right]^2 \quad (22)$$

$$k_{ro} = (S_t - S_w)^{1/2}\left[\left(1 - S_w^{1/m}\right)^m - \left(1 - S_t^{1/m}\right)^m\right]^2 \quad (23)$$

Where $h_o^{cr.}$ critical oil pressure head, [L], h_{ow} oil-water capillary pressure head $(= h_o - h_w)$, [L], h_{aw} air-water capillary pressure head $(= h_a - h_w)$, [L], h_{ao} air-oil capillary pressure head $(= h_a - h_o)$, [L], S_w water saturation, S_a air saturation, S_t total liquid saturation, $\bar{S}_w$ effective water saturation, $\bar{S}_t$ effective total liquid saturation, k_{rw} relative permeability of water, k_{ro} relative permeability of oil, S_r residual or irreducible saturation of water phase. Here α, n and $m\left(= 1 - 1/n\right)$ are Van Genutchten's soil parameters, β_{ao} & β_{ow} are fluid-dependent scaling coefficients.

NUMERICAL RESULTS IN ONE DIMENSION AND DISCUSSION

A theoretical work presented by Kaluarachchi and Parker (1989) used as a verification to the present numerical model. They used Galerkin's finite element method for modeling of one-dimensional infiltration and redistribution of oil in a uniform soil profile. Also, they used a number of methods to determine the capacity terms related to oil and water phases. These methods are the chord-slope scheme and equilibrium scheme.

The problem analyzed here corresponds to a vertical soil column 100 cm long with an oil-free initial condition in equilibrium with a water table located 75 cm below the top surface. The simulation was achieved in two stages. The first stage is the infiltration stage, in which oil was allowed to infiltrate into the column under water equivalent oil pressure head of 3 cm until a total of 5 cm^3/cm^2 of oil had accumulated. The second stage is the redistribution stage, in which the source of oil is cutoff and oil is allowed to redistribute up to 100 hours. A schematic diagram of the problem is illustrated in Fig.3. The boundary conditions and system's parameters, i.e. fluid and soil properties which were used in this simulation are summarized in Tables (1) and (2) respectively.

The initial condition of zero oil saturation was achieved by fixing the initial oil pressure head at each node to the critical oil pressure head, $h_o^{cr.}$ which is defined in eq. (20). The water saturation distribution above the water table that is used in this simulation is initially at capillary equilibrium. This distribution is illustrated in Fig.4. The finite difference mesh consists of 100 grids with a uniform spacing of 1 cm and the time step varied between 0.00001 to 0.01 hours.

As pointed out by Kaluarachchi and Parker (1989), a jump condition in the water saturation versus air-water capillary pressure head function, $S_w(h_{aw})$, will occur during the transition from a two-phase air-water system to a three-phase air-oil-water system. To avoid numerical problems associated with this jump condition, a phase updating scheme is adopted at the end of each time step to index whether the node is a two or three phase system (i.e. oil is absent or present). Once a three-phase condition occurs, reversion to a two-phase condition is not allowed. The criterion for a node to change from the two to the three phase system is that $h_o > h_o^{cr.}$. It is important to note that the part of the domain remaining as an air-water system and consequently the capacity and relative permeability terms related to the oil phase C_o and k_{ro} will become zero and the oil flow equation solution reduce to the identity 0=0. To avoid this problem, minimum cutoff values of capacity and relative permeability terms related to the oil phase should be taken as $C_o = 10^{-6}$ and $k_{ro} = 10^{-6}$ as recommended by Kaluarachchi and Parker (1989).

The duration of the infiltration stage this is calculated from the present model was approximately 0.085 hours. While this value was 0.09 hours as calculated by MOFAT-2D model. There is a good agreement between these values. The total liquid saturation distribution at the end of the infiltration stage as computed from the present model are compared with those calculated by MOFAT-2D model by using chord-slope scheme and there is a good agreement between them as shown in Fig.4. The water saturation distribution at the end of the infiltration stage was identical to initial condition.

Saturation distributions at the end of 100 hours of redistribution are illustrated in Fig.5 and Fig.5. These results are compared with those of results MOFAT-2D model by using chord-slope scheme and equilibrium condition scheme, and, as shown in these figures, there is a good agreement between these results. Equilibrium distributions were calculated from hydrostatics for an oil volume of 5 cm subject to the imposed boundary conditions. The equilibrium condition was defined by Kaluarachchi and Parker (1989) as the fluid distributions at which the total head gradient of both phases with respect to elevation approaches zero. Kaluarachchi and Parker (1989) pointed out that convergence of chord-slope results toward the equilibrium results provides a verification check for the MOFAT-2D numerical model. It is to be noted, however, that whereas the equilibrium distribution indicates no oil above a depth of 43.0 cm, the MOFAT-2D numerical model, and the present model predict an average oil saturation of (7-8)% remaining above this depth even though oil velocities at 100 hours are practically zero.

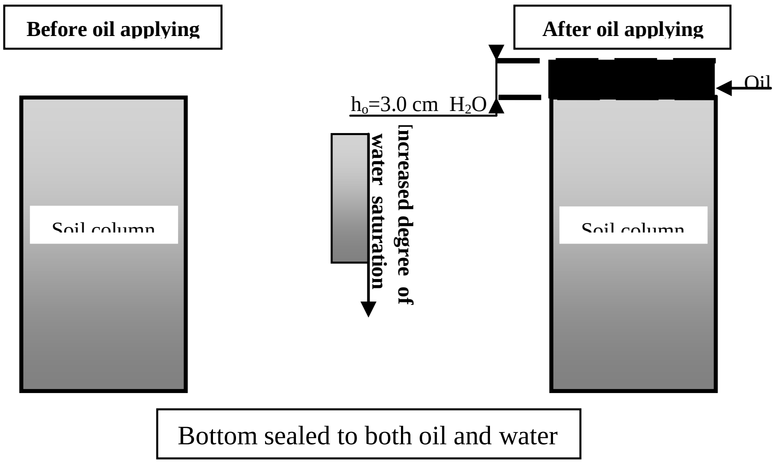

Fig.3: A **schematic diagram for the analyzed problem.**

Table1: Boundary conditions which are used for verification.

Stage	**Phase**	**Boundary conditions**	
		Upper boundary	**lower boundary**
Infiltration	Water	Zero flux	Constant head= 25.0 cm
	Oil	Constant head= 3.0 cm	Zero flux
Redistribution	Water	Zero flux	Constant head= 25.0 cm
	Oil	Zero flux	Zero flux

Table 2: Soil and fluid properties that are used for first verification.

Parameter	n	α	S_r	K_{sw}	β_{ao}	β_{ow}	ρ_{ro}	μ_{ro}	ϕ
Value	3.25	0.05	0.00	50.00	1.80	2.25	0.80	2.00	0.40

All units are given in centimeters and hours.

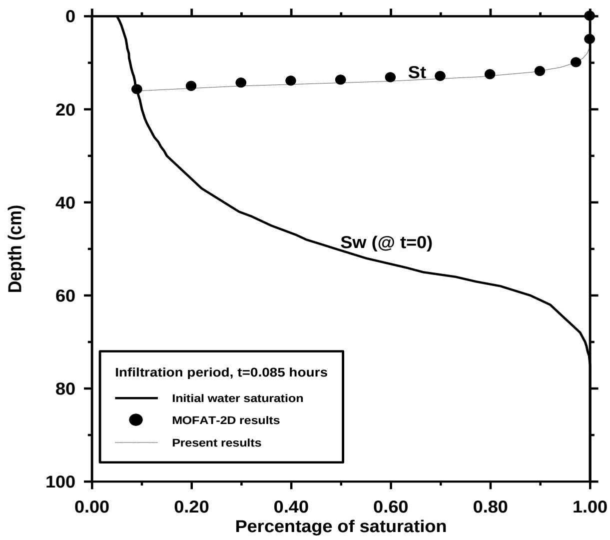

Fig.4: Distribution of initial water saturation and total liquid saturation at the end of the infiltration period.

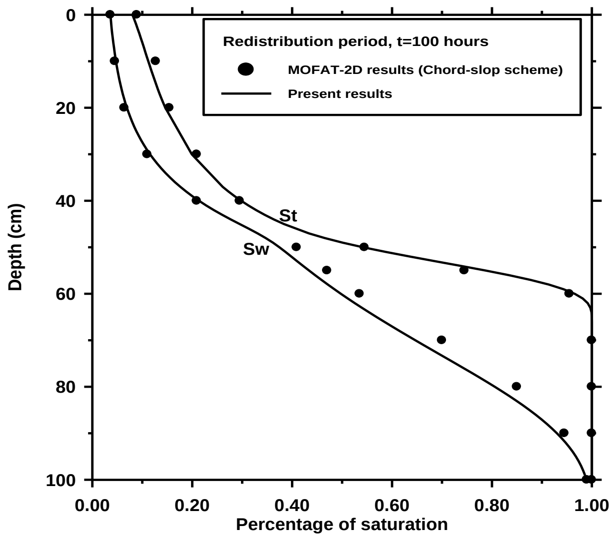

Fig.5: Distribution of water and total liquid saturation at the end of the redistribution period.

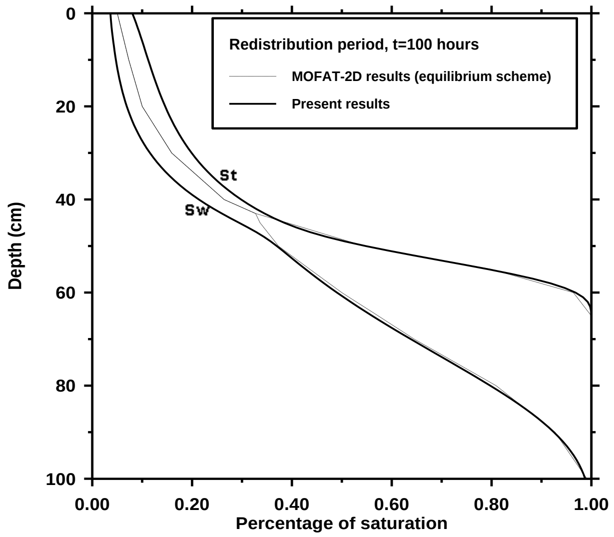

Fig.6: Distribution of water and total liquid saturation at the end of the redistribution period.

The mass balance associated with the above results shows an error in the oil phase during the infiltration stage is largest at the early time (up to 1%) and reduce to less than 0.0005% later times (Fig.7). The present mass balance results can be compared to an analogous lumped finite element solution in MOFAT-2D using the h-based form of the governing equations. The mass balance error associated with results of MOFAT-2D is greater than 1% at any time during the infiltration stage. This is because the finite element approximation may suffer from oscillatory solutions. Such oscillations are not present in any finite difference solutions. Because the only difference between the two solution producers as disscused by Celia et al. (1990) is the treatment of the time derivative term, these results imply that diagonalized time matrices are to be preferred. Thus the unsaturated flow equation is one that benefits from mass lumping in finite element approximation.

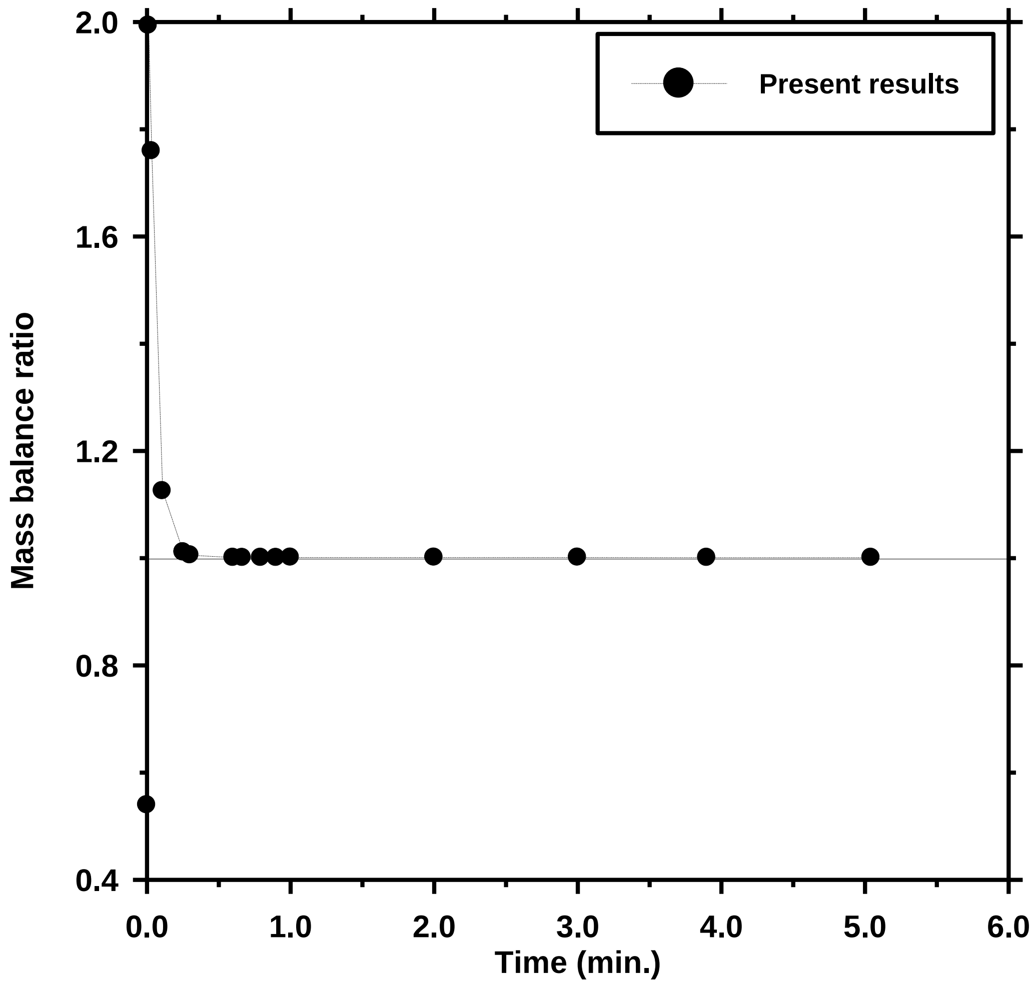

Fig.7: Mass balance of oil as a function of time, using the h-based form of equations.

MODEL IMPLEMENTATION

A computer program written in DIGITAL VISUAL FORTRAN (Version 5.0) was developed to implement the model described above. Inherent in any subsurface modeling algorithms are assumptions and limitations. The major assumptions include:- the pressure in the air phase is constant and equal to atmospheric pressure, both water and NAPL viscosities and densities are pressure independent, relative permeability of water is a function of water saturation, relative permeability of NAPL is a function of air and water saturations, capillary pressure is a function of water saturation, air saturation is a function of NAPL pressure, Darcy’s equation for multiphase flow is valid, intrinsic permeability is a function of space and there is no inter-phase mass transfer (i.e ; the NAPL is truly immiscible in water).

The major limitations include:- the model can not treat highly pressurized systems in which the viscosity and density of the three phases are a function of pressure, fractured systems are not treated, transport of dissolved NAPL is not treated.

CONCLUSIONS

The following conclusions can be deduced :-

(**1**) The numerical solution based on the potential form of the governing equations with techniques consisted of Implicit Finite Difference, Newton-Raphson and Gauss-Elimination schemes showed to be an efficient procedure in solving one- dimensional water and LNAPL flow through the unsaturated-saturated zone in three fluid phase's system.
(**2**) The maximum LNAPL saturation occurred below the source of the contaminant during LNAPL infiltration. During redistribution, the LNAPL saturation had a maximum value at the advancing of the LNAPL infiltration front.
3) Mass balance associated with the results presented above show that the finite element approximation may suffer from oscillatory solutions. Such oscillations are not present in any finite difference solutions.

REFERENCES

Bear, J., “Dynamics of fluids in porous media”. Elsevier, New York, 1972.

Cary, J.W., J.F. McBride, and C.S. Simmons, “Observations of water and oil infiltration into soil: Some simulation challenges”. Water Resources Research, 25(1), 73-80, 1989.

Celia, M.A., E.T. Bouloutas, and R.L. Zarba, “A general mass-conservation numerical solution for the unsaturated flow equation”. Water Resources Research, 26(7), 1483-1496, 1990.

Cooley, R.L., “Some new procedures for numerical solution of variably saturated flow problems”. Water Resources Research, 19(5), 1271-1285, 1983.

El-Kadi, A.I., “Applicability of sharp-interface models for NAPL transport: 1. infiltration”. Ground Water, 30(6), 849-856, 1992.

Faust, C.R., “Transport of immiscible fluids, within and below the unsaturated zone : A numerical model”. Water Resources Research, 21(4), 587-596, 1985.

Faust, C., J. Guswa, and J. Mercer, “Simulation of three-dimensional flow of immiscible fluids within and below unsaturated zone”. Water Resources Research, 25(12), 2449-2464, 1989.

Kaluarachchi, J.J., and J.C. Parker, “An efficient finite element method for modeling multiphase flow”. Water Resources Research, 25, 43-54, 1989.

Kim, J., and M.Y. Corapcioglu, “Modeling dissolution and volatilization of LNAPL sources migrating on the groundwater table”. J. of Contaminant Hydrology, 65, 137-158, 2003.

Kueper, B., and E. Frind, “Two-phase flow in heterogeneous porous media: 1. Model development”. Water Resources Research, 27(6), 1049-1057, 1991.

Kueper, B., and E. Frind, “Two-phase flow in heterogeneous porous media: 1. Model application”. Water Resources Research, 27(6), 1059-1070, 1991.

Parker, J. C., and R. J. Lenhard, “A Model for hysteretic constitutive relations governing multiphase flow: 1. saturation-pressure relations”. Water Resources Research, 23(12), 2187-2196, 1987.

Parker, J. C., R. J. Lenhard, and T. Kuppusamy, “A parametric model for constitutive properties governing multiphase flow in porous media”. Water Resources Research, 23(4), 618-624, 1987.

Marsman, A., "The influence of water percolation on flow of light non-aqueous phase liquid in soil". PH.D. Thesis, Wageningen University, Wageningen 2002.

Sleep, B.E., and J.F. Sykes, "Modeling the transport of volatile organics in variable saturated media". Water Resources Research, 25(1), 81-92, 1989.

Suk, H., "Development of 2- and 3-D simulator for three phase flow with general initial and boundary conditions on the fractional flow approach". PH.D. Thesis, Pennsylvania State University, 2003.

Van Genuchten, M., "A closed-form equation for predicting the hydraulic conductivity of unsaturated soils''. Soil Sci. Soc. Am. J.,44,892-898,1980.

SYMBOLS

A	Coefficient matrix	$[M^0 L^0 T^0]$
C_f	Specific fluid capacity	$[M^0 L^0 T^0]$
$e_{f\,\max}$	Maximum change in the fluid pressure head	[L]
g	Acceleration due to gravity vector	$[L\,T^{-2}]$
h_a	Air pressure head	[L]
h_{ao}	Air-oil capillary pressure head	[L]
h_{aw}	Air-water capillary pressure head	[L]
h_o	Oil pressure head	[L]
h_{ow}	Oil-water capillary pressure head	[L]
$h_o^{cr.}$	Critical oil pressure head	[L]
h_w	Water pressure head	[L]
i	Grid identification in Z coordinates	$[M^0 L^0 T^0]$
K	Hydraulic conductivity	$[L\,T^{-1}]$
K_{fs}	The conductivity when the medium is saturated with fluid f	$[L\,T^{-1}]$
k_r	Relative hydraulic conductivity	$[M^0 L^0 T^0]$
k	The intrinsic permeability tensor of the medium in eq. (2)	$[M^0 L^0 T^0]$
k	Iteration index	$[M^0 L^0 T^0]$
n	Time step identification (if it is superscript)	$[M^0 L^0 T^0]$
non	The n^{th} grid identification	$[M^0 L^0 T^0]$
nor	The number of rows	$[M^0 L^0 T^0]$
n, m	Van Genuchten's soil parameters	$[M^0 L^0 T^0]$
P_f	Fluid pressure of phase f	$[M\,L^{-1}\,T^{-2}]$
Q_f	Source or sink of phase f	$[M\,L^{-3}\,T^{-1}]$
q	Volumetric flux (or Darcy's flux)	$[L\,T^{-1}]$
r	The residual due to approximation	$[M^0 L^0 T^0]$
S_a	Degree of air saturation	%
S_o	Degree of oil saturation	%
S_r	Degree of residual wetting fluid saturation	%
S_t	Degree of total liquid saturation	%

S_w	Degree of water saturation	%
$\bar{S}_t$	Degree of effective total liquid saturation	%
$\bar{S}_w$	Degree of effective water saturation	%
t	Time coordinate	[T]

Greek symbols

α	Van Genuchten's soil parameter	$[L^{-1}]$
β_{ij}	Fluid-dependent scaling coefficient	$[M^0 L^0 T^0]$
δ	The difference between the approximation and exact solution	[L]
ε	Convergence tolerance	[L]
μ_f	Dynamic viscosity of fluid f	$[M\ L^{-1} T^{-1}]$
μ_{ro}	Ratio of oil to water viscosity	$[M^0 L^0 T^0]$
ρ_f	Density of phase f	$[M L^{-3}]$
ρ_{ro}	Ratio of oil to water density	$[M^0 L^0 T^0]$
ρ_w	Density of water at standard temperature and pressure	$[M L^{-3}]$
ϕ	Porosity of the medium	$[L^3 L^{-3}]$
ω	Damping parameter	$[M^0 L^0 T^0]$
Δt	Time step size	[T]
ΔZ	Vertical increment in Z-direction	[L]

DEVELOPING COMPRESSIBLE TURBULENT FLOW AND HEAT TRANSFER IN CIRCULAR TUBE WITH UNIFORM INJECTION OR SUCTION

Asst.Prof.Dr.Ihsan Y.Hussain
Mech.Engr.Dept.
College of Engineering
University of Baghdad
Baghdad-Iraq

Ayad M. Salman
Mechanical Engineer
Energy & Fuel Research Center
University of Technology
Baghdad-Iraq

Adil A. Mohammed
Mechanical Engineer
Baghdad-Iraq
Adekef@yahoo.Com

ABSTRACT

In the present work , a numerical study has been made for the developing compressible turbulent flow and heat transfer in circular tube with uniform injection or suction. The study included the numerical solution of the continuity, momentum and energy equations together with the two equations of the (k-ε) turbulence model, by using the Finite Difference Method (FDM). The air was used as the working fluid, and the circular passage was composed of tube with diameter (20.0) cm , and the length was 130 (hydraulic diameter) .The Reynolds number of the flow was ($Re=1.78x10^6$), and the Mach number (M=0.44) the ratio of the transverse velocity at the wall (v_w) to the axial velocity at inlet (U_{in}), $\Omega=(v_w/U_{in})$, for suction equal(0.001) and for injection (-0.001).. The wall of the tube was heated with constant wall temperature (T_w) and in other case with constant heat flux (Q_w) as a thermal boundary condition. The development of both hydrodynamic and thermal boundary layers occurs simultaneously. The computational algorithm is capable of calculating the hydrodynamic parameters such as the velocities , friction factor , turbulence structure which includes the Reynolds stress and the turbulent kinetic energy and eddy viscosity. Besides, the thermal parameters are also predicted, such as the temperature, Nusselt number, and the turbulent heat fluxes.The Results showed that the hydrodynamic and thermal entrance length is increased with the increasing of Reynolds number. The suction caused a flatten for the velocity profile and thus decreasing the hydrodynamic entrance length, and caused an increase in the Nusselt number and decreasing the local coefficient of friction, but injection caused a steeping of the velocity profile , and thus increasing the entrance hydrodynamic length and caused a decrease in the Nusselt number and increase the local coefficient of friction. Turbulent kinetic energy and turbulent heat flux are decreased with

suction and increased with injection .Predictions have been obtained which are in good agreement with results obtained by past experimental and theoretical work.

الخلاصة

يتضمن البحث الحالي دراسة نظرية عددية للجريان المضطرب الأنضغاطي غير تام التطور مع انتقال الحرارة خلال مجرى أنبوبي مع حالة حقن أو سحب باستخدام طريقة الحل العددي لمعادلات الاستمرارية والزخم والطاقة مع معادلتي نموذج الاضطراب (k-ε) باستخدام طريقة الفروق المحددة (FDM) ، الحسابات العددية منفذة باستخدام الهواء كمائع عمل يمر خلال مجرى أنبوبي قطره (20) سم وطوله يساوي (130) قطر هايدروليكي، رقم رينولد للهواء يساوي ($1.78x10^6$) وبرقم ماخ يساوي (M=0.44)، تم تسخين جدار الأسطوانة باستخدام شرط درجة حرارة الجدار ثابتة مرة وأخرى باستخدام شرط فيض حراري ثابت كذلك استخدم مرور الهواء عبر الجدار (v_w) باتجاهين كشرطين حديين وبنسبة Ω =(v_w/U_{in}), الأول في حالة خروج الهواء من الأنبوب (امتصاص) وكانت النسبة (0.001) والأخرى دخول الهواء إلى الأنبوب (حقن) وكانت النسبة (-0.001) . تحدث عملية التطور الهيدروديناميكي والحراري آنيا" . أمكانية الحل العددي تتضمن حساب الصفات الهيدروديناميكية مثل مركبات منحنيات السرعة ومعامل الاحتكاك ، هيكل الاضطراب مثل منحنيات إجهاد رينولدز والطاقة الحركية المضطربة واللزوجة الدوامية ، كذلك تم حساب الصفات الحرارية مثل توزيع درجات ورقم نسلت والفيض الحراري المضطرب لمنطقة الحساب . بينت النتائج زيادة طول الدخول الهيدروديناميكي والحراري بزيادة رقم رينولدز ، كما بينت أن حالة الامتصاص تسبب استواء منحنى السرعة وقصر طول الدخول الهيدروديناميكي وزيادة رقم نسلت كما يسبب نقصان معامل الاحتكاك الموضعي والعكس فأن الحقن يؤدي إلى تحدب منحنى السرعة وزيادة طول الدخول الهيدروديناميكي وانخفاض رقم نسلت مع نقصان في قيمة معامل الاحتكاك الموضعي . الطاقة الحركية المضطربة والفيض الحراري المضطرب يقلان خلال عملية الامتصاص بينما يزيدان خلال عملية الحقن. لتأكيد النتائج العددية فقد تم مقارنتها مع نتائج البحوث السابقة وكان التوافق بين النتائج جيداً ويؤكد موثوقية الخطوات العددية المقترحة في حسابات الجريان المضطرب وانتقال الحرارة خلال المجرى الأنبوبي .

KEY WORDS: Flow and Heat Transfer, Developing, Compressible, Turbulent , Injection and Suction, Circular Tube.

INTRODUCTION

The behavior of fluid flow over the surface of a porous material with mass transfer at the boundary is encountered in a wide range of applications such as, aerodynamic boundary layer control, wall suction to delay separation and transition from laminar to turbulent flow, transpiration or sweat cooling of heated surfaces, which is applied to gas turbine blades, ram-jet intakes, rocket walls, combustion chamber walls exposed to high temperature gases, and so on. In this cooling method, cooling is forced through a porous wall and injected into the high temperature stream. In this way the wall temperature is reduced by forming a heat insulating layer between the hot air and the wall. In addition, heat is removed from the wall by the cooling fluid passing through the interstices. The control of the establishment length in the inlet region of a channel. It is found that the injection of fluid increases the rate of growth of the boundary layer .The characteristics of flow with condensation are analogous in many respects to the flow of fluid over a porous surface with mass transfer at the wall. **(Hasan , 1984).** For internal flow through channels with porous walls (suction or injection), there exists many applications such as in the fields of transpiration cooling, gaseous diffusion, boundary-layer control and ultrahigh filtration. As an effective boundary layer control method, fluid flow in channels or pipes with fluid suction or injection through the wall surface was first investigated by mechanical engineers as early as 1904. Early researchers only focused on fluid flow past a flat surface suction or injection in a part of the whole surface, it was, assumed that the quantity of fluid removed from the stream by suction , so small that only fluid particles in the immediate neighborhood of the wall were suked away, this was equivalent to saying that the ratio of suction velocity to free stream velocity (Ω) was very small , say (Ω =0.0001 to 0.01) , the condition of no slip at the wall is retained with suction present, as well as, the expression for shearing stress at the wall. **(Schilichting , 2000)**.

The present work investigates the effects of injection or suction on the development of compressible and turbulent flow and heat transfer through circular tube. The governing continuity , momentum and energy equations are solved numerically by using Finite Difference Method (FDM). The simultaneous development of both hydrodynamic and thermal boundary layers will be considered with uniform injection or suction through the wall.

GOVERNING EQUATIONS

Steady state, two dimensional axis-Symmetric , compressible , developing turbulent flow(both hydrodynamically and thermally), with uniform injection or suction, and negligible thermal dissipation and body forces and axial diffusion effects will be assumed.

Accordigly the governing, continuity , momentum and energy conservation , kinetic energy of turbulence (k) and viscous will be as follows :-

Continuity Equation.

$$\frac{\partial(\rho u)}{\partial z}+\frac{1}{r}\frac{\partial(\rho v)}{\partial r}=0 \tag{1}$$

Momentum equation in radial direction ;

$$\rho\left(v\frac{\partial v}{\partial r}+u\frac{\partial v}{\partial z}\right)=-\frac{\partial p}{\partial r}+\left[\frac{1}{r^2}\frac{\partial}{\partial r}\left\{r^3\mu_{eff}\frac{\partial}{\partial r}\left(\frac{v}{r}\right)\right\}\right]+\frac{\partial}{\partial z}\left(\mu_{eff}\frac{\partial v}{\partial z}\right)+s_r \tag{2}$$

Where ; $$s_r=\frac{1}{r^2}\frac{\partial}{\partial r}\left\{r^3\mu_t\frac{\partial}{\partial r}\left(\frac{v}{r}\right)\right\}+\frac{\partial}{\partial z}\left(\mu_t\frac{\partial u}{\partial r}\right)-\frac{2}{3}\rho\frac{\partial k}{\partial r}$$

Momentum equation in axial direction ;

$$\rho\left(v\frac{\partial u}{\partial r}+u\frac{\partial u}{\partial z}\right)=-\frac{\partial p}{\partial z}+\left[\frac{1}{r}\frac{\partial}{\partial r}\left\{r\mu_{eff}\frac{\partial u}{\partial r}\right\}\right]+\frac{\partial}{\partial z}\left(\mu_{eff}\frac{\partial u}{\partial z}\right)+s_z \tag{3}$$

Where; $s_z=\frac{1}{r}\frac{\partial}{\partial r}\left\{r\mu_t\frac{\partial v}{\partial z}\right\}+\frac{\partial}{\partial z}\left(\mu_t\frac{\partial u}{\partial z}\right)-\frac{2}{3}\rho\frac{\partial k}{\partial z}$ $\mu_{eff}=\mu+\mu_t$

Energy equation

$$\rho\left(v\frac{\partial T}{\partial r}+u\frac{\partial T}{\partial z}\right)=\frac{1}{r}\frac{\partial}{\partial r}\left(r\frac{\mu_{eff}}{\Pr_{eff}}\frac{\partial T}{\partial r}\right)+\frac{\partial}{\partial z}\frac{\mu_{eff}}{\Pr_{eff}}\frac{\partial T}{\partial z} \tag{4}$$

Equation of state (Perfect gas) ;

$$P=\rho\Re T \tag{5}$$

Sutherlands law of viscosity

$$\frac{\mu}{\mu_0}=\left(\frac{T}{T_0}\right)^{3/2}\left(\frac{T_0+S}{T+S}\right) \tag{6}$$

Where; T_0 =273.16 , μ_0 =1.708x10 kg/m.sec , S=110 .

(k-ε) Model ;

Kinetic energy (k) equation :-

$$\rho\left(v\frac{\partial k}{\partial r}+u\frac{\partial k}{\partial z}\right)=\frac{1}{r}\frac{\partial}{\partial r}\left(r\frac{\mu_t}{\sigma_k}\frac{\partial k}{\partial r}\right)+\frac{\partial}{\partial z}\left(\frac{\mu_t}{\sigma_k}\frac{\partial k}{\partial z}\right)+G-\rho\varepsilon \tag{7}$$

Viscous dissipation (ε) equation :-

$$\rho\left(v\frac{\partial \varepsilon}{\partial r}+u\frac{\partial \varepsilon}{\partial z}\right)=\frac{1}{r}\frac{\partial}{\partial r}\left(r\frac{\mu_t}{\sigma_\varepsilon}\frac{\partial \varepsilon}{\partial r}\right)+\frac{\partial}{\partial z}\left(\frac{\mu_t}{\sigma_\varepsilon}\frac{\partial \varepsilon}{\partial z}\right)+C_{\varepsilon 1}\frac{\varepsilon}{k}G-C_{\varepsilon 2}\rho\frac{\varepsilon^2}{k} \tag{8}$$

$$G=\mu_t\left[2\left\{\left(\frac{\partial v}{\partial r}\right)^2+\left(\frac{\partial u}{\partial z}\right)^2\right\}+\left(\frac{\partial v}{\partial z}+\frac{\partial u}{\partial r}\right)^2\right] \tag{9}$$

Boundary Conditions ;

Entrance condition

$u=U_{in}$, $v=0$, $t=T_{in}$ (10)

$$k_{in}=C_k u_{in}^2 \qquad \varepsilon_{in}=C_\mu k_{in}^{\frac{3}{2}} \Big/ \left(0.5D_h C_\varepsilon\right)$$

, (11)

C_ε =0.03 , C_k=0.003 , D_h = (12)

Exit Condition

$$\frac{\partial u}{\partial z} = \frac{\partial k}{\partial z} = \frac{\partial \varepsilon}{\partial z} = 0 \quad , \quad \frac{\partial T}{\partial z} = Cons\tan t \tag{13}$$

Wall and Center line Conditions

$u(R,z)=0$, $v(R,z)=v_w$ (14)

$\Omega = v_w / U_{in}$ (15)

For the center line:-

$$\frac{\partial u}{\partial r}(0,z)=0 \ , \ v(0,z)=0 \tag{16}$$

Temperature boundary condition:-

$$T(R,z) = T_w \quad \text{(constant wall temperature)} \tag{17}$$

$$\lambda \frac{\partial T}{\partial r}(R,z) = Q_w \quad \text{(constant wall heat flux)} \tag{18}$$

Flow Through Porous Wall

$$\Omega = \frac{V_w}{U_{in}} \tag{20}$$

$$\Psi = \frac{\dot{m}_{wall}}{\dot{m}} = \frac{\rho \pi D L V_w}{\rho \frac{\pi D^2}{4} U_{in}} = 4 \frac{V_w}{U_{in}} \frac{L}{D} \tag{21}$$

$$\Psi = 4\Omega Z^* \tag{22}$$

NUMERICAL SOLUTION.

The governing equations will be solved numerically by using (Explicit Finite Differences Method) **(Ayad, 2003)**, the node – point has subscripts (i , j) denoting cylindrical coordinate in (r , z) directions. The coordinates for each node are ($r=i\Delta r$), ($z=j\Delta z$) .

The convection terms of the axial momentum equation will be changed to finite differences by using back-ward differences. The pressure gradient will be changed to algebraic term by using (Upwind Differences). For the (Diffusion Terms) in the right side of the equation, the (Central Differences) will be used . The following final form is obtained :-

$$a_1 u_{(i,j)} = a_2 u_{(i+1,j)} + a_3 u_{(i,j+1)} + a_4 u_{(i-1,j)} + a_5 u_{(i,j-1)} - \frac{p_j - p_{(j-1)}}{\Delta z} + Su \tag{23}$$

where :-

$$a_1 = \frac{\rho_{(i,j)} v_{(i,j)}}{\Delta r} + \frac{\rho_{(i,j)} u_{(i,j)}}{\Delta z} + \frac{r_{(i+0.5,j)} \mu_{eff(i+0.5,j)}}{r_{(i,j)} (\Delta r)^2} + \frac{r_{(i-0.5,j)} \mu_{eff(i-0.5,j)}}{r_{(i,j)} (\Delta r)^2} + \frac{\mu_{eff(i,j+0.5)}}{(\Delta z)^2} + \frac{\mu_{eff(i,j-0.5)}}{(\Delta z)^2} + \frac{\mu_{t(i,j+0.5)}}{(\Delta z)^2} + \frac{\mu_{t(i,j-0.5)}}{(\Delta z)^2}$$

$$a_2 = \frac{r_{(i+0.5,j)} \mu_{eff(i+0.5,j)}}{r_{(i,j)} \Delta r^2}, \quad a_3 = \frac{\mu_{eff(i,j+0.5)} + \mu_{t(i,j+0.5)}}{\Delta z^2}, \quad a_4 = \frac{r_{(i-0.5,j)} \mu_{eff(i-0.5,j)}}{r_{(i,j)} \Delta r^2}$$

$$a_5 = \frac{\rho_{(i,j)} u_{(i,j)}}{\Delta z} + \frac{\mu_{eff(i,j-0.5)} + \mu_{t(i,j-0.5)}}{\Delta z^2}$$

$$Su = \frac{r_{(i+1,j)} \mu_{t(i+1,j)}}{4 r_{(i,j)} \Delta r \Delta z} v_{(i+1,j+1)} - \frac{r_{(i-1,j)} \mu_{t(i-1,j)}}{4 r_{(i,j)} \Delta r \Delta z} v_{(i-1,j+1)} - \frac{r_{(i+1,j)} \mu_{t(i+1,j)}}{4 r_{(i,j)} \Delta r \Delta z} v_{(i+1,j-1)} + \frac{r_{(i-1,j)} \mu_{(i-1,j)}}{4 r_{(i,j)} \Delta r \Delta z} v_{(i-1,j-1)} - \frac{1}{3} \frac{\rho_{(i,j+1)} \kappa_{(i,j+1)} - \rho_{(i,j)} \kappa_{(i,j-1)}}{\Delta z}$$

The mass balance equation for a typical control volume gives ;

$$\dot{m}_{in} + \dot{m}_{wall} = m \tag{24}$$

$$\dot{m}_{in} = \int_0^R 2\pi \rho_{(i,j)} u_{(i,j)} r dr \tag{25}$$

$$\dot{m} = \int_0^R 2\pi \rho_{(i,j)} u_{(i,j)} r dr \pm 4\Omega \Psi Z^* \tag{26}$$

The (+ve) sign in equation (26) is for suction and the (-ve) sign is for injection. The mean pressure difference ($\overline{p}_j - \overline{p}_{(j-1)}$) in equation (23) can be calculated by (mass conservation) **(Caretto & et.al,1972)** as :-

$$\overline{p}_j = \overline{p}_{(j-1)} + \frac{\dot{m} - 2\pi \rho_{(i,j)} \int_0^R \alpha_{(i,j)} r dr}{2\pi \rho_{(i,j)} \int_0^R \beta r dr} \tag{27}$$

The continuity equation is converted to algebraic form by using the (Back Ward Differences), the following final form is obtained:-

$$v_{(i,j)} = \frac{r_{(i-1,j)}\rho_{(i-1,j)}}{r_{(i+1,j)}\rho_{(i,j)}} v_{(i-1,j)} + \frac{\Delta r}{\Delta z} \frac{r_{(i,j)}}{\rho_{(i,j)} r_{(i+1,j)}} \left(\rho_{(i,j-1)} u_{(i,j-1)} - \rho_{(i,j)} u_{(i,j)}\right)$$

(28)

To convert the two equations for (k-ε) model to the numerical form we use the (Backward Differences) for the convective term and the (Central Differences) for diffusion term , the result is ;

$$c_1 k_{(i,j)} = c_2 k_{(i+1,j)} + c_3 k_{(i,j+1)} + c_4 k_{(i-1,j)} + c_5 k_{(i,j-1)} + S_k \qquad (29)$$

Where ;

$$c_1 = \frac{\rho_{(i,j)} v_{(i,j)}}{\Delta r} + \frac{\rho_{(i,j)} u_{(i,j)}}{\Delta z} + \frac{r_{(i+0.5,j)} \mu_{t(i+0.5,j)} + r_{(i-0.5,j)} \mu_{t(i-0.5,j)}}{r_{(i,j)} \sigma_k (\Delta r)^2} + \frac{\mu_{t(i,j+0.5)} + \mu_{t(i,j-0.5)}}{\sigma_k (\Delta z)^2}$$

$$c_2 = \frac{r_{(i+0.5,j)} \mu_{t(i+0.5,j)}}{r_{(i,j)} \sigma_k (\Delta r)^2},\ c_3 = \frac{\mu_{t(i,j+0.5)}}{\sigma_k (\Delta z)^2},\ c_4 = \frac{\rho_{(i,j)} v_{(i,j)}}{\Delta r} + \frac{r_{(i-0.5,j)} \mu_{t(i-0.5,j)}}{r_{(i,j)} \sigma_k (\Delta r)^2}$$

$$c_5 = \frac{\rho_{(i,j)} u_{(i,j)}}{\Delta z} + \frac{\mu_{t(i,j-0.5)}}{\sigma_k (\Delta z)^2},\ S_k = G_{(i,j)} - \rho_{(i,j)} \varepsilon_{(i,j)}$$

Dissipation energy (ε) equation.

$$d_1 \varepsilon_{(i,j)} = d_2 \varepsilon_{(i+1,j)} + d_3 \varepsilon_{(i,j+1)} + d_4 \varepsilon_{(i-1,j)} + d_5 \varepsilon_{(i,j-1)} + S_\varepsilon \qquad (30)$$

define the following coefficient:-

$$d_1 = \frac{\rho_{(i,j)} v_{(i,j)}}{\Delta r} + \frac{\rho_{(i,j)} u_{(i,j)}}{\Delta z} + \frac{r_{(i+0.5,j)} \mu_{t(i+0.5,j)} + r_{(i-0.5,j)} \mu_{t(i-0.5,j)}}{r_{(i,j)} \sigma_\varepsilon (\Delta r)^2} + \frac{\mu_{t(i,j+0.5)} + \mu_{t(i,j-0.5)}}{\sigma_\varepsilon (\Delta z)^2} + \frac{C_{\varepsilon 2} \rho_{(i,j)} \varepsilon_{(i,j)}}{k_{(i,j)}}$$

$$d_2 = \frac{r_{(i+0.5,j)} \mu_{t(i+0.5,j)}}{r_{(i,j)} \sigma_\varepsilon (\Delta r)^2},\ d_3 = \frac{\mu_{t(i,j+0.5)}}{\sigma_\varepsilon (\Delta z)^2},\ d_4 = \frac{\rho_{(i,j)} v_{(i,j)}}{\Delta r} + \frac{r_{(i-0.5,j)} \mu_{t(i-0.5,j)}}{r_{(i,j)} \sigma_\varepsilon (\Delta r)^2}$$

$$d_5 = \frac{\rho_{(i,j)} u_{(i,j)}}{\Delta z} + \frac{\mu_{t(i,j-0.5)}}{\sigma_\varepsilon (\Delta z)^2},\ S_\varepsilon = \frac{C_{\varepsilon 1} G_{(i,j)} \varepsilon_{(i,j)}}{k_{(i,j)}}\ .$$

The energy equation can be converted to algebraic form by using the (Backward Differences) for the diffusion term and (Central Differences) for the convective term , the following linear equation is obtained:-

$$e_1 T_{(i,j)} = e_2 T_{(i+1,j)} + e_3 T_{(i,j+1)} + e_4 T_{(i-1,j)} + e_5 T_{(i,j-1)} \tag{31}$$

Where ;

$$e_1 = \frac{\rho_{(i,j)} v_{(i,j)}}{\Delta r} + \frac{\rho_{(i,j)} u_{(i,j)}}{\Delta z} + \frac{r_{(i+0.5,j)} \mu_{(i+0.5,j)} + r_{(i-0.5,j)} \mu_{eff(i-0.5,j)}}{r_{(i,j)} p_r (\Delta r)^2} + \frac{\mu_{eff(i,j+0.5)} + \mu_{eff(i,j-0.5)}}{p_{r_{eff}} (\Delta z)^2}$$

$$e_2 = \frac{r_{(i+0.5,j)} \mu_{eff(i+0.5,j)}}{r_{(i,j)} p_{r_{eff}} (\Delta r)^2}, \quad e_3 = \frac{\mu_{eff(i,j+0.5)}}{p_{r_{eff}} (\Delta z)^2}, \quad e_4 = \frac{\rho_{(i,j)} v_{(i,j)}}{\Delta r} + \frac{r_{(i+0.5,j)} \mu_{eff(i-0.5,j)}}{r_{(i,j)} (\Delta r)^2 p_{r_{eff}}}$$

A numerical calculations algorithm was developed to solve the above equations numerically, and a computer program was built to implement this algorithm.

RESULTS AND DISCUSSION

The results of the developed computational algorithm for turbulent flow of air through a porous circular tube will be discussed for the following case:-

P_{in} = 1 bar, T_{in} = 100 ^oC, T_w = 100 ^oC, Q_w=1000w/m^2, U_{in}= (90-150) m/s, Re= 1.78 x10^7, M = 0.26 – 0.44, Z* = 130.

The grid size was taken as, (m=500) in axial direction and (n=20) in radial direction.

Fig.1 shows the development of the boundary layer for flow in solid wall with (Re=1.78x10^6) at (Q_w=1000w/m^2). Near the wall, the viscous effects are dominant, so the boundary layer grows in the flow (axial) direction until it reaches apposition ,after that the boundary shape fixed, this mean that flow is fully developed. It can be concluded that the hydrodynamic entrance length is equal to (140) pipe diameter approximately. **Fig.2** shows the radial distribution for the axial velocity profile at constant wall temperature and constant heat flux. **Fig.3** show the effect of Reynolds number on the development of velocity profiles at constant wall temperature and constant heat flux , it is that the velocity increased with the increasing of Reynolds number, the same result is obtained by **(Ayad,2003)**. **Fig.4** shows the dimensionless axial velocity development for various dimensionless radial positions, with constant wall temperature and constant heat flux, the same result is obtained by **(Stephenson,1976)**.

Fig.5 shows the effect of suction and injection on the velocity profiles at constant wall temperature first and constant heat flux second, the velocity profile is flattened at suction and became steeper at injection, the same result is obtained by **(Hasan,1984)**. With the presence of mass transfer through perforations, the velocity profile is altered due to the interaction between the axial flow and the perforation flow, for the injection case, the injection lifts and expands the turbulent boundary layer and thus increases the axial velocity beyond the layer while decreases the velocity within the layer to follow the mass conservation law. As a consequence the axial velocity near the pipe wall decreases and on the contrary, the suction lowers and reduces the boundary layer and thus decreases the velocity outside the layer but increases the velocity inside the layer, and results in an increase of the axial velocity near the pipe wall analysis, this is consistent with the numerical observations of **(Kinney & Sparrow,1970)** for pipe flow with suction through the pipe wall.For suction and injection Ω(+0.001, -0.001) the hydrodynamic length from the entrance to the fully developed velocity profile for the solid wall at constant wall temperature is equal to (130) diameters , decreases to (120) diameters , but for injection increases to (140) diameters, approximately. For Constant heat flux the hydrodynamic length for the solid wall is equal to (140) diameters , for suction decreased to (130) diameters , and for injection increased to (150) diameters ,approximately.

Fig.6 shows the development of turbulent kinetic energy $(2k/u_b^2)$with constant wall temperature , and constant heat flux , notice that the maximum value of the kinetic energy is in the region near the wall , and decreases in turbulent kinetic energy value with the increasing of Reynolds number because the axial velocity profile decreases with the increasing of the Reynolds number , also the hydrodynamic entry length ,at which the turbulent kinetic energy is fully developed , increases with the increasing of the Reynolds number. Fig (9) shows the effect of suction and injection on the turbulent kinetic energy ,turbulent kinetic energy increased with injection and decreased with suction, the same result is obtained by **(Ayad,2003)**.

Fig.7 shows the three dimensional development of the turbulent viscosity with. The turbulent viscosity increases with the increasing of the Reynolds number , so increasing the length needed for the fully developed profile, the same result is obtained by **(Ayad,2003)**.

Fig.8 show the development of air density for Reynolds number at constant wall temperature and constant heat flux , notice that for constant wall temperature the density stay constant near the wall but for constant heat flux decreases because of the increasing of the wall temperature down stream , the same result is obtained by **(Ayad,2003)**, suction increases the density and injection decreases it.

Fig.9 shows the steps of developing Reynolds Stress . Find that the Reynolds Stress equal to zero at maximum velocity near the center line and the maximum value is in the region near the wall, the same result is obtained by **(Ayad,2003)**. Show that the suction causes to flatten the velocity profile then decreases the Reynolds stress but the injection which causes to steeper the velocity profile then decreases the Reynolds stress.

Fig.10 shows the development of the local coefficient of friction , it decreases with the increasing of the Reynolds number because the boundary layer decreases , and the turbulent kinetic energy that enter in calculating the shear stress which can be calculated from the wall function decreases too. **Fig.11** shows the effect of suction and injection, the local coefficient of friction decreases with the suction because that the boundary layer decreases with the suction case so the turbulent kinetic energy decreases , but in the injection case the local coefficient of friction increases because the boundary layer increases , the same result is obtained by **(Moshe,1986)**.

Fig.12 shows development of the isothermal lines, notice that the temperature increases along side with axial flow direction and decrease with radial direction .**Fig.13-a** shows the effect of Reynolds number on the overall heating of the flow. **Fig.13-b** shows the effect of Reynolds Number on the wall temperature. The overall heating of the flow and the wall temperature increase parabolic in the developing region, and decrease with the increasing of Reynolds number, the same result is obtained by **(Ayad,2003)**.

Fig.15 shows the radial distribution of the turbulent heat flux at many positions , the turbulent heat flux values is the maximum near the wall and in the fully developed region because of the high temperature of the heated wall and there is a decreasing toward the center line because of the difference in the temperature between the wall and the fluid **,** the same result is obtained by **(Ayad,2003)** .

Fig.16 shows the axial distribution of the Nusselts number at constant wall temperature and constant heat flux, the maximum value at the entrance region because the thermal boundary layer thickness equal to zero and the heat transfer coefficient by convection is maximuim, after that the thermal boundary layer grows and the coefficient of heat transfer decreases and so the Nusselt number decreases gradually until it reaches constant value , it needs longer length , also for the same reason the Nusselts number increases with the increasing of the Reynolds number for constant wall temperature and constant heat flux, the same result is obtained by **(Ayad,2003)** . **Fig.17** shows the effect of suction and injection on Nusselts number, suction increases the value of Nusselt Number, the same result is obtained by **(Aggarwal & Hollingsworth,1973)** and injection decreases it. **Fig,18** shows the radial temperature development profile at constant wall temperature and constant heat flux . **Fig.19** shows the relation between mean Nusselt Number and Rynolds Number, increasing the Rynolds Number causes significantly increased heat transfer, so increasing Re causing an increase in Nu_{mean} , the same result is obtained by **(Hasan,1984)**.

Comparison of the Results .

Fig.20-a shows the comparison of the velocity profile for the present work which is calculated theoretically with experimental results of **(Aggarwal et al,1972)**, which was done on a porous tube with internal diameter (D=0.02565 m) and length (L=0.2465)m, for Reynolds Number Re(101160) and Z^* =9.3 with rate of suction Ω =(0.0135) . **Fig.20-b** shows the comparison of the development of the profile , at (Re=338000) for the present work with the results of the theoretical work which was done by **(Stephenson,1976)** , on a tube with (D=0.2 m) with (Re=388000) at
Z^* =(0.0 , 0.75, 0.94).

CONCLUSIONS.

The numerical results of the present work show that, the velocity profile, was flattened with suction and steepened with injection, its value was decreased with the increasing of Reynolds number and with suction .The hydrodynamic length, from the entrance to the fully developed region, was increased with the increasing of Reynolds number and with suction, it was decreased with injection. Turbulent kinetic energy was decreased in the region far from the wall and by suction, and it was increased by injection. Reynolds stress was vanished far from the wall; it was increased by injection and decreased by suction. Local coefficient of friction was decreased with suction and with the increasing of Reynolds number, it was increased with injection. Turbulent heat flux for constant wall temperature and constant heat flux has a maximum value near the wall and minimum value in the center line. Decreasing of the wall temperature at constant heat flux and the bulk temperature increases with injection and decrease with suction. Nusselts number was increased with the Reynolds number and with suction, and it was decreased with injection.

REFERENCES

Aggarwal,J.K,(1973) " Heat Transfer for Turbulent flow with Suction in a Porous Tube " J. Heat Mass Transfer , Vol.16.pp.591-609, 1973.

Aggarwal,J.K., Hollingsworth,M.A and Mayhew,Y.R , (1972) " Experimental Friction Factors for Turbulent Flow with Suction in a Porous Tube " J. Heat Mass Transfer. Vol.15.pp.1585-1602, 1972 .

Ayad Mahmoud Salman , (2003) , " Turbulent Forced Convection Heat Transfer in the Developing Flow Through Concentric Annuli " Msc. thesis , Mechanical Engineering Department . University of Technology.

Caretto,L.S., Curr,R.M and Spalding,D.B, (1972), "Two Numerical Methods For Three-Dimensional Boundary Layers," Compt. Meth. Appl. Mech. Engng., Vol. 1, PP. 39-57.

Hasan Abdul – Aziz Hasan , (1984) , " Length to Diameter Ratio Effects on Friction and Heat Transfer of Turbulent Flow in a Porous Tube " Ph.D. thesis , Mech. Eng. Dept., University of Bristol.

Kenny,R.B and Sparrow,E.M , (1970) " Turbulent Flow , Heat Transfer , and Mass transfer in a Tube with Surface Suction " ASME J. of Heat Transfer, PP.117-125 , February 1970 .

Moshe Ben-Reuven , (1984) " The Viscous Wall-Layer Effect in Injected Porous Pipe Flow " AIAA Journal , Vol.24.pp.284-294,1984.

Schlichting,H, (2000), "Boundary Layer Theory,"McGraw-Hill, New York.

Stephenson,P.L , (1976) , " A Theoretical Study of Heat Transfer in Two-Dimensional Turbulent Flow in a Circular Pipe and Between Parallel and Diverging Plates " J. Heat Mass Transfer , Vol.19.pp.413-423, 1976.

NOMENCLATURE

LATIN SYMBOLS

C_f	Local coefficient of friction (= $\tau_w / 0.5\rho u_b^2$)	
C_p	Specific heat at constant pressure	J / kg .^{o}C
D_h	Hydraulic diameter	m
G	Generation term	kg / m. s^3
h	Heat transfer coefficient	w / m .^{o}C
K	Von Karman constant	
L	Length of tube	m
m	Nodes number in z-direction	

$\dot{m}$	Mass flow rate	kg/s
n	Nodes number in r-direction	
Nu	Nusselts number (= hD_h / λ)	
P	Perimeter	
P	Pressure	N/m^2
P_r	Prandtle number	
Q	Heat flux	w/m^2
r	Radial dimension	
Re	Reynolds number (= $U_{in}D_h/\mu$)	
R^*	Dimensionless radial distance(= r/R)	
v	Radial velocity	m/sec
T	Temperature	^oC
u	Axial velocity	m/s
u_b	Axial Bulk velocity	m/s
y	Dimensionless distance from the wall	
z	Axial Cartesian coordinate	m
Z^*	Dimensionless axial length (=z/D)	

Greek Symbols

γ	Coefficient of relaxation	
Ω	Velocity ratio (= v_w /U_{in})	
ε	Dissipation rate of turbulent kinetic energy	m^2/s^3
k	Turbulent kinetic energy	m^2/s^2
λ	Fluid thermal conductivity	$W/m.^oC$
μ	Viscosity	kg/m. s
θ	Dimensionless temperature	
υ_t	Kinematic turbulent viscosity	m / s
ρ	Fluid density	kg /m^3
σ_κ, σ_ε	Turbulent Prandtle number	
$\Re$	Gas Constant	J/kg.K
τ_w	Wall shear stress	N /m^2
Ψ	Fractional mass extraction (= $\dot{m}_w / \dot{m}_{in}$)	

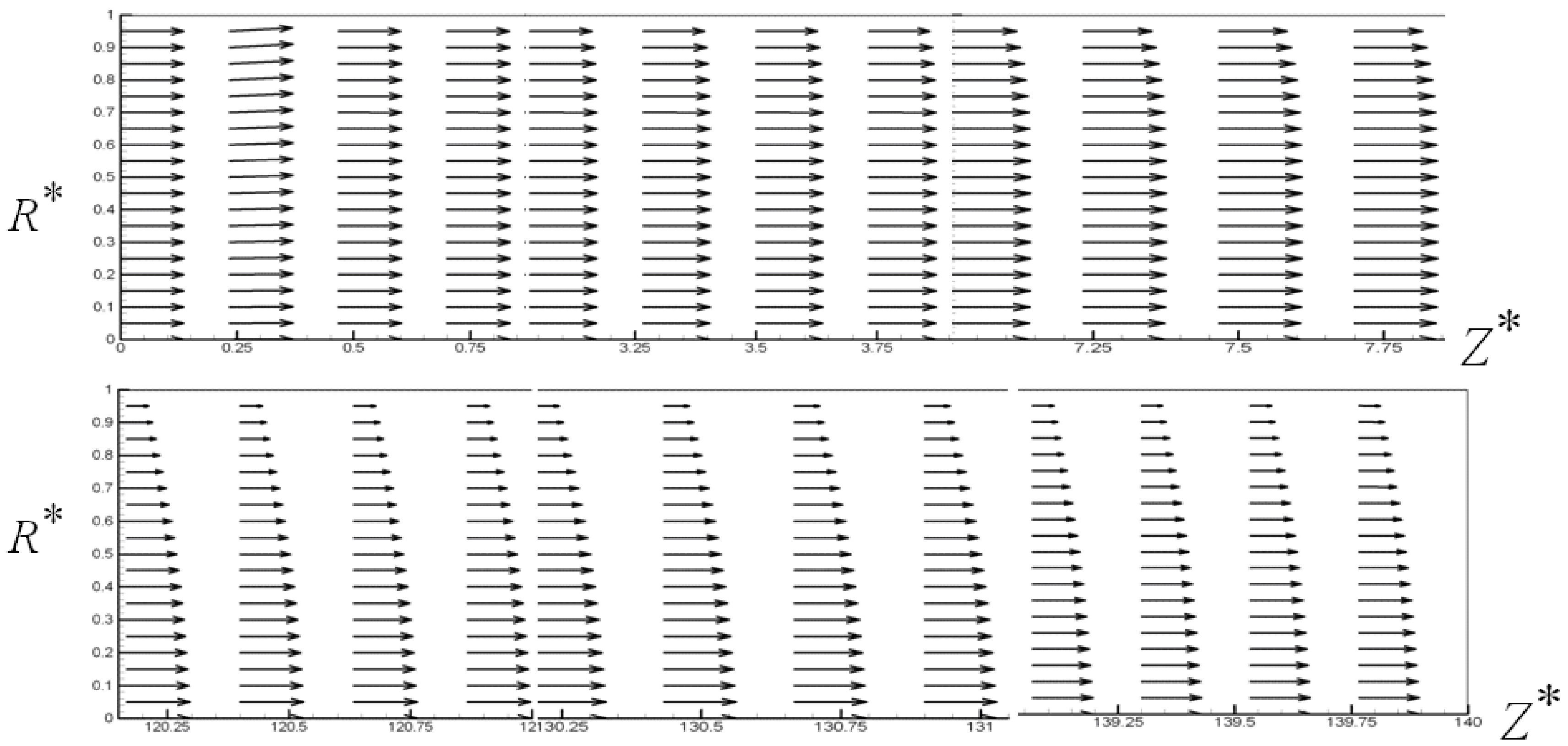

Fig(1).Developing Hydrodynamic Boundary Layer in Circular Tube for Flow with Constant Heat Flux at Re=1.78E+06(solid wall)

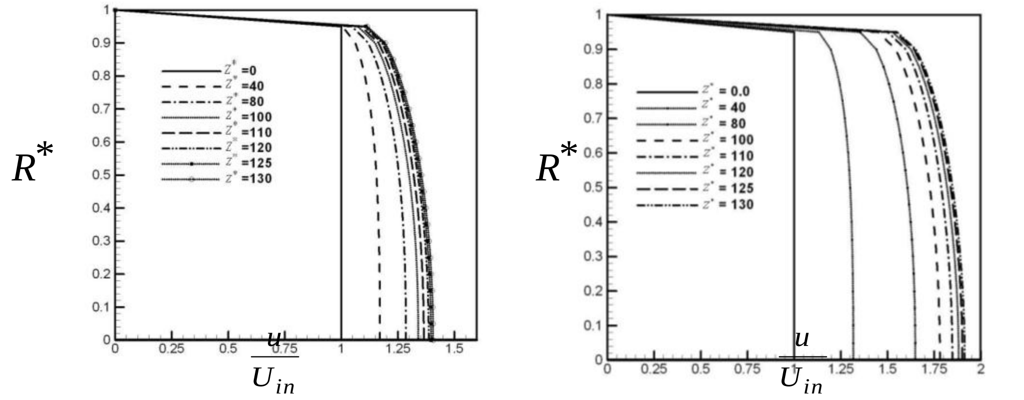

(a). Constant Wall Temperature. **(b). Constant Heat Flux.**

Fig.2 : Developing Axial Velocity for Solid Wall

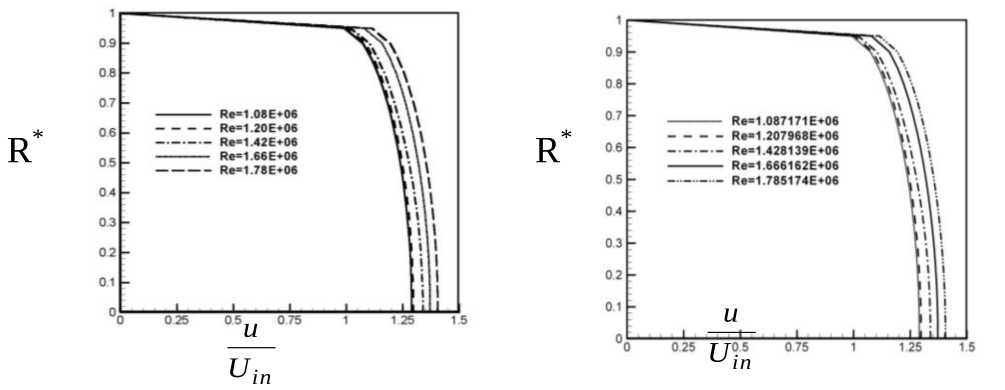

(a). Constant Wall Temperature. **(b). Constant Heat Flux.**

Fig.3: Effect of Reynolds Number on Developing Velocity

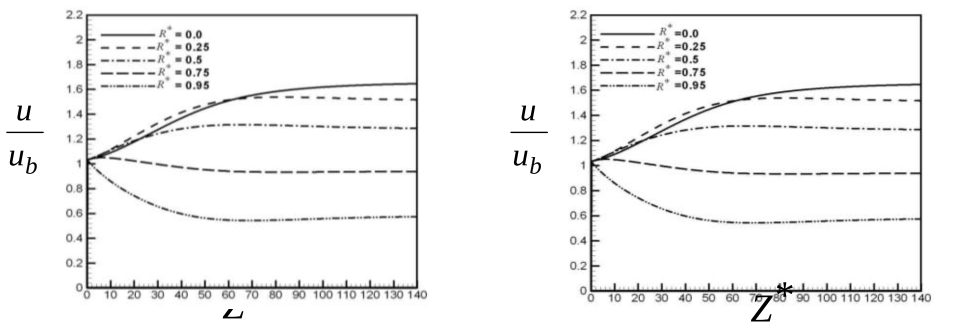

(a). Constant Wall Temperature. **(b). Constant Heat Flux.**

Fig.4: Developing Axial Velocity for Solid Wall

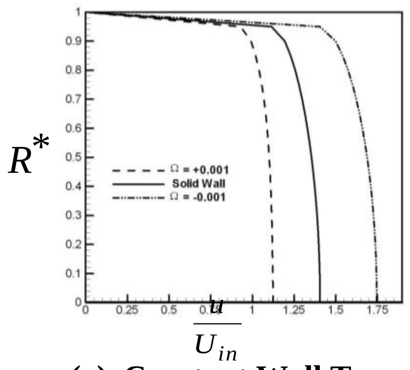

(a). Constant Wall Temperature.

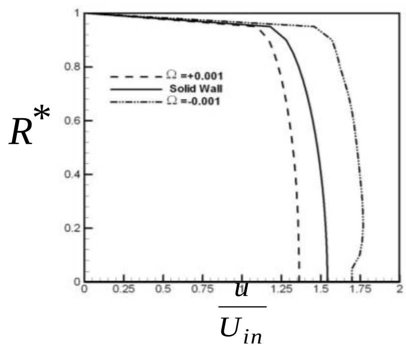

(b). Constant Heat Flux.

Fig.5: Effect of Suction and Injection on Developing Axial Velocity

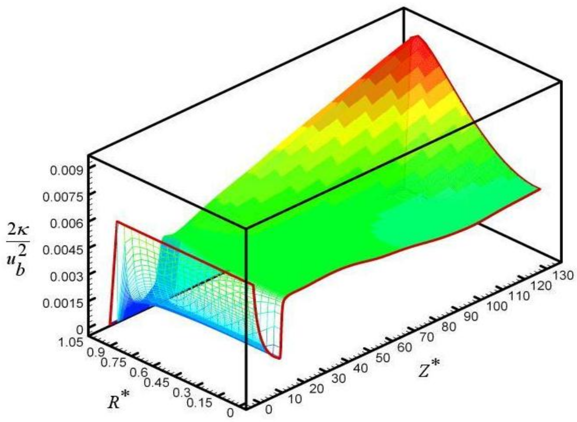

(a). Constant Wall Temperature.

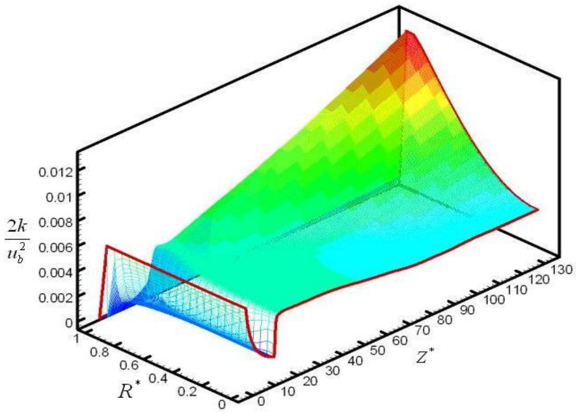

Fig.6: Development of Turbulent Kinetic Energy.

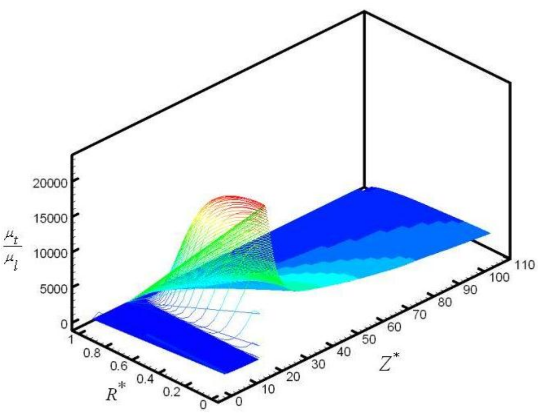

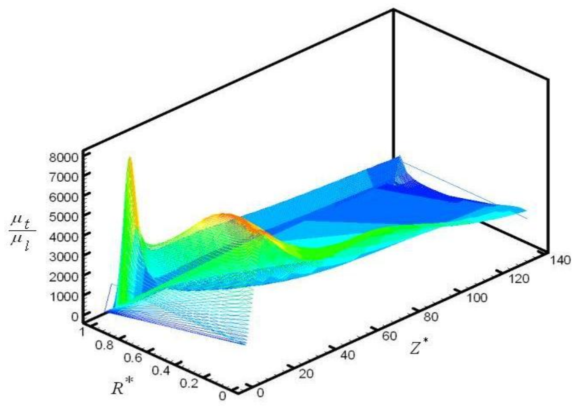

Fig.7: Development of turbulent viscosity for flow with

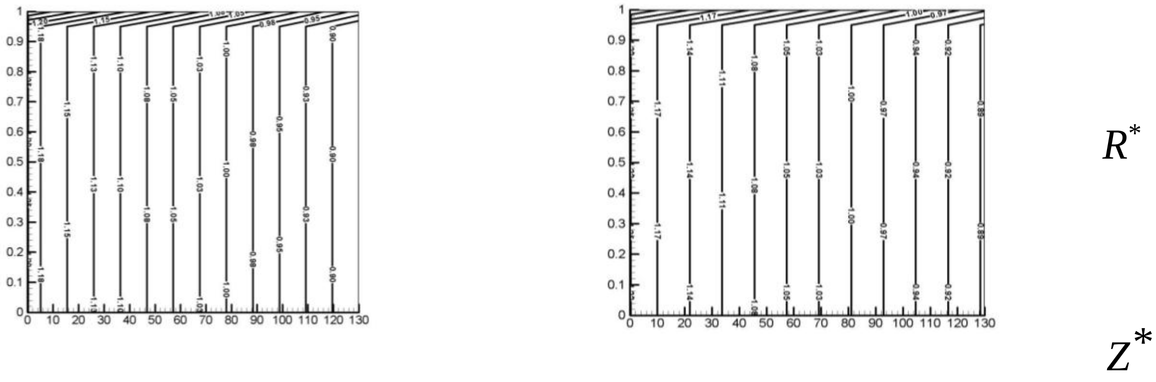

(a). Constant Wall Temperature. **(b). Constant Heat Flux.**

Fig.8: Developing Air Density for Flow with Re=1.78E+06

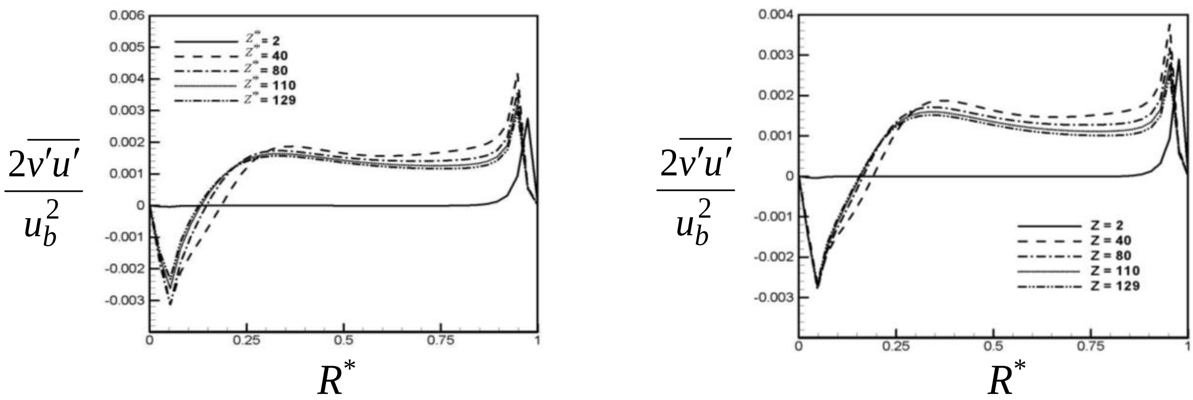

(a). Constant Wall Temperature. **(b). Constant Heat Flux.**

Fig.9: Developing Reynolds Stress for Reynolds Number Re=3.57E+06.

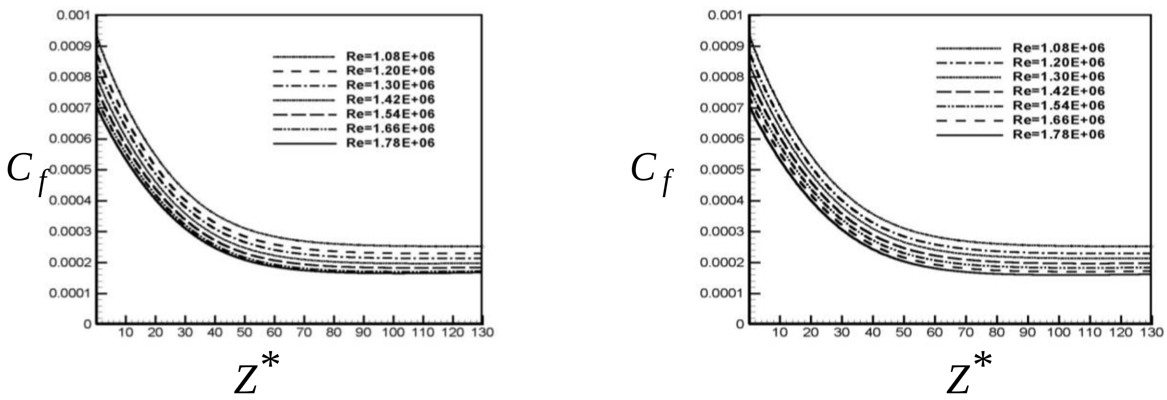

(a). Constant Wall Temperature. **(b). Constant Heat Flux.**

Fig.10: Effect of Reynolds Number on the Local Coefficient of Friction

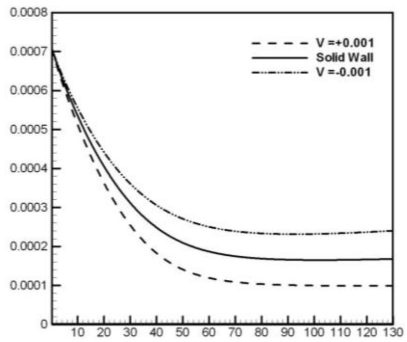

C_f

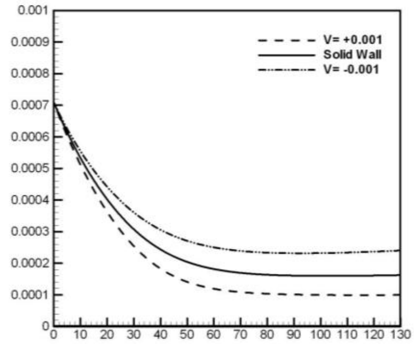

C_f

(a). Constant Wall Temperature. **(b). Constant Heat Flux.**

Z^*

Fig.11: Effect of Suction and Injection on Local Coefficient of Friction.

Z^* Z^*

R^*

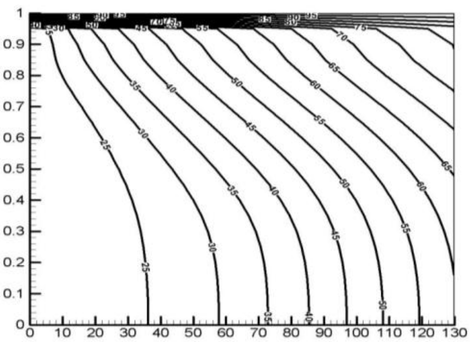

R^*

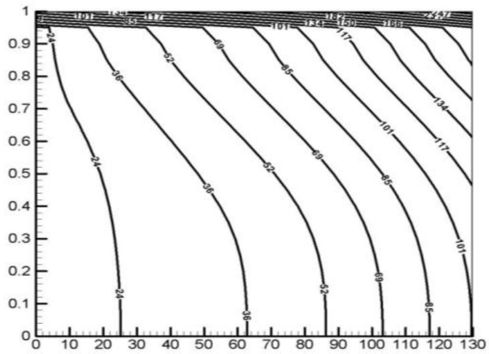

Z^*

(a). Constant Wall Temperature. **(b). Constant Heat Flux.**

Fig.12: Isothermal Lines at Re=1.78E+06 .

$\frac{T_b - T_{in}}{T_w - T_{in}}$

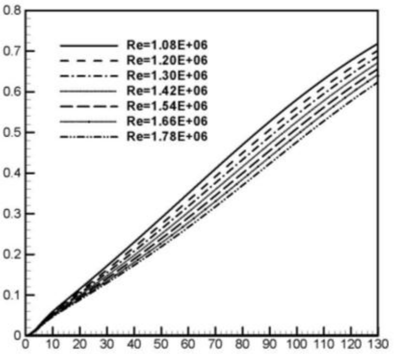

Z

θ_w

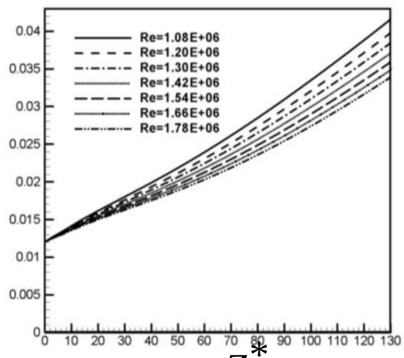

Z^*

(a). Overall Heating. **(b). Wall Temperature.**

Fig.13: Effect of Reynolds Number on Overall Heating and Wall
T

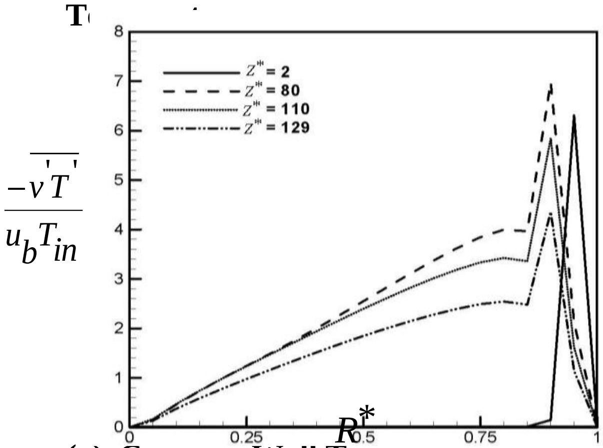

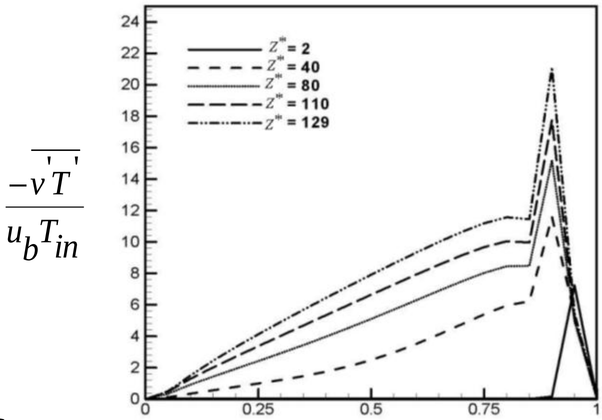

(a). Constant Wall Temperature. **(b). Constant Heat Flux.**

Fig.15: Turbulent Heat Flux Developing Curve .

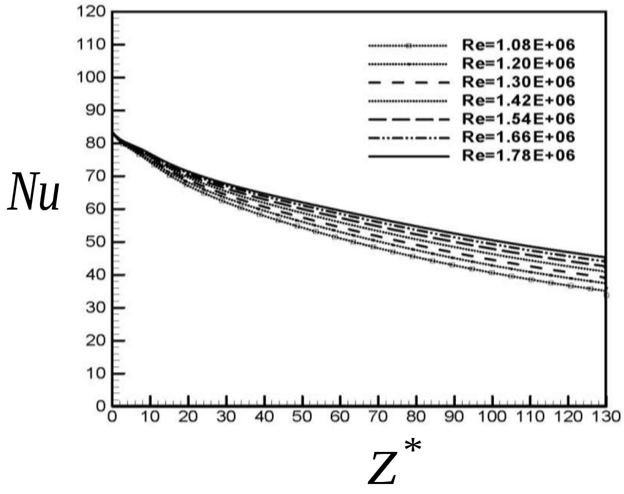

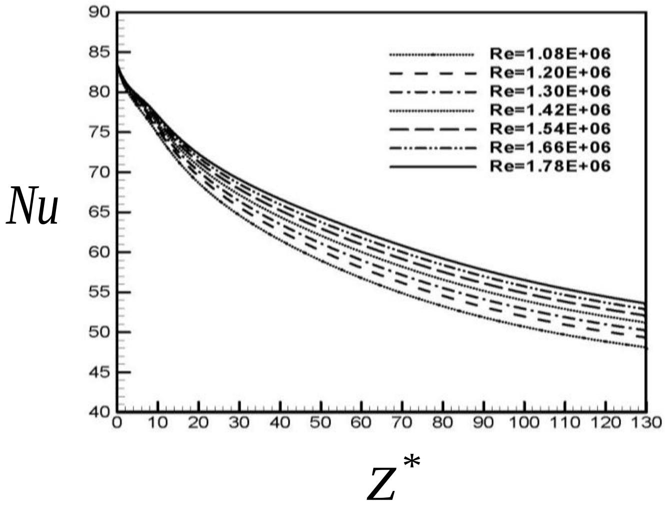

(a). Constant Wall Temperature. **(b). Constant Heat Flux.**

Fig.16: Effect of Reynolds Number on Local Nusselt Number .

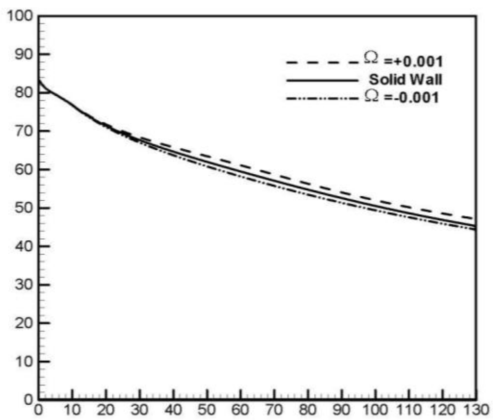

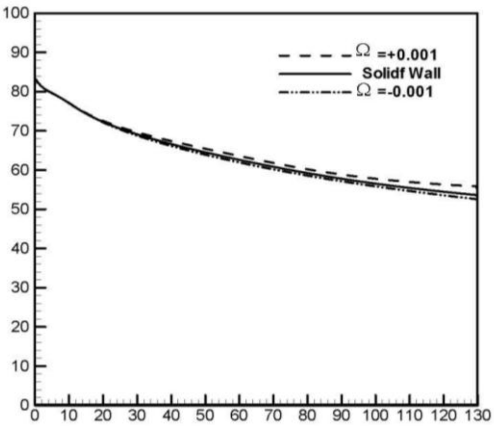

Nu Nu

Z^* Z^*

(a). Constant Wall Temperature. **(b). Constant Heat Flux.**

ection (

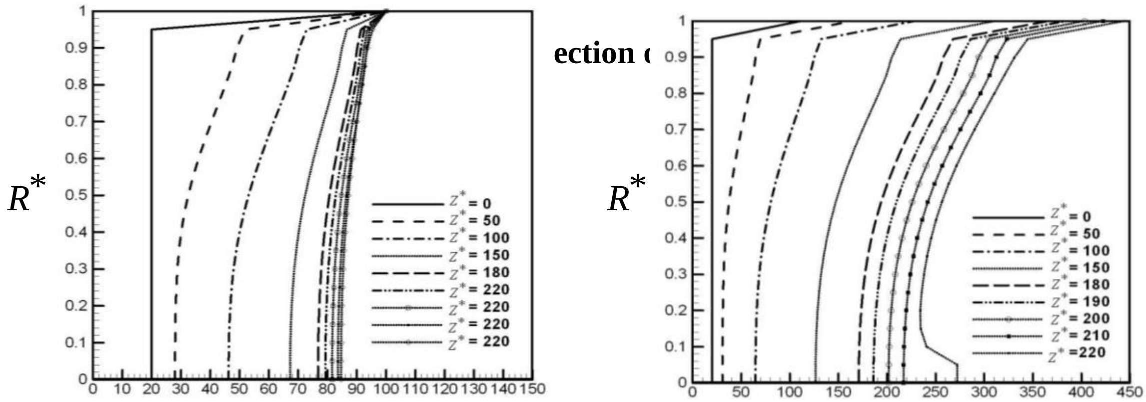

(a). Constant wall temperature. **(b). Constant heat flux.**

Fig.18: Radial Temperature Developing Profile for Solid Wall

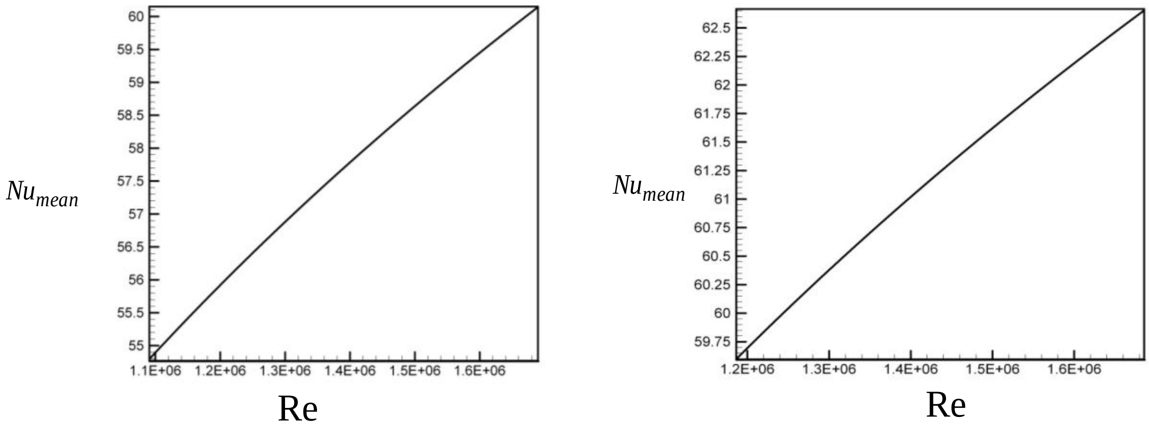

(a). Constant wall temperature. **(b). Constant heat flux.**

Fig.19: The Relation Between Mean Nusselt Number and Rynolds Number

$\frac{u}{u_b}$ $\frac{u}{u_b}$

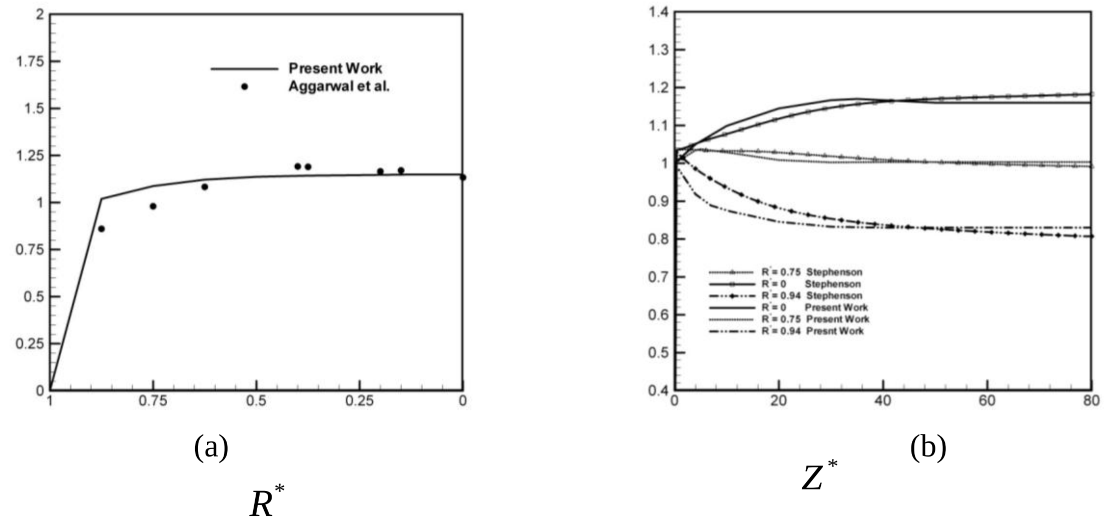

Fig.20: Comparison Between the Present Work and Past Works

AXISYMMETRIC FREE VIBRATION OF THIN PROLATE SPHEROIDAL SHELLS

Dr. Ahmed A. Hassan, Dr. Ala M. Hussein, Mohammed J. Obaid
College of Engineering, Babylon University

ABSTRACT

In this paper a detailed study of the theory of free axisymmetric vibration of thin isotropic prolate spheroidal shells is presented. The analysis is performed according to Rayleigh – Ritz method. This method as well as an approximate modeling technique were attempted to estimate the natural frequencies for the shell. This technique is based on considering the prolate spheroidal as a continuous system constructed from two spherical shell elements matched at the continuous boundaries. Through out the obtained results it is found that this method predicted fairly well the natural frequencies of a prolate spheroidal shell for all values of eccentricities.

الخلاصة

يتناول هذا البحث الدراسة النظرية للاهتزازات الحرة للقشريات نحيفة الجدران البيضوية الشكل المتطاولة المتناظرة المحور المتشابهة الخواص في جميع الاتجاهات ، وقد أجري التحليل النظري بطريقة رايلي–رتز .إن هذه الطريقه بالرغم من كونها تقريبية ، ولكن بالإمكان الاعتماد عليها لحساب الذبذبة الطبيعية لهذه القشريات .

من خلال النتائج وجد إن تلك الطريقة أعطت نتائج جيدة للترددات الطبيعية للقشرة البيضوية المتناظرة المحور لكل قيم أللامركزية.

KEYWORDS

Spheroidal Shells, Thin Prolate , Free Vibration, Axisymmetric

INTRODUCTION

Prolate spheroid shells can be obtained by rotating an ellipse around its major axis, see **Fig.1**. It is worthy to indicate the industrial applications and importance of shell structures. This interest was appreciated today in aerospace, sea vehicles industry and the structure of rocket can be considered as a prolate shells. In such structures the resonance problem may occur, therefore the study of free vibration become very important to prevent the resonance appearance.

The study of free vibration of prolate shells take a considerable attempt in the published literature. several investigators, using a variety of mathematical techniques, have obtained approximate solutions for the natural frequencies of axisymmetric vibrations of thin prolate spheroidal shells.

(De Maggio and Silibiger 1961) obtained a solution for the torsional vibrations of thin prolate spheroidal shell in terms of spheroidal angle functions. **(Kanins 1963)** was concerned with the vibration analysis of spheroidal shells, closed at one pole and open at the other, by means of the linear classical bending theory of shells. Frequency equations are derived in terms of Legender function with complex indices, and axisymmetric vibration of the natural frequencies and mode shapes are deduced for all opining angles ranging from a shallow to closed spherical shell. It was found that for all opening angles the frequency spectrum consist of two coupled infinite sets of modes that can be labeled as bending (or flexural) and membrane modes. It was also found that membrane modes are practically independent of thickness, whereas the bending modes vary with the thickness. The same author concerned with a theoretical investigation of the free vibration of arbitrary shells of revolution by means of the classical bending theory of shells.

A method is developed that is applicable to rotationally symmetric shells with meridional variations (including discontinuities) in Young's modulus, Poisson's ratio, radii of curvature, and thickness. The natural frequencies and the corresponding mode shapes of axisymmetric free vibration of rotationally symmetric shell can be obtained without any limitation on the length of the meridian of the shell. The results of free vibration of spherical and conical shells obtained earlier by means of the bending theory. In addition, parapoloidal shells and sphere-one shell combination are considered, which have been previously analyzed by means of the inextentional theory of shells, and natural frequencies and mode shapes predicted by the bending theory are given.

(Numergut and Brand 1965) determined the lower axisymmetric modes of prolate shell with five values of eccentricity. **(DiMaggio and Rand 1966)** using membrane shell theory in which the effects of bending resistance are ignored. Their work was distinguished by applying their solution to constant thickness membrane shell by means of integrating numerically the equations of motion. It was found that the frequencies associated with higher modes are strongly dependent on the eccentricity ratio.

(Zhu 1995) based upon general thin shell theory and basic equations of fluid-mechanics; the Rayleigh-Ritz's method for coupled fluid-structure free vibrations is developed for arbitrary fully or partially filled in viscid, irrigational and compressible or incompressible fluid, by means of the generalized orthogonality relations of wet modes and the associated Rayleigh quotients.

(Wasmi 1997) used the finite element and modal analysis techniques to investigate the static and dynamic behavior of oblate spheroidal dishes, prolate and the relevant structures. Different types of elements were considered in one dimension, two dimensions and three dimensions.

For framed structures, Euler Bernouilli theory, Tiomshenko theory, integrated Tiomshenko and improved Tiomshenko theories were applied. While for plates and shells, Kerchief's, Zienkiewicz and Mindlin theories were applied. The capability of these trenchancies was investigated in this work to predict the natural frequencies and mode shapes, as well as the static analysis of framed structures and spheroidal dishes. It was found that the natural frequencies of oblate and prolate shells have two types of behavior against increasing the shell thickness and eccentricity, which are the membrane and bending modes. The membrane modes natural frequencies tend to increase with increasing the eccentricity of oblate, while the bending mode natural frequencies decrease with increasing the value of eccentricity.

(Aleksandr Korjanik et al. 2001) investigated the free damped vibrations of sandwich shells of revolution. As special cases the vibration analysis under consideration of damping of cylindrical, conical and spherical sandwich shells is performed. A specific sandwich shell finite element with 54 degrees of freedom is employed. Starting from the energy method the damping model is developed. Numerical examples for the free vibration analysis with damping based on the proposed finite element approach are discussed. Results for sandwich shells show a satisfactory agreement with various references solutions.

(Antoine et, al 2002) investigated the linear and nonlonear vibrations of shallow spherical shells with free edge experimentally and numerically. Combination resonances due to quadratic nonlinearities are studied, for a harmonic forcing of the shell. Identification of the excited modes is achieved through symmetric comparisons between spatial results obtained from a finite element modelling, and spectral information derived from experiments.

This investigation deals with the free vibration characteristics of thin elastic prolate spheroidal shell. The shell is assumed be of isotropic material. The analysis depends on the Rayleigh _ Ritz method.

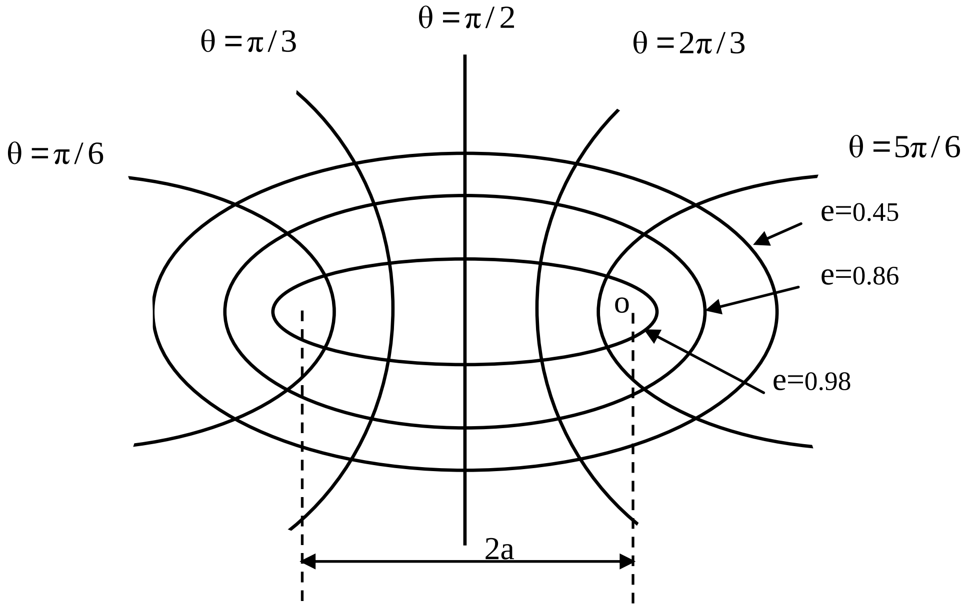

Fig. (1): Prolate spheroidal co-ordinates

MATHEMATICAL ANALYSIS

Through out the review of literature, it is found that even though the governing equations for shells of revolution are well spelt out, nevertheless, the governing equations for prolate spheroidal shells are not available, therefore the approximate energy procedure will be followed.

For a shell undergoing deformation in which the normal to the middle surface of undeformed shell remains straight and of a constant length under deformation, the shell displacements can be expressed as, (**Burroughs 1978)**:

$$w_{\Phi}(\Phi',t) = W(\Phi')e^{iwt}$$

$$u_{\Phi}(\Phi',t) = U_{\Phi}(\Phi')e^{iwt} \quad (1)$$

where, ω denotes the circular frequency. The stress resultants and couples are related to the displacement of the reference surface by the same expressions derived in appendix A with the eccentricity set equal to zero. **(Kalnins 1963)** show that the actual Φ-dependent coefficients of the variables can be written as:

$$W=\sum_{i=1}^{3}\left[A_i P_{ni}(x)+B_i Q_{ni}(x)\right] \tag{2}$$

$$U_\Phi=\sum_{i=1}^{3}-(1+\nu)C_i\left[A_i P'_{ni}(x)+B_i Q'_{ni}(x)\right] \tag{3}$$

$$U_\theta=\sum_{i=1}^{3}-(1+\nu)C_i\left[A_i P'_{ni}(x)+B_i Q'_{ni}(x)\right] \tag{4}$$

$$N_\Phi=\frac{E h}{(1-\nu)R_\Phi}\sum_{i=1}^{3}\left\{(1+C_i\beta_i)\left[A_i P_{ni}(x)+B_i Q_{ni}(x)\right]\right.$$

$$\left.+(1-\upsilon)C_i\cot\Phi\left[A_i P'_{ni}(x)+B_i Q'_{ni}(x)\right]\right\} \tag{5}$$

$$N_\theta=\frac{E.h}{(1-\nu)R_\Phi}\sum_{i=1}^{3}\left\{(1+\nu C_i\beta_i).\left[A_i P_{ni}(x)+B_i Q_{ni}(x)\right]\right.$$

$$\left.-(1-\upsilon)C_i\cot\Phi\left[A_i P_{ni}'(x)+B_i Q_{ni}'(x)\right]\right. \tag{6}$$

$$M_\Phi=\frac{D_b}{R_\Phi^2}\sum_{i=1}^{3}\left[1+(1+\nu)C_i\right]\left\{\beta_i\left[A_i P_{ni}(x)+B_i Q_{ni}(x)\right]\right.$$

$$\left.+(1-\nu)C_i\cot\Phi\left[A_i P'_{ni}(x)+B_i Q'_{ni}(x)\right]\right. \tag{7}$$

$$M_\theta=\frac{D_b}{R_\Phi^2}\sum_{i=1}^{3}\left[1+(1+\upsilon)C_i\right]\left\{\nu\beta_i\right.$$

$$\left.-(1-\nu)\cot\Phi\left[A_i P'_{ni}(x)+B_i Q'_{ni}(x)\right]\right\} \tag{8}$$

$$Q_\Phi=\frac{D_b}{R_\Phi^2}\sum_{i=1}^{3}\left[1+(1+\nu)C_i\right](\nu+\beta_i-1)\left[A_i P'_{ni}(x)+B_i Q'_{ni}(x)\right] \tag{9}$$

Where,

$$C_i=\frac{1+(\beta_i-2)/\left[(1+\nu)(1+\xi)\right]}{1-\nu-\beta_i+\xi(1-\nu^2)\Omega^2/(1+\xi^2)} \tag{10}$$

$$\xi=\frac{12R_\Phi^2}{h^2} \tag{11}$$

$$n_i=-\frac{1}{2}+\sqrt{1/4+\beta_i} \tag{12}$$

$$x=\cos\Phi \tag{13}$$

The value of β_i's are the three roots of the cubic equation:

$$\beta^3 - \left[4+(1-\nu\ )\Omega^2\right]\beta^2 + \left[4+((1-\nu^2)\Omega^2+(1+\xi)(1-\nu^2)\right]$$
$$(1-\Omega^2)\beta + (1-\nu)(1-\nu^2)\left[\Omega^2 - \frac{2}{1-\nu}\right]\left[1+(1+\nu^2)\left[\Omega^2 - \frac{1}{1+\nu}\right]\right] = 0 \tag{14}$$

Where,

$$\Omega^2 = \frac{\rho\omega^2 R_\Phi^2}{E} \tag{15}$$

And:

$$D_b = \frac{Eh}{12(1-\nu^2)} \tag{16}$$

In the above equations *$P_n(x)$, $Q_n(x)$* are the Legendre functions of the first and second kinds, respectively, $P_n'(x), Q_n'(x)$ are the derivatives with respect to (Φ) for the Legendre functions of the first and the second kinds, respectively. *A_i's & B_i's* are arbitrary constants.

The above solutions can be applied to study the free vibration of an elastic spherical shell bounded in general by any two concentric openings.

As the shell is taken to be closed at the apex (Φ=0), and since the Legendre function for the second kind is singular at this point, then the arbitrary constants (*B_i's*) are set equal to zero. For this reason all terms involving *$Q_n(x)$* are omitted.

RAYLEIGH-RITZ METHOD

Rayleigh-Ritz method, which is an extension of the Raleigh's method, helps to determine the natural frequencies and mode shapes with general boundary condition in approximate form.

The Rayleigh-Ritz procedure is essentially statement on the ratio of potential energy to the kinetic energy. At the natural frequency (ω), and assuming separation of variables, the shell displacements may be written as give by **Eq. (1)**. Substituting these in the strain energy expression gives:

$$P = \int_{-h/2}^{h/2}\int_0^{2\pi}\int_0^{2\pi}\frac{1}{2}\left[\sigma_\Phi \in_\Phi' + \sigma_\theta \in_\theta'\right]R_\Phi R_\theta \sin\Phi' d\Phi' d\theta dz \tag{17}$$

Where,

$$\sigma_{\Phi'} = \frac{E}{(1-\nu^2)}\left[\in'_{\Phi'} + \upsilon \in'_{\theta}\right] \qquad , \ \sigma_{\theta} = \frac{E}{(1-\nu^2)}\left[\in'_{\theta} + \nu \in'_{\Phi'}\right] \tag{18}$$

and

$$\in'_{\Phi} = \in^{o}_{\Phi} + zk_{\Phi} \qquad , \in'_{\theta} = \in'_{\theta} + zk_{\theta} \tag{19}$$

An expression for the maximum strain energy ($P_{\max}$) may be obtained upon taking e^{iwt} to be unity and applying the appropriate expressions for σ_{Φ} , σ_{θ} , $\in'_{\Phi}$ and $\in'_{\theta}$ to given by:

$$\begin{aligned}
P_{\max} = \frac{E\,h}{2(1-\nu^2)} \int_0^{2\pi}\int_0^{2\pi} \Bigg\{ & \frac{h^2}{12}\left[\frac{1}{R_\Phi^2}\left[\frac{\partial}{\partial \Phi'}\left[\frac{U_\Phi}{R_\Phi} - \frac{\partial W}{R_\Phi\,\partial \Phi'}\right]\right]\right. \\
& + \frac{\cos^2\Phi'}{R_\Phi^2\ R_\theta^2\ \sin^2\Phi'}\left[U_\Phi - \frac{\partial W}{\partial \Phi'}\right]^2 + 2\,\nu \frac{\cos\Phi'}{R_\theta\ R_\Phi^2\ \sin\Phi'}\left[U_\Phi - \frac{\partial W}{\partial \Phi'}\right]. \\
& \left.\frac{\partial}{\partial \Phi'}\left[\frac{U_\Phi}{R_\Phi} - \frac{\partial W}{R_\Phi\,\partial \Phi'}\right]\right] + \frac{1}{R_\Phi^2}\left[\frac{\partial U_\Phi}{\partial \Phi'} + W\right]^2 \\
& + \frac{1}{(R_\theta\ \sin\Phi')^2}\left(U_\Phi\ \cos\Phi' + W\ \sin\Phi'\right)^2 \\
& + \frac{2\,\nu}{R_\theta\ R_\Phi \sin\Phi'}\left[\frac{\partial U_\Phi}{\partial \Phi'} + W\right]\left(U_\Phi \cos\Phi' + W\ \sin\Phi'\right) \Bigg\} \\
& R_\Phi\ R_\theta\ \sin\Phi' d\Phi'\ d\theta
\end{aligned} \tag{20}$$

The kinetic energy is:

$$K = \int_{h/2}^{h/2}\int_0^{2\pi}\int_0^{2\pi} \frac{1}{2}\rho\left[\left[\frac{\partial u_\theta}{\partial t}\right]^2 + \left[\frac{\partial w}{\partial t}\right]^2\right] R_\Phi R_\theta \sin\Phi' d\Phi' d\theta \tag{21}$$

After integration with respect to (z) and substituting for the appropriate expression, the maximum kinetic will take the form:

$$K_{\max} = \frac{\omega^2 \rho h}{2}\int_0^{2\pi}\int_0^{2\pi} (u_\Phi^2 + w^2) R_\Phi R_\theta \sin\Phi' d\Phi' d\theta \tag{22}$$

Equating the maximum kinetic energy to the maximum potential energy, the natural frequency can be written as:

$$\omega_r^2 = \frac{P_{\max}}{K_{\max}} = \frac{N}{D} \tag{23}$$

Where, N and D represent the equations in numerator and denominator, respectively. Following the procedure of Rayleigh-Ritz’s method, the radial (or transverse) and tangential displacements can be written in power series form as:

$$w(\Phi') = \sum_{i=1}^{3} a_i w_i(\Phi') \qquad u_\Phi(\Phi') = \sum_{i=1}^{3} b_i u_{\Phi i}(\Phi') \tag{24}$$

Where, the a_i's and b_i's are coefficients to be determined.

The functions $W_i(\Phi')$, $U(\Phi')$ satisfy all the geometry boundary conditions of the system. **Eq.(23)** is an exact expression for the frequency according to Rayleigh quotient. In order to use the procedure of Rayleigh-Ritz’s method, **Eq. (24)** is substituted into **Eq.(20)** and **(22)**, then the results are used in **Eq. (23).**

Now substituting **Eq. (24)** into **Eqs. (20)** and **(22)**, and after some mathematical manipulations, the following equation will results:

$$\omega_r^2 = \frac{\alpha}{\Psi} \tag{25}$$

Where,

$$\begin{aligned}
\alpha = \sum_{i=1}^{n} \sum_{i=1}^{n} c_i c_j \frac{Eh\pi}{(1-v^2)} \int_o^{2\pi} \Bigg\{ & \frac{h^2}{12R_\Phi^4} \Big[U_{\Phi i}'' U_{\Phi i}'' - 2U_{\Phi i}'' + W_i'' W_j''' \Big] \sin\Phi' \\
& + \frac{vh^2}{6R_\theta R_\Phi^3} \Big[U_{\Phi i} U_{\Phi i}'' - U_{\Phi i} W'' - U_{\Phi i} W_i' + W' W_i'' \Big] \cos\Phi' \\
& + \frac{h^2}{12R_\theta^2 R_\Phi^2} \Big[U_{\Phi i} U_{\Phi j}' - 2U_{\Phi i} W_i' + W_i' W_j' \Big] \frac{\cos^2\Phi'}{\sin\Phi'} \\
& + \frac{1}{R_\Phi^2} \Big[U_{\Phi i}' U_{\Phi j}' + 2U_{\Phi i} W_i + W_i' W_j' \Big] \sin\Phi' \\
& + \frac{1}{R_\theta^2} \left[U_{\Phi i} U_{\Phi j} \frac{\cos^2\Phi'}{\sin\Phi'} + 2U_{\Phi i} W_i \cos\Phi' + W_i W_j \sin\Phi' \right] \\
& + \frac{2v}{R_\Phi R_\theta} \Big[U_{\Phi i} U_{\Phi i}' \cos\Phi' + U_{\Phi i}' W_i \sin\Phi' - U_{\Phi i} W_i \cos\Phi' + W_i W_j \sin\Phi' \Big] \Bigg\} \\
& R_\Phi R_\theta \, d\Phi'
\end{aligned} \tag{26}$$

$$\Psi = \sum_{i=1}^{n} \sum_{i=1}^{n} c_i c_j \int_0^{2\pi} \left[U_i U_j + W_i W_j \right] R_\Phi R_\theta \sin\Phi' \, d\Phi' \tag{27}$$

An n-term finite sum leads to the estimation of the first frequencies. **Eqs. (26)** and **(27)** gives the physical properties of the shell from the stiffness and mass distribution point of view.

The stiffness and mass of the shell are given by the following two equations respectively:

$$k_{ij} = \frac{E\,h\,\pi}{(1-\nu^2)}\int_0^{2\pi}\Big\{ \frac{h^2}{12\,R_\Phi^4}\left[U'_{\Phi i}U'_{\Phi i} - 2U'_{\Phi i}\,W_i'' + W_i''\,W_j''\right]\sin\Phi'$$

$$+\frac{\nu\,h^2}{6\,R_\theta\,R_\Phi^3}\left[U_{\Phi i}\,U'_{\Phi i} - U_{\Phi i}\,W_i'' - U'_{\Phi i}\;W_i' + W_i'\,W_i''\right]\cos\Phi'$$

$$+\frac{h^2}{12\,R_\Phi^2\,R_\theta^2}\left[U'_{\Phi i}\,U'_{\Phi j} - 2U'_{\Phi i}W_i' + W_i'W_j'\right]\frac{\cos^2\Phi'}{\sin\Phi'}$$

$$+\frac{1}{R_\Phi^2}\left[U'_{\Phi i}U'_{\Phi j} + 2U'_{\Phi i}\,W_j + W_i\;\;W_j\right]\sin\Phi'$$

$$+\frac{1}{R_\theta^2}\left[\;U_{\Phi i}\,U_{\Phi j}\,\frac{\cos^2\Phi'}{\sin\Phi'} + 2U_{\Phi i}\;W_i\cos\Phi'\; + W_i\,W_j\,\sin\Phi'\;\right]$$

$$+\frac{2\nu}{R_\Phi\,R_\theta}\left[U_{\Phi i}\,U'_{\Phi i}\cos\Phi' + U'_{\Phi i}\;W_i\sin\Phi'\; + U_{\Phi i}\,W_i\cos\Phi'\; + W_i\,W_i\sin\Phi'\;\right]\Big\}.$$

$$.\,R_\Phi\,R_\theta\,d\Phi'$$

and

(28)

$$m_{ij} = \int_0^{2\pi}\rho h\pi\left[U_iU_j + W_iW_j\right]R_\Phi R_\theta\,\sin\Phi'\,d\Phi' \tag{29}$$

Then

$$\omega_r^2 = \frac{\sum_{i=1}^{n}\sum_{j=1}^{n} c_i c_j k_{ij}}{\sum_{i=1}^{n}\sum_{j=1}^{n} c_i c_j m_{ij}} \tag{30}$$

The exact frequency is always smaller than the approximate value. In order to minimize the approximate value, which given by **Eq.(30)**, it should be differentiated with respect to c_i and equating the resulting expression to zero, that is:

$$\frac{\partial}{\partial c_i} = \frac{D\partial N/\partial c_i - N\partial D/\partial c_i}{D^2} = 0 \qquad ,i=1,2,3,\ldots\ldots n \tag{31}$$

The only way in which this equation can equal is zero if the numerator equals zero, since D is never equal to zero. The numerator can be written in a more useful form as:

$$\frac{\partial N}{\partial c_i} - \frac{N}{D}\frac{\partial D}{\partial c_i} = 0\;, \qquad i = 1,2,3,\ldots,n \tag{32}$$

$=N/D$

It is as given by equation (23) $\omega_r^2 = \dfrac{N}{D}$, and n is the number of terms in the approximate solution. The infinite degrees of freedom system has been replaced by an n degree of freedom system. Therefore, **Eq. (31)** can be written in a matrix form as:

$$\left[\{K\} - \omega^2\{M\}\right]\{c\} = \{0\} \qquad (33)$$

The stiffness and mass are determined at the edge ($\Phi = \Phi_0$) of the spherical shell using (28 and 29) respectively. The values equated in above equations are then substituted in the following determinant:

$$\begin{vmatrix} k_{11} - \Omega^2 m_{11} & k_{12} - \Omega^2 m_{12} & k_{13} - \Omega^2 m_{13} \\ k_{21} - \Omega^2 m_{21} & k_{22} - \Omega^2 m_{22} & k_{23} - \Omega^2 m_{23} \\ k_{31} - \Omega^2 m_{31} & k_{32} - \Omega^2 m_{32} & k_{33} - \Omega^2 m_{33} \end{vmatrix} = 0 \qquad (34)$$

The value of Ω^2 which make the determinant equal zero represent the natural frequency of the shell.

RESULTS AND DISCUSSION

In order to confirm the accuracy of the theoretical results, these results are compared with the available literature due complexity of obtaining a closed form solution for the free vibration characteristics of a prolate spheroid shell. From **Table (1)** it can be noted that the variation of the natural frequencies of bending modes increase with thickness and with the mode number. This phenomenon can be elaborated due to the fact that the strain energy increased with increasing the ratio of thickness for larger eccentricities ratio.

The non-dimensional frequency coefficients for the first three flexural modes which computed from the present work with (h/a=0.05) are presented in **Table (2)** along with the results of **(Burroghs and Magrab 1978)**. From this table it is seen that there is reasonable agreement between these results, which provide the accuracy of the formulation and results.

Fig.2 shows the non-dimensional natural frequency $(\lambda = \sqrt{\rho / E}\,\omega a)$ of the first three modes of vibration as a function of the eccentricity ratio obtained by the Rayleigh- Ritz's method using the non-shallow shell theory. It is clearly shown that the tendency of the natural frequencies towards higher values as the eccentricity ratio increases. This behavior could be explained by the mode shapes of a closed spherical shell would resemble those of a prolate spheroid up to certain eccentricity. As the eccentricity increases, the bending stress increased and the potential energy increased. Another reason is that the geometry of the prolate shape is stiffer than the spherical shape.

Fig.3 gives the first few natural frequencies as a function of the thickness ratio for a prolate spheroid with (e=0) obtained by RRM. **Fig.4** show the first few natural frequencies as a function of thickness ratio with (e=0.7). All these figures are obtained for $(\nu = 0.3)$ and they depend on the bending as well as the membrane modes using the non-shallow shell theory. It can be noted that the variation of the natural frequency of the bending modes increases with thickness and with the mode number. This phenomenon can be elaborated due to the fact that the strain energy increased with increasing the thickness ratio. Also, for larger eccentricity ratio, the variations are more pronounced than for smaller eccentricities.

Fig.5 shows the effect of eccentricity ratio on the first membrane mode. It is seen that the natural frequency increased with increasing the eccentricity ratio. The eccentricity ratio affects the natural frequency hardly at the lower range, while this effect decreased when the eccentricity ratio beyond 0.8.

The mode shapes of the first three modes of the prolate spheroid shell are shown in **Fig.8**, in which both the transverse and tangential displacements are illustrated. This figure shows that the modes of the transverse displacement occurs at a position in which the tangential; displacement has maxima and vice versa.

CONCLUTIONS

The main conclutions from the present work can be summarized as;

1- Natural frequencies are seen to have two types of behaviour against increasing the thickness to major radius ratio. One type, which is associated with the bending modes, tends to increase with thickness, while the other type, which is associated with membrane mode, remains unaffected by the thickness variation.
2- Both bending and membrane modes natural frequencies tend to increase with increasing eccentricity ratio.
3- The natural frequency tends to increase with increasing the ratio of thickness of the shell.

APPENDIX

The principal curvatures of the surface as a function of the angle of inclination (Φ) in the following form.

$$R_{\Phi} = \frac{a(1-e^2)}{(1-e^2\cos^2\Phi')^{3/2}}$$

$$R_{\theta} = \frac{a}{(1-e^2\cos^2\Phi')}$$

Where (Φ') is the angle in the space between the vertical axis and the normal vector, it is given by

$$\cos\Phi' = \frac{\sin\beta}{\sqrt{1-e^2\cos^2\beta}} \; ,$$

(e) is the eccentricity ratio of the spheroidal shell , which is given by;

$$e = \frac{1}{\cosh\alpha} = \frac{1}{c}$$

The strains, expressed in terms of displacement can be written as:

$$\varepsilon_{\Phi}^{\circ} = \frac{1}{R_{\Phi}}\left[\frac{\partial u_{\Phi}}{\partial \Phi'} + w\right]$$

$$\varepsilon_{\theta}^{\circ} = \frac{1}{R_{\theta}\sin\Phi'}\left[u_{\Phi}\cos\Phi' + w\sin\Phi'\right] = \frac{1}{R_{\theta}}\left[u_{\Phi}\cot\Phi' + w\right]$$

$$k_{\Phi} = \frac{1}{R_{\Phi}}\frac{\partial}{\partial\Phi'}\left[\frac{1}{R_{\Phi}}\left(u_{\Phi} - \frac{\partial w}{\partial \Phi'}\right)\right]$$

$$k_{\theta} = \frac{1}{R_{\Phi}\sin\Phi'}\left[\frac{\cos\Phi'}{R_{\Phi}}\left(u_{\Phi} - \frac{\partial w}{\partial\Phi'}\right)\right]$$

If E, ν are as in nomenclature then, the forces and moments per unit length will be

$$N_{\Phi} = \frac{Eh}{1-\nu^2}\left[\varepsilon_{\Phi}^{0} + \varepsilon_{\theta}^{0}\right]$$

$$N_{\theta} = \frac{Eh}{1-\nu^2}\left[\varepsilon_{\theta}^{0} + \nu\varepsilon_{\Phi}^{0}\right]$$

$$M_{\Phi} = \frac{Eh^2}{12(1-\nu^2)}\left[K \;\; + \nu K \;\;\right]$$

$$M_{\theta} = \frac{Eh^2}{12(1-\nu^2)}\left[K_{\theta} + \nu K_{\Phi}\right]$$

Substituting the relevant expressions get:-

$$N_{\Phi} = \frac{E\,h}{1-\upsilon^2}\left[\frac{1}{R_{\Phi}}\left(\frac{\partial u_{\Phi}}{\partial \Phi'} + w\right) + \frac{\upsilon}{R_{\Phi}}\left(u_{\Phi}\cot\Phi' + w\right)\right]$$

$$N_{\theta} = \frac{E\,h}{1-\upsilon^2}\left[\frac{1}{R_{\theta}}\left(u_{\Phi}\cot\Phi' + w\right) + \frac{\upsilon}{R_{\Phi}}\left(\frac{\partial u_{\Phi}}{\partial \Phi'} + w\right)\right]$$

$$M_{\Phi} = \frac{E\,h^3}{12(1-\upsilon^2)}\left[\frac{1}{R_{\Phi}}\frac{\partial}{\partial \Phi'}\frac{1}{R_{\theta}}\left(u_{\Phi} - \frac{\partial w}{\partial \Phi'}\right) + \frac{\upsilon\cos\Phi'}{R_{\Phi}\,R_{\theta}\sin\Phi'}\left(u_{\Phi} - \frac{\partial w}{\partial \Phi'}\right)\right]$$

$$M_{\theta} = \frac{E\,h^3}{12(1-\upsilon^2)}\left[\frac{\cos\Phi'}{R_{\Phi}\,R_{\theta}\sin\Phi'}\left(u_{\Phi} - \frac{\partial w}{\partial \Phi'}\right) + \frac{\upsilon}{R_{\Phi}}\frac{\partial}{\partial \Phi'}\left(\frac{1}{R_{\theta}}\left(u_{\Phi} - \frac{\partial w}{\partial \Phi'}\right)\right)\right]$$

Table (1): Dimensionless natural frequency coefficients for the axisymmetric free vibration of a prolate spheroidal shell.

Mode Number	**E=0.3**	**e=0.7**		
	h/a=0.01	**h/a=0.05**	**h/a=0.01**	**h/a=0.05**
1	**0.0**	**0.0**	**0.0**	**0.0**
2	**0.16**	**0.16**	**0.725**	**0.725**
3	**0.18**	**0.19**	**0.87**	**0.89**
4	**0.2**	**0.23**	**0.91**	**0.93**

Table (2): Comparison of other estimates of Ω for the flexural modes of a thin prolate spheroidal shell with e=0.7

Mode Number	**Present Work h/a=0.05**	**Reference [9]**
2	**0.725**	**0.73**
3	**0.89**	**0.90**
4	**0.93**	**0.95**

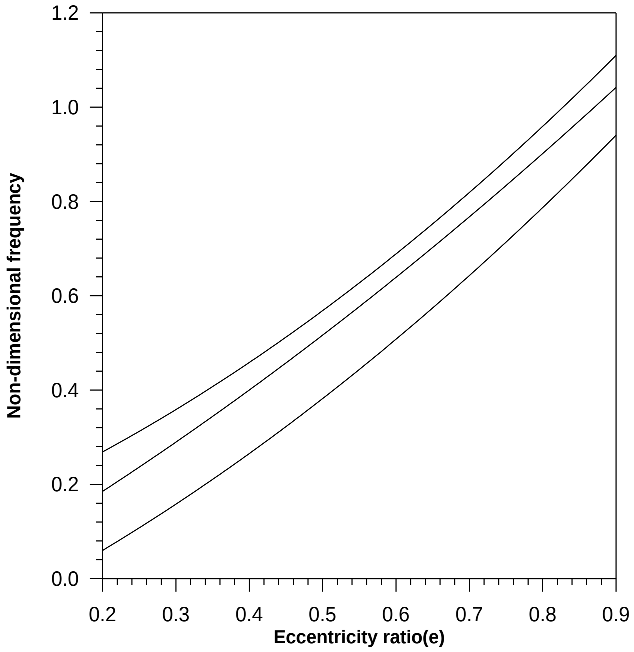

Fig.(2): Effect of eccentricity on the first three bending modes obtained by RRM

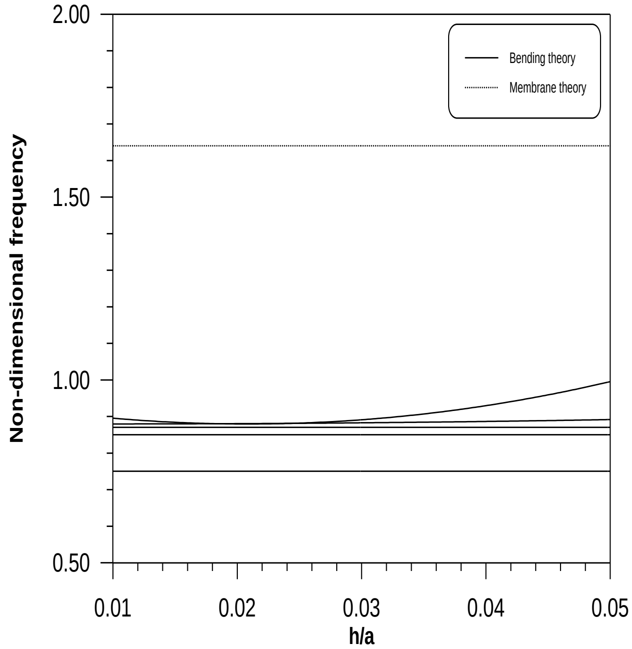

Fig. (3): Effect of the eccentricity ratio on the natural frequency of a full sphere (e=0) obtained by RRM

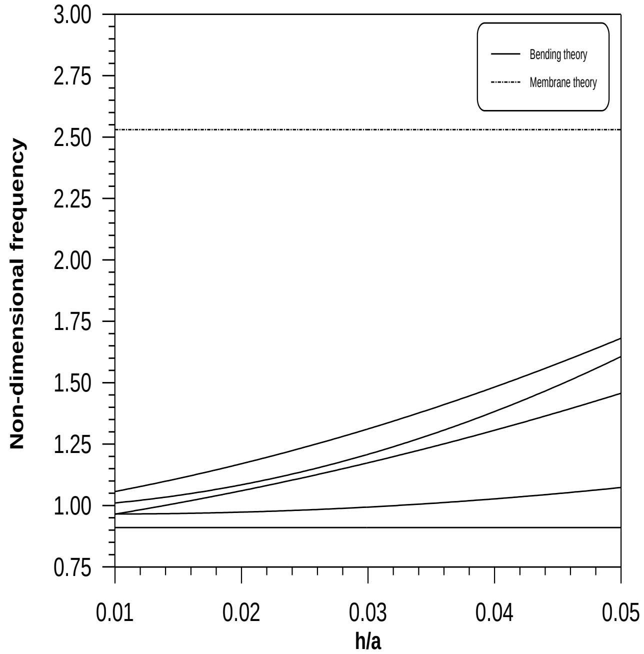

Fig. (4): Effect of the thickness ratio on the natural frequency of a prolate spheroidal shell (e=0.7) obtained by RRM

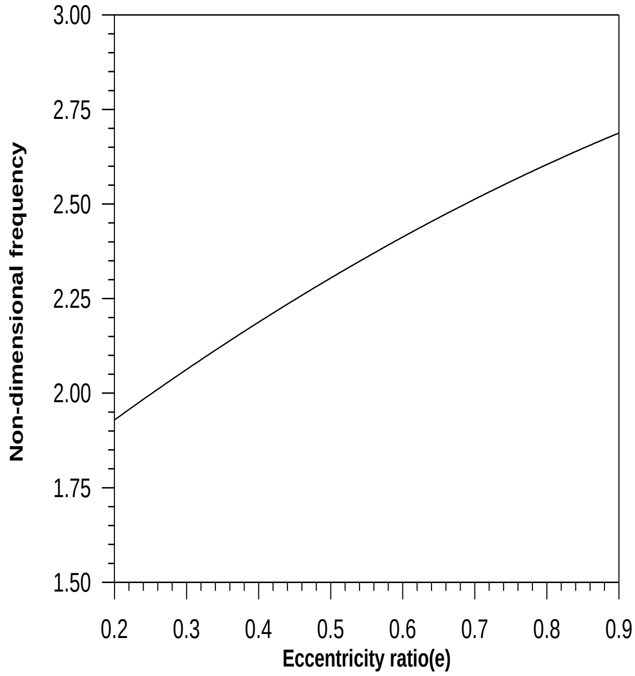

Fig.(5): Effect of eccentricity on the first membrane mode

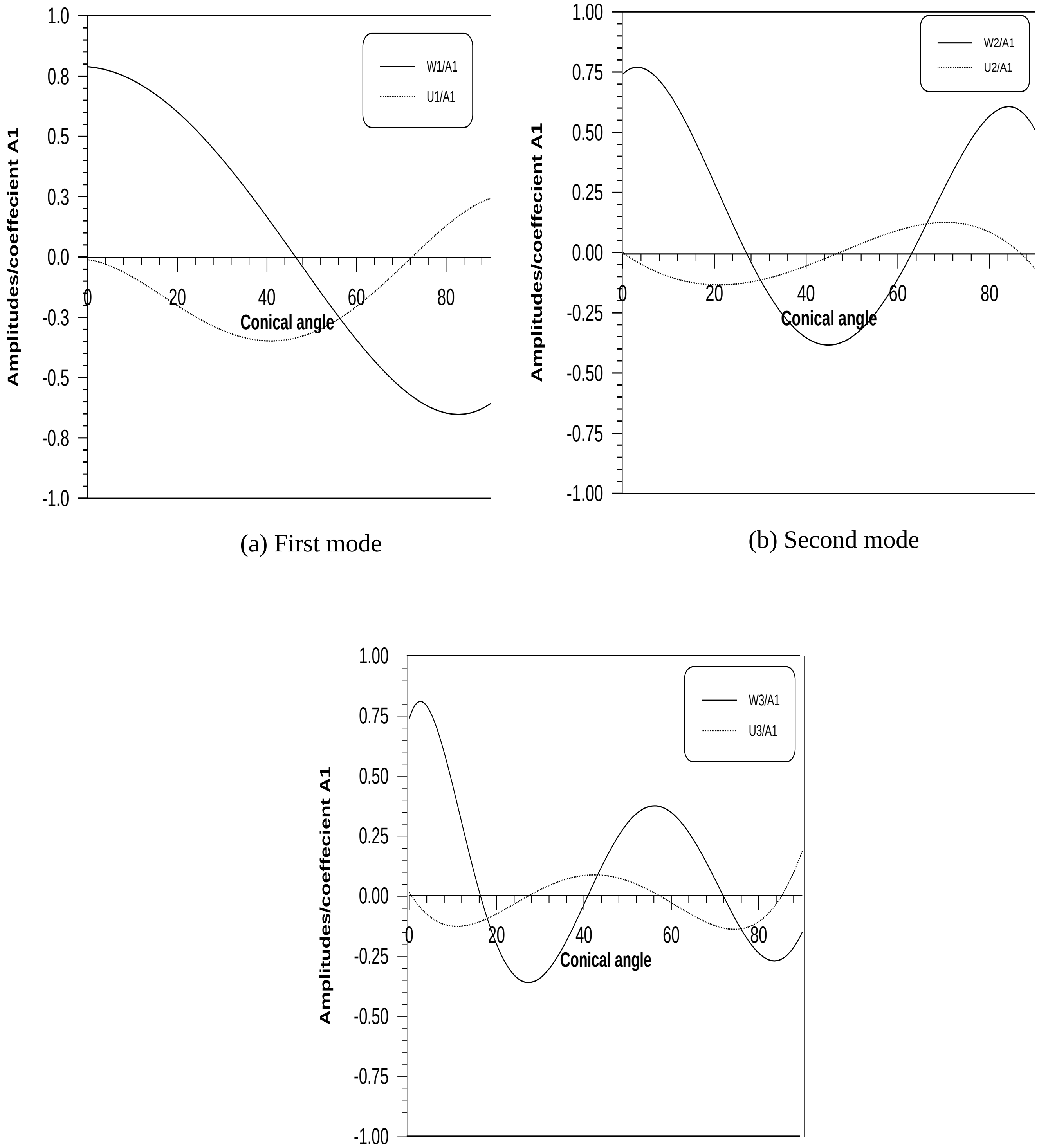

(a) First mode

(b) Second mode

(c) Third mode

Fig. :(6) Mode shape associated with the first three natural frequency of non-shallow spheroidal shell (e=0.7) obtained by RRM

REFERENCES

Aleksandr Korjanik et al, “Free Damped Vibrations of Sandwich Shells of Revolution”, J. of Sandwich Structures and Materials, Vol. (3), PP. 171-196, 2001.

Antoine, et al, “Vibrations of Shallow Spherical Shells and Gonges”, J. of Sound & Vibration, 2002

Burroughs, C.B. and Magrab, E. B., “Natural Frequencies of Prolate Spheroidal Shells of Constant Thickness”, J. of Sounds and Vibration, Vol. 57, PP. 571-581, 1978.

Dimaggio, F. L., and Silibiger, A.,”Free Extensional Torsional Vibrations of a Prolate Spheroidal Shell”,,J.Accoust. Soc.,Amer.,Vol. 33, PP. 56, 1961.

Dimaggio, F.L., and Rand R., "Axisymetrical Vibrations of Prolate Spheroidal Shells", J. Acoust. Soc. Amer. Vol. 40, PP.179-189, 1966.

Kalnins A. “Free Nonsymmetric Vibrations of Shallow Spherical Shells”, J. of App. Mech., PP. 225-233, 1963.

Kalnins, A. and Wilkinson, F.P., ”Natural Frequencies of Closed spherical shells”, ,J. App. Mech. Vol. 9,PP.,65, 1965.

Kraus, H.,”Thin Elastic Shells”, John Wiley and Sons, New York 1967

Numergut, P. J., and Brand R.S., “Axisymmetric Vibrations of a Prolate Spheroidal Shell”, J. Acoust. Soc. Amer., Vol. 38, PP.262-265, 1965.

Shiraishi, N. and Dimaggio, F.L.,”Perturbation Solutions of a Prolate Spheroidal Shells” J. Acoust. Soc. Amer. Vol. 34, PP. 1725-1731, 1962.

Wilfred, E. Baker “Axisymmetric Modes of Vibration of Thin spherical Shell”, J. Acoust. Soc. Amer.,Vol.33PP. 1749-1785, 1961.

Wasmi, H. R. Ph.D. Thesis,”Static and Dynamic Numerical and Experimental Investigation of Oblate and Prolate Spheroidal Shells with & without Framed Structure” Baghdad University, 1997.

Zhu, F., "Rayleigh – Ritz Method in Coupled Fluid – Structure Interaction Systems and Its Applications", J. Sound and Vibration Vol. 186(4), PP. 543-550, 1995.

NOMENCLATURE

A_i Arbitrary constants.

a Major semi-axis of a prolate spheroid shell.

B_i Arbitrary constants.

b Minor semi-axis of a prolate spheroid shell.

$c_{i,j}$ Element of the boundary conditions matrix.

D_b Bending stiffness ($E.h^3/12(1-v^2)$).

E Young's modulus of elasticity (N/ m^2).

e Ecentricity ratio($\sqrt{1-b^2}/a^2$).

h Shell thickness(mm).

M_ϕ, M_θ Moments per unit length (Nm/m).

N_ϕ, N_θ Membrane forces per unit length (N/m).

$P_n(x)$ Legendre function of the first kind.

$P_n'(x)$ First derivative of the Legendre function of the first kind.

$P_n''(x)$ Second derivative of the Legendre function of the first kind.

$Q_n(x)$ Legendre function of the second kind.

$Q_n'(x)$ First derivative of the Legendre function of the second kind.

Q_ϕ Transverse shearing force per unit length (N/m).

R_ϕ, R_θ Principal radii of curvatures of a prolate shell.

t Time (sec).

u_θ, u_θ Tangential displacement (m).

w Transverse or radial displacement (m).

$\in_\theta, \in_\theta$ Strains.

Φ' Inclination angle of a prolate spheroid.

Φ Inclination angle of a spherical shell model.

Φ_0 Opening angle of the approximate spherical shell.

λ Non-dimensional frequency parameter $((\rho/E)^{1/2}\omega.a)$.

θ Angle of rotation in the meridian direction

ρ Density (kg/m ^{3}).

Ω Non-dimensional frequency parameter $((\rho/E)^{1/2}\omega.R)$.

ω Circular frequency (rad/sec).

ω_0 $(E/\rho)^{1/2}h/d$.

$\sigma_\Phi, \sigma_\theta$ Stress resultants (N/m ^{2}).

ν Poisson's ratio.

NATURAL CONVECTION FROM SINGLE FINNED TUBE IMMERRSED IN A TILTED ENCLOSURE

Ass.Prof.Dr.Ikhlase M. Fayed, Hadi R. Roomi
University of Technology / Mech. Eng. Dept.

ABSTRACT

Heat transfer rates of a single horizontal finned tube immersed in water –filled enclosure tilted at 30 degrees are measured .The results serve as a baseline case for a solar water heating system with a heat exchanger immersed in integral collector storage. Tests were made with both adiabatic and uniform heat flux boundary conditions. Natural convection flow in enclosure is interpreted from measured water temperature distributions. Formation of an appropriate temperature difference that drives natural convection is determined .Correlations for the overall heat transfer coefficient in terms of the Nusselt and Rayleigh numbers are reduced to the form $Nu = 0.716Ra^{0.247}$ For $2 \times 10^5 \le Ra \le 2 \times 10^7$ Based on the diameter of the immersed tube .Comparison the present work results with others gave a good agreement.

KEY WORDS: Solar energy, Natural convection, Heat exchanger

الخلاصة:

قيس معدل انتقال الحرارة من أنبوب منفرد مغمور في ماء داخل مغلف . المغلف مائل عن الأفق بزاوية ^{o} ٣٠ . ممكن تمثيل النتائج لمنظومة تسخين بالطاقة الشمسية لمبادل حراري مغمور في مجمع الطاقة الشمسية أجريت الاختبارات لحالة العزل الحراري من جميع الجهات بوجود شروط حدية بثبوت درجة حرارة المائع مرة والحالة الثانية العزل الحراري من جميع الجهات ما عدا السطح العلوي إذ يتعرض لثبوت الفيض الحراري ممكن تمثيل جريان انتقال الحرارة بالحمل الحر داخل المغلف من خلال قياس درجات الحرارة داخله . العلاقة التجريبية لانتقال الحرارة بالحمل الحر ممكن تمثيلها بدلالة عدد نسلت ورقم رايلي من خلال العلاقة التجريبية التالية:

$Nu=0.716Ra^{0.247}$ for $2\times10^5 \le Ra \le 2\times10^7$

قيست العلاقة على أساس قطر الأنبوب المغمور. قورنت نتائج البحث الحالي مع بحوث سابقة وحصل على توافق جيد.

INTRODUCTION

One obstacle to the wide spread use of solar water heating systems is either high initial cost .A potential method of reducing cost is to use components made of plastic rather than metal .One system concept **Fig.1** embodies an expensive bag for collection and storage .An immersed heat exchanger made of many tubes transfers the stored energy to the potable water circulated through the tubes. The heat transfer process in the collector and immersed heat exchanger **Fig.2** involves the interaction of negatively buoyant plumes within the tube bundle and a large –scale buoyant flow within the collector. Natural convection heat transfer characteristics from horizontal tube in an unbounded fluid have been studied extensively .(Morgan 1975) assembled the widely disparate data and proposed Nusselt versus Ralyeigh number correlations .Over the range of measured Rayleigh numbers of interest here, the recommended correlations are

$Nu = 0.480 Ra_D^{\ 0.25}$, For $2\times10^5 \le Ra_D \le 2\times10^7$ And (1a)

$Nu = 0.125 Ra_D^{\ 0.333}$, For $2\times10^5 \le Ra_D \le 2\times10^7$ (1b)

with a given uncertainty of $\pm 5\%$. (Churchill and Chu 1975) developed a correlation for a wide range of Raleigh numbers,

$$Nu = \left[0.60 + 0.387 \left\{ \frac{Ra}{\left[1 + (0.559/Pr)^{9/16} \right]^{16/9}} \right\} \right]^2 ,10^{-5} \le Ra_D \le 10^{12} \quad (2)$$

Experiment uncertainty was provided. (Lienhard 1973) obtained a correlation for laminar convection from a balance of the buoyant and the viscous forces of an arbitrarily shaped immersed isothermal body,

$Nu = 0.52 Ra_{\ell}^{\ 0.25}$ (3)

Where the length scale is equal to the distance that a fluid particle travels in the boundary layer on the body .For the horizontal cylinder, $\ell = \pi \ D/2$

Heat transfer in two –dimensional tilted rectangular enclosures with differentially heated surfaces has been studied for $10^3 \le Ra \le 10^6$ (Ozoe et al 1975, Sundstrom et al 1996, Canaan et al 1996 Keyhani et al 1995, Keyhani et al 1996).Similar to the large scale circulating pattern sketched in **Fig.2**, the dominant flow is a stable circulating flow that rises along the heating wall, turns and then sinks along the cold wall. A vertical temperature gradient can develop in the core region of the tilted enclosure .For $Ra \ge 10^5$ instabilities in the flow have been found (Hart and J.E. 1971).

Most studies of heat transfer from enclosed bodies, including horizontal tube boundless, consider cases where the bounding walls drive the convective heat transfer for example, (Sparrow et al 1983, Warrington et al 1981, Farrington et al 1986, Farrington et al 1986).

Experimental studies of smooth tubes, finned tubes, and coiled tubes immersed in vertical storage tanks have yielded heat transfer correlations in the form $Nu = C\,Ra^{\ n}$ (Farrington et al 1986, Khalillolahi et al 1986).More analogous to the combined ICS/ heat exchanger are studies of transient natural convection in vertical enclosures with an immersed heat source or sink (Khalillolahi et al 1986).

As a first step toward developing appropriate heat transfer correlations, the heat transfer coefficient from a single horizontal finned tube in as tilted water-filled enclosure has been measured in the present work. The temperature field within the enclosure is described using local temperature measurement .These results provide a base case for a solar water heating system with a heat exchanger immersed in integral collector storage

APPARATUS

The collector is a rectangular stainless steel enclosure with inside dimensions of 121.9 cm (width) $\times$94.0 cm (length) $\times$ 10.2 cm (depth) tilted at $(30^\circ\ c)$ with respect to horizontal **Fig.3**.

The top side of the enclosure is a removable door to which the heat exchanger and instrumentation are mounted (3mm diameter) for insertion of the thermocouples are located in the door and along the bottom face. Additional ports are used to fill and drain the enclosure.

A uniform heat flux boundary condition that simulates solar irradiation during charging is provided by heater attached to the top face of the enclosure.
As indicated in **Fig.3**, temperatures in the enclosure were measured along the length (z-axis), width (x-axis) and depth (y-axis) by using copper-constantan thermocouple.

The immersed heat exchanger, shown in **Fig.4**, is 100.6 cm long and inner and outer diameters are respectively (19 mm) and (23mm) also the inner and outer diameter for the fins are respectively (23 mm) and (25 mm), elbows and two 11 cm long vertical brass tubes .The total length of the heat exchanger is 128.4 cm.

Water temperatures surrounding the tube were measured with four thermocouple probes placed at 90° increments, 1.1 cm from the outside wall of the tube **Fig.5**.

A constant temperature flow to the heat exchanger was maintained by the cold water supply, which includes four electric water heaters to precondition the inlet water and a large water storage tank. The flow rate was controlled with a gate valve at the outlet of the heat exchanger.

Temperatures, mass flow rate, and power input to the resistance heaters are recorded every 10 minute.

EXPERIMENTAL APPARATUS AND PROCEDURE

Thirteen transient experiments, described in table 1,were conducted over a range of tube flow rates and levels of simulated insulation .Charge ,discharge and combined charge /discharge modes with isothermal and stratified initial conditions were investigated .The experiments were begun with the insulated enclosure filled with hot quiescent water($\approx 65^{\circ}\,c$).During the discharge experiments (Nos.1 to 5) water at constant inlet temperature of $(25^{\circ}\,c)$ flowed through the tube .Flow rates of 0.015,0.030 and 0.050 kg/s were studied .The experiments were continued until water in the enclosure cooled to about $(30^{\circ}\,c)$.The combined charge/discharge experiments (Nos.6 to 12) were conducted in the same manner except a uniform heat flux was applied to the top face of the enclosure .These experiments were terminated after 10 hours. The charging experiment (No.13) was conducted without flow through the tube .It was terminated when fluid at the top of the enclosure reached $(90^{\circ}\,c)$.

DATA ANALYSIS

The data analysis was carried out assuming that the natural convection process is quasi-steady. At each time step, the overall heat transfer rate of the heat exchanger tube was determined from measured values of mass flow rate and temperature rise.

$$Q^{\bullet} = m^{\bullet} c_p (T_{out} - T_{in}) \quad (4)$$

Water properties were evaluated at the average of the inlet and outlet bulk temperatures.
The overall natural convection film coefficient was determined from

$$h = \frac{Q^{\bullet}}{A\ \Delta T_{nc}} \quad (5)$$

Where

$$\Delta T_{nc} = T_{\infty} - T_w \quad (6)$$

The value of T_w used in eq. (6) is the average of the wall temperatures at top and bottom of the tube at the mid –point of its length in the flow direction (thermocouple Nos.26 and 27 in **Fig.5**) T_{∞} was calculated from thermocouples are (T_{22}, T_{23}, T_{24} and T_{25}), the Nusselt and Rayliegh numbers at each time step are determined as

$$Nu = \frac{hD}{k}, \quad (7)$$

$$Ra = \frac{g\beta D^3 \Delta T_{nc}}{\nu\alpha} \qquad (8)$$

Fluid properties are calculated at the film temperature equal to the average of T_w and T_∞.The Nusselt numbers and the Rayleigh numbers are correlated in the form of $Nu = C\,Ra^{\,n}$ using statistical software package .Although there are a number of possible choices for the characteristic length, the data for the single finned tube are found to be well correlated using outer tube average diameter.

RESULTS AND DISCUSION

Measurement of temperature distribution in the enclosure is presented first. The formation of an appropriate temperature difference that drives free convection is discussed Correlations for the overall heat transfer coefficient in terms of the Nusselt and Rayleigh numbers are then developed .They compared to existing correlations for a single tube in an enclosure to determine the effect of the enclosure for the fin of the tube.

TEMPERATURE DISTRIBUTIONS WITHIN THE ENCLOSURE

Discharge of an initially isothermal enclosure –Results from experiment No.1 to No.3 establish the time –dependence of temperature for an initially isothermal enclosure .Data for experiment No.1 are presented in **Fig.6** to **Fig.8**. **Fig.6** includes data obtained from all thermocouples in the enclosure as a function of time ;for the duration of the experiment , temperatures are spatially uniform except near the tube and the lower wall of the enclosure The maximum difference in water temperature within the enclosure is less than $3^\circ\ c$ .Most measurement are within $1^\circ\ c$.

A closer look at the temperatures near the tube for one 30 minute period beginning at t=2 hours is shown in **Fig.7** .The data indicate the existence of slightly hot zone above the tube and a cold plume sinking from the tube .After two hours, the water 1.1 cm on either side of the tube (thermocouples Nos.23 and 25)is $1.5^\circ\ c$ cooler than that of the region above the tube (thermocouples Nos.21 and 22) and $2.4^\circ\ c$ warmer than the water just below the tube (thermocouples Nos.24) .Addititionally ,the temperatures at the sides of the tube are on average $2^\circ\ c$ above those measured in the middle and bottom portions of the enclosure .The fluid temperatures at the top ,sides and bottom of the tube retain their relative values over the entire 11.5 hours of experiment No.2.

Readings of the seven thermocouples (Nos.11to7) along the horizontal line in the mid y-z plane (x=0)are plotted in **Fig.8** for the same 30minute period as that of fig .6.The water along the bottom surface of the enclosure is slightly colder than the bulk of the fluid in the enclosure .The maximum temperature difference between the reading of the thermocouple located closest to the bottom (No.17) and the average of the other six thermocouples (Nos.11 to 16)is less than $2^\circ\ c$,and the average difference was $1^\circ\ c$ .Based on this difference ,we infer that cold water sinking from the tube flows along the bottom of the enclosure .

Charge with no heat transfer –Heating during charging results in high degree of thermal stratification in the absence of heat transfer to the tube .The effect of applied heat flux is demonstrated in experiment No.13,in which the initially isothermal enclosure become thermally stratified when 920W/m^2 was applied to the top face of the enclosure .Water temperatures along the mid y-z plane (x =0)are plotted in **Fig.9** for the seven -hour experiment .After seven hours, a temperatures difference of $47^\circ\ c$ existed between positions
z = 4.4 cm (thermocouples No.21) and z =87.6 cm (thermocouple No.7).

Discharge of initially stratified enclosure- In experiments Nos.4 and 5,effect of the initial thermal stratification on the temperature distributions in the enclosure was investigated .The level of stratification is characterized by a factor suggested by (Wu et al 1987) equal to the mass weighted mean square temperature divided by the total mass of fluid in the volume considered:

$$ST = \frac{\sum_i m_i (T_i - T_{avg})^2}{\sum_i m_i} \qquad (9)$$

Fig.10 shows the temperature measured during experiment No.4 with the nine thermocouples located in the mid y-z plane in the enclosure (x =0).At the beginning of this experiment, the top one-third of the enclosure was filled with $65^{\circ}\ c$ water and the bottom one-third was filled with $29^{\circ}\ c$ water. During the filling process ,the enclosure developed a stratified zone in the vicinity of the tube .The initial ST is 31.1 K^2,based on the topmost one-sixth of the enclosed water volume(0 cm $\leq z \leq$15.2 cm).As the experiment proceeded ,temperature measurement indicate that a relatively cool flow sinks from the tube and flows down the rear surface of the enclosure .After one hour of operation, this wall plume cools the upper region and middle region the enclosure between z = 0 m and z ~ 0.7 m .It plunges to the relatively cold lower region between ~ 0.7 m and ~ 0.9 m and heats the water in the region .Early in the discharge process, the circulating flow is constrained to lie above the colder fluid near the bottom of enclosure .As the discharge process continues, the region that is colder than the plume becomes an increasingly smaller fraction of the enclosure volume.

In experiment No.5,the top half of the enclosure was filled with $65^{\circ}\ c$ water and the bottom one-fourth was filled with $49^{\circ}\ c$ water .After the filling process, the fluid in the region near the tube was nearly isothermal ;the initial St equals 2.7 K^2.Water temperatures are plotted in **Fig.11** as a function of time .Similar to experiment No.4,for which the initial ST is much greater, the wall plume cools the upper region of the enclosure (0 m to~ 0.6 m from the top)and heats the middle region (~ 0.6 m to~ 0.7 m from the top). Compared with experiment No.4 ,the region cooled by the wall plume is larger and the not heated any region because of the relatively hot water in the middle and bottom portions of the enclosure .The momentum of the wall plume is most likely less due to the smaller temperature difference between the plume and the surrounding water. The circulating flow formed by the wall plume rapidly grows with time and moves toward the bottom of the enclosure .After an hour of operation ,the enclosure is isothermal from z ~0.15 to z ~0.8.Once the enclosure becomes isothermal ,it remains so except for a small warmer zone above the tube .

Combined charge/discharge of an initially isothermal enclosure –In the combined charge discharge experiments, the level of stratification in the enclosure is determined by the strength of the cold sinking plume relative to that of a warm buoyant wall flow on the front face .In the region near the tube ,the applied heat flux promotes stratification .The degree of stratification near the tube higher than that in the previously described discharge experiments with an initially isothermal enclosure .

For experiment No.9 for which the applied heat flux was 960 W/m^2,the center portion of the enclosure , (0.2 m $\leq z \leq$0.8 m)is nearly isothermal .On the other hand ,water near the tube is stratified at the beginning of the experiment and remains so for the duration of the experiment. **Fig.12** shows the water temperature near the tube for 30 minutes after two hours of operation. The temperature of water at the sides of the tube(thermocouples Nos.23 and 25) is $5.3^{\circ} c$ lower than that of the region above the tube (thermocouples No.22 to 21) and $4.7^{\circ}\ c$ higher than that of the sinking cold plume (thermocouples No.24) .It is $1^{\circ}\ c$ higher than the temperature measured by the (thermocouples No.20) .Thus, as opposed to the isothermal discharge experiments, in this case, the temperature measured by the (thermocouples No.20) does not correctly represent the oncoming temperature that characterizes natural convection .

Combined charge/discharge with an initially stratified enclosure-Temperatures measured in the combined charge /discharge experiment with initial thermal stratification (experiment No.12 with an initial ST=14.1K^2)are plotted in **Fig.13**.The temperature distributions along the length of the enclosure indicate that the cold plume sinking from the tube descends into the enclosure until it is neutrally buoyant. Because the plume cannot fully penetrate the lower cold region of the enclosure, the circulating flow gradually extends to the bottom of the enclosure as energy is removed .In the isothermal region ,the effect of the cold plume on the overall structure of the flow tends to dominate that of heat input on the front face ,as can be seen by the nearly constant temperatures over the middle portion of the enclosure for 0.5< t<10 hr .In the portion of the enclosure below the isothermal region ,the enclosure remains stratified ,and the temperature increases due to the addition of heat at the front face .At the top of enclosure ,near and above the tube ,effects of heat input dominate the flow and temperature fields.

HEAT TRANSFER CORRELATIONS

Using the statistical software we get the correlation between the Nusselat number and Rayleigh Number in form $Nu = 0.716Ra^{0.247}$, For $2 \times 10^5 \le Ra \le 2 \times 10^7$ (10)

As shown in **Fig.14** .Compare the present work with (Liu et al 2001) then we find the carve of present work is lower than curve of (Liu et al 2001) with the value [27%] respectively, as shown in **Fig.15**.

CONCLUSION

Measurements of water in the enclosure permit interpretation of the flow field. As energy is transferred to the tube under any level of initial stratification, a cold plume sinks from the tube and flows to the rear surface of the enclosure 0This plume promotes a circulating flow that promotes overall mixing in the mid – section of the enclosure. If there is either heat input on the front face or significant initial stratification near the immersed tube, stratification will persist during the discharge process.

Measurements of water temperatures near the tube and the tube wall temperature permit calculation of a Rayleigh number during the cooling process. For $2\times10^5 \le Ra \le 2\times10^7$, dimensionless heat transfer coefficients are correlated by $Nu = 0.716Ra^{0.247}$.Rayleigh number is based on the temperature difference between the water temperatures near the tube and the temperature of the tube wall.

Nomenclature

A	out heat transfer area of tube,m^2
Cp	specific heat of water, J/kg.°c
C	Empirical constant used in $Nu = CRa^n$
D	Tube average diameter ,m
h	Natural convection heat transfer coefficient, W/m^2.°c
i	Enclosure node at constant temperature, used in ST
k	Thermal conductivity of fluid,W/m.°c
ℓ	Length scale used in Ra
$\dot{m}$	Mass flow rate in tube ,kg/s
n	Empirical exponent in $Nu = CRa^n$
Nu	Nusselt number,hD/k
Pr	Prandtl number, ν/ α
$\dot{Q}$	Total energy transferred through the tube bundle ,W
Ra	Rayliegh number ,g β $D^3(T_w-T_\infty)$/ (ν α)
Re	Tube Reynolds number
R^2	Coefficient of determination
ST	Stratification factor ,eq.(9),K^2
t	Time ,s
T_{avg}	Average or stirred temperature of the enclosure , °c
Ti	Water temperature at node I , °c
Tin	Water temperature at the inlet of exchanger, °c

Tnc Refer to temperature difference that drives natural convection, °c
Tout Water temperature at the outlet of exchanger, °c
Tw Temperature of outer tube wall, °c
T_∞ Storage water temperature that drives natural convection, °c
x,y,z Cartesian coordinates

Greek symbols

α Thermal diffusivity,m^2/s
β Coefficient of volumetric thermal expansion,
Δ Refers to temperature difference , $°c^{-1}$
θ Inclination angle of the enclosure, degrees relative to horizontal
ν Kinematic viscosity,m^2/s

REFERENCES

Canaan, R.E., and Klein, D.E., "An experimental investigation of natural convection heat transfer within horizontal spent-fuel assemblies," Nuclear Technology, 116, No.3, pp. (306-318), 1996.

Churchill, S.W., and Chu, H.H.S., “Correlating equations for laminar and turbulent free convection from a horizontal Cylinder.” University of Penney vania, Journal of Mass and Heat Transfer. , vol., 18, pp (1049-1055).1975.

Farrington, R.B. and Bingham C.E., "Test and analysis of immersed heat exchangers," .Solar Energy Research Institute, SERI Report#TR-253-2866, 1986.

Farrington, R.B.," Test Results of immersed coil heat exchangers and liquid storage tanks used in the packaged systems program," Solar Energy Research Institute, SERI Report#TR-254-2841, 1986.

Hart, J.E., "Stability of the flow in the differentially Heat inclined Box", Journal of Fluid Mechanics, 47, No.3, pp. (547-576) 1971.

Keyhani, M.and Dalton, T., "Natural convection heat transfer in horizontal Rod-bundles Enclosures," Journal of Heat Transfer, 118, No.3, pp. (598-605) 1996.

Keyhani, M.and Luo, L., "Numerical study of Natural convection heat transfer in horizontal Rod-bundles, "Nuclear Science and Engineering, 119, No.2, pp. (116-127) 1995.

Khalillolahi,A.,and Sammakia,B., "Unsteady natural convection generated by a heated surface within an enclosure ," ,Numerical Heat Transfer,9,No.6, pp.(715-730), 1986.

Lienhand, J.H., "On the commonality of equations for natural convection from immersed Bodies "International Journal of Heat and Mass Transfer, 16, No.11, pp (2121-2123), 1973.

Liu, W.Davidson,J.Hand Kulacki ,F.A.,” Natural Convection From a Single Tube Immersed in a Tilted thin Enclosure ”Proceed dings of International Conference on Energy Conversion and Application(ICECA'2001),Huazhong University of Science and Technology Press,1.PP(408-413), Wuhan,China,2001.

Morgan, V. T. ,”The overall convective Heat Transfer from smooth Circular Cylinders ”Advances in Heat Transfer , Hartntt ,J.,and Trvine, T. Tr. ,Eds., vol.,11, Wiley. Interscience, Now York, pp (199-264).1975.

Ozoe ,H.,Sayama ,H.,and Churchill,S.W., " Natural convection in an inclined Rectangular channelat averious Aspect Ratios and Angles-Experimental Measurements," International Journal of Heat and Mass Transfer,18,No.12, pp.(1425-1431) ,1975.

Sparrow, E.M., and Charm chi, M., “Natural convection Experiments in an Enclosure between Eccentric or concentric vertical Cylinders of Different Height and Diameter “University of Minnesota state, Journal of Mass and heat transfer, vol.20, NO.1. pp (133-143). 1983.

Sundstrom, L.-G., and Kimura, S., "On laminar free convection in inclined rectangular enclosures,"", Journal of Fluid Mechanics, 313, pp. (343-366), 1996.

Warrington, R. O., and Crupper, G.,”Natural convection Heat Transfer between Cylindrical tube Bundles and a Cubical Enclosure “, University of Minnesota state, Journal of heat transfer, vol.103, February, pp (103-107), 1981.

Wu,L.,and Bannerot,R.B. "Experimental study of the effect of water extraction on thermal stratification in storage ,"Solar Engineering,1,pp(445-451) ,1987.

Table 1.Experimental operating conditions

Run No.	Operating Mode	Initial ICS Temperature $(^{\circ}c)$	Nominal m° (kg/s)	Re	T_{in} $^{\circ}c$	Heat Flux (W/m^2)	Ra	Nu	Δt (hr)
1	Discharge	62	0.015	1133~1306	25	0	2×10^{5}~9.75×10^{6}	15 ~ 33	11.5
2	Discharge	70	0.03	2267~2584	25	0	4.9×10^{5}~1.9×10^{7}	17.6~42.7	10.8
3	Discharge	75	0.05	3779~4214	25	0	4.1×10^{5}~2×10^{7}	17.6 ~ 46	10.0
4	Discharge	Stratified Top at 65 Bottom at 29	0.05	3774~3952	25	0	3.4×10^{5}~9.7×10^{6}	16.7 ~39.5	4..3
5	Discharge	Stratified Top at 65 Bottom at 48	0.05	3774~4076	25	0	4.5×10^{5}~8×10^{6}	17.6 ~ 40	9.0
6	Charge/Discharge	64	0.03	2420~2581	25	260	4.5×10^{5}~8×10^{6}	25 ~ 38.6	10.0
7	Charge/Discharge	67	0.03	2420~2581	25	480	1.9×10^{6}~1.15×10^{7}	27.7 ~ 41.9	10.0
8	Charge/Discharge	75	0.03	2445~2687	25	700	2.12×10^{7}~1.23×10^{7}	31 ~ 42	10.0
9	Charge/Discharge	62	0.03	2445~2609	25	960	3.38×10^{6}~1.2×10^{7}	33.5 ~ 41	10.0
10	Charge/Discharge	68	0.15	1276~1370	25	920	4.16×10^{6}~9.37×10^{7}	30 ~ 38	10.0
11	Charge/Discharge	61	0.05	3912~4119	25	920	4.8×10^{6}~1.3×10^{6}	32 ~ 37	10.0
12	Charge/Discharge	Stratified Top at 81 Bottom at 44	0.03	2420~2661	25	920	4.47×10^{6}~8.19×10^{7}	34.5 ~ 49	10.0
13	Charge	27	0	No flow	25	920	-	-	7.0

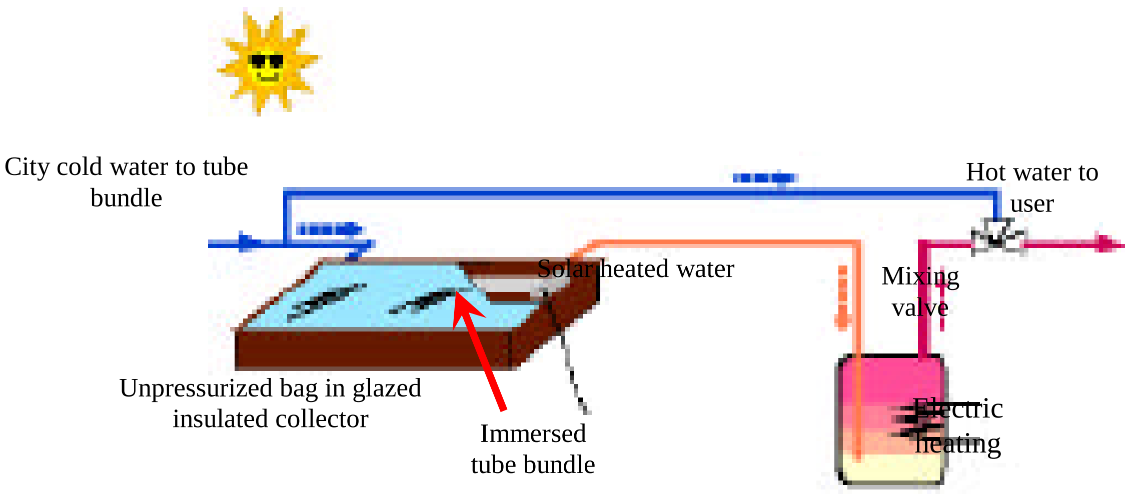

Fig (1). Conceptual system for a low cost collector and a load-side heat exchanger

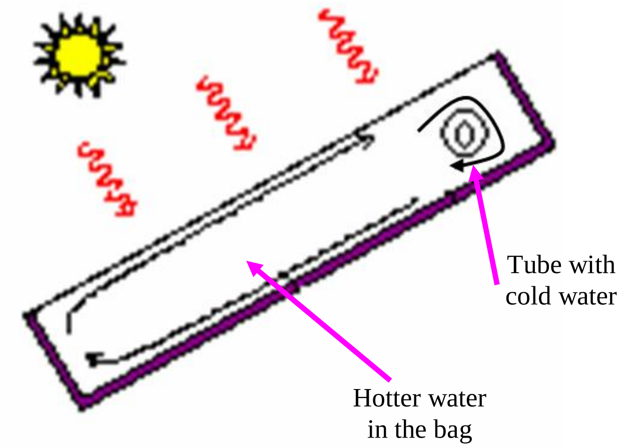

Fig (2). Buoyancy driven flow inside the inclined solar collector with an immersed heat exchanger

Fig (3). Enclosure and locations of thermocouples
Note: All dimensionsin (cm)

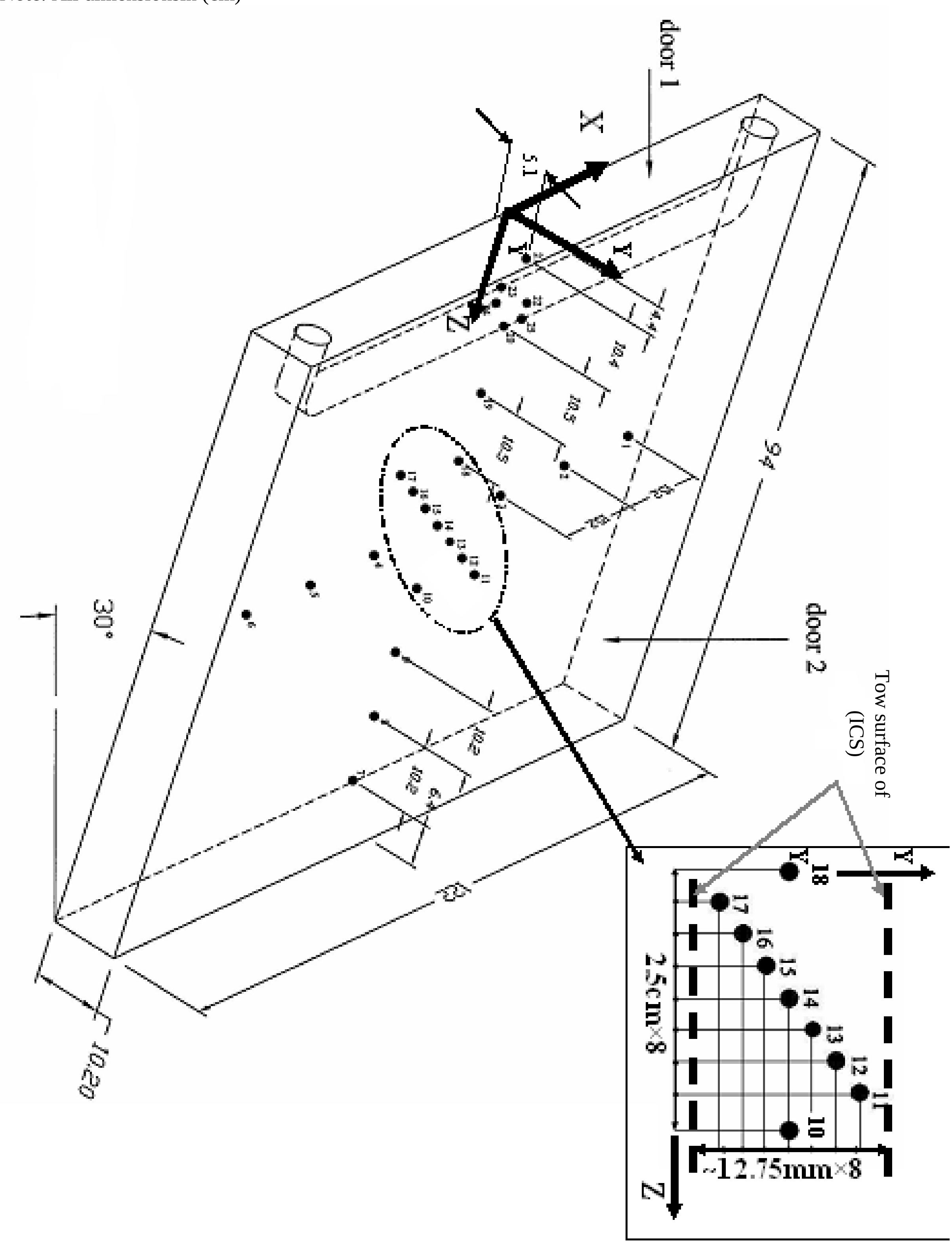

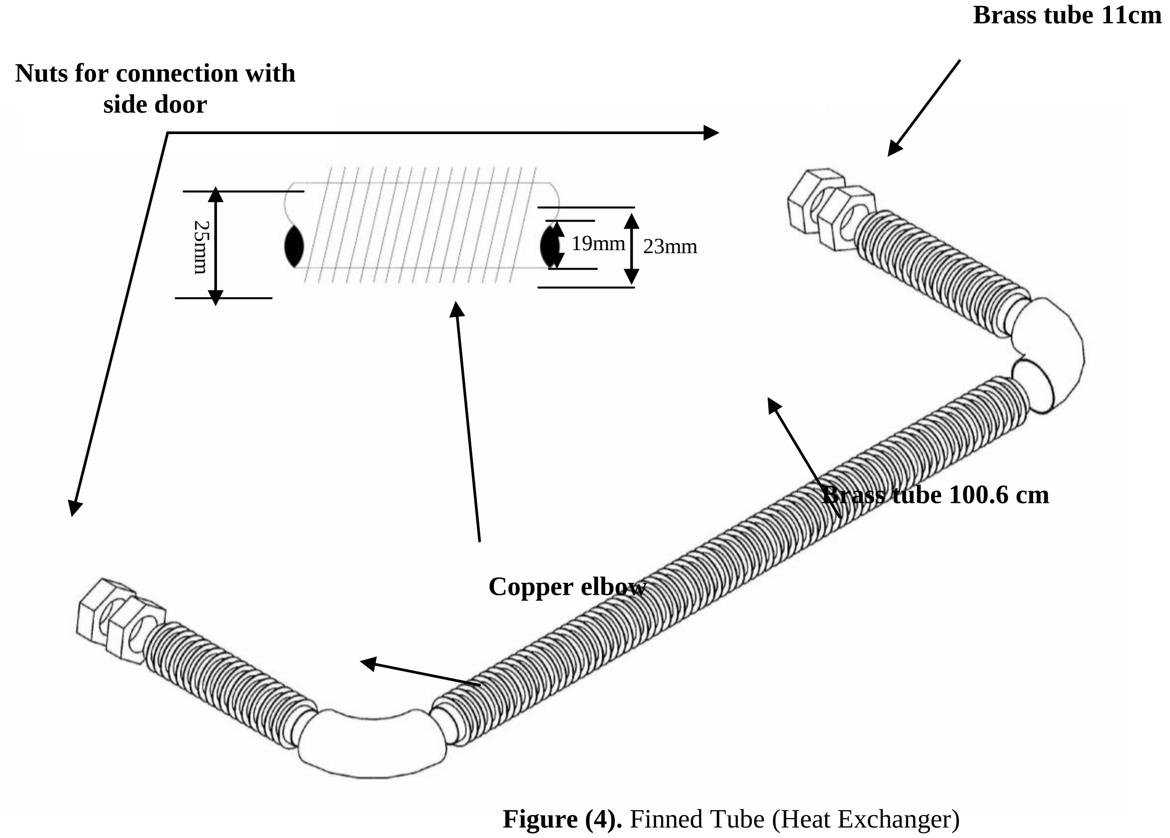

Figure (4). Finned Tube (Heat Exchanger)

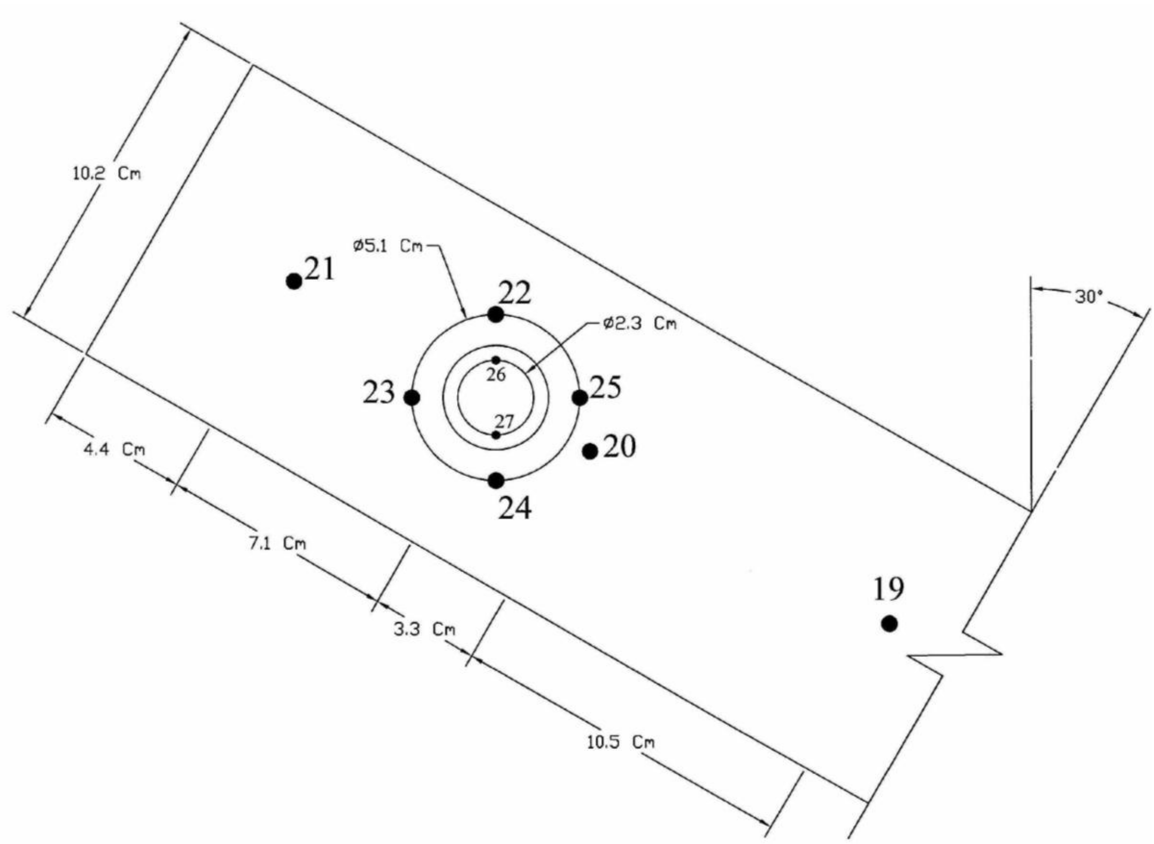

Fig (5). The thermocouples around the heat exchanger

Time (h:m)

Fig (6). Water temperatures inside the enclosure for experiment No.1

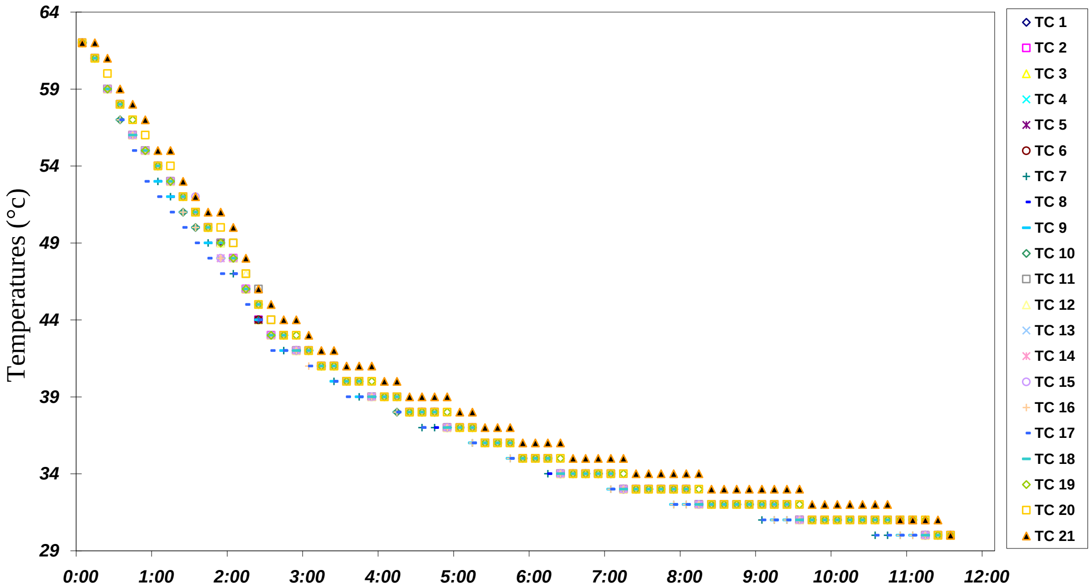

Time (h:m)

Fig (7). Water temperatures in the top portion of the enclosure over a 30 minute interval during experiment No. 1

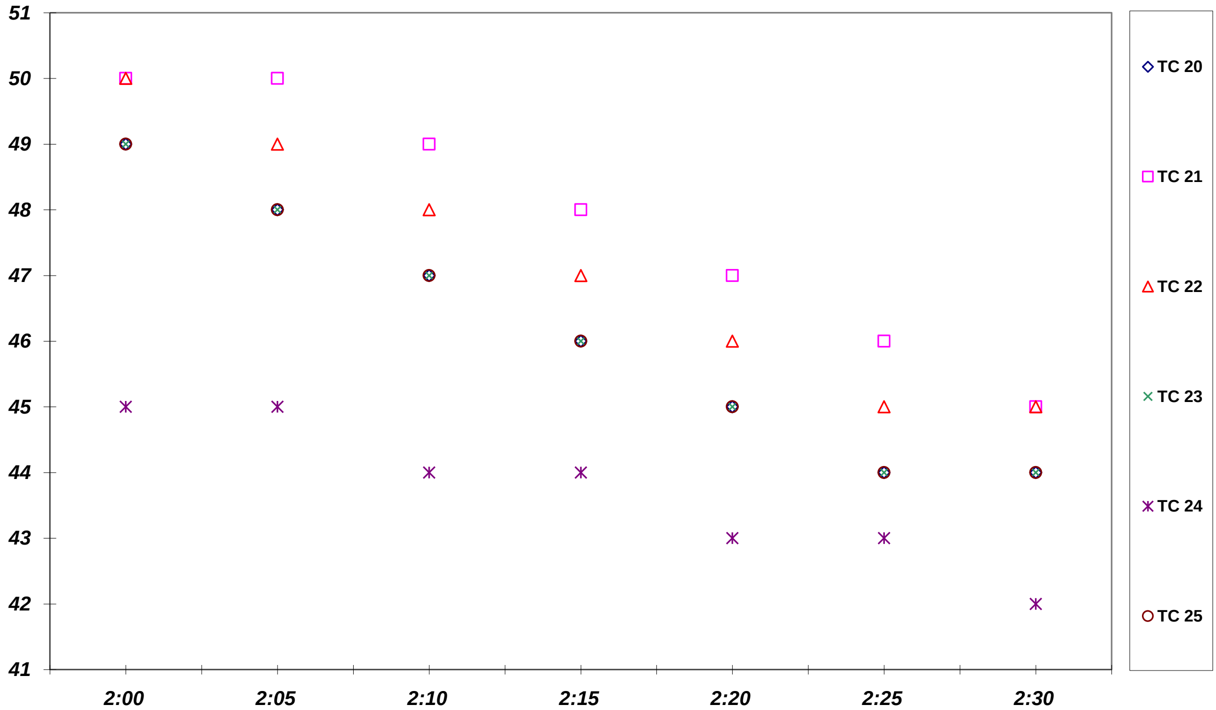

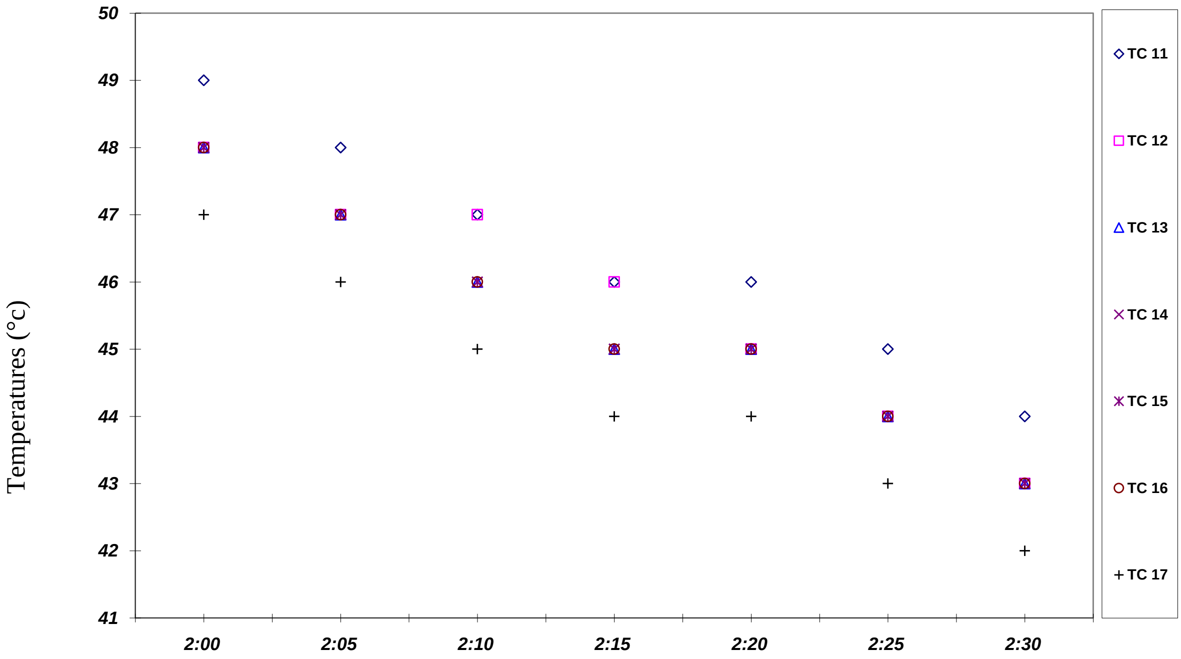

Fig (8). Water temperatures distribution along the horizontal line in the mid y-z plane over a 30 minute interval in experiment No.1

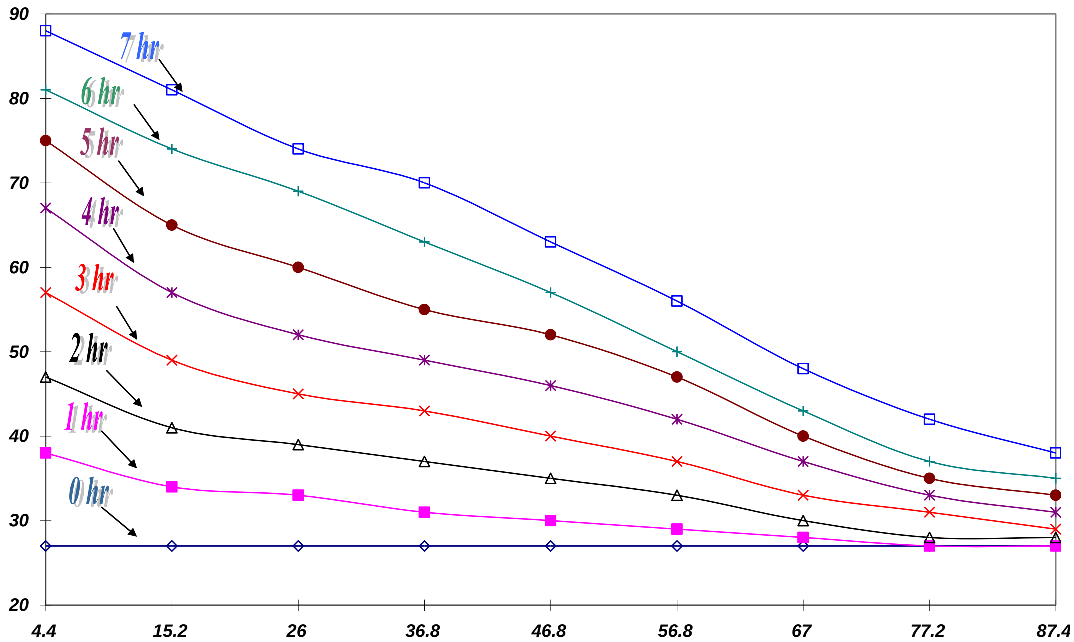

Distance from the top (z), m

Fig (9). Hourly water temperatures distribution in the enclosure during the charging experiment No.13

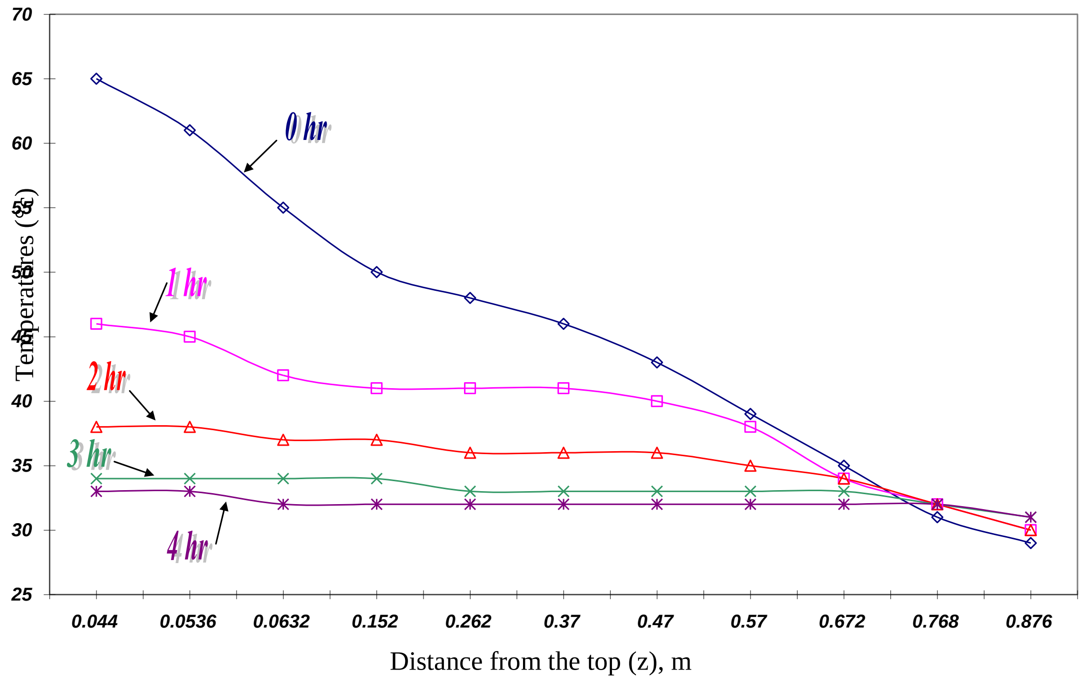

Fig (10). Hourly water temperatures distribution in discharging experiment No.4

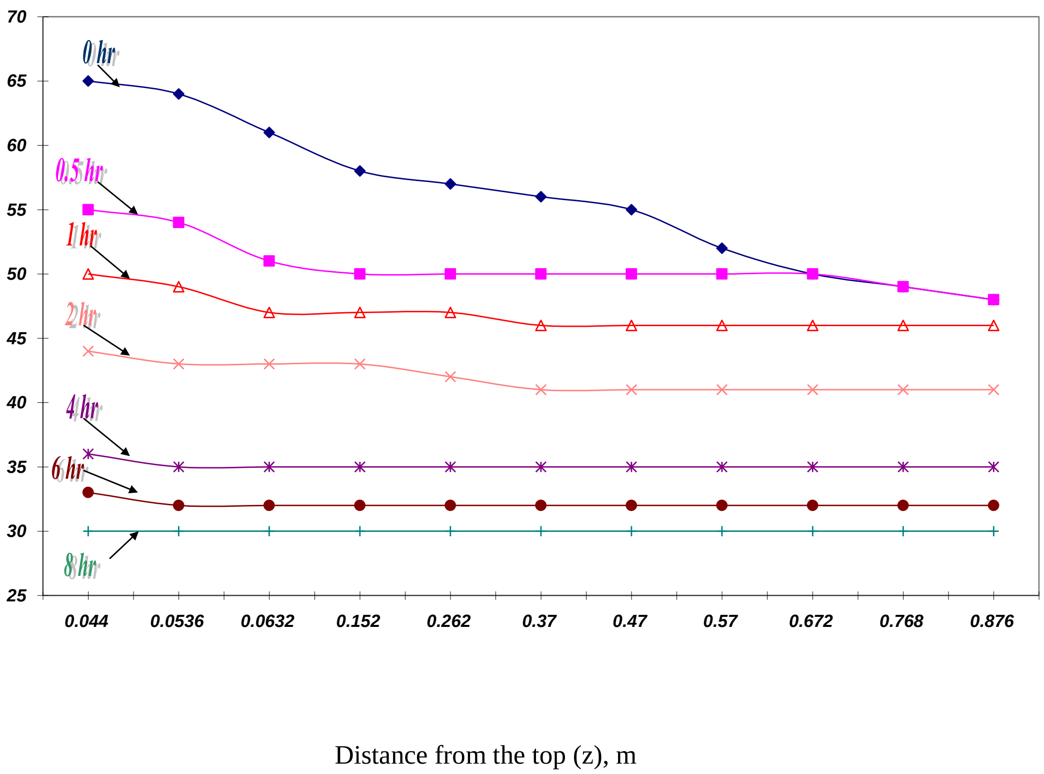

Fig (11). Hourly water temperatures distribution in discharging experiment No.5

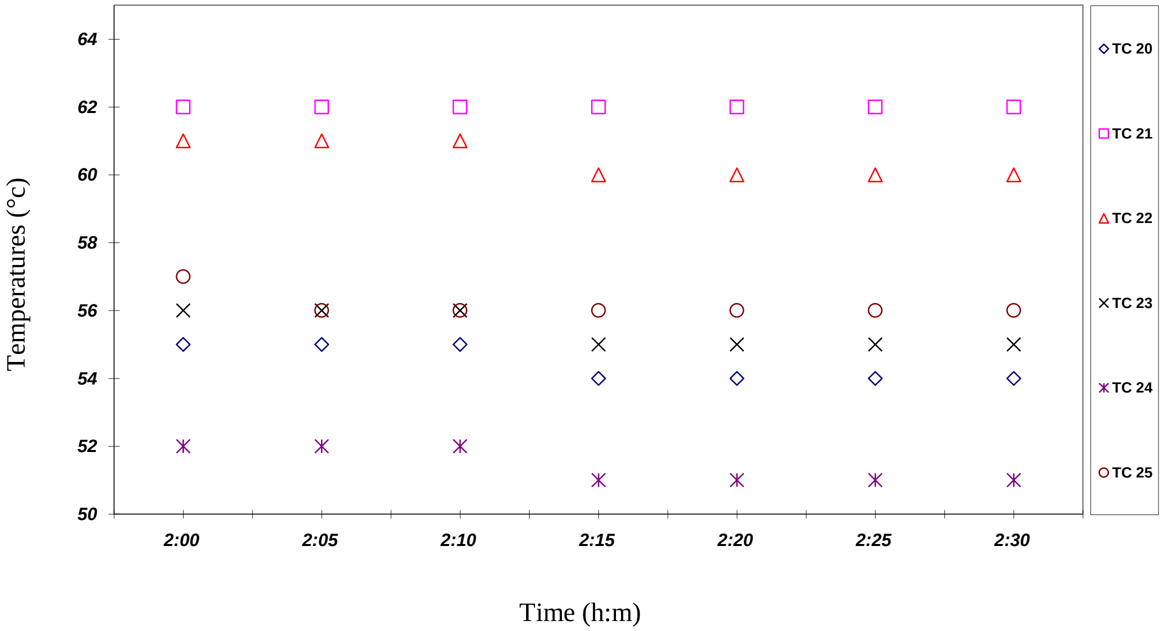

Fig (١٢). Water temperatures in the top portion of the enclosure over a 30 minute interval during experiment No. ٩

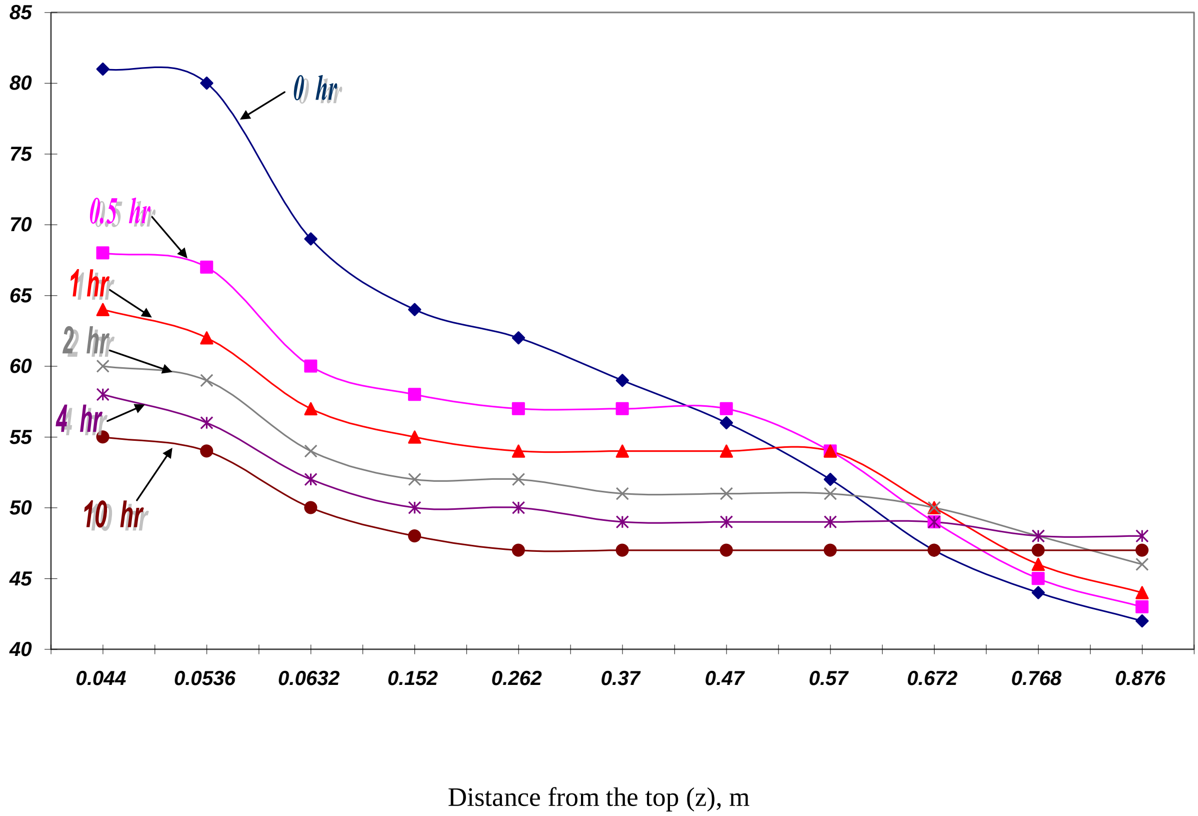

Fig (13). water temperatures distribution in the mid y-z plane in combined charge/discharging experiment No.12

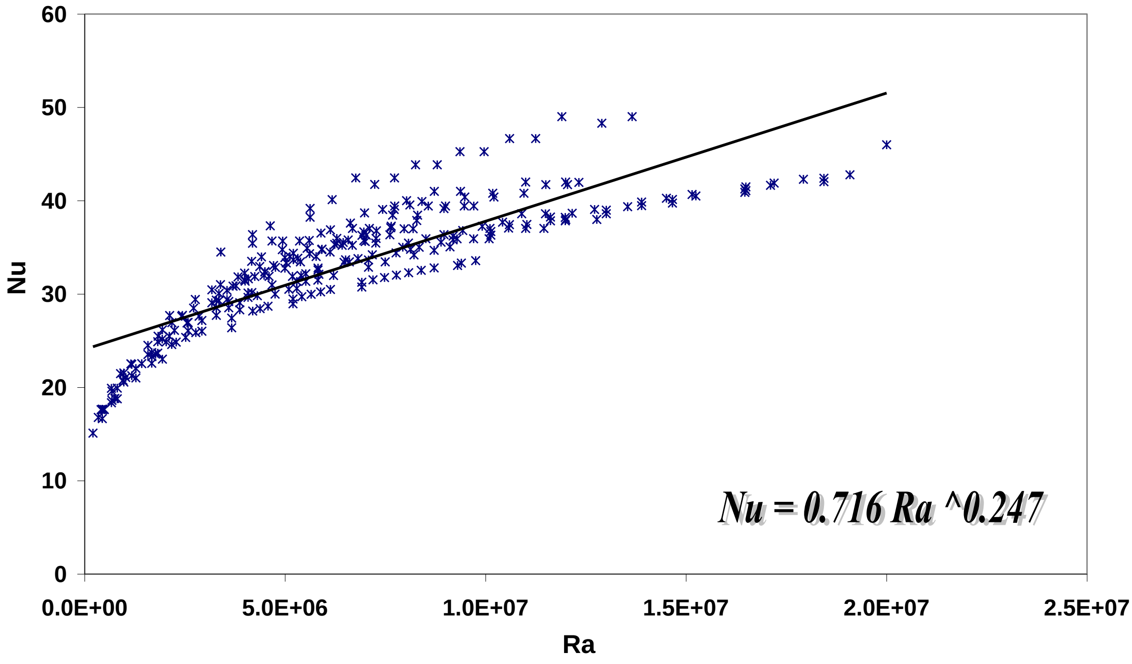

Fig(14). Nusselt number correlation and measured values for experiments 1-12.

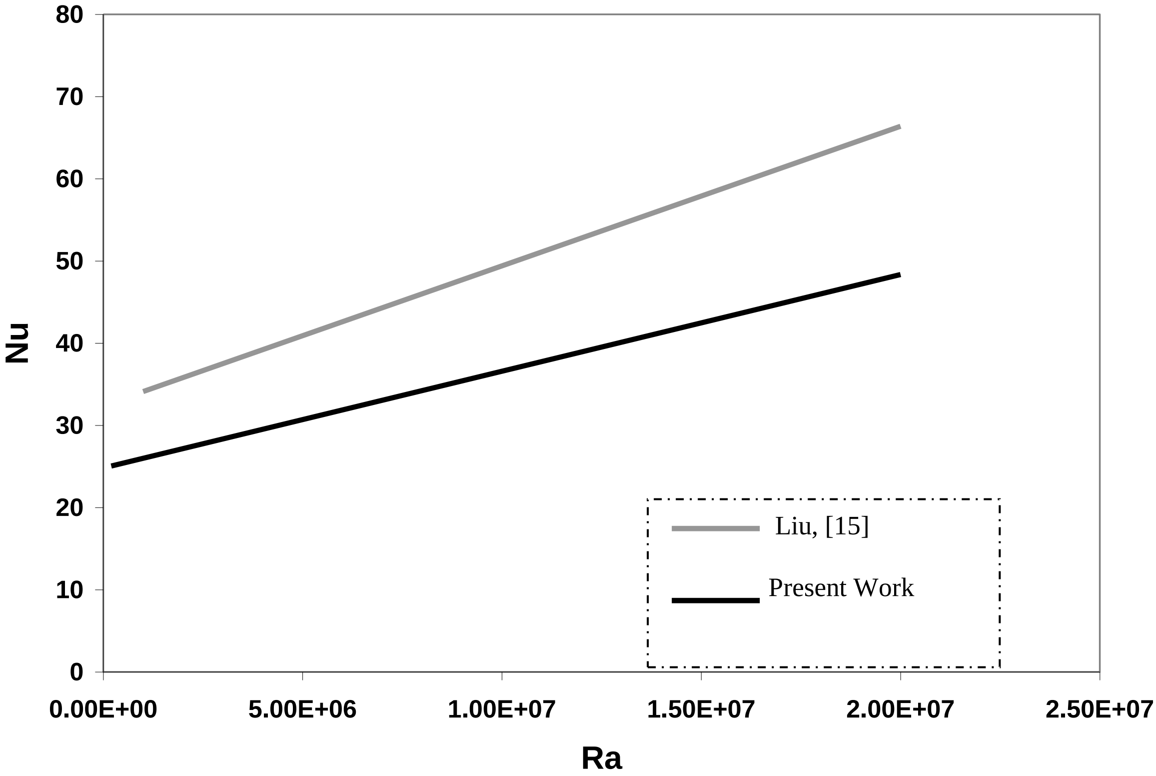

Fig (15). Comparing of the result

INFLUENCE OF DEFECT IN THE CONCRETE PILES USING NON-DESTRUCTIVE TESTING

Prof. Dr. Mosa Al-Mosawe
Department of Civil Engineering, College of Engineering, University of Baghdad.

Prof. Dr. Yousef Al-Shakarchi
Department of Civil Engineering, College of Engineering, University of Baghdad.

Dr. A'amal A-Saidi
Department of Civil Engineering, College of Engineering, University of Baghdad.

ABSTRACT

This paper presents the results of experimental investigation carried out on concrete model piles to study the behaviour of defective piles. This was achieved by employing non-destructive tests using ultrasonic waves. It was found that the reduction in pile stiffness factor is found to be about (26%) when the defect ratio increased from (5%) to (15%). The modulus of elasticity reduction factor as well as the dynamic modulus of elasticity reduction factor increase with the defect ratio.

الخلاصة

يستعرض هذا البحث النتائج للدراسة المختبرية التي أجريت على نماذج من ركائز خرسانية متضررة ودراسة تصرفها عند تعرضها للاحمال. تم أنجاز ذلك من خلال الفحص غير الاتلافي بواسطة الموجات فوق الصوتية. وقد بينت النتائج بأن مقدار النقصان في معامل جساءة الركيزة (٢٦%) عندما تزداد نسبة الضرر من (٥%) الى (١٥%). كما أن عامل النقصان لمعامل المرونة أضافة الى عامل النقصان بمعامل المرونة الديناميكي يزداد بزيادة نسبة الضرر.

INTRODUCTION

There is a number of factors, which should be considered in the design of bored piles beyond the routine computation procedures. A review of these factors reveals serious defects, such as, the loss of continuity along the pile length, and the shaft may contain cracks, voids, inclusion, etc. These defects may not affect the pile performance in the short term. However, the long-term behavior may be important, particularly when a pile is subjected to bending stresses (Al-Mosawe and Al-Obaydi, 2002).

Pile defects can be divided broadly into two categories (Poulos, 1997):

- Geotechnical defects, which arise from either a misassessment of the in-situ conditions during design or else from construction-related problems.
- Structural defects, which are generally related to construction and which result in the size, strength and/or stiffness of the pile being less than assumed in design, see Figure (1).

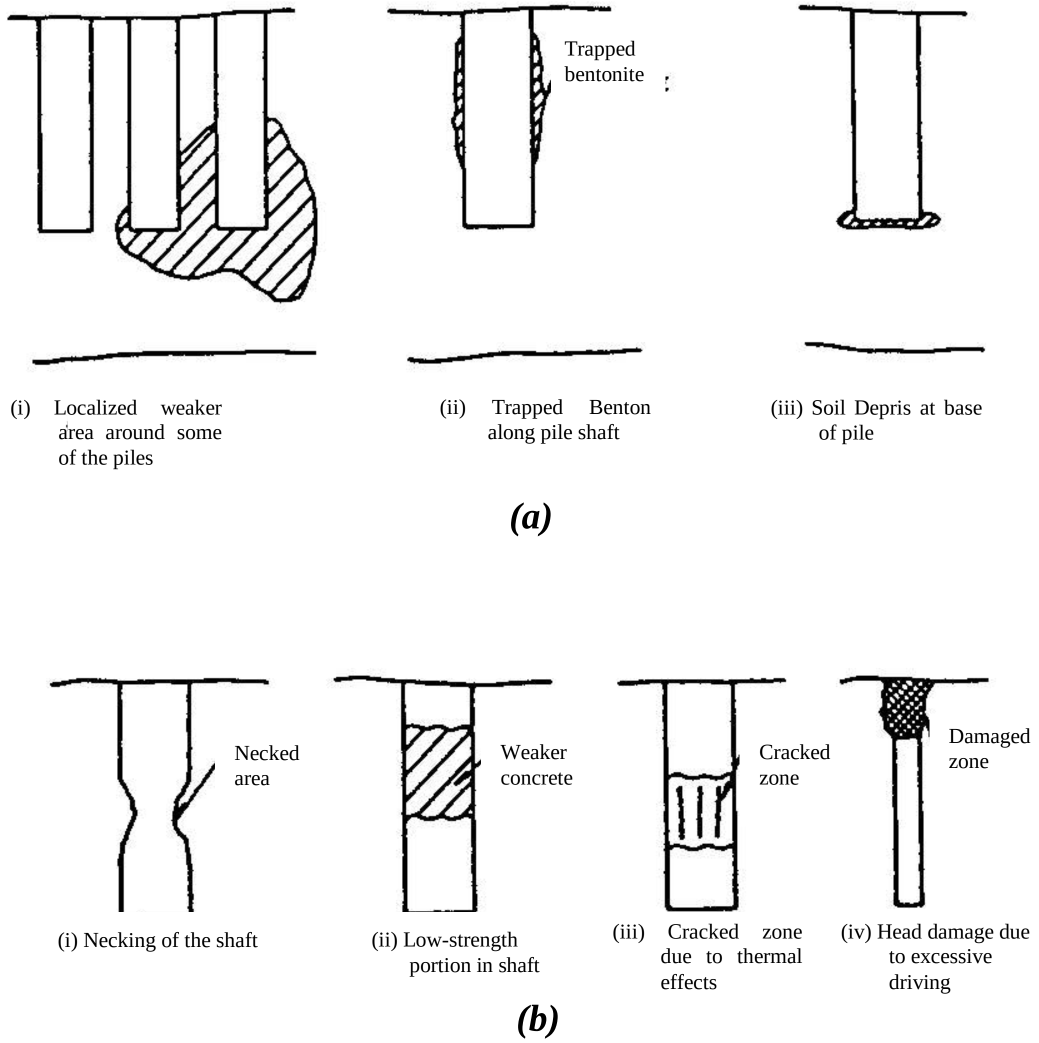

Fig (1) Examples of (a) Typical Geotechnical Defects; (b) Typical Structural Defects (after Poulos, 1997).

In many cases in the past, it was assumed that the defective pile would not carry any load and an additional pile or piles have been installed within the group to compensate for the defective pile. Such a procedure is both costly and time-consuming, and it is therefore of some interest to examine whether the defective pile can still function satisfactorily. Therefore, a quick non-destructive method of testing the pile is devised where defects in concrete along the length of the pile could be estimated to a fair degree of accuracy.

EFFECT OF DEFECTIVE PILE

The presence of defects leads to a reduction in pile axial stiffness; at higher load levels, this reduction can be severe and gives the appearance of a reduction in axial load capacity. If failure of the pile occurs because of structural defect, there is a sudden and dramatic increase in settlement. With geotechnical defects, the apparent loss of load capacity is characterized by a more gradual increase in settlement with increasing load. The ability of the group to redistribute the pile loads from defective pile to intact piles results in a less severe reduction in axial stiffness than the case of a single defective pile. However, the presence of defective piles will generally lead to the development of lateral deflection and rotation of the group, and induces additional bending moments in the piles, even under purely axial applied loading (Poulos, 1997).

CONCRETE MIX DESIGN

The ACI 211.1-91 method is used for concrete mixes to obtain the required compressive strength. The required compressive strength is 30 N/mm^2. Mixing proportions were (1:1.85:1.7), and water - cement ratio (w/c ratio by weight) is 0.5. The water used for mixes was the normal potable water supplied by the municipality, which was used also for curing concrete samples.

Samples Moulds

Two types of moulds were used for sampling:

- The first type was steel cube moulds (150 mm × 150 mm × 150 mm). These cubic samples were used to find the compressive strength of concrete.

- The second type was a plastic cylindrical mould of a diameter (55 mm), with variable lengths (100 mm, 200 mm, 300 mm, 400 mm, and 500 mm). These samples were used for ultrasonic pulse velocity tests, and model pile tests.

Ultrasonic Pulse Velocity Test

Ultrasonic pulse velocity test is one of the non-destructive methods to find some of the physical properties of the concrete; the compressive strength, and the dynamic modulus of elasticity of concrete. Non-destructive tests reflect the actual properties of concrete, while the destructive tests (cylinder or cube compression test) carried out on a standard prepared and cured samples, seem to be too far from the actual conditions.

Many researchers tried to suggest a general limit for the ultrasonic wave velocity. One of them was Jones and Gatifield (1963) who suggested limits for the ultrasonic wave velocity in concrete, as given in Table (1):

Table (1) Velocity a longitudinal ultrasonic pulse for different concrete types (Jones and Gatifield, 1963).

Concrete Type	*Pulse velocity (km/sec.)*
Very Good	More than 4.58
Good	3.66 – 4.57
Moderate	3.05 – 3.66
Poor	2.14 – 3.00
Very Poor	Less than 2.14

Concrete Samples Tested:

The dimensions of the cylindrical concrete piles used are listed in Table (2). The ultrasonic device (Pundit) was used to measure the ultrasonic wave speed through the concrete samples by using the direct method.

Table (2) Cylindrical Concrete Samples Tested.

Test No.	*Length of Pile (mm)*	*Type of Pile*	*Type of Defect*	*Defect Ratio*	*Location of Defect*
1	100	Sound	–	–	–
2	100	Defected	Neck	5%	1/3 length
3	100	Defected	Neck	10%	1/3 length
4	100	Defected	Neck	15%	1/3 length
5	200	Sound	–	–	–
6	200	Defected	Neck	5%	1/3 length
7	200	Defected	Neck	10%	1/3 length
8	200	Defected	Neck	15%	1/3 length
9	300	Sound	–	–	–
10	300	Defected	Neck	5%	1/3 length
11	300	Defected	Neck	10%	1/3 length
12	300	Defected	Neck	15%	1/3 length
13	300	Defected	Neck	5%	1/2 length
14	300	Defected	Neck	5%	2/3 length
15	300	Defected	External void	5%	1/3 length
16	300	Defected	External void	10%	1/3 length
17	300	Defected	External void	15%	1/3 length
18	300	Defected	External void	5%	1/2 length
19	300	Defected	External void	5%	2/3 length
20	300	Defected	Internal void	5%	1/3 length

21	300	Defected	Internal void	5%	1/2 length
22	300	Defected	Internal void	5%	1/3 length
23	300	Defected	Void (Internal Void)	1%	1/3 length
24	300	Defected	Void (Internal Void)	1%	1/2 length
25	300	Defected	Void (Internal Void)	1%	2/3 length
26	400	Sound	–	–	–
27	400	Defected	Neck	5%	1/3 length
28	400	Defected	Neck	10%	1/3 length
29	400	Defected	Neck	15%	1/3 length
30	500	Sound	–	–	–
31	500	Defected	Neck	5%	1/3 length
32	500	Defected	Neck	10%	1/3 length
33	500	Defected	Neck	15%	1/3 length

Note:
- Pile diameter (55 mm).
- Defect ratio, is the defect volume compared to the total volume of the pile.

The tests have been performed according to the British standard (BS 1881-Part 203-1086), and to the American standard (ASTMC597-83-1991).

The ultrasonic test was executed as described above, where the longitudinal wave velocity was measured by the direct method, and the type of concrete is determined from (Table (1)). The concrete strength was determined using the following formula (Raouf et al., 1986):

$$f_{cu} = 2.016e^{0.61V} \quad \text{....................(1)}$$

where:

f_{cu} = Concrete compressive strength (MPa).

V = Wave velocity measured by direct method (km/sec.).

The relation between dynamic modulus of elasticity and the compressive strength of concrete is descried in (CP110: 1972) by the following equation:

$$E_D = 22 + 2.8\sqrt{f_{cu}} \quad \text{....................(2)}$$

where:

E_D = Dynamic modulus of elasticity for concrete (GPa).

The expression for the static modulus of elasticity of concrete, E_c, as mentioned in (BS 8110) is:

$$E_c = 1.25\ E_D - 19 \quad\text{.....(3)}$$

where:

E_c = Static modulus of elasticity for concrete (GPa).

Results and Discussion

The results of ultrasonic pulse velocity test are shown in Table (3).

Table (3) The Results of Ultrasonic Pulse Velocity Test.

Test No.	Length of pile (mm)	Type of pile	Type of Defect	Defect Ratio	Location of Defect	Pulse Velocity (km/sec)	Concrete type (see Table (1)	f_{cu} (MPa)	$E_D \times 10^3$ (MPa)	$E_C \times 10^3$ (MPa)
1	100	Sound	–	–	–	4.17	Good	25.66	36.18	26.23
2	100	Defected	Neck	5%	1/3 length	3.52	Moderate	17.23	33.62	23.03
3	100	Defected	Neck	10%	1/3 length	2.44	Poor	8.90	30.35	18.94
4	100	Defected	Neck	15%	1/3 length	1.73	Very poor	5.78	28.73	16.91
5	200	Sound	–	–	–	4.17	Good	25.60	36.17	26.21
6	200	Defected	Neck	5%	1/3 length	3.57	Moderate	17.81	33.82	23.27
7	200	Defected	Neck	10%	1/3 length	2.59	Poor	9.77	30.75	19.44
8	200	Defected	Neck	15%	1/3 length	1.87	Very poor	6.30	29.03	17.28
9	300	Sound	–	–	–	4.11	Good	24.70	35.92	25.89
10	300	Defected	Neck	5%	1/3 length	3.57	Moderate	17.81	33.82	23.27
11	300	Defected	Neck	10%	1/3 length	2.56	Poor	9.65	30.70	19.37
12	300	Defected	Neck	15%	1/3 length	1.88	Very poor	6.35	29.06	17.32
13	300	Defected	Neck	5%	1/2 length	3.52	Moderate	17.23	33.62	23.03
14	300	Defected	Neck	5%	2/3 length	3.49	Moderate	16.93	33.52	22.90
15	300	Defected	External Void	5%	1/3 length	3.50	Moderate	17.05	33.56	22.95
16	300	Defected	External Void	10%	1/3 length	2.40	Poor	8.70	30.26	18.82
17	300	Defected	External Void	15%	1/3 length	1.75	Very poor	5.86	28.78	16.97

18	300	Defected	External Void	5%	1/2 length	3.61	Moderate	18.23	33.96	23.44
19	300	Defected	External Void	5%	2/3 length	3.53	Moderate	17.4	33.68	23.10

Table (3): Continue.

Test No.	*Length of pile (mm)*	*Type of pile*	*Type of Defect*	*Defect Ratio*	*Location of Defect*	*Pulse Velocity (km/sec)*	*Concrete type (see Table (1)*	*f_{cu} (MPa)*	*$E_D \times 10^3$ (MPa)*	*$E_C \times 10^3$ (MPa)*
20	300	Defected	Internal Void	5%	1/3 length	3.41	Moderate	16.14	33.25	22.56
21	300	Defected	Internal Void	5%	1/2 length	3.46	Moderate	16.64	33.42	22.78
22	300	Defected	Internal Void	5%	2/3 length	3.38	Moderate	15.85	33.15	22.43
23	300	Defected	Internal Defect (Gap in Concrete)	1%	1/3 length	3.99	Good	22.98	35.42	25.28
24	300	Defected	Internal Defect (Gap in Concrete)	1%	1/2 length	4.00	Good	23.13	35.47	25.33
25	300	Defected	Internal Defect (Gap in Concrete)	1%	2/3 length	3.95	Good	22.40	35.25	25.07
26	400	Sound	–	–	–	4.10	Good	24.60	35.89	25.86
27	400	Defected	Neck	5%	1/3 length	3.54	Moderate	17.50	33.71	23.14
28	400	Defected	Neck	10%	1/3 length	2.40	Poor	8.72	30.27	18.84
29	400	Defected	Neck	15%	1/3 length	1.70	Very Poor	5.68	28.67	16.84

30	500	Sound	–	–	–	4.14	Good	25.25	36.07	26.09
31	500	Defected	Neck	5%	1/3 length	3.60	Moderate	18.12	33.92	23.40
32	500	Defected	Neck	10%	1/3 length	2.43	Poor	8.90	30.35	18.94
33	500	Defected	eck	15%	1/3 length	2.04	Very Poor	6.99	29.40	17.75

Whenever there is a defect, the pulse velocity decreases, and this means that the mechanical properties has been affected and transformed to lower strength and lower modulus of elasticity.

The wave velocity for the defect piles was found proportional to defect ratio, and this relation is not affected by the defect type, Table (3).

The results of ultrasonic tests are shown in Figures (2) to (5). In Figure (2), the relation between the modulus of elasticity reduction factor, r_c (where $r_c = (1 - E_{cd}/E_{cs})\times 100$, in which E_{cd} is the modulus of elasticity for defected pile and E_{cs} is the modulus of elasticity for sound pile) or the dynamic modulus of elasticity reduction factor, r_d ($r_d = (1 - E_{dd}/E_{ds})\times 100$, where E_{dd} is the dynamic modulus of elasticity for defected pile and E_{ds} is the dynamic modulus of elasticity for sound pile) and the defect ratio (the defect volume compared to the total volume of the pile).

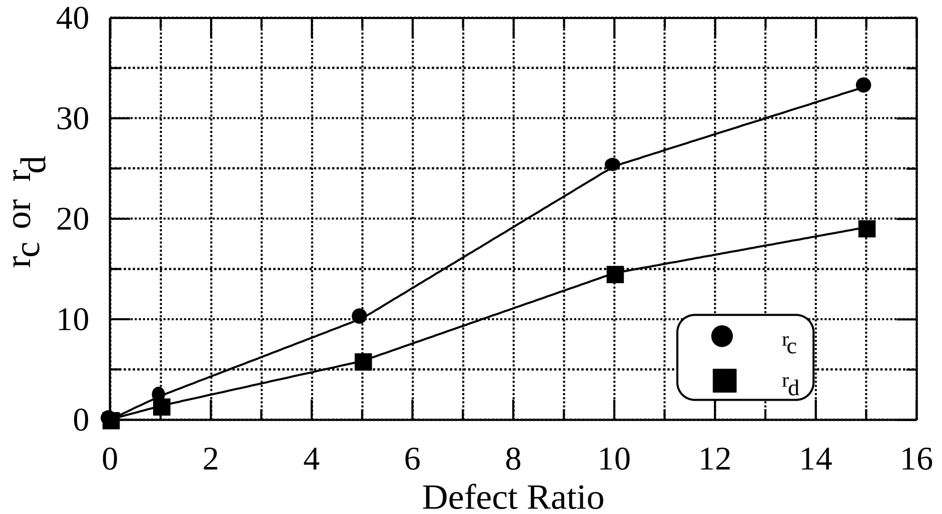

Fig. (2) The Relation Between Defect Ratio and Reduction Factor in Static or Dynamic Modulus of Elasticity of Concrete.

It can be noticed that the reduction factors, r_c increases to about (45%) while the factor r_d increases to about (20%) when the defect ratio is (15%).

The presence of voids in defected concrete mass causes a reduction in the pulse velocity, V, of the ultrasonic waves. This is seen in Figure (3) in which the pulse velocity decreases with increase of defect ratio.

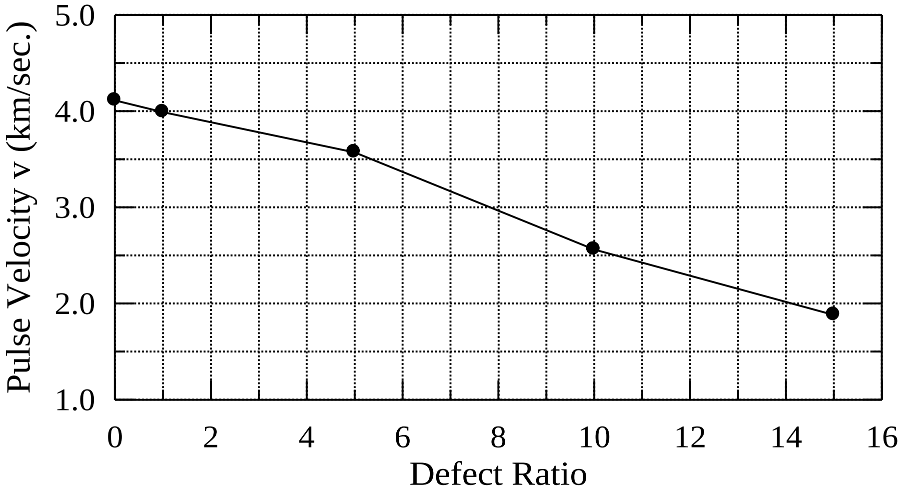

Fig (3) The Relation Between Defect Ratio and Pulse Velocity.

The pulse velocity decreases to about (50%) when the defect ratio increase from (5%) to (15%)

Figure (4) shows the relation between the concrete compressive strength reduction factor, (r) (where r = (1 – f_{cud}/f_{cus})×100, in which f_{cud} is the concrete compressive strength for defective pile and f_{cus} is the concrete compressive strength for sound pile) and the defect ratio. It can be noticed that the factor r increase with the increase of defect ratio. The increase in r is found to be about (45%) when the defect ratio increases from (5%) to (15%).

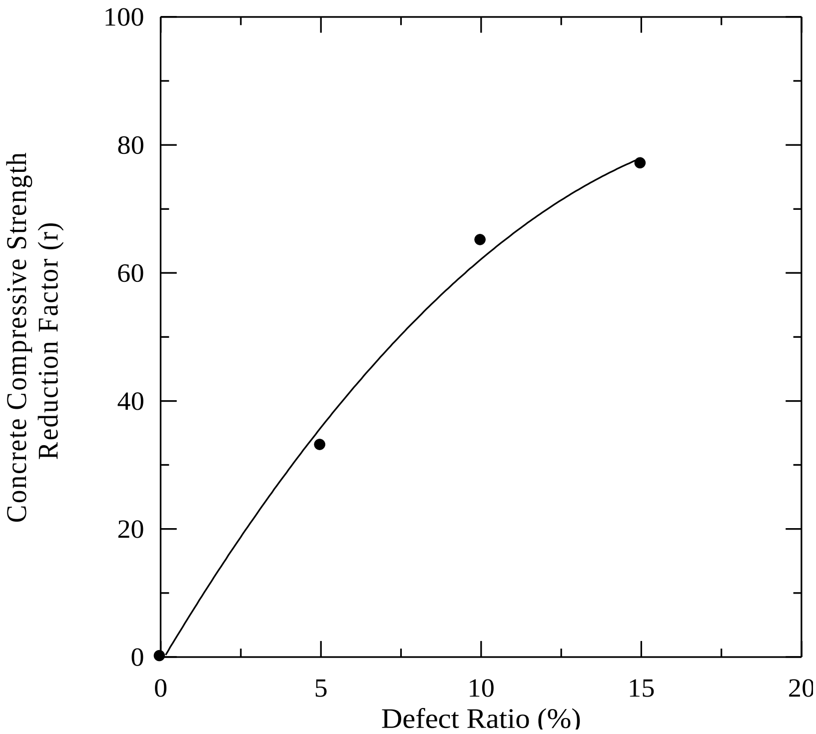

Fig (4) The Relation Between Defect Ratio and Concrete Compressive Reduction Factor (r).

Fig (5) shows a relationship between the defect ratio and pile stiffness reduction factor, R_{ks} (where R_{ks} = (stiffness for defected pile / stiffness) for sound pile)×100). The stiffness factor decreases with the increase in defect ratio. The reduction in the factor R_{ks} is found to be about (26%) when the defect ratio increase from (5%) to (15%).

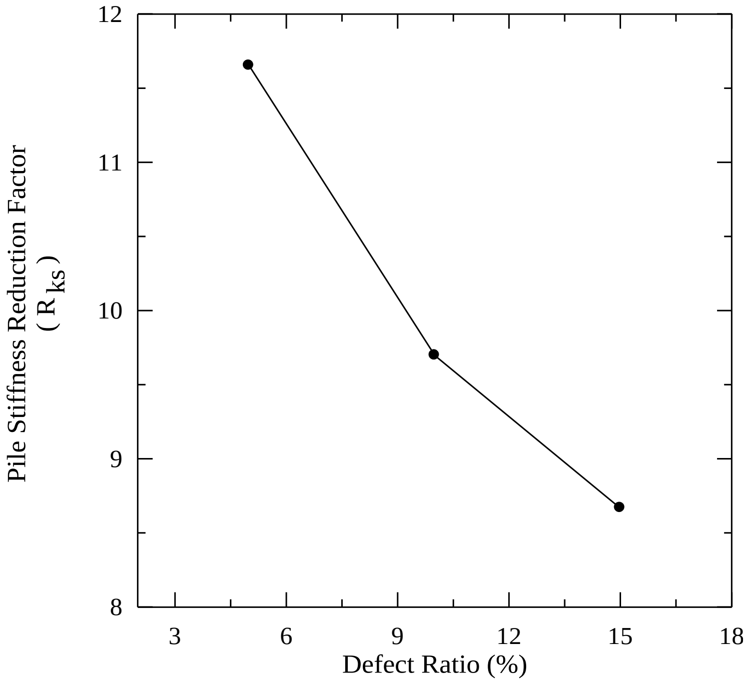

Fig (5) The Relation Between Defect Ratio and Pile Stiffness Reduction Factor (R_{ks}).

CONCLUSIONS

The results of this research indicated that when the defect ratio increases from 5 to 15, then:

a- The pulse velocity decreases to about (50%).

b- The reduction factor r_c increases to about (45%), while the factor r_d increases to about (20%).

c- The reduction in pile stiffness factor is found to be about (26%).

d- The decrease in concrete strength is found to be about (45%).

References:

-ACI Committee (211.1-91) Standard Practice for Selecting Proportions for Normal, Heavy weight, and Mass Concrete", ACI Manual of Concrete Practice, Part 1, 1991.

-Al-Mosawe, M. J. A. and Al-Obaydi, A. H., (2002), "Thermal Analysis in Large Diameter Bored Piles", 6th International Conference on Concrete Technology for Developing Countries, 21-24 October, 2002, Amman, Jordan, pp.763-772.

-ASTM C597-83, (1991), "Test for Pulse Velocity Through Concrete", American Society for Testing and Materials, 1991.

-BS 1881: Part 203: 1986, “Recommendations for Measurement of Velocity of Ultrasonic Pulses in Concrete”, British Standards Institution, London.

-CP 110, 1972, "The Structural Use of Concrete", Code of Practice, Part 1, "Design Materials and Workmanship".

-Jones, R. and Gatfield, Exl., (1963), “Testing Concrete by an Ultrasonic Pulse Technique”, London Her Majesty’s Stationary Office, 1963, pp.15-16.

-Poulos, H. G., (1997), "Behaviour of Pile Groups Containing Defective Piles", Proceeding of 14th International Conference of Soil Mechanics and Foundation Engineering", Hamburg, Vol.2, pp.670.

– زين العابدين رؤوف محمد، فريدة يونس، وبريئة محمد صالح، "السيطرة على نوعية الخرسانة بأستخدام الذبذبات فوق الصوتية"، وقائع ندوة التعليم المستمر، ١٩٨٦.

SACRIFICIAL ANODE CATHODIC PROTECTION OF LOW CARBON STEEL IN SEA WATER

Dr. Aprael S. Yaro **Dr. Khalid W. Hameed**
University of Baghdad / College of Engineering

ABSTRACT

Cathodic protection is a corrosion-prevention technique which uses the electrochemical properties of metals to insure that the structure to be protected becomes the cathode of an electrolytic cell.
Laboratory evaluation was conducted on zinc electrode as anode material that used for sacrificial anode cathodic protection (SACP)of carbon steel.
Rate of zinc consumption during cathodic protection of carbon steel pipeline carrying seawater (4 % w/v NaCl solution) were measured by the loss in weight technique. Variables studied were seawater temperature (0-45^{o} C), flow rate (5-900 lit/h), pH (2-12) and duration time (1-4 h). It was found that the rate of zinc consumption increases with increasing seawater temperature, flow rate and duration time and decreases with pH increase. Under the mentioned operating conditions, the rate of zinc consumption during cathodic protection of steel ranged from 5.65×10^{-3} to 98.9×10^{-3} g/cm^2.day.

For the system under investigation, the cell responsible for cathodic protection is Zn/NaCl/Fe.

INTRODUCTION

Corrosion is an electrochemical process in which a current leaves a structure at the anode site, passes through an electrolyte and reenters the structure at the cathode site. Current flows because of a potential difference between the anode and cathode that is the anode potential is more negative than the cathode potential, and the difference is the driving force for the corrosion current. The total system-anode, cathode, electrolyte and metallic connection between anode and cathode is termed a corrosion cell (Shrier(1), 1976 and Halford, 1985).

Corrosion control is a process in which humans are very much in control of materials and environments can regulate the rate of corrosion, keeping it within acceptable or at least predictable limits for life of the structure (Trethewey and Chamberlain, 1996).

There are many methods for corrosion control as illustrated some of them (Bosich, 1970 and Schweitzer, 1987),(cathodic protection, anodic protection ,protective coating such as paint ,corrosion-resistant metals and alloys ,addition of inhibitors , very pure metals, ….etc).

The selecting method depends on many factors such as cost,efficiency, availability, contamination of environment with corroding metal, …etc.

Cathodic protection is unique amongst all the methods of corrosion control in that if required it is able to stop corrosion completely, but it remains within the choice of the operator to accept a lesser, but quantifiable, level of protection. Manifestly, it is an important and versatile technique. In principle, cathodic protection can be applied to all the so-called engineering metals.

In practice, it is most commonly used to protect ferrous materials and predominantly carbon steel. It is possible to apply cathodic protection in most aqueous corrosive environments, although its use is largely restricted to natural near-neutral environments (soils, sands and waters, each with air access). Thus, although the general principles outlined here apply to virtually all metals in aqueous environments, it is appropriate that the emphasis, and the illustrations, relate to steel in aerated natural environments (Shrier, (2), 1994 and Almardy, 1999).

Cathodic protection involves the application of a direct current (DC) from an anode through the electrolyte to the surface to be protected. This is often through of as "overcoming" the corrosion currents that exist on the structure. There is no flow of electrical currents (electrons) through the electrolyte but flow of ionic current. Cathodic protection eliminates the potential differences between the anodes and cathodes on the corroding surface. A potential difference is then created between the cathodic protection anode and the structure such that the cathodic protection anode is of a more negative potential than any point on the structure surface. Thus, the structure becomes the cathode of a new corrosion cell. The cathodic protection anode is allowed to corrode; the structure, being the cathode, does not corrode (Brown and Root, 2003 and Jezmar, 2003).

There are two proved methods of applying cathodic protection: sacrificial anode (galvanic) and impressed current. Each method depends upon a number of economic and technical considerations and as certain advantages. For every structure, there is a special cathodic protection system dependent on the environment of the structure (Scully, 1975).

Current distribution in cathodic protection system is dependent on several factors, the most important of which are driving potential, anode and cathode geometry, spacing between anode and cathode and the conductivity of the aqueous environment which is favorable toward good distribution of current (Shrier (2), 1994)

Structures commonly protected are the exterior surfaces of pipelines, ships' hulls, jetties, foundation piling, steel sheet-piling and offshore platforms. Cathodic protection is also used on the interior surfaces of water-storage tanks and water-circulating systems. However, since an external anode will seldom spread the protection for a distance of more than two or three pipe-diameters, the method is not suitable for the protection of small-bore pipework. Cathodic protection has also been applied to steel embedded in concrete, to copper-based alloys in water systems and exceptionally to lead-sheathed cables and to aluminum alloys, where cathodic potentials have to be very carefully controlled (Halford, 1985 and Davies, 2001).

The present work considered the sacrificial anode cathodic protection. The effect of temperature (0-45^{o} C), flow rate (5-900 lit/h), pH (2-12) and time (1-4 h) on the rate of zinc consumption during cathodic protection of steel tube exposed to seawater (4 %w/v *NaCl* in distilled water). The rate of zinc consumption was determined by the loss in weight technique.

EXPERIMENTAL WORK

The apparatus shown in figure (1) was used to study the variables, temperature (0-45^{o} C), flow rate (5-900 lit/h), pH (2-12) and time (1-4 h) in the sacrificial anode cathodic protection system.

The container vessel was filled with seawater (4% (w/v) *NaCl*), then adjusting the pH and temperature to the desired values. Before each run, the zinc strip was weighted and fixed at the inlet of the steel tube by rubber stopper and was electrically connected by an insulated copper wire to the steel tube outlet as shown in figure (1).The zinc strip is extending along the steel tube to ensure uniform current and potential distribution along the tube wall.

The seawater was pumped from the vessel by the pump through the rotameter to measure the desired flow rate, then the seawater inter from the below the steel tube and out from upper the steel tube to return to the vessel again (i.e. the seawater is circulated between the vessel and steel tube for desired time).After each run the zinc strip was rinsed in distilled water and brush to remove the corrosion products, dried with clean tissue then immersed in the benzene and acetone, dried again, and then re-weighted to determine the weight loss. The steel tube is also rinsed and dried by the same way above in order to re-use another time. After each run the vessel is emptied from the solution and washed with distilled water, then filled with a new prepared solution for new run.

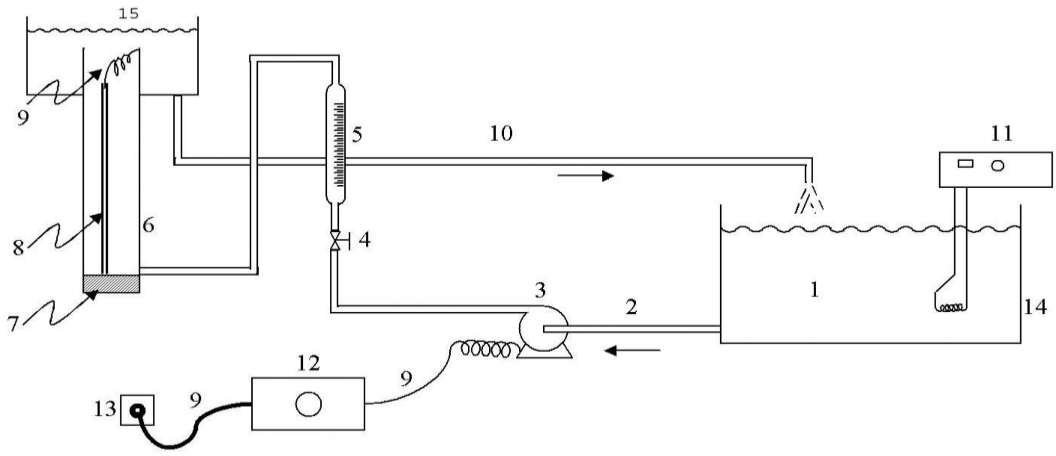

1. Electrolyte (seawater)	2. Feed forward Pipe	3. Pump	4. Valve	5. Rota meter
6. Tube steel	7. Rubber stopper	8. Zinc strip	9. Copper wire	10. Feedback pipe
11. Heater or chiller	12. Variac	13. Electric source	14. Insulated vessel	15. Overflow

Fig. 1, Schematic diagram of apparatus used in sacrificial anode test system

RESULTS AND DISCUSSION

Time effect

Figures 2,3 and 4 show the rate of zinc consumption (dissolution), as an instead of corrosion rate of steel, with time at different temperatures, different flow rates and different pH, respectively. Where the rate of zinc dissolution increases with increasing time and this is normal case. But this increasing is not equally with time, where the dissolution rate in the first hour is more than second hour and so on. The reasons of that are attributed to continuous growth of the corrosion products layer with time, which affects the transport of oxygen to the metal surface and the activity of the surface and hence the corrosion rate. Also, the cathodic reactions will result an increase in pH with time either by the removal of hydrogen ions ($2H^+ + 2e \rightarrow H_2 \uparrow$) or by the generation of hydroxyl ions ($2H_2O + 2e \rightarrow H_2 \uparrow + 2OH^-$ and $O_2 + 2H_2O + 4e \rightarrow 4OH^-$) both reasons are reduced the corrosion rate of steel and hence the dissolution rate of zinc.

Temperature effect

Figures 2, 5 and 6 show the effect of temperature on the rate of zinc dissolution with time with different flow rates and with different pH's, respectively. The increase in the rate of zinc dissolution with increasing seawater temperature (particularly from 15 to 30^o C) may be explained in terms of the following effects:

1. A temperature increase usually increases the reaction rate which is the corrosion rate and according to the Freundlich equation (Shrier (2), 1976):

$$Corrosion\,\mathrm{rate} = \mathrm{k}\,\mathrm{C}_{\mathrm{O_2}}^{\mathrm{n}} \tag{1}$$

Where k is rate constant of reaction, C_{O2} (concentration of oxygen) and n is order of reaction. The rate constant (k) varying with temperature according to Arrhenius equation (Shrier (2), 1976):

$$k = k_o e^{-E/RT} \tag{2}$$

Where k_o is constant, E is activation energy, R is universal gas constant and T is temperature. Then from this formula ($k = k_o e^{-E/RT}$) indicates that the k is increased with increasing temperature and then the corrosion rate which is leads to increasing the rate of zinc dissolutions.

2. Increasing seawater temperature leads to decreasing seawater viscosity with a consequent increase in oxygen diffusivity according to stokes-Einstein equation (Cussler, 1984 and Konsowa and El-Shazly, 2002):

$$\frac{\mu D}{T} = \mathrm{constant} \tag{3}$$

Where μ is the seawater viscosity and D is the diffusivity of the dissolved oxygen. As a result of increasing the diffusivity of dissolved oxygen, the rate of mass transfer of dissolved oxygen to the cathode surface increases according to the following equation (Konsowa and El-Shazly, 2002):

$$J = k_d C_{O_2} = \frac{D}{\delta_d} C_{O_2} \tag{4}$$

With a consequence increase in the rate of zinc dissolution. Where k_d is mass transfer coefficient and J is mole flux of oxygen.

3. The decreases in seawater viscosity with increasing temperature improve the seawater conductivity with a consequent increase in corrosion current and the rate of corrosion.
4. On the other hand, increase of temperature reduce the solubility of dissolved oxygen with a subsequent decrease in the rate of oxygen diffusion to the cathode surface and the rate of corrosion.

It seems that within the present range of temperature effects 1, 2 and 3 are predominating.

Flow rate effect

Figures 3, 5 and 7 show the effect of solution flow rate on the zinc dissolution with time, with different temperatures and with different pH’s, respectively. It can be seen from figures 3, 5 and 7 that the dissolution rate of zinc increases with increasing the flow rate. This may be attributed to the decrease in the thickness of hydrodynamic boundary layer and diffusion layer across which dissolved oxygen diffuses to the tube wall of steel with consequent increase in the rate of oxygen diffusion which is given by equation 4. Then the surface film resistance almost vanishes, oxygen depolarization, the products of corrosion and protective film are continuously swept away and continuous corrosion occurs. The flow rate of seawater may also caused erosion which combined with electrochemical attack.

pH effect

Figures 4, 6 and 7 show the effect of pH on dissolution of zinc with time, with different temperatures and with different flow rates, respectively. It can be seen from these figures that the rate of zinc dissolution increases with decreasing of pH (particularly at range of pH 5 to 2). Within the range of about 5 to 12 the corrosion rate of steel and hence dissolution rate of zinc is slightly dependent of the pH, where it depends almost on how rapidly oxygen to the metal surface. Although it was expected that at very high of pH value (12), the dissolution rate of zinc is much reducing because the steel becomes increasingly passive in present of alkalies and dissolved oxygen, but the nature of electrolyte (seawater) prevent that where chloride ions depassivate iron even at high pH. Within the acidic region (pH<5) the ferrous oxide film (resulting from corrosion) is dissolved, the surface pH falls and steel is more direct contact with environment. The increased rate of reaction (corrosion) is then the sum of both an appreciable rate of hydrogen evolution and oxygen depolarization.

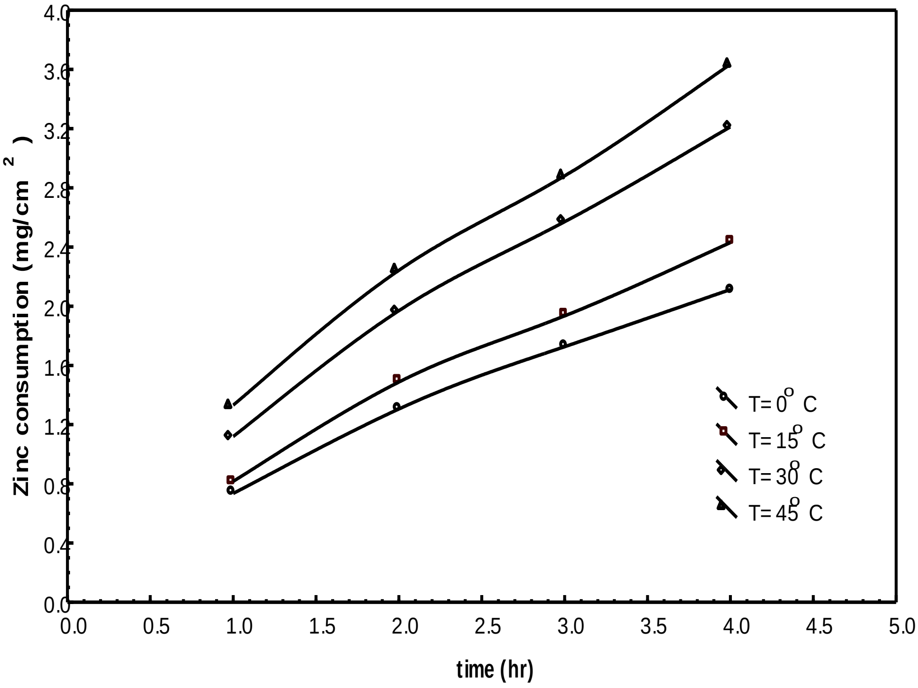

Fig. 2, Zinc consumption with time for different temperatures at flow rate=600 lit/h and pH=8

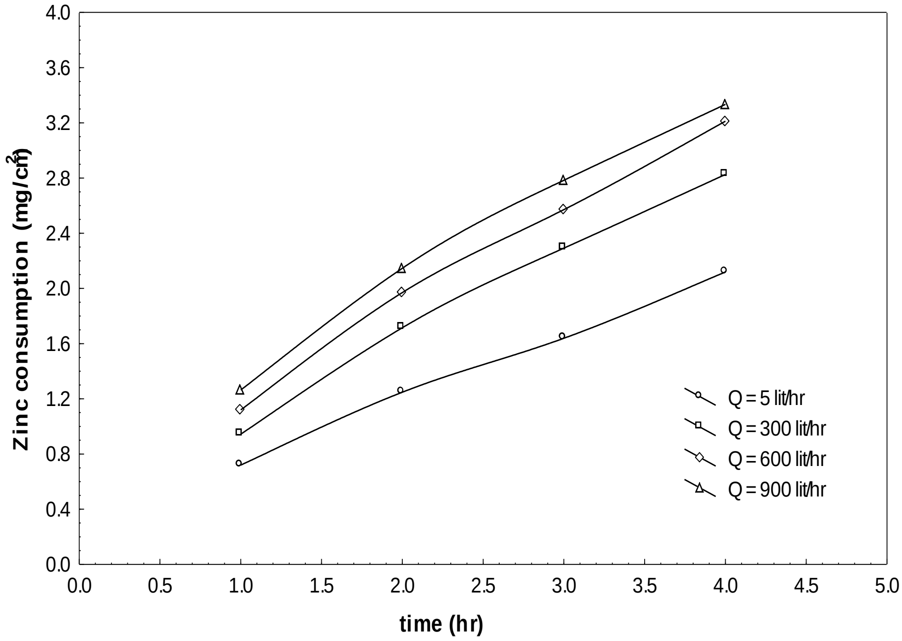

Fig. 3, Zinc consumption with time for different flow rate at temperature=30^{o} C and pH=8

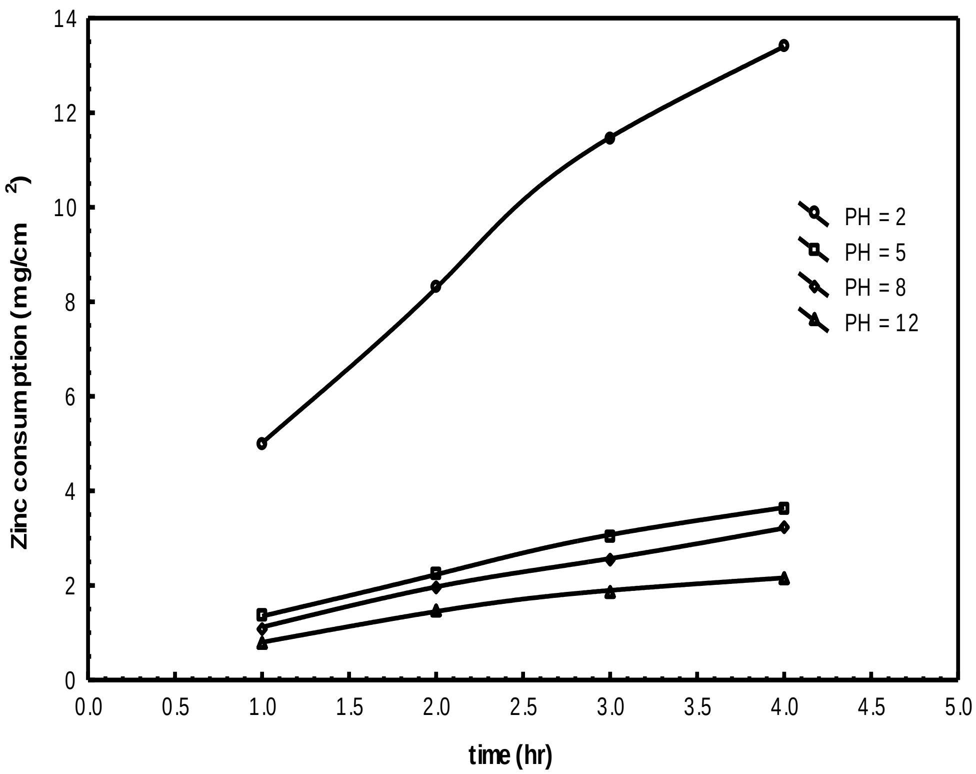

Fig. 4, Zinc consumption with time for different pH's at temperature 30^{o} C and flow rate=600 lit/h

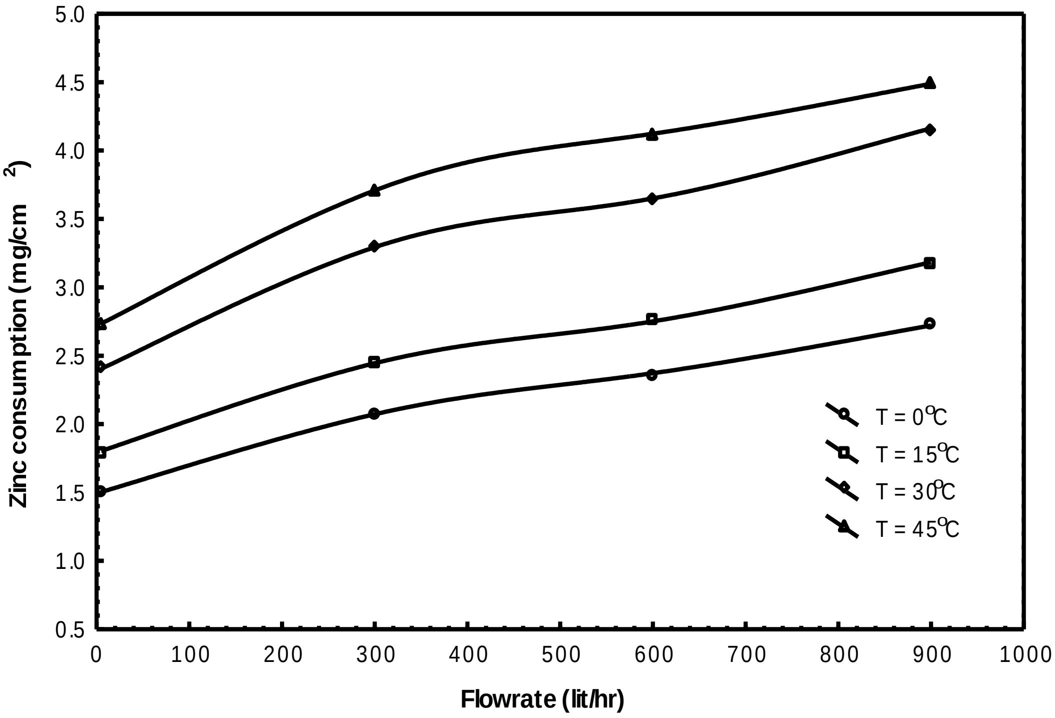

Fig. 5, Zinc consumption with flow rate for different temperatures at time=4 h and pH=5

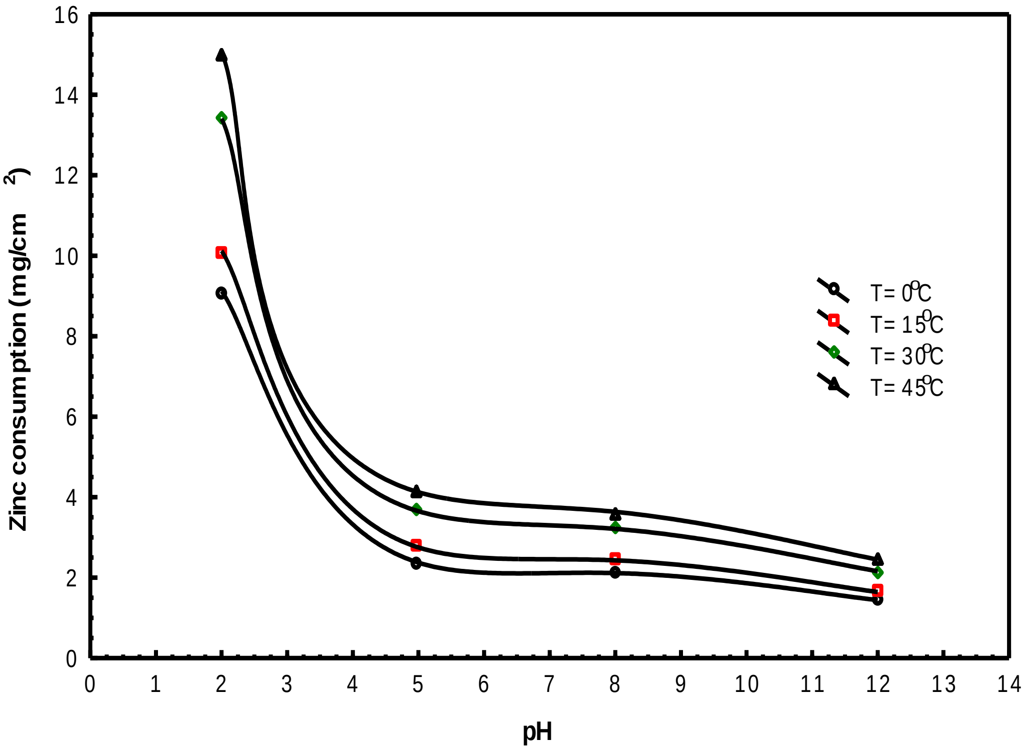

Fig. 6, Zinc consumption with pH for different temperatures at time=4 h and flow rate=600 lit/h

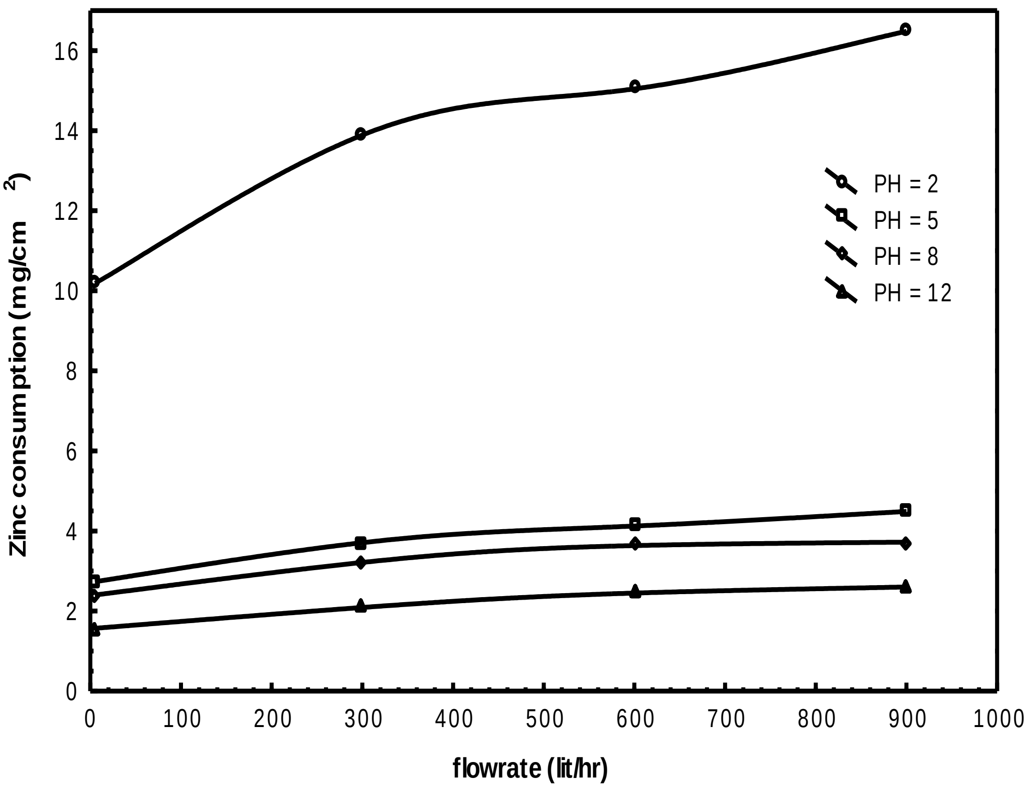

Fig. 7, Zinc consumption with flow rate for different pH's at time=4 h and temperature=45^{o} C

CONCLUSION

From the results obtained in the present work the following conclusion can be drawn: The study of sacrificial anode cathodic protection of short steel tube using zinc strip extended axially in the pipe revealed that under the present range of conditions of temperature, flow rate, pH of seawater and protection time, the rate of zinc consumption increases with increasing temperature, flow rate and time and with decreasing of pH. Zinc consumption during first hour is greater than during second hour and so on. The zinc consumption with very low pH is very high and the cathodic protection becomes unreliable.

REFERENCES

- Al-Mardy, S. M. (1999), "*Design of fuzzy logic controller for the cathodic protection of underground pipelines*", M. Sc. Thesis

- Bosich, F. J. (1970), "*Corrosion prevention for practicing engineers*", Barnes and Noble Inc.

- Brown, P. E. and Root, m. (2003), "*The failure analysis experts*", Cathodic Protection for Deep Water Pipelines, Houston-Texas.

- Cussler, E. L. (1984), "*Mass transfer in fluid systems*", Cambridge University press, Cambridge, UK.

- Davies, K. G. (2003), "*Cathodic protection in practice*". (internet site: www.npl.co.uk)

- Halford, G. E. (1985), "*Introduction to cathodic protection*".

- Jezmar, J. (2003), "*Monitoring methods of cathodic protection*".

- Konsowa, A. H. and El-Shazly, A. A. (2002), Elsevier, Desalination, **153**, pp 223-226.

- Schweitzer, A. P. (1987), "*What every engineer should know about corrosion*".

- Scully, J. C. (1975), "*The fundamental of corrosion*", 2nd edition.

- Shrier (1), L. L. (1976), "*Corrosion 1, metal/environment reactions*", Newnes-Butterworth.

- Shrier (2), L. L. (1976), "*Corrosion 2, corrosion control*", Newnes-Butterworth.

- Shrier (2), L. L. (1994), "*Corrosion 2, corrosion control*", 3rd edition, Newnes-Butterworth.

- Trethewey, K. R. and Chamberlain, J. (1996), "*Corrosion for scientist and engineering*", 2nd edition.

Numerical Simulation of Heat Transfer Problem in Hot and Cold Rolling Process

Ass.Prof. Dr. Ihsan Y. Hussain

Mech. Engr. Dept.
College of Engineering
University of Baghdad
Baghdad – Iraq

ABSTRACT

An efficient numerical model had been developed to model the thermal behaviour of the rolling process. An Eulerian formulation was employed to minimize the number of grid points required. The model is capable to calculate the temperature distribution, the heat penetration depth, the convection heat transfer coefficient of cooling, the flow of metal through the roll gap, and the heat generation by plastic deformation and friction. The roll is assumed to rotate at constant speed, and the temperature variations are assumed to be cyclically steady state and localized with a very thin layer near the surface. The Conventional Finite Difference (CFDM) based on cylindrical coordinates was used to model the roll, and a Generalized Finite Difference Method (GFDM) with non-orthogonal mesh was employed in the deformed strip region and the roll-strip interface area. An upwind differencing scheme was selected to overcome the numerical instability resulting from the high velocity (high Peclet number) involved in the rolling process. The equations of the strip and roll are then coupled together and solved simultaneously. Both cold and hot rolling heat transfer behaviours, velocity distribution, and heat generation by deformation and friction under typical rolling conditions were presented to demonstrate the feasibility and capability of the developed numerical model. It has been found that, while the strip is under deformation, the bulk temperature inside the strip increases continuously; this is largely controlled by the deformation energy. On the other hand, the strip surface temperature changes much more drastically and it is mainly controlled by the friction heat and the roll temperature. The roll acts like a heat sink, because the coolant heavily cools it. Thus, as soon as the strip hits the roll its surface temperature drops. Since considerable friction and deformation heat are created along the interface and transferred from the neighboring sub-layer, the surface temperature picks up rapidly. Finally, the results of the temperature distribution for both cold and hot rolling and the heat generation by deformation and friction obtained from the present study were compared with previous published work to verify the validity of the numerical solution. Good acceptable agreements were obtained.

الخلاصة

تم التوصل إلى نمــوذج عددي لنمذجه التصرف الحراري لعمليه ألدرفلة (Rolling Process). استخدمت صيغه أويلر العددية (Eulerian Formulation) لتقليل عدد نقاط ألشبكه (Mesh) اللازمة للحل العددي. للنموذج العددي القابلية على حساب توزيع درجات الحرارة ، عمق انتشار الحرارة (Heat Penetration Depth)، معامل انتقال الحرارة لمائع التبريد (Cooling Heat Transfer Coefficient)، جريان المعدن خلال عمليه الدرفلة (Flow of Metal in Rolling)، الحرارة المتولدة بسبب التشوه اللدن للمعدن (Heat Generation by Plastic Deformation and Friction). تم افتراض ثبوت السرعة الدورانيه للدرفيـل وان التغيرات التي تطـرأ علـى درجـات الحـرارة تكـون علـى هيئـه قشـرة رقيقـه (Very Thin Layer) علـى سـطح الـدرفيل. طريقـة للفروقات المحددة التقليدية (Conventional Finite Difference Method) المبنية على أساس الإحداثيات القطبية (Polar Coordinates) هي الأكثر ملائمة والتي استخدمت لإيجاد توزيع درجات الحرارة للدرفيـل. بينما استخدمت طريقة الفرو قات المحددة المعمّمة(Generalized Finite Difference Method) لنمذجة درجات الحرارة للمناطق التي تكون فيها خطوط الشبكه غير متعامدة (Non-orthogonal Mesh) و المتمثلة بالمنطقة التي يتشوه فيها المعدن. لقد اختير نسق لفرو قات الصاعد للنقاط المواجهة للجريان (Up-wind Differencing Scheme) للتغلب على عدم الاستقراريه العددية الناتجة من السرع العالية أو عدد بكلت العالي (High Peclet Number) الذي تتضمنه عمليه الدرفلة. تم حل معادلتي المعدن المدرفـل (Strip) والدرفيـل (Roll) آنيا (Simultaneously). تمت دراسة حالتي الدرفلة على البارد وعلى الساخن معا، عرضت نتائج التصرف الحراري و توزيع السرع وتوزيع الحرارة المتولدة بالتشوه والاحتكاك بمقتضى الشروط الحدودية النموذجية لإيضاح اقدرة النموذج الذي تم التوصل اليه. وجد في الدراسه الحالية، أثناء تشوه المعدن (Strip)، أن مقدار درجه الحرارة في داخله تزداد بصوره مستمرة، وأن طاقة التشويه تسيطر عليها بصوره كبيره. من ناحية أخرى فأن درجه حرارة سطح المعدن تتغير بصوره أكثر أثاره والتي تكون طاقه الاحتكاك ودرجه الحرارة داخل الدرفيل تسيطرعليها بصوره رئيسيه. أن التبريد العالي الذي يتعرض لـه الدرفيل، سيكون لـه أثر كبير أشبه بالغور الحراري(Heat Sink). حيث عند اصطدام المعدن بالدرفيل فأن درجه حرارة سطح الدرفيل تهبط. بسبب حرارتي التشوه والاحتكاك اللتان تنشآن على طول سطح التلامس (Interface) أضافه إلى الحرارة المنتقلة من الطبقة المجاورة للمعدن المشوه فأن درجه حرارة سطح المعدن ترتفع بسرعة. أخيرا، نتائج توزيعات درجه الحرارة والحرارة

المتولدة بسبب التشوه والاحتكاك التي تم التوصل لها قورنت بنتائج عمل مسبق للتحقق من مدى صحة الحل العددي. لقد وجد

توافق جيد من المقارنة بين النتائج المحسوبة من البحث الحالي والنتائج المحسوبة في عمل مسبق.

KEY WORDS: Thermal Behaviour, Hot and Cold Rolling , Roll and Strip, Velocity and Temperature Distribution

INTRODUCTION

The process of plastically deforming metal by passing it between rolls is known as Rolling, **(Dieter 1986).** It can be considered as one of the most important of manufacturing process. Numerous investigations, numerical, analytical, and experimental have been carried out on rolling. In hot or cold rolling the main objective is to decrease the thickness of the metal. Ordinarily little increase in width occurs, so that decreases in thickness will result in an increase in length. As predicted by **(Lahoti and Altan 1975)** the energy consumed in plastic deformation is transformed into heat while a small portion of the energy is used up in deforming the crystal structure in material. This heat generation coupled with heat transfer within the deforming material and to the environment gives a temperature distribution in the deformed peace. As mentioned by **(Karagiozis and Lenard 1988),** a (± 1) percent variation of the temperature may cause (10) percent change in strength, which in turn will cause significant change in roll loads. As well as, the adequate cooling of roll and the rolled products is of a considerable concern to rolls designers and operators. Improper or insufficient cooling not only can lead to shorten roll life, due to thermal stresses, but it can also significantly affect the shape or crown of the roll and result in buckled strips or bunted edges. Considerable work has been done on modeling of the thermal behavior of rolling process. (Johnson and Kudo 1960) used upper pound technique to predict the strip temperatures. **(Lahoti *et al.* 1998)** used a two-dimensional finite difference model to investigate the transient strip and a portion of the roll behavior. **(Sheppard and Wright 1980)** developed a finite difference technique to predict the temperature profile during the rolling of the aluminum slab**. (Zienkiewicz *et al.* 1981)** submitted a general formulation for coupled thermal flow of metal for extrusion and rolling by using finite element method. **(Patula 1981)** with an Eulerian formulation attained a steady state solution for a rotating roll subjected to prescribed surface heat input over one portion and convective cooling over an other portion of the circumference. **(Bryant and Heselton 1982)** based on the idea of “rotating line sources of heat” and the strip modeling based on the theory of heat conduction in a “semi infinite body” they found that the knowledge of heat transfer mechanisms in hot rolling was essential to the study of many areas of the process. **(Bryant and Chiu 1982)** derived a simple model for the cyclic temperature transient in hot rolling work rolls. **(Tseng 1984)** investigated both the cold and hot rolling of steel by considering the strip and roll together. (Tseng ***et al.*** 1990) developed an analytical model **(Forier integral technique)** to determine the temperature profiles of the roll and strip simultaneously**. (Remn 1998)** used the Laplace and inverse transform analytic technique to study the two dimensional unsteady thermal behavior of work rolls in rolling process. **(Chang 1998)** used Finite difference formulations in the rolling direction and analytical solutions were applied normal to this direction, making computational more efficient. The experimental work done by **(Karagiozis and Lenard 1988)** shows the dependence of the temperature distribution during hot rolling of a steel slab on the speed of rolling, reduction ratio and initial temperature were investigated.

The purpose of the present study is to effectively analyze the thermal behavior of rolling process for hot and cold rolling by considering the roll and strip simultaneously for two cases of rolling conditions (see **Table 1** and **Fig. 1**) by using a suitable numerical methods.

MATHEMATICAL FORMULATION

The mathematical formulations of the problem will be presented in this article. The following assumptions were made;

1. The strip and roll are long compared with the strip thickness therefore; axial heat conduction can be neglected.
2. The steady state conditions are considered for both strip and roll.
3. Since tremendous rolling pressure builds up in the interface then, the surface roughness became insignificant, and the film is very thin, on the order of micron, therefore, the thermal resistance of the film can be neglected.
4. The constant friction coefficient was assumed along the interface.
5. No increase in width, so that the vertical compression of the metal is translated into an elongation in the rolling direction.

Using an Eulerian description, the energy equation of the strip for a planer steady state problem as shown in **(Tseng 1984)** is;

$$u\frac{\partial T_s}{\partial x}+v\frac{\partial T_s}{\partial y}=\alpha_s\left(\frac{\partial^2 T_s}{\partial x^2}+\frac{\partial^2 T_s}{\partial y^2}\right)+q_d/\rho_s c_s \qquad \textbf{\textit{(1)}}$$

where (u) and (v) are the velocity component in (x and y) directions respectively which should satisfy the equation of continuity, (α, ρ and c) are the thermal diffusivity, density and specific heat respectively, (q_d) is the rate of heat generation by deformation per unit volume and the subscript (s) refers to the strip properties.

With respect to a fixed Eulerian reference frame, the governing partial differential equation of the roll temperature (T_r) as shown in **(Tseng 1990)** is;

$$\frac{\omega}{\alpha_r}\frac{\partial T_r}{\partial \theta}=\frac{\partial^2 T_r}{\partial r^2}+\frac{1}{r}\frac{\partial T_r}{\partial r}+\frac{1}{r^2}\frac{\partial^2 T_r}{\partial \theta^2} \qquad \textbf{\textit{(2)}}$$

where (r) and (θ) are the cylindrical coordinates; (ω) is the roll angular velocity; and the subscript (r) refers to the roll properties.

The concept of the thermal layer has also been applied to a numerical analysis by (Tseng 1984) and in the present study, it has been improved computational accuracy.

According to **(Tseng 1984),** (δ/R) can be found as a function of the Peclet number ($Pe=R^2\omega/\alpha_r$). Alternately, following **(Patula 1981),** showed that ($\delta/R\le 4.24/\sqrt{Pe}$), when ($\sqrt{Pe}$ >>***0***), a condition satisfied in most commercial strip rolling.

Based on a numerical study of **(Tseng 1984**) the;

$$\delta/R=7/\sqrt{Pe} \qquad \textbf{\textit{(3)}}$$

is large enough for the present numerical model.

For rolling situations involving high speeds, the penetration would be significantly less where ($Pe=R^2\omega/\alpha_r$). Conversely, for lower rotational speeds, the penetration would be greater.

In the present study (second case) and as reported by (Tseng 1990), the mean film coefficient of the water-cooling spray is about (3.4 W/cm^2.^{o}C) over about 30 degrees of the roll circumference. The secondary cooling produced by water puddling varies from (0.28 to 0.85 W/cm^2.^{o}C) as shown in **Fig. 2**. The two peak squares represent the entry and exit cooling. Puddling covers the remaining area.

As well as for the first case, the convection heat transfer for water cooling spray varies from (0.85 W/cm^2.^{o}C to 3.4 W/cm^2.^{o}C) along the roll. The heat transfers coefficient as presented in Fig. (4) varies as half sine curve to simulate both the entry and exit cooling. Then, from **Fig.3**. the heat transfer coefficient can be written as;

$$H(\theta) = 0.85 + 2.55\left|\sin(\theta)\right| \qquad \textbf{\textit{(4)}}$$

Then, the two cases of water-cooling spray, **Figs. 2** and **3** are considered in the present study to simulate the entry and exit cooling during the rolling.

The flow of metal under the arc of contact is determined by assuming that the volume flow rate through any vertical section is constant. A metal strip with a thickness (t_o) enters the bite at the entrance plane (XX) with velocity (u_o). It passes through the bite and leaves the exit plane (YY) with a reduction thickness (t_f) and velocity (u_f) as shown in **Fig. 4**.

Since equal volumes of metal must pass at any vertical section, then;

$$Wt_o u_o = Wtu = Wt_f u_f \qquad \textbf{\textit{(5)}}$$

where (W) is the width of strip; (u) is the velocity at any thickness (t) intermediate between (t_o) and (t_f).

At only one point along the arc of contact between the roll and strip is the surface velocity of the roll (V_r) equal the velocity of the strip. This point is called the neutral point or no-slip point and indicated in **Fig. 4** by point (N).

If large back tension or heavy draught is applied, the neutral point shifts toward the exit plane and the metal will slip on the roll surface, this (back tension) condition is considered in the present study.

There are two components of velocity, one of these in (x) direction is denoted by (u) and the other in (y) direction is denoted by (v). Recall **eq**. *(5)*, then;

$$Wt_o u_o = Wt_f u_f = \underbrace{Wtu = Wt_n V_r} \qquad \textbf{\textit{(6)}}$$

Thus;

$$u = \frac{t_n}{t} V_r \qquad \textbf{\textit{(7)}}$$

When the equation of continuity is satisfied, then;

$$\frac{\partial u}{\partial x} + \frac{\partial v}{\partial y} = 0 \qquad \textbf{\textit{(8)}}$$

Substitute eq. ***(7)*** in **eq. *(8)*,** thus;

$$\frac{\partial}{\partial x}\left(\frac{t_n}{t}V_r\right)+\frac{\partial v}{\partial y}=0 \qquad \textbf{\textit{(9)}}$$

After some arrangement the **eq.** ***(9)*** gives;

$$dv=\frac{t_n}{t^2}V_r\,\frac{dt}{dx}dy \qquad \textbf{\textit{(10)}}$$

After integration **eq.** ***(10)*** becomes;

$$v=\frac{t_n}{t^2}V_r\,\frac{dt}{dx}y \qquad \textbf{\textit{(11)}}$$

where (dt/dx) is the slope of the arc of contact at any (x).

In the present study for the second case, the deformation heat is distributed in the strip in proportion to the local effective strain rate and same as that distributed in **(Tseng 1984);**

$$\varepsilon_{eff}=\sqrt{(\varepsilon_x)^2+(\varepsilon_y)^2} \qquad \textbf{\textit{(12)}}$$

Or;

$$\varepsilon_{eff}=\sqrt{\left(\frac{\partial u}{\partial x}\right)^2+\left(\frac{\partial v}{\partial h}\right)^2} \qquad \textbf{\textit{(13)}}$$

In general, the deformation heat is proportional to both the strain rate and the flow stress, then;

$$Q_d\propto\varepsilon_{eff}\sigma_s)_{flow} \qquad \textbf{\textit{(14)}}$$

where (Q_d) is the deformation heat generation (Kw); (ε_{eff}) is the strip effective strain rate (1/s) and ($\sigma_s)_{flow}$) is the strip flow stress (N/cm^2).

The distribution assumed in **eq.** ***(14)*** implies that the flow stress variation is small compared with very large strain rate as predicted by (Zienkiewicz *et al.* 1981) and **(Tseng 1984),** then;

$$Q_d\propto\varepsilon_{eff} \qquad \textbf{\textit{(15)}}$$

Substitute **eq.** ***(8)*** with (y=h) and ***(7)*** in **eq.** ***(13)***, then;

$$\varepsilon_{eff}=\sqrt{2}\,\frac{\partial}{\partial x}\left(\frac{h_n}{h}V_r\right) \qquad \textbf{\textit{(16)}}$$

After differentiation the **eq.** ***(16)***, then;

$$\varepsilon_{eff}=-\sqrt{2}\,\frac{h_n}{h^2}V_r\,\frac{dh}{dx} \qquad \textbf{\textit{(17)}}$$

where (h_n) is the half thickness of the strip at the neutral point.

In the present study for the second case, the friction heat is distributed along the interface in proportion to the magnitude of the slip (relative velocity) between the roll and the strip as shown in **Fig**. **5**, then;

$$Q_{fr} \propto V_{slip} \tag{18}$$

where (Q_{fr}) is the heat generation by friction (kW).

It is well known from **Fig. 8** that the slip velocity is;

$$V_{slip} = \left| V_r - \sqrt{u^2 + v^2} \right| \tag{19}$$

As well as, the heat generated by deformation and friction for the first case study is assumed to be uniformly distributed in the bite and interface.

The input data of the heat generation by deformation and friction will be obtained from direct measurement of the power (**Table 1**) and it is considered in the present study.

As shown by **(Tseng 1984),** before entering and after exit the strip into and from the roll bite, the strip loses heat to the coolant by convection, see **Fig. 6**, then;

$$-k_s \frac{\partial T_s}{\partial n} = H_\infty (T_s - T_\infty) \tag{20}$$

In the present study and in **(Dieter 1986 and Tseng 1984),** since the strip velocity is high, the conduction term, ($\partial^2 T_s / \partial x^2$) becomes small in comparison with the convection term, ($u\,\partial T_s / \partial x$). Thus the billet temperature should be the initial strip temperature (T_o).

The boundary condition as shown by **(Tseng 1984)** at some distance downstream from the exit contact point may be assumed to be;

$$\partial T_s / \partial x = 0 \tag{21}$$

As showed by **(Tseng 1984)** because of the symmetry, the lower horizontal boundary having;

$$\partial T_s / \partial y = 0 \tag{22}$$

The boundary condition for the roll circumference is;

$$-k_r \frac{\partial T_r(R,\theta)}{\partial r} = H(\theta)\{T_r(R,\theta) - T_\infty\} \tag{23}$$

where ($H(\theta)$) is the heat transfer coefficient explained previously.

Since the roll is rotate rapidly, and all temperatures vary within a very thin layer near the surface, only a thin layer needs to be modeled. The interior boundary condition as shown by **(Tseng 1984)** becomes;

$$\partial T_r\left((R-\delta),\theta\right)/\partial r = 0 \qquad \textbf{\textit{(24)}}$$

The strip is assumed to be in contact the roll and each moves relative to the other, creating the friction heat along the interface. Mathematically, as shown by **(Tseng 1984)** this boundary condition may be expressed as;

$$k_s\left(\frac{\partial T_s}{\partial n}\right)_b + k_r\left(\frac{\partial T_r}{\partial n}\right)_b - q_{fr} = 0 \qquad \textbf{\textit{(25)}}$$

where ($\partial/\partial n$) represents differentiation along the normal of the boundary (positive outward); see **Fig. 9**; and (q_{fr}) is the friction heat generated along the interface and the subscript (b) refers to the boundary. All special derivatives for the points at the interface must be formulated using points located in their respective sides as follows;

$$k_s\left(\frac{\partial T_s}{\partial n}\right)_b = q_1 + q_2 \qquad \textbf{\textit{(26)}}$$

Then, from **Fig. 7**;

$$\sin\beta_o = \frac{q_2}{k_s\left(\frac{\partial T_s}{\partial y}\right)_b},\ \cos\beta_o = \frac{q_1}{k_s\left(\frac{\partial T_s}{\partial x}\right)_b} \qquad \textbf{\textit{(27)}}$$

Substituting **eq.** ***(27)*** in **eq.** ***(26)***, thus;

$$k_s\left(\frac{\partial T_s}{\partial n}\right)_b = k_s\left(\frac{\partial T_s}{\partial x}\right)_b \cos\beta_o + k_s\left(\frac{\partial T_s}{\partial y}\right)_b \sin\beta_o \qquad \textbf{\textit{(28)}}$$

where the angle (β_o) specifies the direction as shown in **Fig. 7.**

Because the two bodies are in intimate contact, temperature equality at the interface is also assumed;

$$(T_s)_b = (T_r)_b \qquad \textbf{\textit{(29)}}$$

Replacing $(\partial T_s/\partial n)_b$ by the directional derivatives **eq.** ***(28)*** and $(\partial T_r/\partial n)_b$ by $(\partial T_r/\partial r)_b$ and from **Fig. 7**, **eq.** ***(25)*** becomes;

$$\left(\frac{\partial T_s}{\partial x}\right)_b \cos\beta_o + \left(\frac{\partial T_s}{\partial y}\right)_b \sin\beta_o + \frac{k_r}{k_s}\left(\frac{\partial T_r}{\partial r}\right)_b - \frac{q_{fr}}{k_s} = 0 \qquad \textbf{\textit{(30)}}$$

`NUMERICAL SOLUTION

In this article, the task of constructing the numerical method for solving the governing partial differential **eqs. *(1)*** and ***(2)***.

The essence of GFDM is its ability to obtain the needed derivative expression at a given point as a function of arbitrarily located neighboring points. As reported by **(Tseng 1984)** for any sufficiently differentiable function, *T(x,y)*, in a given domain has Taylor series expansion about a point (x_o,y_o) up to second order terms can be written as;

$$T_{si} = T_{so} + m_i\left(\frac{\partial T_s}{\partial x}\right)_o + n_i\left(\frac{\partial T_s}{\partial y}\right)_o + \frac{m_i^2}{2}\left(\frac{\partial^2 T_s}{\partial x^2}\right)_o + \frac{n_i^2}{2}\left(\frac{\partial^2 T_s}{\partial y^2}\right)_o + m_i n_i\left(\frac{\partial^2 T_s}{\partial x \partial y}\right)_o \qquad \textbf{\textit{(31)}}$$

where ($T_i=T(x_i,y_i)$, $T_o=T(x_o,y_o)$, $m_i=x_i-x_o$)and ($n_i=y_i-y_o$). Five independent equations, similar to **eq.** *(31)*, can be obtained by using five arbitrarily located neighboring points (x_i,y_i), $i=1,\ldots,5$, as shown in **Fig. 8.**

If the first special derivatives ($\partial T_s/\partial x \ldots \partial^2 T_s/\partial x\partial y$) at point (x_o,y_o) can computed in terms of the functional values at five neighboring points, see **Fig. 8**. In matrix form, as mentioned in **(Tseng 1984);**

$$\begin{bmatrix} m_1 & n_1 & m_1^2/2 & n_1^2/2 & m_1 n_1 \\ m_2 & n_2 & m_2^2/2 & n_2^2/2 & m_2 n_2 \\ m_3 & n_3 & m_3^2/2 & n_3^2/2 & m_3 n_3 \\ m_4 & n_4 & m_4^2/2 & n_4^2/2 & m_4 n_4 \\ m_5 & n_5 & m_5^2/2 & n_5^2/2 & m_5 n_5 \end{bmatrix} \begin{Bmatrix} \partial T_s/\partial x \\ \partial T_s/\partial y \\ \partial^2 T_s/\partial x^2 \\ \partial^2 T_s/\partial y^2 \\ \partial^2 T_s/\partial x\partial y \end{Bmatrix} = \begin{Bmatrix} T_{s1} - T_{so} \\ T_{s2} - T_{so} \\ T_{s3} - T_{so} \\ T_{s4} - T_{so} \\ T_{s5} - T_{so} \end{Bmatrix} \qquad \textbf{\textit{(32)}}$$

Or;

$$\lfloor A_{i,j} \rfloor \{DT_{sj}\} = \{T_{si} - T_{so}\} \qquad i\ ,j=1,2,\ldots,5 \qquad \textbf{\textit{(33)}}$$

Inverse of the matrix $[A_{i.j}]$ leads to;

$$\{DT_{si}\} = \lfloor B_{i,j} \rfloor \{T_{si} - T_{so}\} \qquad i\ ,j=1,2,\ldots,5 \qquad \textbf{\textit{(34)}}$$

where $[B_{i,j}]$ is the inverse of $[A_{i.j}]$. Rearranging **eq. *(34)*,** then;

$$\{DT_{si}\} = [B_{i,j}]\{T_{sj}\} \qquad i=1,\ldots,5,\ j=0,\ldots,5 \qquad \textbf{\textit{(35)}}$$

where;

$$B_{io} = -\sum_{j=1}^{5} B_{ij} \qquad \textbf{\textit{(36)}}$$

Finally the special derivatives at point (x_o,y_o) can be found as reported by **(Tseng 1984)** as;

$$\left(\frac{\partial T_s}{\partial x}\right)_o = \sum_{j=o}^{5} B_{1j} \quad T_{s\,j} \tag{37a}$$

$$\left(\frac{\partial T_s}{\partial y}\right)_o = \sum_{j=o}^{5} B_{2j} \quad T_{s\,j} \tag{37b}$$

$$\left(\frac{\partial^2 T_s}{\partial x^2}\right)_o = \sum_{j=o}^{5} B_{3j} \quad T_{s\,j} \tag{37c}$$

$$\left(\frac{\partial^2 T_s}{\partial y^2}\right)_o = \sum_{j=o}^{5} B_{4j} \quad T_{s\,j} \tag{37d}$$

Substituting the **eqs. *(36)*, *(37a)*, *(37b)*, *(37c)* and *(37d)*** in the strip governing **eq. *(1)*,** an algebraic approximation for each internal point was as reported by **(Tseng 1984);**

$$T_{so} = \frac{q_d \big/ \rho_s c_s - \sum_{j=1}^{5}\left(u_o B_{1j} + v_o B_{2j} - \alpha_s B_{3j} - \alpha_s B_{4j}\right)T_{sj}}{u_o B_{1o} + v_o B_{2o} - \alpha_s \left(B_{3o} + B_{4o}\right)} \tag{38}$$

For the boundary points, spatial care is required. Substituting **eq. *(30)*** with $\left(\partial T_r / \partial r\right)_b = \left(\left(T_{ro} - T_r\right) / \Delta r\right)$ and ($\Delta r = r_o - r_j$) into **eq. *(31)*,** from **eq. *(30)*** after the final substitution, eliminate $\left(\partial T_s / \partial x\right)_o$ or $\left(\partial T_s / \partial y\right)_o$. If ($\beta_o \neq 0$ or $\neq \pi$), keep $\left(\partial T_s / \partial x\right)_o$ and find;

$$T_{si} = \left(1 + a_1 n_i\right)T_{so} + \left(m_i + a_2 n_i\right)\left(\frac{\partial T_s}{\partial x}\right)_o + a_3 n_i + \frac{1}{2}\left(\frac{\partial^2 T_s}{\partial x^2}\right)_o m_i^2 + \frac{1}{2}\left(\frac{\partial^2 T_s}{\partial y^2}\right)_o n_i^2 + \left(\frac{\partial^2 T_s}{\partial x \partial y}\right)_o m_i n_i \tag{39}$$

where;

$$a_1 = \frac{k_r}{k_s \Delta r \sin \beta_o} \tag{40}$$

$$a_2 = -\cot \beta_o \tag{41}$$

$$a_3 = -\frac{1}{k_s \sin \beta_o}\left(\frac{k_r}{\Delta r} T_r + q_{fr}\right) \tag{42}$$

As reported by **(Tseng 1984),** upon providing four arbitrary selecting neighboring points, **Fig. 9**, four independent equations similar to **eq. *(39)*** can be obtained by following the procedure similar to that for treating the internal points, then;

$$[D_{ij}]\ \{DT_{sj}\} = \left\{f_i - T_{so}\right\} \qquad i, j = 1, \ldots\ldots, 4 \tag{43}$$

where;

$$D_{i1} = \frac{m_i + a_2 n_i}{1 + a_1 n_i}\ , \qquad D_{i2} = \frac{m_i^2}{2(1 + a_1 n_i)}\ , \qquad D_{i3} = \frac{n_i^2}{2(1 + a_1 n_i)}$$

$$D_{i4} = \frac{m_i n_i}{1 + a_1 n_i}\ , \qquad f_i = \frac{T_{si} - a_3 n_i}{1 + a_1 n_i}$$

and $\{DT_{si}\}$ is column matrixes containing the four derivatives of **eq. *(39)*.**

Again, inversion of $[D_{ij}]$ leads to;

$$\{DT_{si}\} = [E_{ij}]\{f_j\} \qquad i=1,\dots,4,\ j=0\dots,\ 4 \tag{44}$$

where $[E_{ij}]$ is the inverse of $[D_{ij}]$, $f_o=T_{so}$, and $E_{io} = -\sum_{j=1}^{4} E_{ij}$. Thus, the special derivatives at the boundary points, (x_o,y_o) become;

$$\left(\frac{\partial T_s}{\partial x}\right)_o = \sum_{j=0}^{4} E_{1j} f_j \tag{45a}$$

$$\left(\frac{\partial^2 T_s}{\partial x^2}\right)_o = \sum_{j=0}^{4} E_{2j} f_j \tag{45b}$$

And;

$$\left(\frac{\partial^2 T_s}{\partial y^2}\right)_o = \sum_{j=0}^{4} E_{3j} f_j \tag{45c}$$

Substituting **eq. (45a)** in **eq. (28)** and determining $(\partial T_s / \partial y)_o$, then;

$$\left(\frac{\partial T_s}{\partial y}\right)_o = a_2 \sum_{j=0}^{4} E_{1j} f_j + a_1 f_o + a_3 \tag{45d}$$

Substituting the **eqs. *(45a)*, *(45b)*, *(45c)* and *(45d)*** into strip governing **eq. *(1)*,** an algebraic relationship for the boundary point (x_o,y_o) was as reported by **(Tseng 1984);**

$$T_{so} = \frac{\sum_{j=1}^{4}\left[\alpha_s\left(E_{2j} + E_{3j}\right) - \left(u_o + a_2 v_o\right)E_{1j}\right]\left(T_{sj} - a_3 n_j\right)/\left(1 + a_1 n_j\right) - a_3 v_o + q_d / \rho_s c_s}{\left(u_o + a_2 v_o\right)E_{1o} + a_1 v_o - \alpha_s\left(E_{2o} + E_{3o}\right)} \tag{46}$$

Upwind scheme was employed to achieve numerical stability, then;

$$T_{si} = T_{so} + m_i\left(\frac{\partial T_s}{\partial x}\right)_o + n_i\left(\frac{\partial T_s}{\partial y}\right)_o \tag{47}$$

Two simultaneous equations were obtained by using two neighboring points (*1* and *2*). After rearranging these two equations into matrix form, then;

$$\left(\frac{\partial T_s}{\partial x}\right)_o = \sum_{j=0}^{2} F_{1j} T_{sj} \tag{48a}$$

$$\left(\frac{\partial T_s}{\partial y}\right)_o = \sum_{j=0}^{2} F_{2j} T_{sj} \tag{48b}$$

Substitute the **eqs. *(60a)*** and ***(60b)*,** and those in **eqs. *(49c)*** and *(49d**)*** to the strip governing **eq. *(1)*,** the first upwind GFDM equation for each internal point was as reported by **(Tseng 1984);**

$$T_{so} = \frac{q_d/\rho_s c_s - \sum_{j=1}^{2}\left(u_o F_{ij} + v_o F_{2j} - \alpha_s B_{3j} - \alpha_s B_{4j}\right)T_{sj} + \alpha_s \sum_{j=3}^{5}\left(B_{3j} + B_{4j}\right)T_{sj}}{u_o F_{1o} + v_o F_{2o} - \alpha_s\left(B_{3o} + B_{4o}\right)} \tag{49}$$

For the typical boundary condition described in **eq. *(30)*,** and using the same notations as in **eqs. *(39)*** and ***(43)*** for (a_i and f_j), respectively, point (*1*) is again to be an upwind point, **Fig. 9**, then;

$$T_{si} = \left(1 + a_1 n_i\right)T_{so} + \left(m_i + a_2 n_i\right)\left(\frac{\partial T_s}{\partial x}\right)_o + a_3 n_i + (all\ terms = 0) \tag{50}$$

Or;

$$\left(\frac{\partial T}{\partial x}\right)_o = \sum_{j=0}^{1} G_j f_j \tag{51}$$

And;

$$\left(\frac{\partial T}{\partial y}\right)_o = a_2 \sum_{j=0}^{1} G_j f_j + a_1 f_o + a_3 \tag{52}$$

where $G_1 = -G_o = \left(1 + a_1 n_1\right)/\left(m_1 + a_2 n_1\right)$.

Substitute the **eqs. *(51)*, *(52)*, *(45b)*** and ***(45c)*** into strip governing **eq. *(1)*,** an upwind GFDM relationship for a boundary point (x_o,y_o) was as reported by **(Tseng 1984);**

$$T_{so} = \frac{\alpha_s \sum_{j=1}^{4}\left(E_{2j} + E_{3j}\right)f_j - \left(u_o + a_2 v_o\right)G_1 f_1 - a_3 v_o + q_d/\rho_s c_s}{\left(u_o + a_2 v_o\right)G_o + a_1 v_o - \alpha_s\left(E_{2o} + E_{3o}\right)} \tag{53}$$

The roll governing eq. ***(2)***, is approximated by using second order central differencing for the conduction terms (right side) and first order up wind differencing for the convection terms (left side).

The temperature profile becomes identical in a plot of normalized temperature, $T_r^* = H_o(T_r - T_\infty)/q_o$, against, $r^* = r/R$, which will certainly simplify further parametric study and high accuracy.

Then, in dimensionless form the roll governing **eq. *(2)*** becomes;

$$\frac{1}{r_o^*}\frac{\partial T_r^*}{\partial r^*} + \frac{1}{r_o^{*2}}\frac{\partial^2 T_r^*}{\partial \theta^2} + \frac{\partial^2 T_r^*}{\partial r^2} = Pe\frac{\partial T_r^*}{\partial \theta} \tag{54}$$

where the superscript (*) refers to the dimensionless quantity.

By using four arbitrary located neighboring points as shown in **Fig.10**, then the roll governing eq. ***(2)*** becomes;

$$\frac{T_{r4}^* - 2T_{ro}^* + T_{r2}^*}{\Delta r^{*2}} + \frac{1}{r_o^*}\frac{T_{r4}^* - T_{r2}^*}{2\Delta r^*} + \frac{1}{r_o^{*2}}\frac{T_{r3}^* - 2T_{ro}^* + T_{r1}^*}{(2\Delta\theta)^2} = Pe\frac{T_{ro}^* - T_{r1}^*}{\Delta\theta} \tag{55}$$

Rearranging the above equation, an algebraic approximation for roll internal nodes is;

$$T_{ro}^* = \left\{a_{r1}T_{r1}^* + a_{r2}T_{r2}^* + a_{r3}T_{r3}^* + a_{r4}T_{r4}^*\right\}/a_{ro} \tag{56}$$

where;

$$a_{r1} = \frac{1}{\left(2r_o^*\Delta\theta\right)^2} + \frac{Pe}{\Delta\theta}\,, \qquad a_{r2} = \frac{1}{\left(\Delta r^*\right)^2} + \frac{1}{2r_o^*\Delta r^*}\,, \qquad a_{r3} = \frac{1}{\left(2r_o^*\Delta\theta\right)^2}$$

$$a_{r4} = \frac{1}{\left(\Delta r^*\right)^2} + \frac{1}{2r_o^*\Delta r^*}\,, \qquad a_{ro} = \frac{Pe}{\Delta\theta} + 2\left(\frac{1}{\left(2r_o^*\Delta\theta\right)^2} + \frac{1}{\left(\Delta r^*\right)^2}\right)$$

RESULTS AND DISCUSSION

This article presents the numerical results of the present work, besides, a verification of the computational model will also be made.

Fig. 11 show the horizontal component of velocity for the first case study. In the billet region, the strip has velocity (u) only, i.e., (v=0). Since equal volumes of metal must pass at any vertical section through the roll gap and the vertical elements remain undistorted (no increase in width), **eq. *(13)*** requires that the exit velocity must be greater than entrance velocity, therefore, the velocity (u) of the strip must be steadily increased from entrance to exit. the exit product region having (u) velocity only, i.e., (v=0).

The vertical component of velocity (v) for the first case study and for different lines are shown in **Fig.12**. In the billet, the streamlines are horizontal and having horizontal component of velocity (u) only and (v=0). After entering the bite the streamlines have curved shapes and the slopes of these curves gradually decrease from entrance to exit. Then the velocity (v) gradually diminishes from entrance to exit as shown in **eq. *(11)*** and in **Figs.12**. The horizontal and vertical components of the velocity for the second case study are similar to those in the first case but the different in the elevations

As mentioned by many authors such as **(Tseng 1984)** and **(Lahoti *et al.* 1978),** rolling a mild steel as shown in **Table 1,** consume about (90) percent of the total power in the deformation of the strip and in the friction loss at the interface. Moreover, according to **(Zienkiewicz *et al.* 1981)** and **(Tseng 1984)** who measured both the plastic work and the temperature rise in a tensile experiment. It was found that for steels, copper and aluminum, the heat rise represents (86.5, 90.5-92 and 95) percent, respectively, of the deformation energy which is converted into heat.

In the present study, this (90) percent estimated is used, i.e., that (6.5) percent of (90) percent of total power is dissipated as friction heat along the interface.

The resulting values of the heat generation by deformation and friction were summarized in the **Table 2** for the first and second case study. In the first case, the heat generation by deformation and friction are distributed. In the second case, the heat generation by deformation is then distributed to the strip in proportion to the local effective strain rate as shown in **eqs. *(15)*** and ***(17)*** and **Fig.13**. Note that the highest strip deformation (strain rate) occurs near the bite entry and diminishes monotonically toward the end of the bite as shown in **Fig.13.** Thus, the highest heat generation by deformation occurs near the bite entry too and diminishes monotonically toward the end of the bite as shown in **eq. *(19)*** and **Fig. 13.**

Also, the strip is to be moved relative to the roll creating friction heat along the interface as recorded in **eq. *(19),*** i.e., the friction heat is then distributed in proportion to the (relative velocity between the strip and roll as recorded in **eq. *(18)*** and in **Fig.14**. The maximum slip occurs at the first point of contact at the interface because the roll draws the thick strip into the bite. Then, the slip velocity decreases gradually until sticking at the final point of contact as shown in **Fig. 14.**

Figs.15 and **16**, indicate that the roll temperature variations are limited within a very thin layer, about (1) percent of the radius, which consistent with the associated boundary condition eq. ***(24)***. The surface temperature rapidly increases at the bite due to great heat generated by the friction and transferred from the strip. As the roll leaves the bite, the roll surface temperature immediately decreases due to heat convected to the coolant and heat conducted into the immediate sub surface layer.

As well as, as shown in **Figs. 15** and **16** the different in temperatures between the final and initial points of contact for the first case study is less than for the second case. This means, using several small coolant sprays (second case) is more efficient than one large spray (first case).

Figs. 17 and **18** indicate that while the strip is under deformation, the bulk temperatures inside the strip increase continuously; this is largely controlled by the deformation energy. On the other hand, the strip surface temperature changes much more drastically and it is mainly controlled by the friction heat and the roll temperature.

The coolant heavily cools the roll; it acts like a heat sink. Thus, as soon as the strip hits the roll its surface temperature drops as shown in **Figs. 17** and **18**. Since considerable friction and deformation heat are created along the interface and transferred from the neighboring sub layer, the surface temperature picks up rapidly.

Beyond the bite, **Figs.17** and **18**, the strip temperature tends to be uniform. In this region, the heat convected to the air has been assumed to be negligible. For high-speed rolling (rather than the considered limits), the product temperature behaves parabolically rather than elliptically as implied by **eq. *(1)*.** In other words, the boundary conditions that are assumed in the product should not have a noticeable effect on the bite region.

The interface heat fluxes results for uniform and non-uniform heat generation distributions are shown in **Figs.19** and **20**. At the initial contact stage, as anticipated, a very large amount of heat is transferred to the roll. In fact, the roll surface temperature is about (25 ^{o}C and 11.0362 ^{o}C) lower than that of the strip as shown in **Figs. 15, 16, 17** and **18.**

To satisfy the boundary condition **eq. *(29),*** a step change of surface temperatures are expected to occur at the initial contact point (*x=0*). The induced heat flux to the roll at (*x*=0) as shown in **Figs. 19** and **20**, also ensure the above findings that a large amount of heat is transferred to the roll from strip and the interface friction at the initial contact stage.

It is believed that in the previous studies, the strip initial temperatures were close to that of the roll. Therefore, the strip is not expected to have a temperature drop at the initial contact stage. However, it is note worthy that at very high rolling speeds, measuring the local temperature change in the bite could be a big challenge as mentioned previously in **(Tseng 1984).**

In hot rolling, the strip is normally rolled at elevated temperatures at which re-crystallization proceeds faster than work hardening. In addition, the hot strip is generally rolled at thicker gages and lower speed than that of the cold strip.

The gages specified in the first case are still suitable for hot rolling. Two focuses are considered. The first focuses on the effect of changing the entering temperature to (900 ^{o}C). The second, changing velocity by slowing the roll speed from (1146.6 to 573.3 cm/s). The other operating conditions are similar to those discussed for cold rolling.

Fig. 21 depicts the roll temperature distribution for the two hot rolling cases consider (V_r=1146.6 and 573.3 cm/s). A comparison of **Fig.21** with **Fig.17** indicates that the temperature profile between the hot and cold rolling is mainly in magnitude but not in shape.

Both the interface heat flux and speed govern the temperature magnitude. As shown in **Fig. 22** at speed of (1146.6 cm/s), the heat flux increases about four times for the hot to cold rolling. The corresponding increase of temperature is also found to be about four times too as shown in **Fig. 21.**

Fig. 21 shows except in the bite region, the roll temperature is reducing about (15) percent with the speed slowed to (50) percent, and the different in the bite region is much smaller and the maximum temperature occurs at the end the arc of contact. For example, the corresponding decrease of the peak temperature is less than (2) percent. The temperature decrease due to slowing the speed is mainly due to decrease of the heat flux **Fig. 22**.

Figs. 21 and **23** also show that near the bite, very large temperature variations are within a very thin layer. The layer thickness (δ), consistent with the previous finding, is dependent on the speed, or more precisely, the roll Peclet number as shown in **eq.** ***(3).***

The strip temperatures for the two hot rolling cases are presented in **Fig. 24**. In the bite region, the strip temperature, similar to the roll temperatures, is not noticeably affected by changing the speed within the range consider. In the down stream region ($x>x_o$), the strip center temperature drops faster in the slower strip. By contrast, the surface temperatures are not sensitive to the speeds considered. This figure also indicates the temperature drop in the initial contact stage is much large than its counterpart for the clod strip, as shown in **Fig. 24**. When the strip entry temperature rises from (65.6 ^{o}C) to (900 ^{o}C) from cold to hot rolling, the temperature drop increases approximately from (25 ^{o}C) to (649 ^{o}C), reflecting the great increase in the temperature different between the strip and roll a head of the bite.

The shape of the heat input distribution to the roll (q_r) governs the roll and strip temperatures in the roll gap region. As shown in **Figs.18** and **23** with a parabolic distribution of (q_r) of the second case study, the location of the maximum temperature shifts to the interior of the arc of contact (heating zone). Although, the cumulative energy input is still increasing beyond ($\Phi/2$), the flux is decreasing, yet the effect of the type of heat distribution on the temperature distribution away from the roll gap should be minimal as shown in **Figs 21** and **23.**

CONCLUDING REMARKS

1. While the heat generation by deformation occurs in the strip or by friction at the strip-roll interface and the heat removal is at the roll surface, then, both strip and roll should be considered together and solved simultaneously.

2. The highest heat generation by the deformation and friction occurs at the entrance to the bite and diminishes gradually toward the end of the bite.

3. The results show that the extremely large temperature drop at the interface and large temperature variation in both roll and strip are found. Such high temperature variations could create very large (δ) thermal stresses within the thin layer and this stresses lead to the roll wear or roll failure, then proper control of this stresses could significantly extend the roll life.

4. Several small coolant sprays (second case) are more efficient than one large spray (first case).

5. The temperature decreases due to slowing the roll speed. This is mainly due to decrease the total input power that led to decrease of the heat flux at the interface.

6. The shape of the heat input distribution (uniform or parabolic heat input) to the roll governs the location of the peak temperature.

Finally, the comparison of the present results with published findings by (Tseng 1984) shows that the computational scheme used is effective and reliable. However, it is believed that the greatest uncertainty in analysis will arise not from the numerical scheme, but from the input data, in particular, the friction energy, the location of the neutral point (or the forward slip), and the heat transfer coefficient of coolant.

Table 1 : Operational Parameters for the First and Second Case Studies.

Operational Parameters	First Case, for Coil 45, Tseng 1984.	Second Case, for Coil 32, Tseng 1984
Strip Material.	Mild Steel.	Mild Steel.
Roll Material.	Cast Steel.	Cast Steel.
Coolant.	Water.	Water.
Entry Gauge.	0.15 cm.	0.085 cm.
Exit Gauge.	0.114 cm.	0.057 cm.
Roll Speed.	1146.6 cm/s.	1219 cm/s.
Forward Slip.	0	0
Strip Width.	63.5 cm.	81.3 cm.
Roll Diameter.	50.8 cm.	50.8 cm.
Total Input Energy.	3694 kW.	3340 kW.
Strip Entry Temperature.	65.6 ^{o}C.	65.6 ^{o}C.

Both the roll and the strip have the following thermal properties: -

Thermal conductivity (k_r, k_s); 0 .4578 W/cm.^{o}C

Thermal diffusivity (α_r ,α_s); 0.1267 cm^2/s

Table 2 : Amounts of the Heat Generation by Deformation and Friction.

Case Number	Heat Generation by Plastic Deformation Q_d (kW)	Heat Generation by Friction Q_{fr} (kW)
١st	٢٤٥٠	١٩٨
٢nd	٢٦٨٩	٢١٧

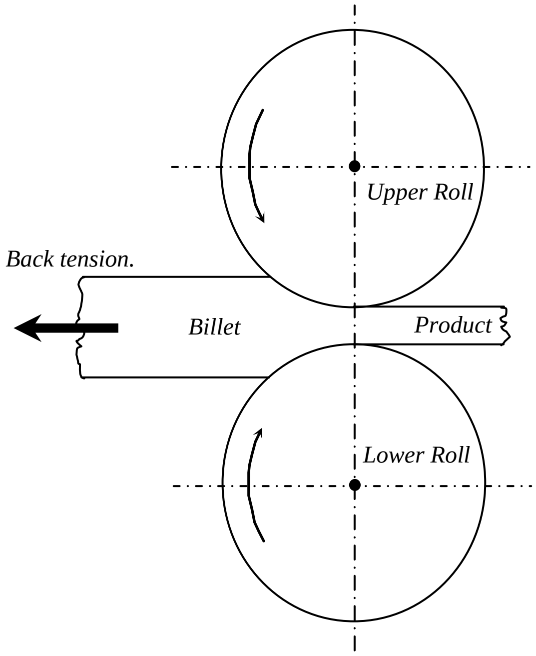

Fig. 1: Typical Arrangement of Rolls for Rolling Process.

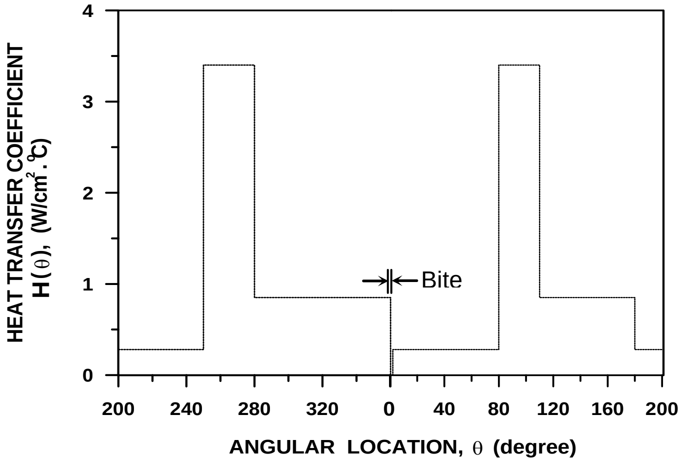

Fig. 2: Cooling Heat Transfer Coefficient, Tseng 1984

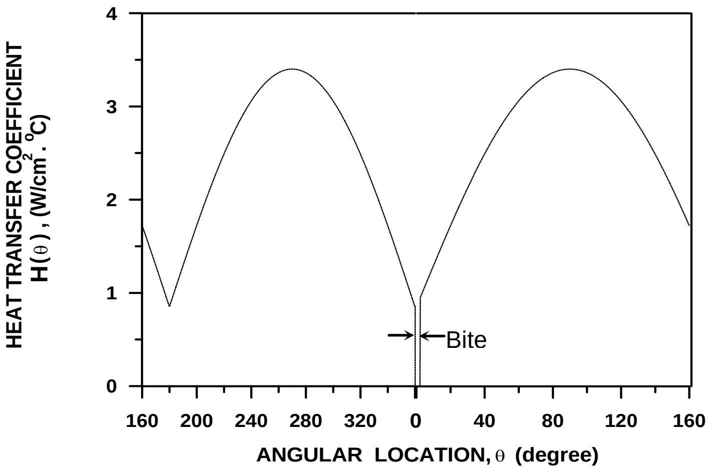

Fig. 3: Heat Transfer Coefficient that Varies as A Half Sine Curve,Patula 1981

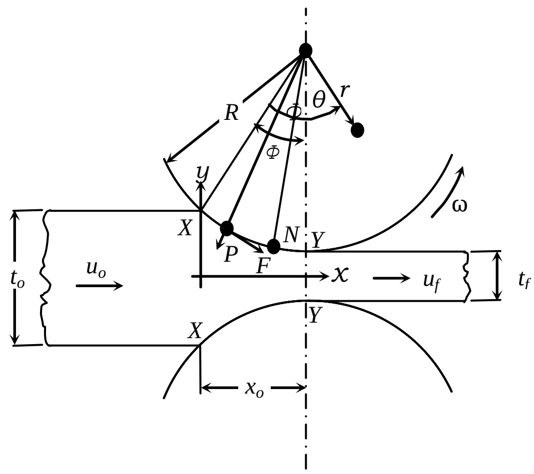

Fig. 4: Forces Acting During Rolling,Dieter 1986

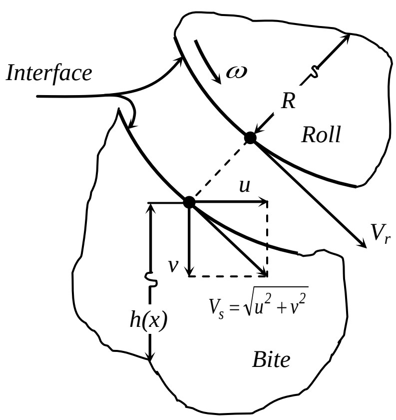

Fig. 5: The Relative Velocity between the Roll and Strip.

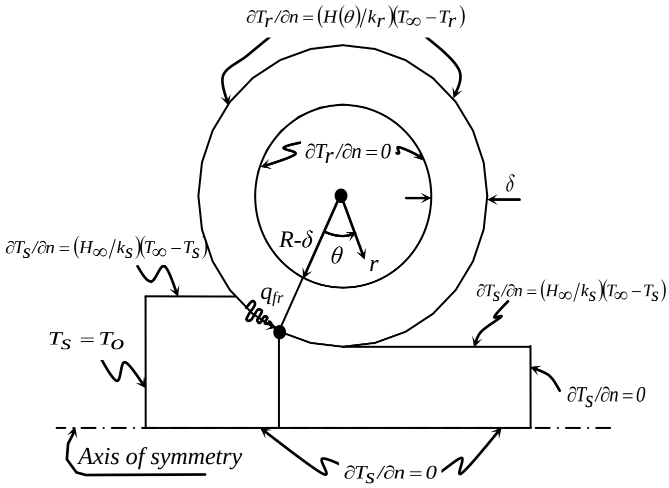

Fig. 6: Typical Boundary Conditions for Strip, Roll and Interface Region, Tseng 1984

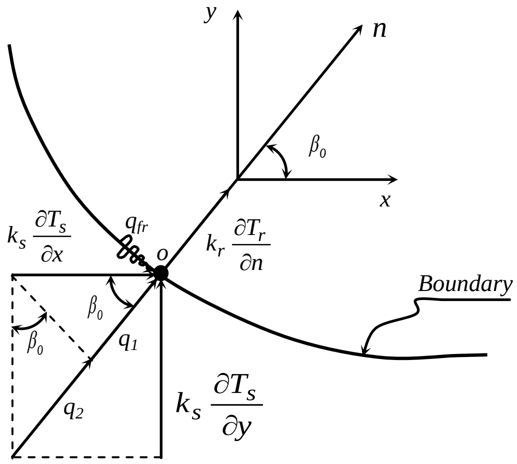

Fig. 7: The Components of Interface Heat Flux.

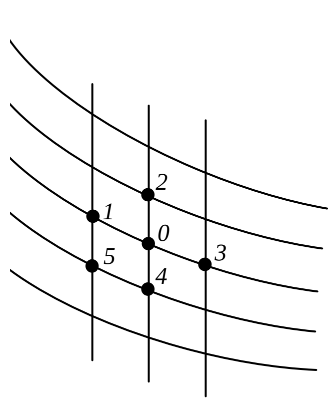

Fig. 8: The Grid Arrangement for the Strip Internal Nodes, Tseng 1984

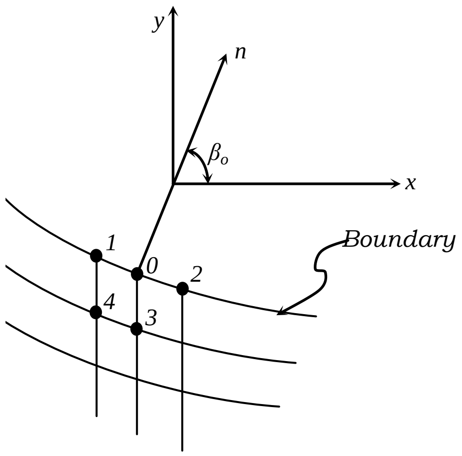

Fig. 9: The Grid Arrangement for the Strip Boundary (Interface) Nodes, Tseng1984

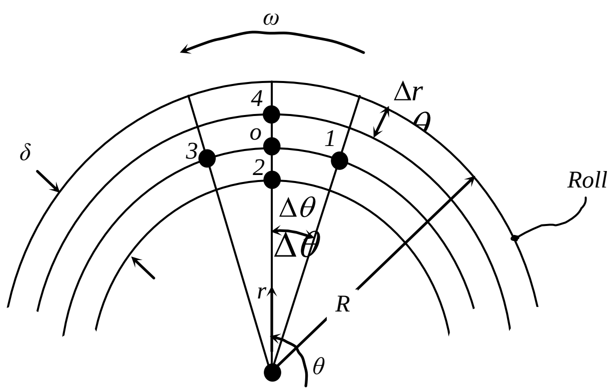

Fig. 10: Neighboring Points Arrangement for Roll Internal Nodes.

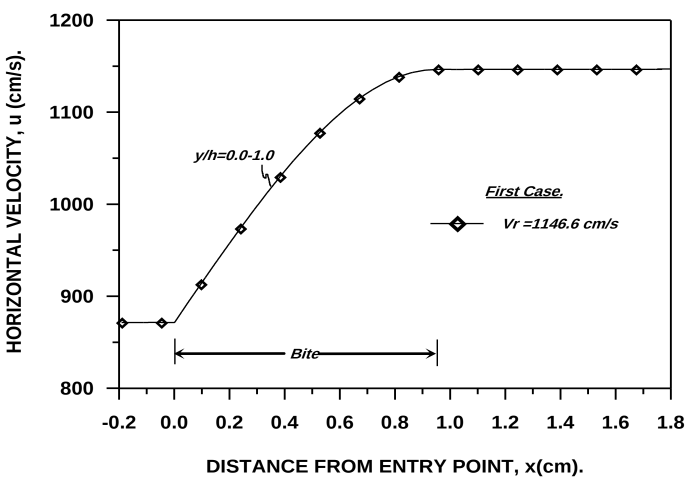

Fig. 11: Horizontal Component of Strip Velocity.

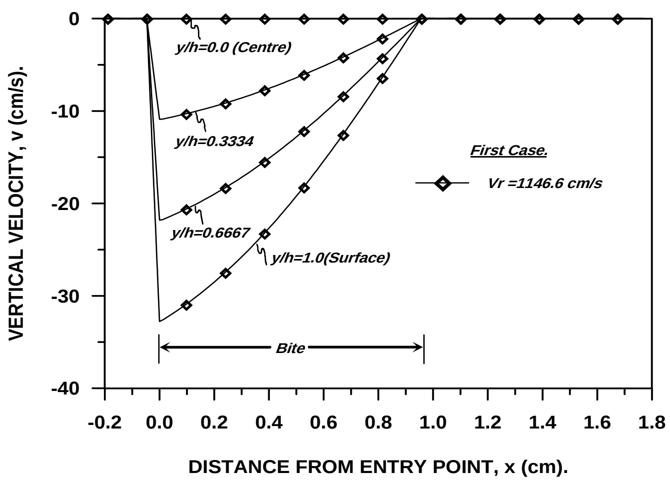

Fig. 12: Vertical Component of Strip Velocity.

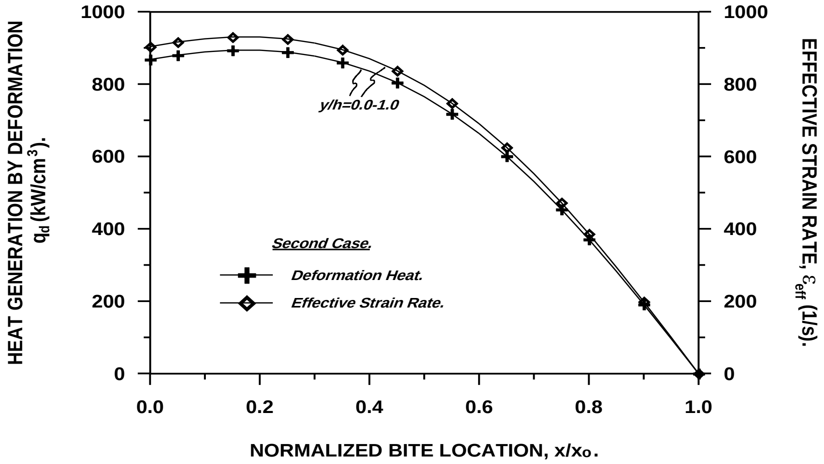

Fig. 13: Effective Strain Rate and Heat Generation by Deformation.

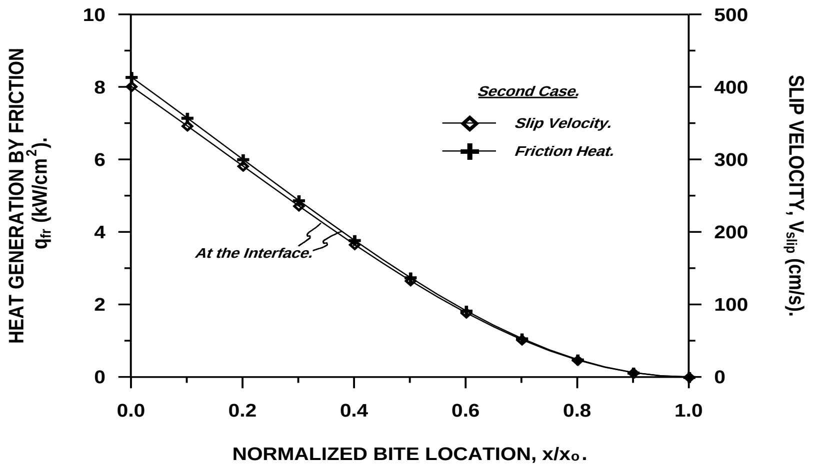

Fig. 14: Slip Velocity and Heat Generation by Friction.

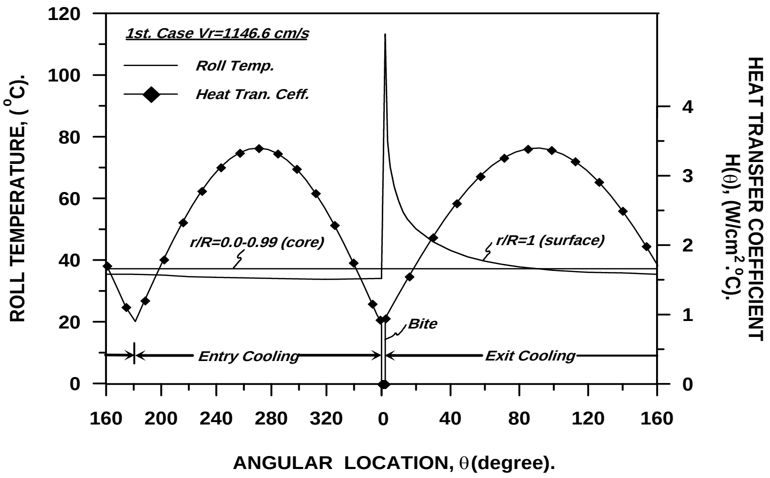

Fig. 15: Heat Transfer Coefficient and Roll Temperature for Cold Rolling Case.

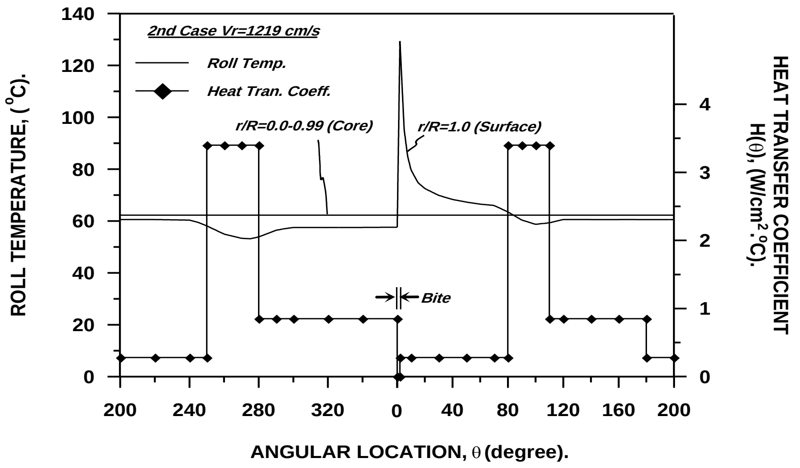

Fig. 16: Heat Transfer Coefficient and Roll Temperature for Cold Rolling Case.

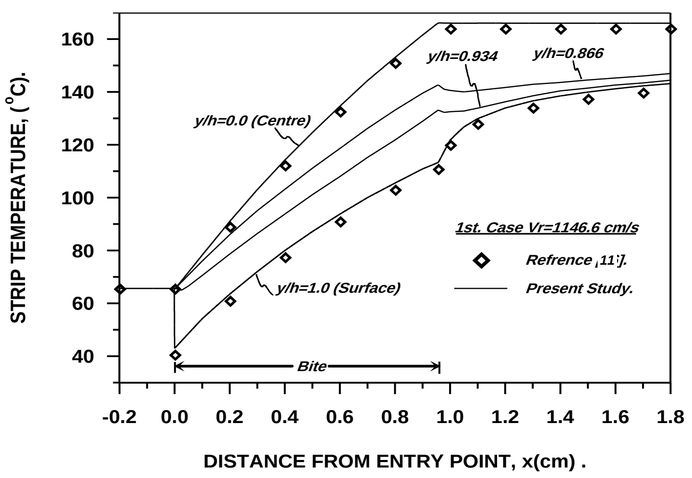

Fig. 17: Comparison of the Strip Temperature for Cold Rolling.

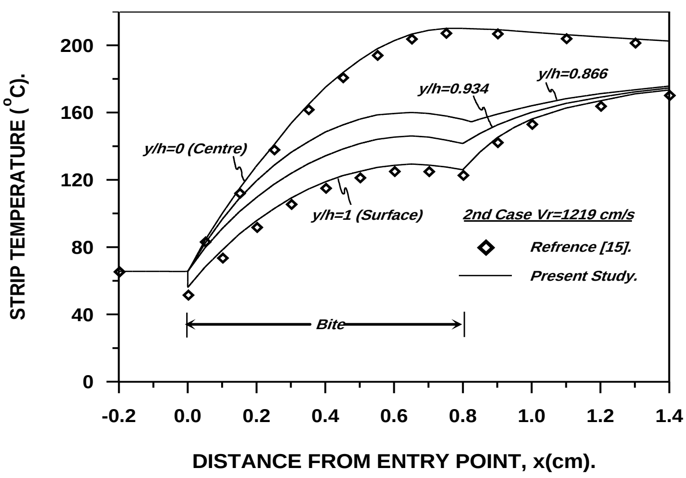

Fig. 18: Comparison of the Strip Temperature for Cold Rolling.

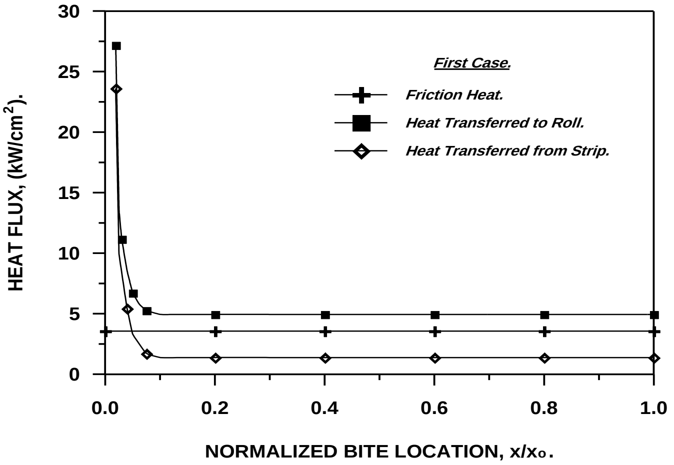

Fig. 19: Distributions of the Interface Heat Flux.

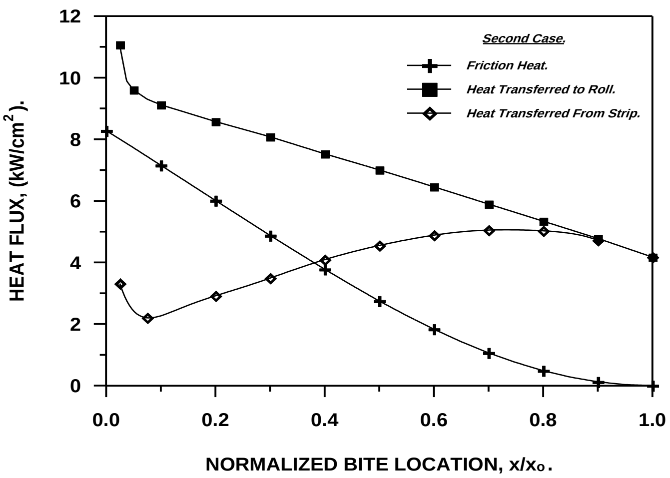

Fig. 20: Distributions of the Interface Heat Flux.

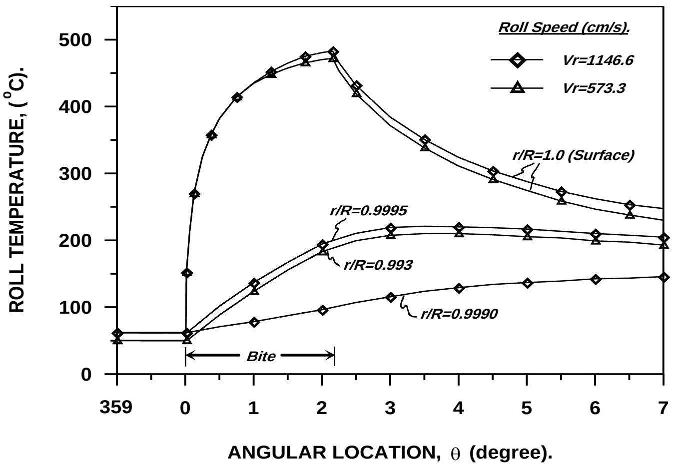

Fig. 21: Roll Temperature near the Bite for Hot Rolling Cases.

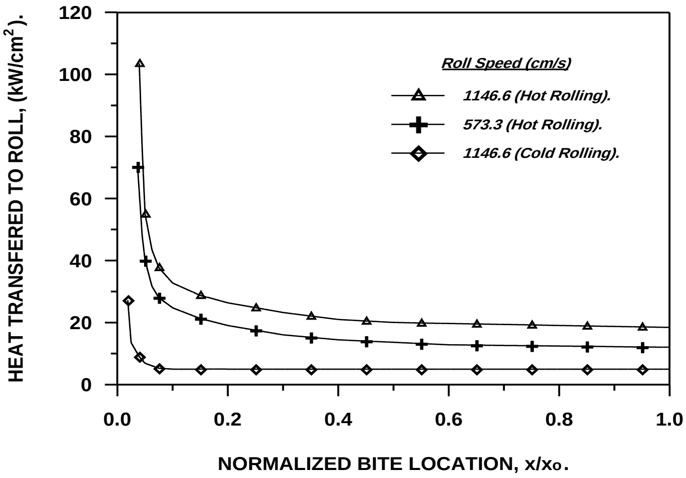

Fig. 22: Distributions of the Interface Heat Flux to Roll.

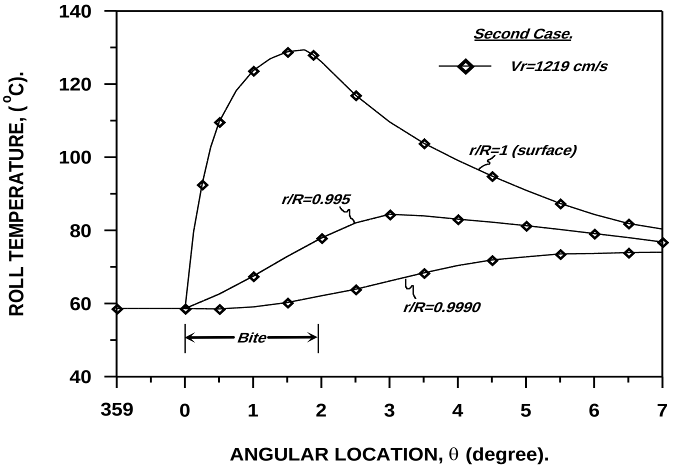

Fig. 23: Roll Temperature near the Bite for Cold Rolling Case.

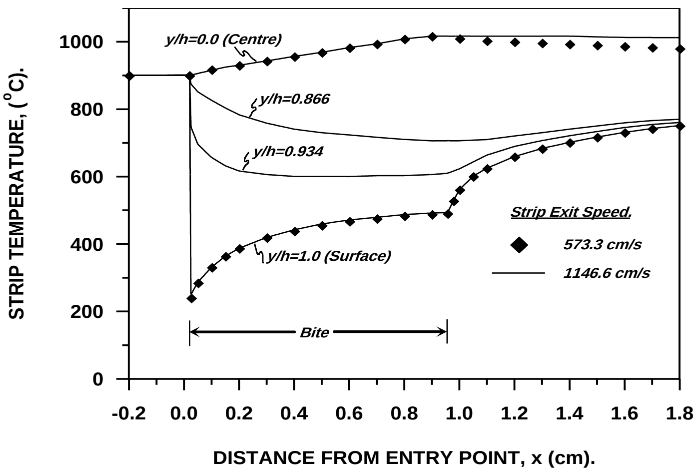

Fig. 24) Strip Temperature for Hot Rolling Cases.

REFERENCES

Bryant, G. F. and Heselton, M. O., ”*Roll Gap Temperature Models for Hot Mills*,” Metals Technology, 1982, Vol. 9, pp. 469-476.

Bryant, G. F. and Chiu, T. S. L., “*Simplified Roll Temperature Model (Spray Cooling and Stress Effects)*,” Metals Technology, 1982, Vol. 9, pp. 485-492.

Chang, D. F., “ *An Efficient Way of Calculating Temperatures in the Strip Rolling process*,” ASME, Journal of Manufacturing Science and Engineering, 1998, Vol. 120, pp. 93-100.

Dieter, “*Metals Metallurgy*,” Mc Graw-George, E-Hill Book, Dieter company, Third addition, 1986.

Johnson, W. and Kudo, H., “*The Use of Upper-Bound Solutions for the Determination of Temperature Distributions in Fast Hot Rolling and Axi-Symmetric Extrusion Process,”* International Journal of Mechanical Science, 1960, Vol. 1, PP. 175-191.

Karagiozis, A. N. and Lenard, J. G., ”*Temperature Distribution in A Slab During Hot Rolling*,” ASME, Journal of Engineering Materials and Technology, 1988, Vol. 110, pp.17-21.

Lahoti, G. D. and Altan, T., “*Predication of the Temperature Distribution in Axi-Symmetric Compression and Torsion*,” ASME, Journal of Engineering Materials and Technology, 1975, Vol. 97, pp.113-120.

Lahoti, G. D., Shah S. N. and Altan, T., ”*Computer Aided Heat Transfer Analysis of the Deformation and Temperatures in Strip Rolling*,” ASME, Journal of Engineering for Industry, 1978, Vol. 100, pp. 159-166.

Patula, E. T., “ *Steady-State Temperature Distribution in A Rotating Roll Subjected to Surface Heat Fluxes and Convective Cooling*,” ASME, Journal of Heat Transfer, 1981, Vol. 103, pp. 36-41

Remn-Min Guo, “ *Two Dimensional Transient Thermal Behavior of Work Rolls*,” ASME, Journal of Manufacturing Science and Technology, 1998, Vol. 120, pp. 28-33.

Sheppard, T. and Wright, D. S., ”*Structural and Temperature Variations During Rolling of Aluminum Slabs*,” Metals Technology, 1980, Vol. 7, pp. 274-281.

Tseng, A. A., “*A Numerical Heat Transfer Analysis of Strip Rolling,*“ ASME, Journal of Heat Transfer, 1984, Vol. 106, PP. 512-517.

Tseng, A. A., “*A Generalized Finite Difference Scheme for Convection Dominated Metal Forming Problems*,” International Journal for Numerical Methods in Engineering, 1984, Vol.20, pp. 1885-1900.

Tseng, A. A., Tong, S. X., Maslen, S. H. and Mills, J. J., “ *Thermal Behavior of Aluminum Rolling*,” ASME, Journal of Heat Transfer, 1990, Vol. 112, pp. 301-308.

Zienkiewicz, O. C., Onate, E. and Heinrich, J. C., “*A General Formulation for Coupled Thermal Flow of Metals Using Finite Elements*,” International Journal for Numerical Method in Engineering, 1981, Vol. 17, pp. 1497-1514.

NOMENCLATURE

Symbol	*Description*	*Unit*
Bi	Biot Number.	-
c	Specific Heat.	KJ/kg.^{o}C
F	Tangential Force.	N
H	Heat Transfer Coefficient.	W/m^2 .^{o}C.
h	Half Thickness of Strip.	m
k	Thermal Conductivity.	W/m.^{o}C
P	Pressure.	N/m^2
Pe	Peclet Number.	-
Q	Heat Generation.	kW
q	Heat Generation Rate, Heat Friction Rate.	kW/m^3 or

		kW/m^2
R	Roll Radius.	m
r, θ	Cylindrical Coordinate.	-
Re	Reynolds Number.	-
T	Temperature.	^oC
t	Thickness.	m
u, v	Horizontal and Vertical Velocity.	m/s
V	Velocity.	m/s
W	The Width of the Strip.	m
x,y	Cartesian Coordinate.	m

Abbreviations

CFDM	Conventional Finite Difference Method.	-
Coef.	Coefficient.	-
Eq.	Equation.	-
Fig.	Figure.	-
GFDM	Generalized Finite Difference Method.	-
Ref.	Reference.	-
Temp.	Temperature.	^oC
Tran.	Transfer.	-

Greek Symbols

α	Thermal Diffusivity.	m^2/s
ρ	Density.	kg/m^3
ω	Roll Angular Velocity.	rad/s
δ	Heat Penetration Depth.	m
Φ	Bite Angle.	Degree
σ	Plain Strain Yield Stress.	N/m^2
ε	Local Strain Rate.	1/s
β	Angle Specified the Direction.	Degree

MATHEMATICAL SIMULATION OF FLOW THROUGH HOLLOW FIBRE MEMBRANE UNDER CONSTANT HYDRAULIC CONDUCTIVITY

Riyadh Zuhair Al-Zubaidy
Asst. Prof.
Department of Water Resources Engineering, University of Baghdad

ABSTRACT

Distilled water flow through a virgin hollow fibre membrane, HFM is considered as steady nonuniform since the fibre's wall hydraulic conductivity coefficient is kept constant along the fibre and unchanged during the operation. Under these conditions, two well known laws were used to mathematically simulate the hydraulic flow through the HFM. These two laws are: the Darcy's Law, to simulate the flow thought the fibre wall, and the Hagen-Poiseuille's Law, to simulate the laminar flow through the fibre channel.

Laboratory measurements were carried out to provide necessary data for the calibration and verification of the mathematical model that was developed based on the Darcy's and Poiseuille's laws. A good agreement was obtained between the measured and predicted flowrate values under the same conditions.

The developed Mathematical model can be used as a tool to investigate the hydraulic performance of commercial HFM modules. A comparison was made between two commercially available of HFM modules of the same material but differ in the fibre sizes; it was found that there is a difference between its performance and the efficiency of the operation energy.

الخلاصة

عند استخدام ماء نقي فان الجريان في الأغشية الليفية المجوفة البكر يكون جريانا مستقرا لثبات الايصالية الهيدروليكية على امتداد الليف ولا تتغير إثناء التشغيل. في هذه الحالة أمكن استعمال قانونين معروفين لتمثيل الجريان خلال الأغشية الليفية المجوفة هما قانون دارسي لتمثيل الجريان خلال جدار الليف وقانون هايكن- بويزل لتمثيل الجريان الطباقي خلال قناة الليف.

أجريت قياسات مختبريه على الجريان خلال الأغشية الليفية المجوفة لتوفير البيانات الضرورية لمعايرة وبرهنة صحة عمل النموذج الرياضي المعد اعتمادا على قانوني دارسي وبويزل. كان التطابق جيد بين القياسات المختبرية وتلك المستنبطة من النموذج الرياضي تحت نفس الظروف.

يمكن استعمال النموذج الرياضي المعد كأداة لتحري الأداء الهيدروليكي للأغشية الليفية المجوفة التجارية. تمت مقارنة الأداء الهيدروليكي لمنتجين متوفرة تجاريا من الأغشية الليفيةمن نفس النوع مع اختلاف في ابعاد الليف ووجد إن هنالك اختلاف كبير في الأداء وفي كفاءة الطاقة اللازمة للتشغيل.

KEYWORDS : Hollow fibre membrane, Mathematical simulation, Mathematical Model

INTRODUCTION:

Hollow fibre membrane, HFM, shows a number of advantages over traditional water filtration technique which makes it attractive to potable water industry, with the high water quality produced using the HFM, which meets the stringent potable water regulations, makes the use of HFM to grow rapidly within the last decade.

Several different commercial HFM modules, used for microfiltration and ultrafiltration treatment of water, are available in the market. Even if they are made of the same material, they differ in their capacity, diameter and length of the fibre, number of fibres used, and pot length.

Many theoretical and experimental studies were carried out to evaluate the performance of the HFM and a number of mathematical models based on different hydraulic relations and simplification assumptions were developed.

The main objective of this study is to develop and verify a mathematical model to simulate the flow through the HFM under constant hydraulic conductivity based on the combination of Darcy's and Hagen-Poiseuille's Laws. The developed mathematical model with the solution procedure applied on computer is a useful tool for engineers to examine the performance of the HFM.

MATHEMATICAL SIMULATION OF THE FLOW THROUGH HFM

The mathematical simulation of steady flow through the HFM under constant hydraulic conductivity was developed based on two basic formulas governing the flow through the membrane wall and the fibre channel as described in the following sections.

Flow through HFM Wall

The flow through the HFM wall is a radial flow, **Fig. (1)**. An expression for the Darcy's law for redial flow through the wall of a fibre segment of ΔS length can be derived from the basic Darcy's formula by transforming its cartesian coordinate system into polar coordinate system, that is:

$$q = 2\pi \Delta S\, K \frac{TMB}{\ln(\frac{r_t}{r_n})} \tag{1}$$

Where

q = volumetric flowrate, L^3/T,

K= hydraulic conductivity of the porous media, L/T,

TMP = transmembrane pressure head, L,

K= hydraulic conductivity of the porous media, L/T,

r_t= fibre outer radius, L, and

r_n= fibre inner radius, L.

The hydraulic conductivity, K, is a measure of the ability of water to flow through a porous medium. It depends on the fluid properties and the porous medium properties through the intrinsic permeability.

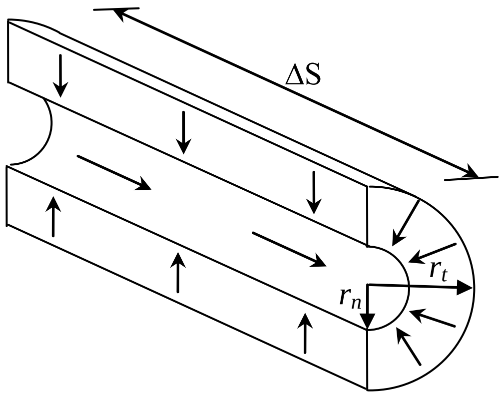

Fig. (1). Schematic diagrams of longitudinal cross sections along a HFM.

The Head Losses through HFM Channel

The head loss along the HFM channel segment can be estimated based on Poiseulle's Law for laminar flow. Poiseulle's Law in term of pressure head along a HFM channel segment of ΔS length may be written as:

$$h_l = \frac{8q\mu\Delta S}{\rho g\pi r_n^4} \tag{2}$$

In which:
h_l = head loss, L,
g = gravitational acceleration, L/T^2,
L = circular channel segment length, L,
μ= water viscosity, M/ (L.T), and
ρ = water density, M/L^3.

APPLICATION OF DARCY'S AND POISEULLE'S LAWS TO THE FLOW OF HFM

Fig. (2) shows a schematic diagram of a single HFM in an actual fibre module. The pot length, L_{pot}, is required to seal the fibres by using a special sealant of molding thermoplastic material so that all the flowrate of the module will be thought the fibre channels outlets only.

The fibre has two outlets at both ends that mean that flow of the fibre membrane module is symmetrical. Therefore, the flowrate calculations will be carried out on one half of the fibre and is doubled for actual fibre flowrate.

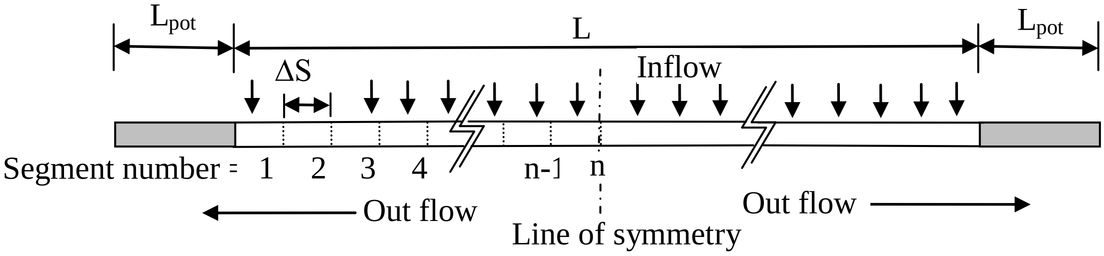

Fig.(2). A schematic diagram of a HFM in an actual module.

By dividing the fibre membrane length under consideration into n equal segments of a length equal to ΔS, then **Eq. (1)** is used to calculate the flowrate through segment as:

$$q_1 = 2\pi \Delta S\, K \frac{TMB_1}{\ln(\frac{r_t}{r_n})} \tag{3}$$

By assuming the fibre segments, Δ*S*, is short enough so that variation of transmembrane pressure, *TMP*, between the two ends of each segment is considered small and is neglected. The *TMP* throughout 1st segment may be written as:

$$TMP_1 = h_{ap} - hl_{pot} \tag{4}$$

In which:
h_{ap} = applied pressure head, L, and
hl_{pot}= head loss through the pot length, L.

The head loss throughout the fibre channel along the pot length may be calculated by applying Poiseulle's Law, **Eq. (2)**, that is:

$$hl_{pot} = \frac{8(q_1 + q_2 + \dots\dots\dots + q_n)\mu L_{pot}}{\rho g \pi r_n^4} \tag{5}$$

Where L_{pot} is the pot length, L.
Now, The expression for flowrate through 1st segment, **Eq. (3)**, may be written as:

$$q_1 = \frac{2\pi \Delta S\, K\, (h_{ap} - \frac{8(q_1 + q_2 + \dots\dots\dots + q_n)\mu L_{pot}}{\rho g \pi r_n^4})}{\ln(\frac{r_t}{r_n})} \tag{6}$$

Rearranging and rewriting

$$(C_2 + 1)q_1 + C_2(q_2 + q_3 + \dots\dots + q_n) - C_1 = 0 \tag{7}$$

In which

$$C_1 = 2\pi \Delta S\, K \frac{h_{ap}}{\ln(\frac{r_t}{r_n})} \tag{8}$$

and

$$C_2 = 16 \Delta S\, K L_{pot} \frac{\mu}{\rho g r_n^4 \ \ln(\frac{r_t}{r_n})}$$

(9)

In general, **Eq. (7)** may be written as:

$$(C_2+1)q_1+C_2\sum_{i=2}^{n}q_i-C_1=0 \tag{10}$$

In which *i* is the segment number.

A similar expression can be obtained for the 2nd segment. The TMP along the segment can be written as:

$$TMP_1=h_{ap}-hl_{pot}-hl_1 \tag{12}$$

In which hl_1 is the head loss along the 1st segment, which may be obtained by using Poiseulle's Law, **Eq. (2)**, that is:

$$hl_1=\frac{8(0.5q_1+q_2+........+q_n)\mu\Delta S}{\rho g\pi r_n^4} \tag{13}$$

When calculating the head loss thought 1st segment, the flowrate thought is not fully developed it varies from o to q_1. Then it was assumed that the flowrate through the walls of this segment varies linearly along the segment and the average was taken to calculate the head loss. Then expression for flowrate through segment 1 may be written as:

$$q_2=-\frac{2\pi\Delta SK\left(h_{ap}-\frac{8(q_1+q_2+.......+q_n)\mu L_{pot}}{\rho g\pi r_n^4}-\frac{8(0.5q_1+q_2+q_3+......+q_n)\mu\Delta S}{\rho g\pi r_n^4}\right)}{\ln(\frac{r_t}{r_n})} \tag{14}$$

By defining

$$C_3=16\Delta S^2K\frac{\mu}{\rho gr^4\ln(\frac{r_t}{r_n})} \tag{15}$$

and arranging and rewriting

$$(C_2+0.5)q_1+(C_2+C_3+1)q_2+(C_2+C_3)(q_3+q_4.......+q_n)+-C_1=0 \tag{16}$$

or

$$(C_2+0.5)q_1+(C_2+C3+1)q_2+(C_2+C_3)\sum_{j=3}^{n}q_j-C_1=0 \tag{17}$$

A similar equation may be obtained for the remaining segments, which may be written in general form as:

$$\sum_{j=1}^{i-1}(C_2+((j-1)+0.5)C_3))q_j+(C_2+(i-1)C3+1)q_i+(C_2+(i-1)C_3))\sum_{j=i+1}^{n}q_j-C_1=0$$
(18)

By applying **Eq. (10)** to the 1st segment and **Eq. (18)** to the 2nd segment through the nth segment, the resultant is a system of linear equations with n unknowns represents the flowrate throughout each segment, which may be written as shown in **Table 1**.

Table 1. The resulting system of linear equation.

Equation no.	q_1	q_2	q_3	q_4	--------	q_n	R.H.S
1	C_2+1	C_2	C_2	C_2	---------	C_2	C_1
2	C_2+0.5 C_3	C_2+C_3+1	C_2+C_3	C_2+C_3	---------	C_2+C_3	C_1
3	C_2+0.5 C_3	C_2+1.5C_3	C_2+2C_3+1	C_2+2C_3	--------	C_2+2C_3	C_1
4	C_2+0.5 C_3	C_2+1.5C_3	C_2+2.5C_3	C_2+3C_3+1	--------	C_2+3C_3	C_1
⋮	⋮	⋮	⋮	⋮	⋮	⋮	⋮
n	C_2+0.5 C_3	C_2+1.5C_3	C_2+2.5C_3	C_2+3.5C_3	--------	C2+(n-1)C_3+1	C_1

The above system of n simultaneous equations can be solved for the flowrate using any method for solving a system of linear equations. Having obtaining the values of the flowrate of each segment, the transmembrane pressure can be calculated for each segment.

MATHEMATICAL MODEL VERIFICATION

The developed mathematical model was calibrated and verified by using gathered laboratory experimental data to check the performance of the model and the validity of the assumptions made.

Laboratory experiments were carried out on polypropylene, PP, HFM with inner and outer diameters of 0.39mm and 0.65mm, respectively. The fibres were divided into four sets each set consist of ten fibres. The flowrate, under a constant head of 2m, of each set was measured with its initial length, and then the flowrate is measured each time after reducing the length as shown in **Table (2)**.

Table (2). Measured flowrate values.

Set no.	Length (cm)	Measured flowrate (ml/min)	Set no.	Length (cm)	Measured flowrate (ml/min)
1	50	18.1	3	50	18.6
	40	17.02		40	16.82
	30	14.84		30	14.84
	20	11.2		20	11.89
	10	5.9		10	6.48
2	45	18.1	4	45	18.14
	30	15.23		30	14.41
	15	8		15	7.84

The first step toward the mathematical model verification is the calibration of the hydraulic conductivity coefficient. The value of this coefficient was calibrated using the data of the first set with initial length of 50cm only. The conductivity coefficient is adjusted until the predicted flowrate value matches the experiment value. The conductivity coefficient value was found to be $4.64*10^{-7}$ cm/s.

The Mathematical model was used then to generate the flowrate values of the fibre sets by just changing the fibres length. **Fig. (3)** shows the measured and mathematical model predicted flowrate values. A segment length of 1cm was adopted in all calculations of the study. A good agreement between the measured and predicted flowrates values can be noticed with a correlation coefficient of 0.996.

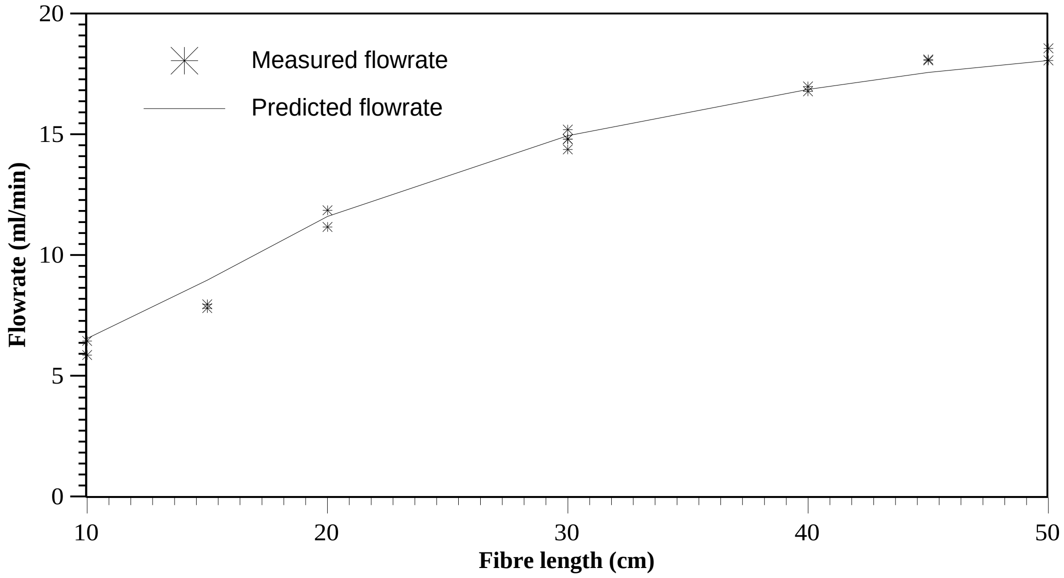

Fig. 3. Comparison between measured and predicted flowrate values.

APPLICATION OF THE MATHEMATICAL MODEL

The developed mathematical model being verified can be used to study the hydraulic performance of HFM rather than carrying out time consuming laboratory tests.

The mathematical model was applied to investigate the hydraulic performance of two types of virgin HFM modules.

First Type of HFM Module

Specifications of the first type HFM module are listed in **Table 3**.

Table 3. Specification of the first type HFM module.

Item	Value
Fibre inner diameter	0.25mm
Fibre outer diameter	0.55mm
Number of fibres per module	20 000
Effective fibre length	97cm
Pot length	10cm
Total effective area	$33.5m^2$
Normal Module operation flowrate	120-240 lmh/bar

In the factory, the measured flowrate of the fibres module with RO permeate is 2,000 lmh/bar at 20°C. This given permeability can be reached by the mathematical model under a hydraulic conductivity coefficient of $2.32x10^{-5}$ m/s.

The flowrate variation as a percentage of the total fibre flowrate a long a single fibre length is shown in **Fig. 4**. As it may be seen that more that 99.3% of the flowrate is just from the first 10cm of the fibre length.

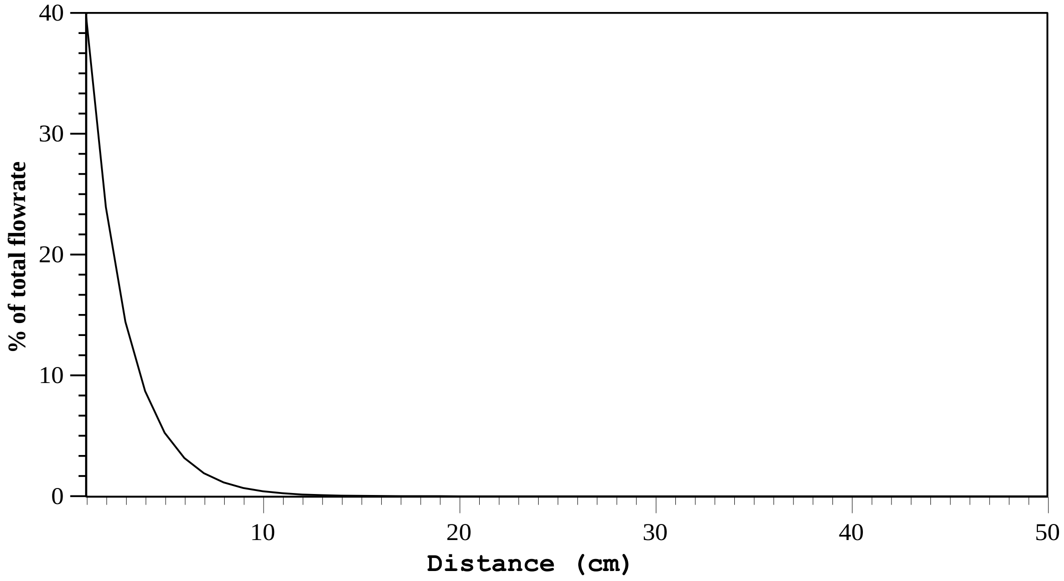

Fig. 4. The flowrate variation as a percentage of total flowrate along a single fibre length.

Fig. 5 shows the TMP variation as a percentage of the total applied pressure head along the single fibre length. It is clear that most of the applied head will be used to derive water from the first 10cm.

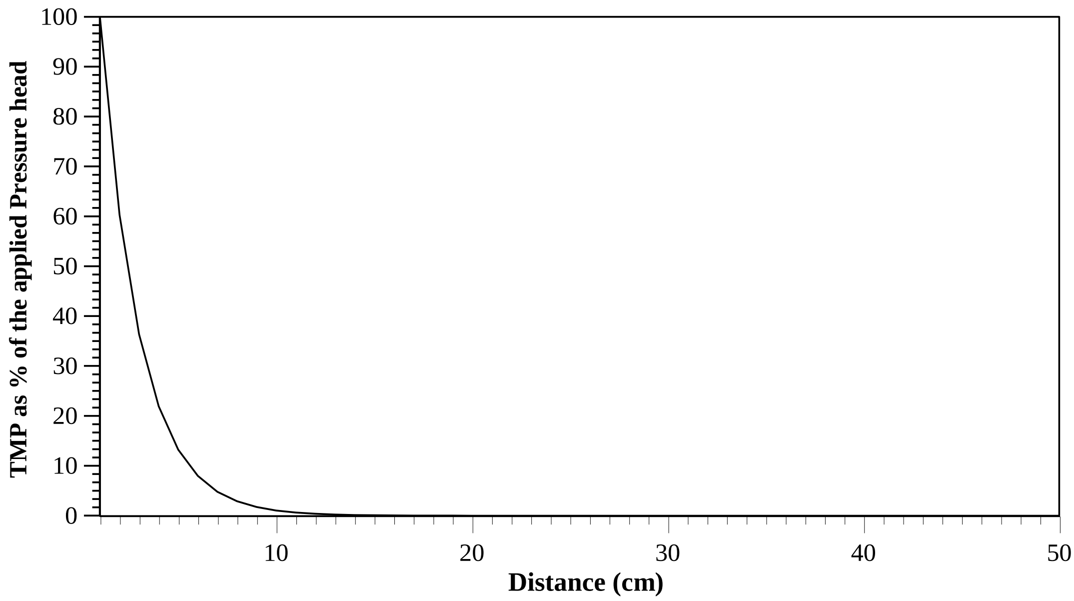

Fig 5. The TMP variation as a percentage of the total applied head along a single fibre length.

The flowrate of a single fibre is reduced when placed in actual fibre module because of the headloss through the module pot. The flowrate of the single virgin fibres will be reduced from 2000 lmh/bar down to 336.4 lmh/bar when placed in a full module.

The TMP variation as a percentage of the total applied pressure head and flowrate variation as a percentage of the total flowrate along the fibre length are independent of the applied pressure head. Thus, the flowrate variation along the fibre as a percentage of total flowrate will be the same as in **Fig. 4**.

Fig. 6. Shows the TMP variation along the fibre with a pot of a 10cm length. A great reduction in the TMP may be noticed when comparing the TMP variation of **Fig. 5,** of a single fibre, with that of **Fig. 6,** a fibre in an actual module. 83.2% of the total applied energy will be lost through the pot length.

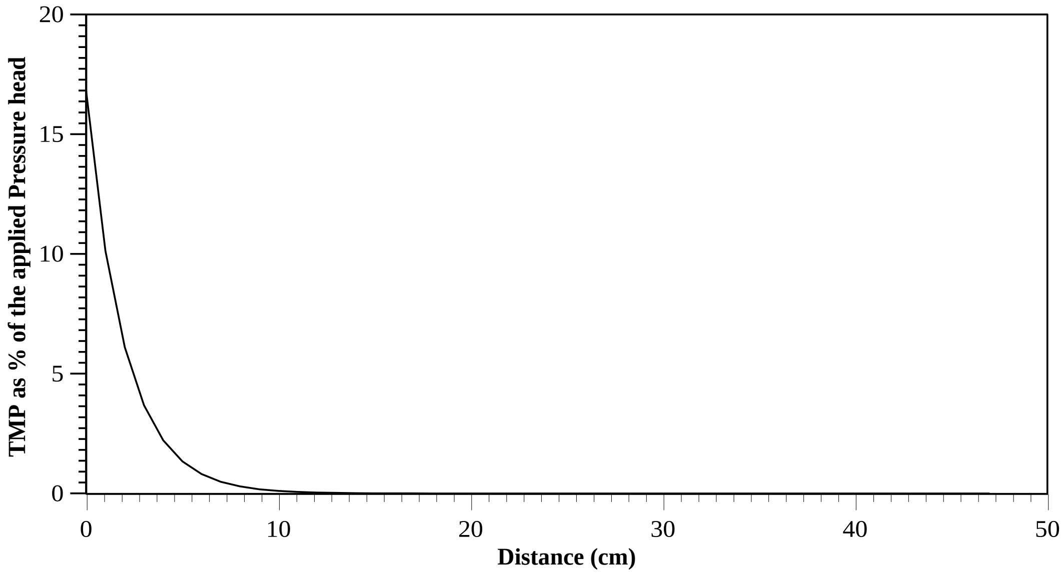

FIG 6. The TMP variation as a percentage of the total applied head along the fibre length.

Second Type of HFM Module

Specifications of the second type of HFM module are listed in **Table 4**.

Table 4. Table 3. Specification of the second type HFMe module.

Item	Value
Fibre inner diameter	0.8mm
Fibre outer diameter	1.2mm
Effective fibre length	144.75cm
Pot length	4cm
Total effective area	$35m^2$
Module Max operation flowrate	357 lmh/bar

The hydraulic conductivity coefficient was found to be $2.57*10^{-7}$cm/s at which max operation permeability was reached.

The flowrate variation a long the fibre length as a percentage of the total fibre flowrate is shown in **Fig. 7**. As it may be seen that the ratio between the flowrate at the module outlet and that at its middle is about 1.1%.

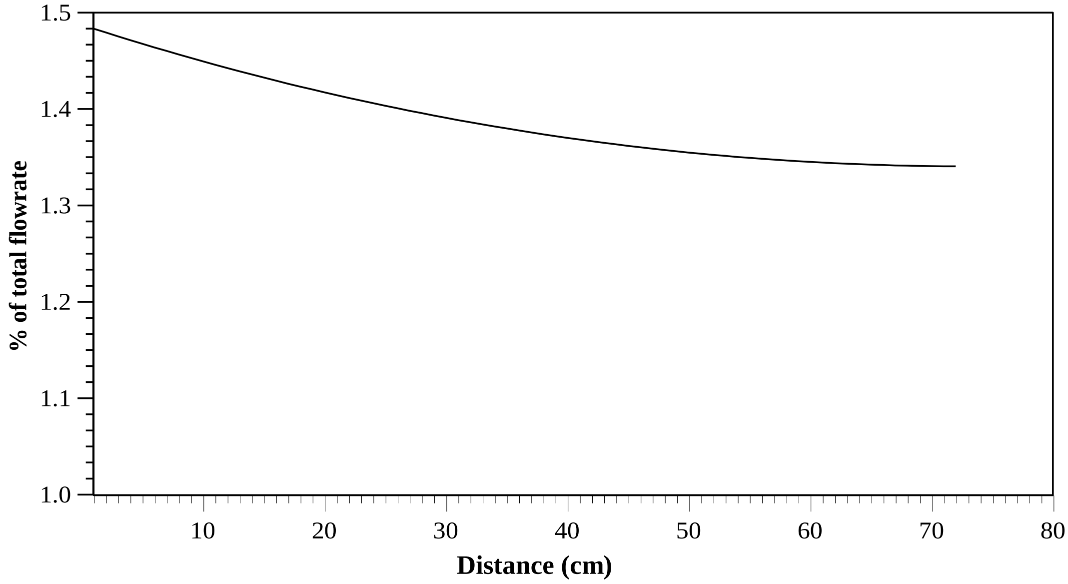

Fig. 7. The flowrate variation along the fibre length as a percentage of total flowrate.

Fig. 8 shows the TMP variation along the fibre length as a percentage of the total applied pressure head. Due to large fibre diameter and the short length of the pot the head losses through it is very small. The difference between the maximum and the minimum TMP along the fibre is less than 10%.

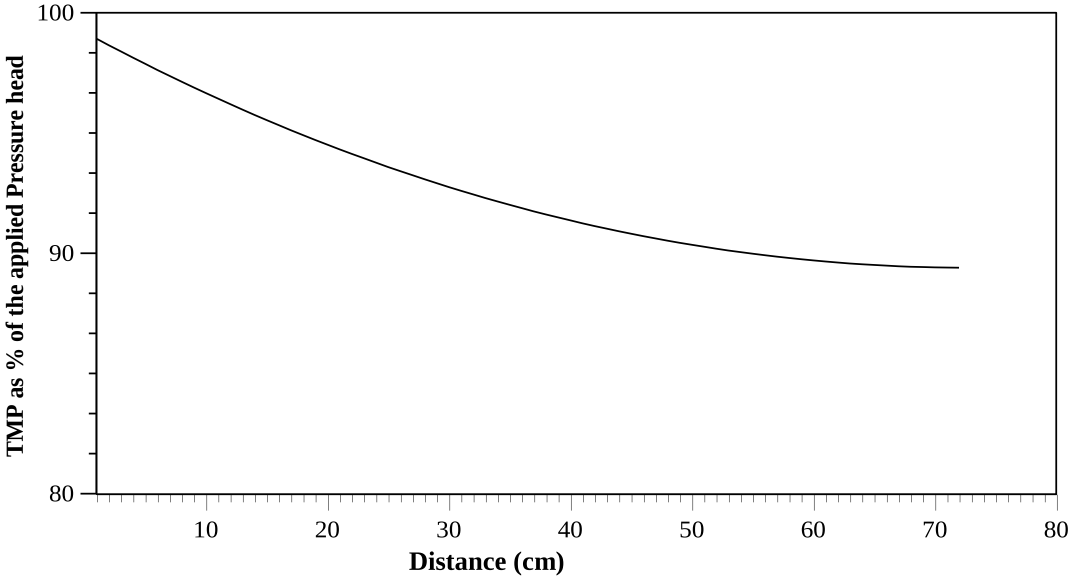

FIG 6. The TMP variation along the fibre length as a percentage of the total applied head.

CONCLUSIONS

- The flow though the HFM under the condition of constant hydraulic conductivity could be simulated mathematically by applying the Darcy’s Law and Poiseulle’s Laws. A Good agreement was found between the laboratory and predicted data under the same conditions.
- A great difference in the performance of two the commercial HFM was noticed.
- The TMP variation as a percentage of the total applied pressure head and flowrate variation as a percentage of the total flowrate along the HFM length are independent of the applied pressure head
- The head losses through the pot length could be so high and consumes 80% of the total applied pressure head.

RECOMMENDATIONS

The following recommendations were suggested to study:

- The variation of the hydraulic conductivity along the fibre length under normal operation conditions.
- The mathematical simulation of the hydraulic flow through the hollow fibre membrane under variable hydraulic conductivity.
- Optimizing the HFM module design.

REFERENCE

- Baker, R. W., Membrane Technology and Applications, 2nd Edition, John Wiley and Sons Ltd, England, 2004.
- Technical data provided by the Technical Director for Memcor Ltd, United Kingdom, part of US Filter company, 2005.
- W. S. Winston HO and Kamaleh K. SirkAr, "Membrane Hand book", 1992, Van Nostrand Reinhold, New York.
- X-Flow B.V., The XIGATM Concept and Operation Manual, 2005, at http://www.x-flow.com/import/assetmanager/1/3161/CAPF-XIGA-0143.pdf.

LIST OF SYMBOLS

ΔS= length of the fibre segment, L.
μ= water viscosity, L.T.
HFM= hollow fibre membrane.
h_{ap} = applied head, L.
h_l = head loss, L.
hl_{pot}= pressure head loss through the pot length, L.
K= hydraulic conductivity of the porous media, L/T.
L_{pot} = length HFM module pot, L
q = volumetric flowrate, L^3/T.
r_t= fibre outer radius, L, and
r_n= fibre inner radius, L.
TMP = transmembrane pressure, L.

EFFECT OF TRANSVERSE BASE RESTRAINT ON THE CRACKING BEHAVIOR OF MASSIVE CONCRETE

Dr. Adnan F. Ali
Ass. Professor
Baghdad University

Dr. Omar Al-Farouq Al-Damluji
Ass. Professor
Baghdad University

Ala'a H. A. Al-Zuhairi
Lecturer
Baghdad University

ABSTRACT

The effect of considering the third dimension in mass concrete members on its cracking behavior is investigated in this study. The investigation includes thermal and structural analyses of mass concrete structures. From thermal analysis, the actual temperature distribution throughout the mass concrete body was obtained due to the generation of heat as a result of cement hydration in addition to the ambient circumstances. This was performed via solving the differential equations of heat conduction and convection using the finite element method.

The finite element method was also implemented in the structural analysis adopting the concept of initial strain problem. Drying shrinkage volume changes were calculated using the procedure suggested by ACI Committee 209 and inverted to equivalent temperature differences to be added algebraically to the temperature differences obtained from thermal analysis.

Willam-Warnke model with five strength parameters is used in modeling of concrete material in which cracking and crushing behavior of concrete can be included. The ANSYS program was employed in a modified manner to perform the above analyses.

A thick concrete slab of 1.5m in thickness and 10m in length was analyzed for different widths 2, 4, 8, and 10m to produce different aspect ratios (B/L) of 0.2, 0.4, 0.8, and 1.0 respectively. The results of the analyses show an increase in cracking tendency of mass concrete member as the aspect ratio of the same member is increased due to the effect of transverse base restraint. Accordingly, such effect cannot be ignored in the analysis of base restrained mass concrete structures subjected to temperature and drying shrinkage volume changes.

الخلاصة

في هذا البحث، تم إجراء تحري عن تأثير أخذ البعد الثالث في أعضاء الخرسانة الكتلية بنظر الاعتبار على تشققها. وتتضمن الدراسة إجراء التحليل الحراري والإنشائي لمنشآت الخرسانة الكتلية. ويتم الحصول على التوزيع الحقيقي لدرجات الحرارة خلال جسم الخرسانة الكتلية من خلال التحليل الحراري للمسألة نتيجة للحرارة المتولدة جراء إماهة السمنت بالإضافة إلى الظروف الجوية المحيطة. وهذا يجرى من خلال حل المعادلتين التفاضليتين للتوصيل والحمل الحراري باستخدام طريقة العناصر المحددة.

كما إن طريقة العناصر المحددة أستخدمت أيضا في التحليل الأنشائي وذلك بتبني فكرة مسألة الأنفعال الابتدائي. كذلك يتم احتساب التقلصات الحجمية المرافقة لجفاف الخرسانة بالاعتماد على الطريقة المقترحة من قبل معهد الخرسانة الأمريكي لجنة ٢٠٩ والتي يتم تحويلها إلى ما يكافئها من تغير في درجات الحرارة لتضاف جبريا إلى التغيرات بدرجات الحرارة التي تم الحصول عليها من التحليل الحراري.

لقد تم تبني نموذج ويلام-ورانك ذات خمسة معاملات مقاومة لتمثيل مادة الخرسانة إذ يتضمن هذا النموذج تصرف الخرسانة في حالتي التشقق والتهشم. هذا وتم استخدام برنامج ANSYS وبطريقة معدلة لإنجاز التحليلين المشار أليهما أعلاه.

تم تحليل بلاطة خرسانية بسمك ١,٥م وطول ١٠م وبأعراض مختلفة ٢، ٤، ٨ و ١٠م لتحقيق نسب جانبية عرض/طول مختلفة ٠،٠٢، ٠،٠٤، ٠،٠٨و ١،٠٠ على الترتيب. أظهرت نتائج التحليل زيادة في قابلية تشقق أعضاء الخرسانة الكتلية بزيادة النسب الجانبية بسبب تأثير تقييد القاعدة العرضي. وعليه، فأن مثل هذا التأثير لا يمكن إهماله في منشآت الخرسانة الكتلية التي تتعرض لتغيرات في درجات الحرارة و تقلص الجفاف.

KEYWORDS: Mass Concrete, Temperature Difference, Drying Volume Change, Base Restraint, Concrete Cracking.

INTRODUTION

Mass concrete is an expression usually used for any concrete structure with dimensions large enough to cause structural problems during and after the construction period. These problems are mainly the occurrence of cracking due to temperature variations and shrinkage volume changes. Like any solid material, concrete is affected by increase and decrease of temperature. The effect appears as a thermal strain that occurs within the concrete structure when it is prevented or restricted from motion, i.e., restrained. The second category of volume change is the drying shrinkage, which is related to the drying and shrinking of the cement gel.

ACI 207 Committee (ACI Committee 1995) suggested the following equations to be used to calculate the degree of restraint for rigid continuous base restraint.

$$\begin{aligned} K_R &= \left[(L/H-2)/(L/H+1)\right]^{h/H} && \text{for } L/H \geq 2.5 \\ K_R &= \left[(L/H-1)/(L/H+10)\right]^{h/H} && \text{for } L/H < 2.5 \end{aligned} \tag{1}$$

where

L/H = length to height ratio, and

h = the height at which the degree of restraint is calculated.

As can be noticed, ACI 207 Committee neglects the effect of the restraint in the transverse direction and hence, eq. (1) can be applied to the concrete walls only. Therefore, it is the objective of the present study to investigate the effect of transverse base restraint, i.e., effects of 3rd dimension on the behavior of massive concrete and therefore cracking tendency and cracking prevention in such structures.

THERMAL ANALYSIS

Based on Fourier's Law for heat transfer, the heat conduction equation can be expressed as follows (Holman, 1981):

$$k_x \frac{\partial^2 T}{\partial x^2} + k_y \frac{\partial^2 T}{\partial y^2} + k_z \frac{\partial^2 T}{\partial z^2} + \bar{q} = \rho c_p \frac{\partial T}{\partial t} \tag{2}$$

where,

k_x, k_y and k_z = heat conductivity of the material in x, y and z-direction respectively,

T = the difference between absolute and reference temperatures,

$\bar{q}$ = heat generation per unit volume,

c_p = specific heat, and

ρ = density.

On the other hand, heat may transfer by convection according to the following Newton formula (Holman, 1981):

$$q = \int_A h_{cv} \left(T - T_\infty \right) dA \tag{3}$$

where,

h_{cv} = convection heat transfer coefficient (film coefficient).

T_∞ = bulk fluid temperature.

T = temperature.

Both of the above equations may be descritized using Raylieh-Ritz variation process to derive an expression employing the finite difference method to overcome the time-rate nature of the problem, that is,

$$\left[K_e^* \right] \left\{ \Delta\delta_{(t)} \right\} = \left\{ F^* \right\} \tag{4}$$

where,

$$\left[K_e^* \right] = \left[K_e \right] + \frac{[C]}{\Delta t}$$

$$\left\{ F^* \right\} = \left\{ \Delta F_{(t)} \right\} + \frac{[C]}{\Delta t} \left\{ \Delta\delta_{(t-\Delta t)} \right\}$$

Eq. (4) is used in the finite element method to predict the temperature distribution within the mass concrete body invoking the described initial and boundary temperatures as follows:

1. Initial temperature = concrete placement temperature = 20 ^{o}C.
2. Bulk ambient temperature T_∞ which is specified for Baghdad climate according to Kammouna, 2001, from:

$$T_\infty = 29.815 - 15.291 * \cos(0.893t) \tag{5}$$

where, t is time in days.

SHRINKAGE STRAIN CALCULATION

Following the procedure recommended by (ACI Committee 209, 1992) and taking the ambient circumstances and concrete mixing and placing conditions, the drying shrinkage strains may be calculated as a function of time after curing period for concrete which is assumed to be seven days.

Quoting the concept of evaporable moisture content that was adopted by Carlson, 1937, the distribution of drying shrinkage strains may be assessed within the body of mass concrete member. Table (1) shows such distribution in which the values of drying shrinkage strains seem very low. Such observation may be related to the non-convenience of eq. (6) that was suggested by ACI 209 Committee (ACI Committee, 1992) and used to estimate shrinkage strain-time relation.

$$\left(\varepsilon_{sh} \right)_t = \frac{t}{35 + t} \left(\varepsilon_{sh} \right)_u \tag{6}$$

where,

$(\varepsilon_{sh})_t$ = shrinkage strain at any time t (in days), and

$(\varepsilon_{sh})_u$ = ultimate shrinkage strain = $780*10^{-6}$.

As can be seen from eq. (6) 50% only of the ultimate shrinkage strain occurs at 35 days after curing. However, one can conclude from the trend of the drying shrinkage strains as they are decreased with the increase in the width of the slab as the major cause of cracking in large mass concrete members is the temperature variation rather than shrinkage volume changes.

ADOPTED COSTITUTIVE RELATIONSHIP FOR CONCRETE

The concrete was modeled using Willam and Wranke model (Willam and Wranke, 1974) which predicts failure of brittle materials in which the cracking and crushing modes should be accounted for. The criterion for failure of concrete due to a multiaxial stress state can be expressed in the form:

$$\frac{F}{f_c'} - S \geq 0 \qquad (7)$$

where,

F = a function of the principal stress state (σ_{xp}, σ_{yp}, σ_{zp}),

S = failure surface expressed in terms of principal stresses and five input strength parameters as follows:

$f_t{'}$ = ultimate uniaxial tensile strength in MPa

$f_c{'}$ = ultimate uniaxial compressive crushing strength in MPa,

f_{cb} = ultimate biaxial compressive strength in Mpa,

σ_h = ambient hydrostatic stress state in MPa,

f_1 = ambient hydrostatic stress state of biaxial superimposed on hydrostatic stress state in Mpa, and

f_2 = ambient hydrostatic stress state of uniaxial superimposed on hydrostatic stress state in Mpa.

For simplicity, Willam and Warnke, 1974, suggested the following equations to calculate three of strength parameters in terms of $f_c{'}$ in case of $|\sigma_h| \leq \sqrt{3} f_c'$. Thus, the failure surface S can be specified with a minimum two constants, $f_t{'}$ and $f_c{'}$.

$$\begin{aligned} f_{cb} &= 1.2 f_c' \\ f_1 &= 1.45 f_c' \\ f_2 &= 1.725 f_c' \end{aligned} \qquad (8)$$

Failure of concrete is categorized into four domains. In each domain, independent functions were specified to describe the function F and the failure surface S. The failure surface S can be seen in **Fig. (1).**

Compression-Compression-Compression Domain($0 \leq \sigma_1 \leq \sigma_2 \leq \sigma_3$)

In this case, F takes the form:

$$F = F_1 = \frac{1}{\sqrt{15}} \left[(\sigma_1 - \sigma_2)^2 + (\sigma_2 - \sigma_3)^2 + (\sigma_3 - \sigma_1)^2 \right]^{\frac{1}{2}} \qquad (9)$$

and the failure surface S is defined as:

$$S = S_1 = \frac{2r_2\left(r_2^2 - r_1^2\right)\cos\eta + r_2(2r_1 - r_2)\left[4\left(r_2^2 - r_1^2\right)\cos^2\eta + 5r_1^2 - 4r_1r_2\right]^{\frac{1}{2}}}{4\left(r_2^2 - r_1^2\right)\cos^2\eta + (r_2 - 2r_1)^2} \qquad (10)$$

where,

$$cos\,\eta = \frac{2\sigma_1 - \sigma_2 - \sigma_3}{\sqrt{2}\left[(\sigma_1-\sigma_2)^2 + (\sigma_2-\sigma_3)^2 + (\sigma_3-\sigma_1)^2\right]^{\frac{1}{2}}}$$ in which η = angle of similarity, and

$$r_1 = a_0 + a_1\xi + a_2\xi^2$$
$$r_2 = b_0 + b_1\xi + b_2\xi^2$$
$$\xi = \frac{\sigma_h}{f_c'}$$

The undetermined coefficients a_0, a_1, a_2, b_0, b_1, and b_2 are discussed below.

When $\eta = 0^o$, S_1 in eq. (10) is equal to r_1 while if $\eta = 60^o$, S_1 is equal to r_2. Therefore, the function r_1 represents the failure surface of all stress states with $\eta = 0^o$.

The function r_1 is determined by adjusting a_0, a_1, and a_2 such that f_t', f_{cb} and f_1 all lie on the failure surface. Mathematically:

$$\left\{\begin{matrix} \frac{F_1}{f_c'}(\sigma_1 = f_t', \sigma_2 = \sigma_3 = 0) \\ \frac{F_1}{f_c'}(\sigma_1 = 0, \sigma_2 = \sigma_3 = -f_{cb}) \\ \frac{F_1}{f_c'}(\sigma_1 = -\sigma_h^a, \sigma_2 = \sigma_3 = -\sigma_h^a - f_1) \end{matrix}\right\} = \begin{bmatrix} 1 & \xi_t & \xi_t^2 \\ 1 & \xi_{cb} & \xi_{cb}^2 \\ 1 & \xi_1 & \xi_1^2 \end{bmatrix} \begin{Bmatrix} a_0 \\ a_1 \\ a_2 \end{Bmatrix} \quad (11)$$

in which $\xi_t = \frac{f_t'}{3f_c'}$, $\xi_{cb} = \frac{f_{cb}}{3f_c'}$, and $\xi_1 = -\frac{\sigma_h^a}{f_c'} - \frac{2f_1}{3f_c'}$.

The proper values for the coefficient a_0, a_1, and a_2 can be determined through the solution of the simultaneous equations given in eq. (11).

The function r_2 is calculated by adjusting b_0, b_1, and b_2 to satisfy the conditions:

$$\left\{\begin{matrix} \frac{F_1}{f_c'}(\sigma_1 = \sigma_2 = 0, \sigma_3 = -f_c') \\ \frac{F_1}{f_c'}(\sigma_1 = \sigma_2 = -\sigma_h^a, \sigma_3 = -\sigma_h^a - f_2) \\ 0 \end{matrix}\right\} = \begin{bmatrix} 1 & -\frac{1}{3} & \frac{1}{9} \\ 1 & \xi_2 & \xi_2^2 \\ 1 & \xi_0 & \xi_0^2 \end{bmatrix} \begin{Bmatrix} b_0 \\ b_1 \\ b_2 \end{Bmatrix} \quad (12)$$

where,

ξ_2 is defined by: $\xi_2 = -\frac{\sigma_h^a}{f_c'} - \frac{f_2}{3f_c'}$.

and ξ_0 is the positive root of the equation:

$$r_2(\xi_0) = a_0 + a_1\xi_0 + a_2\xi_0^2 \quad (13)$$

in which a_0, a_1, and a_2 are evaluated by eq. (11).

Since the failure surface must remain convex, the ratio r_1/r_2 is restricted to the range ($0.5<r_1/r_2<1.25$), although the upper bound is not considered to restriction since ($r_1/r_2 < 1.0$) for most materials. Also, the coefficients a_0, a_1, a_2, b_0, b_1, and b_2 must satisfy the conditions:

$a_0 > 0$, $a_1 \le 0$, $a_2 \le 0$

$b_0 > 0$, $b_1 \le 0$, $b_2 \le 0$

Therefore, the failure surface is closed and predicts failure under high hydrostatic pressure ($\xi < \xi_2$). This closure of the failure surface has not been verified experimentally and it has been suggested that Von Mises type cylinder is a more valid failure surface for large compressive σ_h-values. Consequently, it is recommended that values of f_1 and f_2 are selected at a hydrostatic stress level in the vicinity of or above the expected maximum hydrostatic stress encountered in the structure.

Eq. (9) describes the condition that the failure surface has an apex at $\xi = \xi_0$. A profile of r_1 and r_2 as a function of ξ is shown in Fig. (2).The lower curve represents all stress state such that $\eta = 0^o$ while the upper curve represents stress state such that $\eta = 60^o$. If the failure criterion is satisfied, the material is assumed to crush.

Tension-Compression-Compression Domain ($\sigma_1 \ge 0 \ge \sigma_2 \ge \sigma_3$)

In this regime, F takes the form:

$$F = F_2 = \frac{1}{\sqrt{15}}\left[(\sigma_2 - \sigma_3)^2 + \sigma_2^2 + \sigma_3^2\right]^{\frac{1}{2}} \tag{14}$$

and S is defined as:

$$S = S_2 = \left(1 - \frac{\sigma_1}{f_t'}\right)\frac{2p_2\left(p_2^2 - p_1^2\right)\cos\eta + p_2(2p_1 - p_2)\left[4\left(p_2^2 - p_1^2\right)\cos^2\eta + 5p_1^2 - 4p_1p_2\right]^{\frac{1}{2}}}{4\left(p_2^2 - p_1^2\right)\cos^2\eta + (p_2 - 2p_1)^2} \tag{15}$$

where $\cos\eta$ is already defined above, and

$$p_1 = a_0 + a_1\chi + a_2\chi^2$$

$$p_2 = b_0 + b_1\chi + b_2\chi^2$$

$$\chi = \frac{1}{3}(\sigma_2 + \sigma_3)$$

The coefficients a_0, a_1, a_2, b_0, b_1, and b_2 are defined by eq. (11) and eq. (12).

If the failure criterion is satisfied, cracking occurs in the plane perpendicular to the principal stress σ_1.

Tension- Tension -Compression Domain ($\sigma_1 \ge \sigma_2 \ge 0 \ge \sigma_3$)

Here the function F takes the form:

$$F = F_3 = \sigma_i \quad ; i = 1,2 \tag{16}$$

and the failure surface S is defined as:

$$S = S_3 = \frac{f_t'}{f_c'}\left(1 + \frac{\sigma_3}{S_2(\sigma_i, 0, \sigma_3)}\right); i = 1,2 \tag{17}$$

If the failure criterion for both i = 1, 2 is satisfied, cracking occur in the planes perpendicular to principal stresses σ_1, σ_2. If the failure criterion is satisfied only for i = 1, cracking occurs only in the plane perpendicular to principal stress σ_1.

Tension- Tension - Tension Domain ($\sigma_1 \geq \sigma_2 \geq 0 \geq \sigma_3$)

In this regime, F takes the form:

$$F = F_4 = \sigma_i \quad ; i = 1,2,3 \tag{18}$$

and S is defined as:

$$S = S_4 = \frac{f_t'}{f_c'} \tag{19}$$

If the failure criterion is satisfied in directions1, 2, and 3, cracking occurs in the planes perpendicular to principal stresses σ_1, σ_2, and σ_3, otherwise, cracking occurs in plane or plane perpendicular to the directions of principal stresses where the failure criterion is satisfied.

IMPLEMENTATION OF THE FINITE ELEMENT METHOD

According to Fung, 1965, the effect of temperature changes on an elastic body subjected to external forces may be determined using one of the followings:

1. Solution of the discretized form of the coupled thermo-elastic equation in which the effect of both temperature and displacement on each other may be determined, i.e. the displacement due to unit temperature change and vice versa. However, this procedure is not usually used especially in problems where the temperature changes are not high enough like in mass concrete problem.

2. When the simplifying assumptions mentioned in (1) above are introduced, the theory is referred to as an uncoupled, quasi-static theory; it degenerates into heat conduction and thermoelasticity as two separate problems. Experience shows that the change of temperature of an elastic body due to adiabatic straining is, in general, very small. If this interaction between strain and temperature is ignored, then the only effects of elasticity on the temperature distribution are effects of change in dimensions of the body under investigation. The change in dimension of a body is of the order of product of the linear dimension of the body L, the temperature rise ΔT, and the coefficient of thermal expansion α. If L = 1m and $\Delta T = 100\ ^oC$, $\alpha = 10*10^{-6}$ per ^oC, the change in dimension is 10^{-3}m, which is negligible in problems of heat conduction.

The equivalent temperature changes to the estimated drying shrinkage strains may be calculated using the following simple relation:

$$\Delta T_{DS} = \frac{\varepsilon_{sh}}{\alpha_c} \tag{20}$$

where,

ΔT_{DS} = drying shrinkage equivalent temperature change,

ε_{sh} = shrinkage strain, and

α_c = coefficient of thermal expansion of concrete.

Then the equivalent temperature changes to drying shrinkage may be added algebraically to the temperature changes resulting from thermal analysis. The effect of this sum of temperatures, which appears as thermal stress and strain, may be detected using the second method described in (2) above. This means that the problem is treated as "an initial stress or strain" problem. The term *"initial stress"* signifies a stress present before deformations are allowed. Effectively, it is a residual stress to be superposed on stress caused by deformation. The effect of temperature changes can be placed as initial strain ε_o, or initial stress and strain σ_o and ε_o. Both are viewed as alternative ways to express the same thing (Cook, 1989).

In a linear elastic material, the stress-strain relation is (Cook, 1989):

$$\varepsilon = \frac{\sigma}{E} + \varepsilon_o \tag{21}$$

where,

ε_o = initial strain = $\alpha_c \Delta T$

or,

$$\sigma = E(\varepsilon - \varepsilon_o) \tag{22}$$

The strain energy U_o is defined as (Cook, 1989):

$$U_o = \int_v \frac{\sigma\varepsilon}{2} dv \tag{23}$$

Substituting eq. (22) into eq. (23):

$$U_o = \int_v \frac{E}{2} (\varepsilon - \varepsilon_o)^2 dv$$

or,

$$U_o = \int_v \frac{E}{2} \left(\varepsilon^2 - 2\varepsilon\varepsilon_o + \varepsilon_o^2\right) dv \tag{24}$$

The third term in the parenthesis in eq. (24) can be omitted since it is independent of nodal displacements. Then its derivative is equal to zero. Thus,

$$U_o = \int_v \frac{E}{2} \left(\varepsilon^2 - 2\varepsilon\varepsilon_o\right) dv \tag{25}$$

Writing $u_o = \frac{E}{2}\left(\varepsilon^2 - 2\varepsilon\varepsilon_o\right) dv$ = is the energy per unit volume. Hence, for a state of multiaxial stresses:

$$u_o = \frac{1}{2} \lfloor \varepsilon \rfloor [D] \{\varepsilon\} - \lfloor \varepsilon \rfloor [D] \{\varepsilon_o\} \tag{26}$$

where

[D] = the constitutive relations matrix for concrete and is defined for linear-elastic material as follows (Cook, 1989):

$$[D] = \frac{E}{(1+\upsilon)(1-2\upsilon)} \begin{bmatrix} (1-\upsilon) & \upsilon & \upsilon & 0 & 0 & 0 \\ \upsilon & (1-\upsilon) & \upsilon & 0 & 0 & 0 \\ \upsilon & \upsilon & (1-\upsilon) & 0 & 0 & 0 \\ 0 & 0 & 0 & \frac{1-2\upsilon}{2} & 0 & 0 \\ 0 & 0 & 0 & 0 & \frac{1-2\upsilon}{2} & 0 \\ 0 & 0 & 0 & 0 & 0 & \frac{1-2\upsilon}{2} \end{bmatrix} \qquad (27)$$

The potential of external load may be expressed as:

$$\Omega_{ex} = -\lfloor u \rfloor \{\phi\} \qquad (28)$$

where,

$\lfloor u \rfloor$ = the displacement field vector, and

$\{\phi\}$ = the load vector.

Furthermore, the potential of body forces is given by:

$$\Omega_{bf} = \lfloor u \rfloor \{\overline{F}\} \qquad (29)$$

where

$\{\overline{F}\}$ = the body force vector, which is any force distributed over the entire volume of the body like the self-weight.

The total potential energy per unit volume can be written in the form (Cook, 1989):

$$\Pi_{p_0} = U_o + \Omega = \frac{1}{2}\lfloor \varepsilon \rfloor [D] \{\varepsilon\} - \lfloor \varepsilon \rfloor [D] \{\varepsilon_o\} - \lfloor u \rfloor \{\phi\} - \lfloor u \rfloor \{\overline{F}\} \qquad (30)$$

The total potential within the element is:

$$\Pi_{p_e} = \int_v \Pi_{p_o} dv \qquad (31)$$

or,

$$\Pi_{p_e} = \frac{1}{2}\int_v \lfloor \varepsilon \rfloor [D] \{\varepsilon\} dv - \int_v \lfloor \varepsilon \rfloor [D] \{\varepsilon_o\} dv - \int_s \lfloor u \rfloor \{\phi\} ds - \int_v \lfloor u \rfloor \{\overline{F}\} dv \qquad (32)$$

Since,

$$\{u\} = [N]\{e\} \qquad (33)$$

where,

[N] = shape function matrix, and

{e} = nodal displacement vector.

Also,

$$\{\varepsilon\} = [B]\{e\} \tag{34}$$

where,

[B] = strain-nodal displacement matrix.

Hence,

$$\Pi_{p_e} = \frac{1}{2}\int_v \lfloor e \rfloor [B]^T [D]\{e\}dv - \int_v \lfloor e \rfloor [B][D]\{\varepsilon_o\}dv - \int_s \lfloor e \rfloor [N]^T \{\phi\}ds - \int_v \lfloor e \rfloor [N]\{\overline{F}\}dv \tag{35}$$

which after simplification and introducing effects of externally applied nodal forces becomes:

$$\Pi_{p_e} = \frac{1}{2}\lfloor e \rfloor [K]\{e\} - \lfloor e \rfloor \{R\} - \lfloor e \rfloor \{F\} \tag{36}$$

where, {F} = externally applied nodal forces vector.

Applying the minimization of the total potential yields:

$$\frac{\partial \Pi_p}{\partial \{e\}} = 0$$

or,

$$[K]\{e\} = \{F\} + \{R\} \tag{37}$$

where, $\{R\} = \int_v [B]^T [D]\{\varepsilon_o\}dv + \int_v [N]^T \{\overline{F}\}dv + \int_s [N]^T \{\phi\}ds$

Eq. (37) will be used in the analysis of the mass concrete due to effects of temperature and drying shrinkage volume changes.

COMPUTER IMPLEMENTATION

Besides the "Graphical User Interface (GUI)" that is commonly used in software packages, ANSYS program proposes a programming language similar to some extent to the conventional FORTRAN language. The proposed language is referred as APDL (ANSYS Parametric Design Language).

A modified ANSYS program is adopted in this study. This consists of a main program and four subprograms. The main program contains the principal steps of analysis and required calls for subprograms. Each of these subprograms is responsible of some limit tasks like:

- Performing the thermal analysis,
- Storing temperature values in a pre-dimensioned array,
- Calculating drying shrinkage strains throughout the concrete body, and
- Conducting the nonlinear structural analysis by considering the effect of concrete aging via updating concrete strength parameters (f_t', f_c', E_c) after deleting the thermal finite element mesh and constructing a new structural one.

Two Types of elements are used in this program:

Thermal Solid 70: This element is an eight-noded brick element with one degree of freedom, temperature, at each node. The element is applicable to a three-dimensional, steady state or transient thermal analysis.

Structural Solid 65:This element is used for the three-dimensional modeling of the concrete with or without reinforcing bars. The element is defined by eight nodes having three degrees of freedom at each node: translations in the global x, y, and z directions. It is capable of considering cracking in tension and crushing in compression.

PROBLEM DESCRIPTION AND RESULTS

To investigate the effect of the transverse base restraint on the cracking behavior of mass concrete member due to temperature variation and drying shrinkage volume changes, a nonlinear finite element analysis was applied to base restrained thick concrete slab. Four different aspect ratios (width/length) were considered for the case of a slab with fixed bottom cast at the first of January (winter concrete placement) in Baghdad. The aspect ratios were 0.2, 0.4, 0.8, and 1.0 and obtained by fixing the length of the slab to 10 meters and varying the width as 2, 4, 8, and 10 meters. In all these cases, the thickness of the slab was taken as 1.5 m.

Thermal and structural analyses were conducted on the slab including all the surrounding circumstances and boundaries utilizing the finite element mesh shown in Fig. (3).

The temperature distribution in the central sections along the length and width directions at some times after concrete placement are shown in Figs. (4) to (15). The assessed final cracking pattern of the concrete slabs with different aspect ratios can be seen in Figs. (16) to (19).

CONCLUSIONS

The following conclusions can be drawn from the results of the analysis:

1. Value of peak temperature increases with increasing aspect ratio (B/L) of the slab. This may be related to the increase in the magnitude of heat generated upon concrete placement due to volume increase.
2. A small temperature drop at the 28th day of concrete age is noticed as the ratio B/L is increased. This is related to the effect of the volume to surface ratio (V/S), since the temperature increases with increasing the aspect ratio (B/L).
3. The number of primary cracks (cracks that extend over the entire thickness) increase with increasing width of the slab, i.e., the aspect ratio. This can be interpreted as a result of the considerable increase in restraint provided by the slab base and the increase in the maximum temperature due to the hydration process after concrete placement.
4. The full-depth cracks are concentrated at the central portion of the slab where the maximum drop in temperature occurs.

From the above and since it was concluded previously that the major cause of cracking in the thick slabs is temperature drop, the effect of the third dimension (width) cannot be ignored when the response (stresses and cracking) of this type of structures is required. Unfortunately, most of the standards like ACI-Committee neglect the effect of the third dimension and assume a uniform temperature distribution.

Table (1) Drying shrinkage strains

d/H (*)	Drying shrinkage strain (10^{-6})			
	Slab width = 2.0m	Slab width = 4.0m	Slab width = 8.0m	Slab width = 10.0m
	After … days	After … days	After … days	After … days

	8	14	28	90	180	8	14	28	90	180	8	14	28	90	180	8	14	28	90	180
0	0.5	3.2	7.5	18.0	24.3	0.2	1.3	3.0	7.1	9.6	0. 1	0.6	1.4	3.3	4.4	0.08	0.48	1.12	2.7	3.6
0.2	0.2	1.3	3.1	7.5	10.3	0.1	0.5	1.2	3.0	4.1	0.04	0.25	0.57	1.4	1.9	0.03	0.2	0.47	1.13	1.5
0.4	0.07	0.4	1.01	2.4	3.2	0.03	0.17	0.4	0.96	1.3	0.01	0.08	0.19	0.44	0.63	0.01	0.07	0.15	0.36	0.48
0.6	0.02	0.1	0.3	0.8	1.1	0.01	0.05	0.12	0.3	0.45	0	0.02	0.05	0.14	0.21	0	0.02	0.04	0.11	0.17
0.8	0	0	0	0	0	0	0	0	0	0	0	0	0	0	0	0	0	0	0	0
1.0	0	0	0	0	0	0	0	0	0	0	0	0	0	0	0	0	0	0	0	0

(*) d/H defines the ratio of the depth from top surface / the slab thickness H.

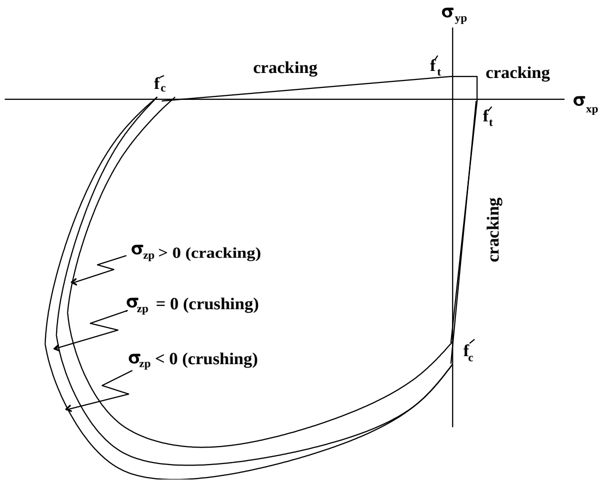

Fig.(1): Failure surface in principal stress space with nearly biaxial stress state, after ANSYS Inc.

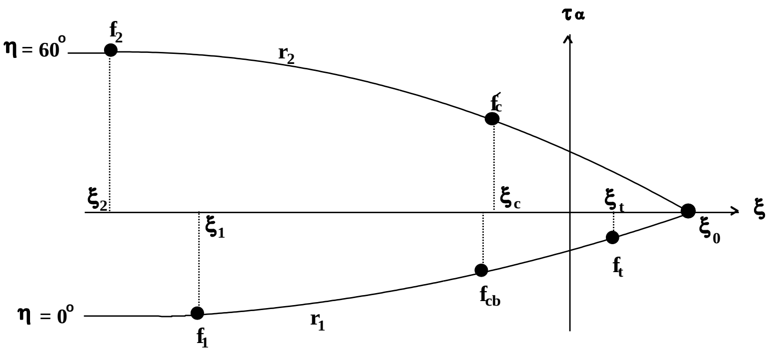

Fig. (2): A profile of the failure surface, after ANSYS Inc.

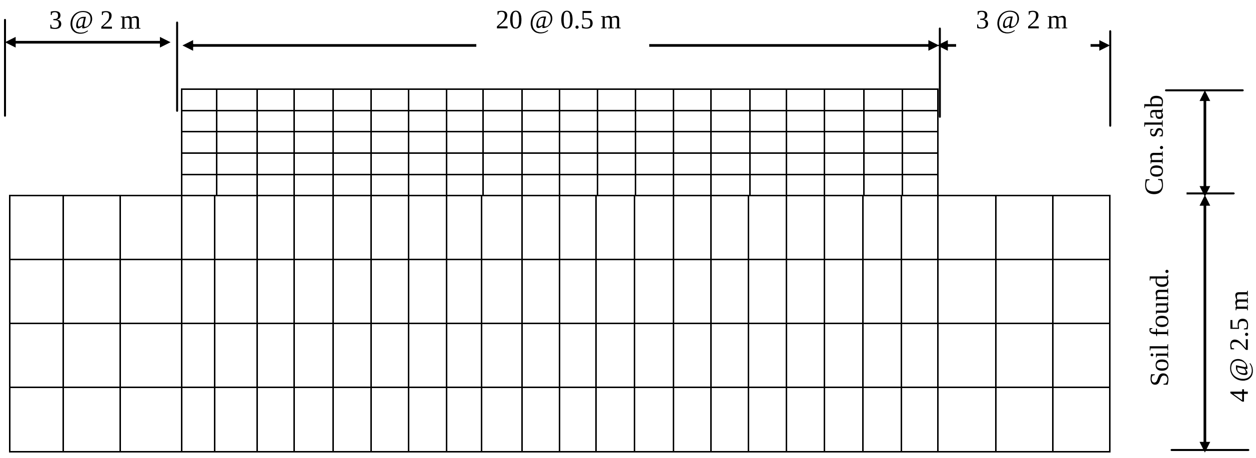

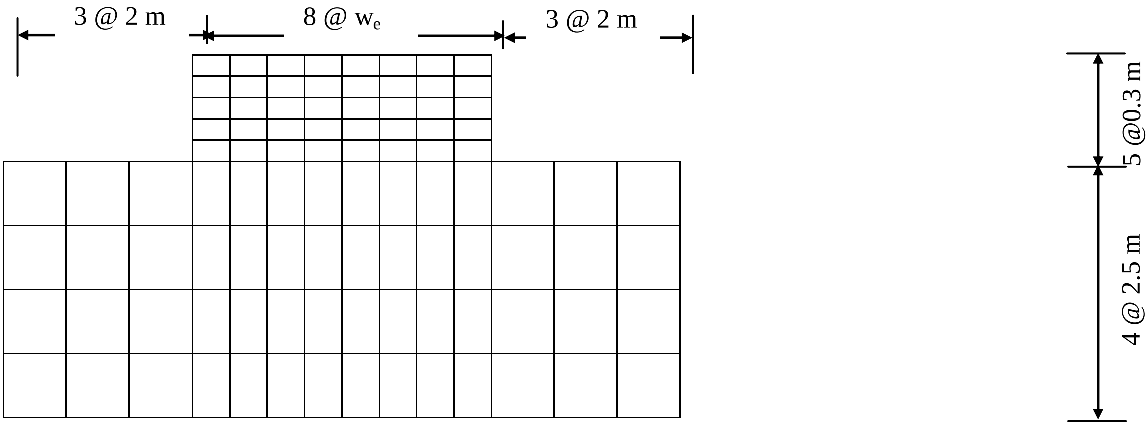

Notes:
- w_e = concrete element width (variable) = 0.25, 0.5, 1.0, or 1.5 m.
- Dimensions are not to scale.

Fig. (3): Finite element mesh for a thick concrete slab problem

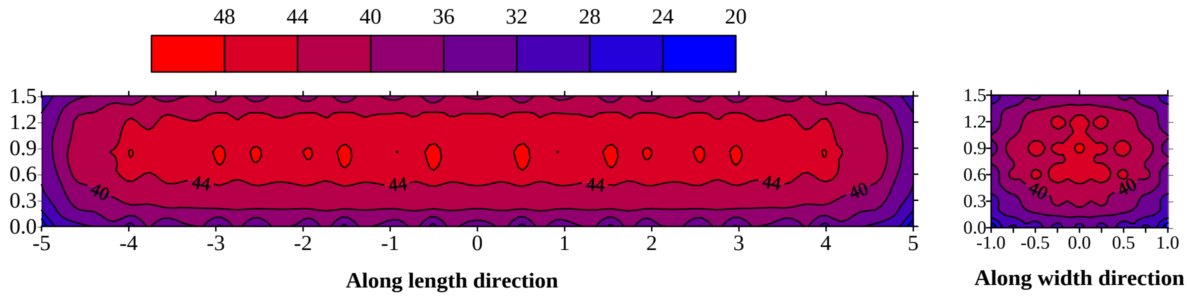

Note: Temperatures are in ^{o}C

Fig. (4): Temperature distribution in a slab with B/L=0.2 (3 days after placement)

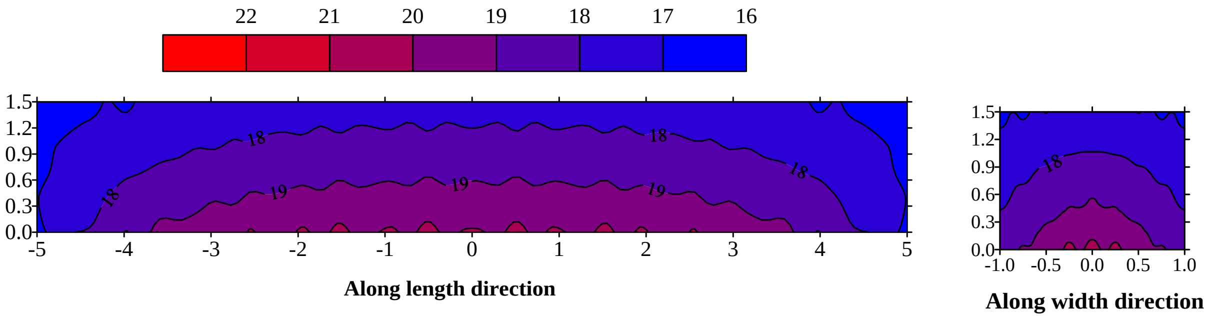

Note: Temperatures are in ^{o}C

Fig. (5): Temperature distribution in a slab with B/L=0.2 (28 days after placement)

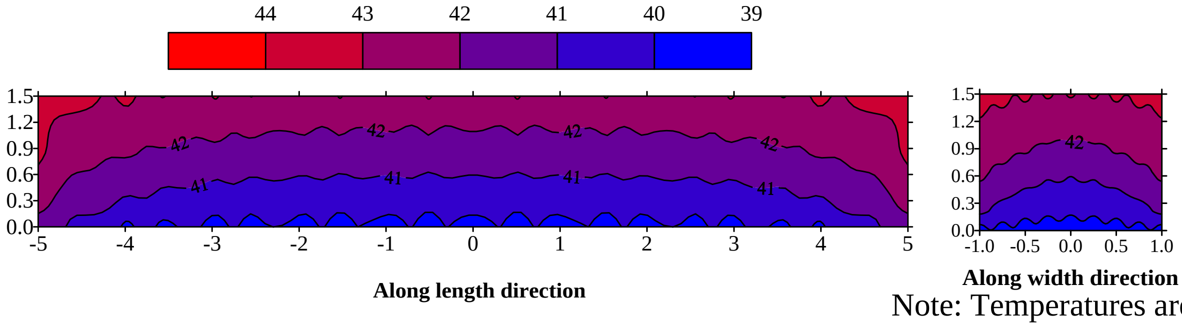

Note: Temperatures are in ^{o}C

Fig. (6): Temperature distribution in a slab with B/L=0.2 (180 days after placement)

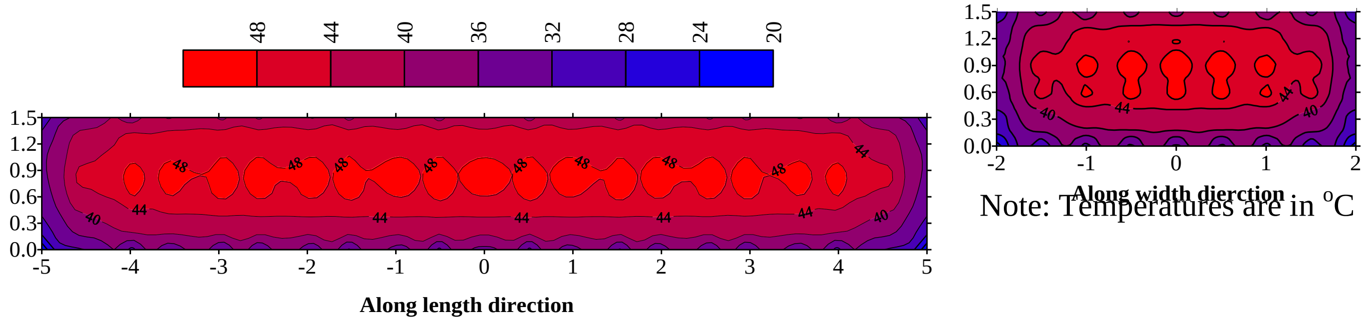

Note: Temperatures are in °C

Fig. (7): Temperature distribution in a slab with B/L=0.4 (3 days after placement)

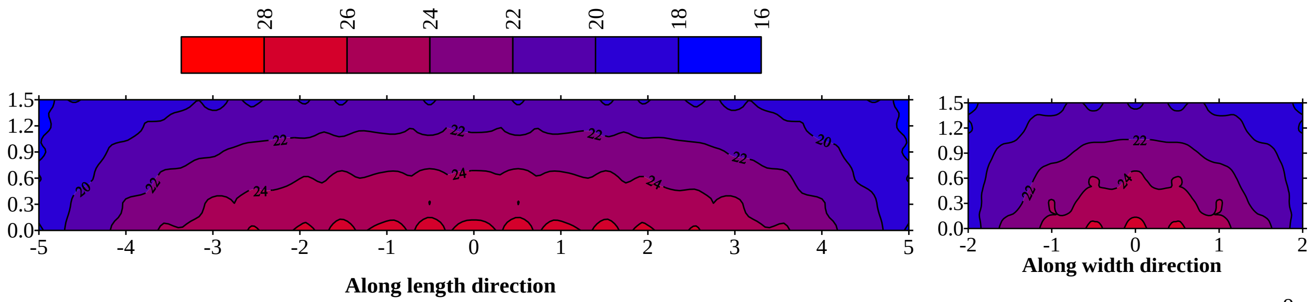

Note: Temperatures are in °C

Fig. (8): Temperature distribution in a slab with B/L=0.4 (28 days after placement)

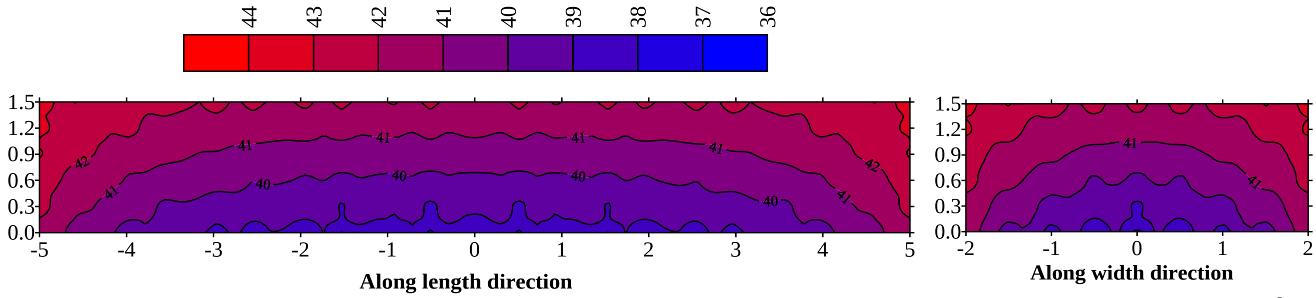

Note: Temperatures are in °C

Fig. (9): Temperature distribution in a slab with B/L=0.4 (180 days after placement)

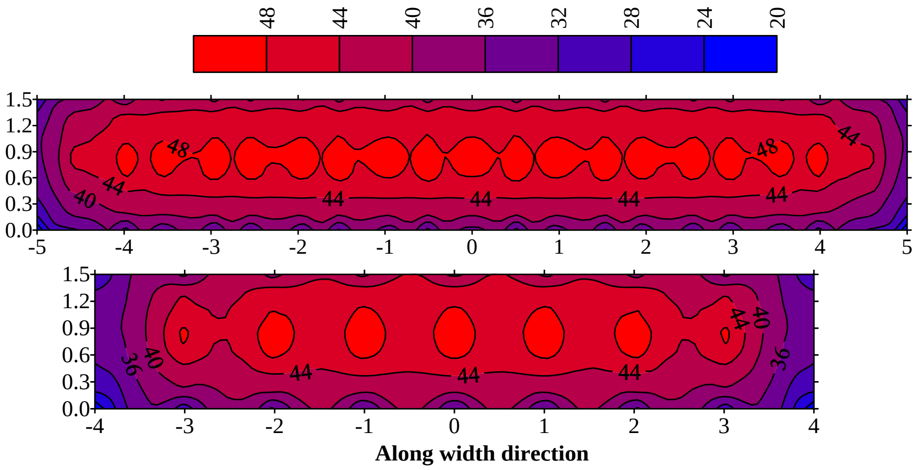

Note: Temperatures are in °C

Fig. (10): Temperature distribution in a slab with B/L=0.8 (3 days after placement)

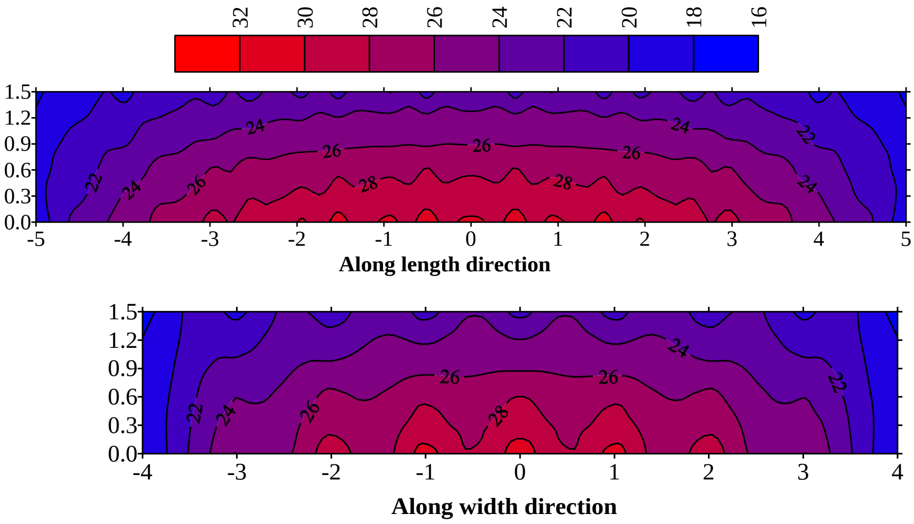

Note: Temperatures are in ^{o}C

Fig. (11): Temperature distribution in a slab with B/L=0.8 (28 days after placement)

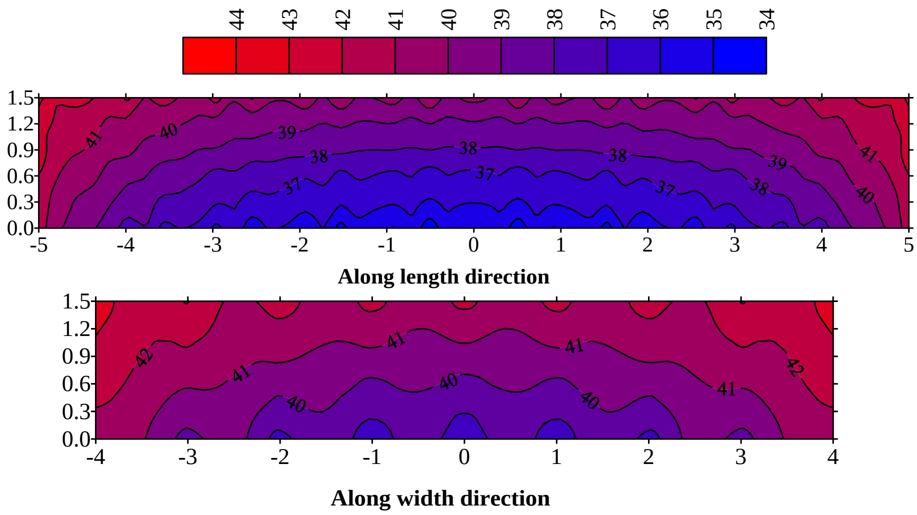

Note: Temperatures are in ^{o}C

Fig. (12): Temperature distribution in a slab with B/L=0.8 (180 days after placement)

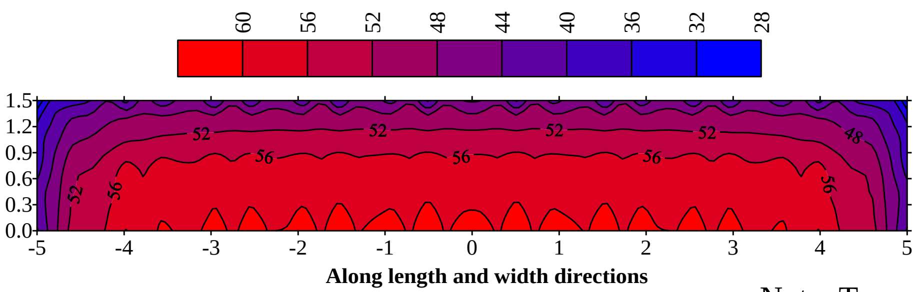

Note: Temperatures are in ^{o}C

Fig. (13): Temperature distribution in a slab with B/L=1.0 (3 days after placement)

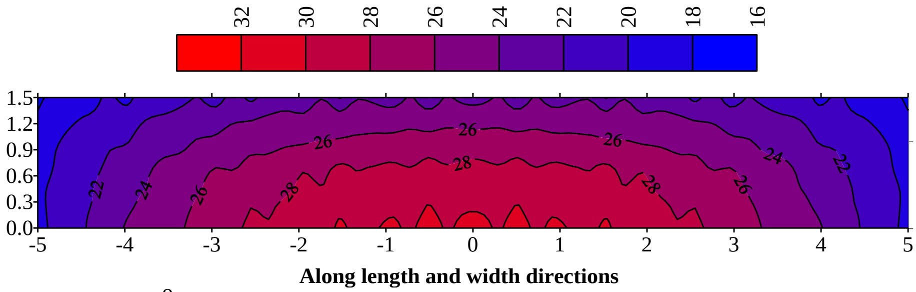

Note: Temperatures are in ^{o}C

Fig. (14): Temperature distribution in a slab with B/L=1.0 (28 days after placement)

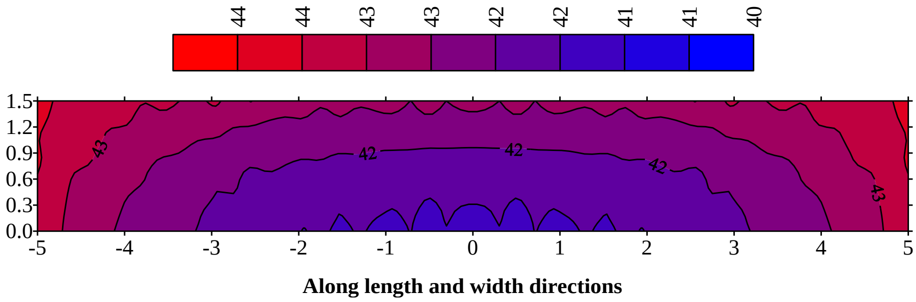

Note: Temperatures are in ^{o}C

Fig. (15): Temperature distribution in a slab with B/L=1.0 (180 days after placement)

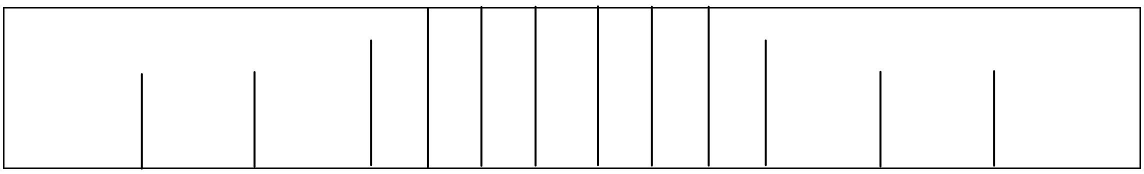

Side view of the central section along length direction

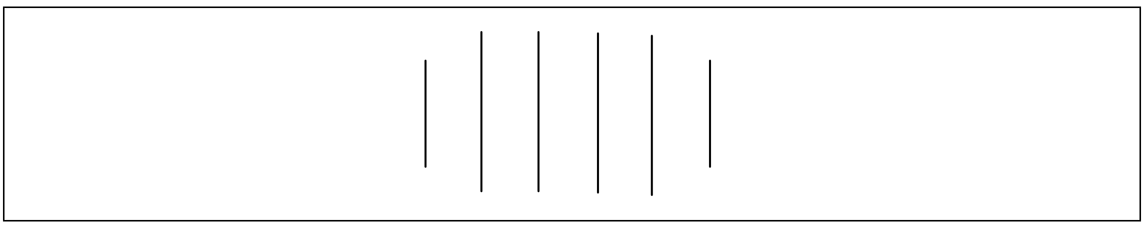

Top view

Fig. (16): Final cracking pattern for slab cast in winter with B/L=0.2

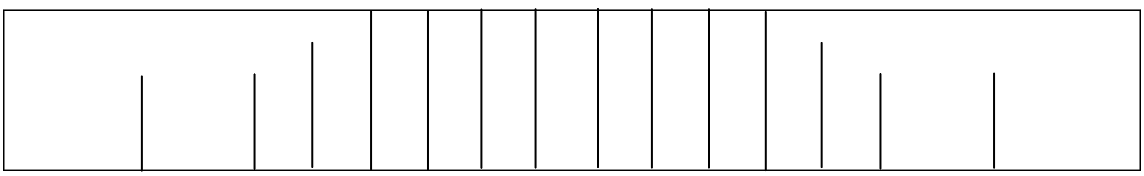

Side view of the central section along length direction

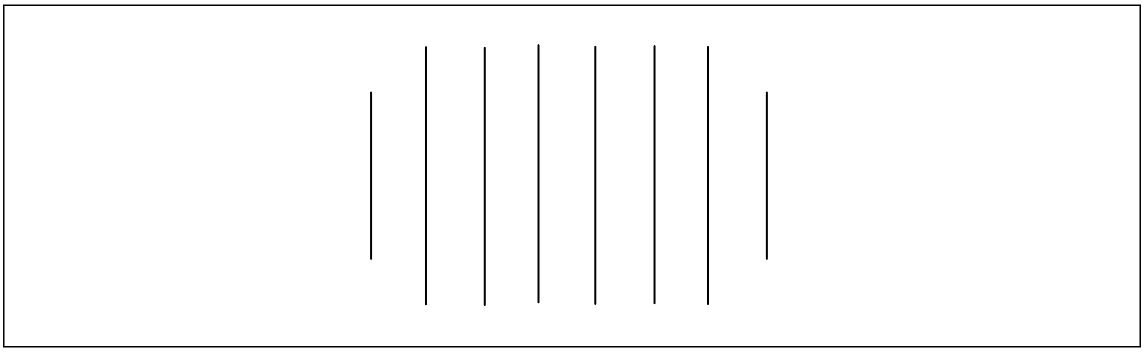

Top view

Fig. (17): Final cracking pattern for slab cast in winter with B/L=0.4

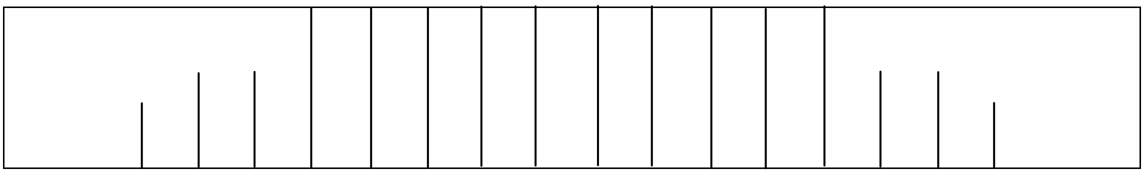

Side view of the central section along length direction

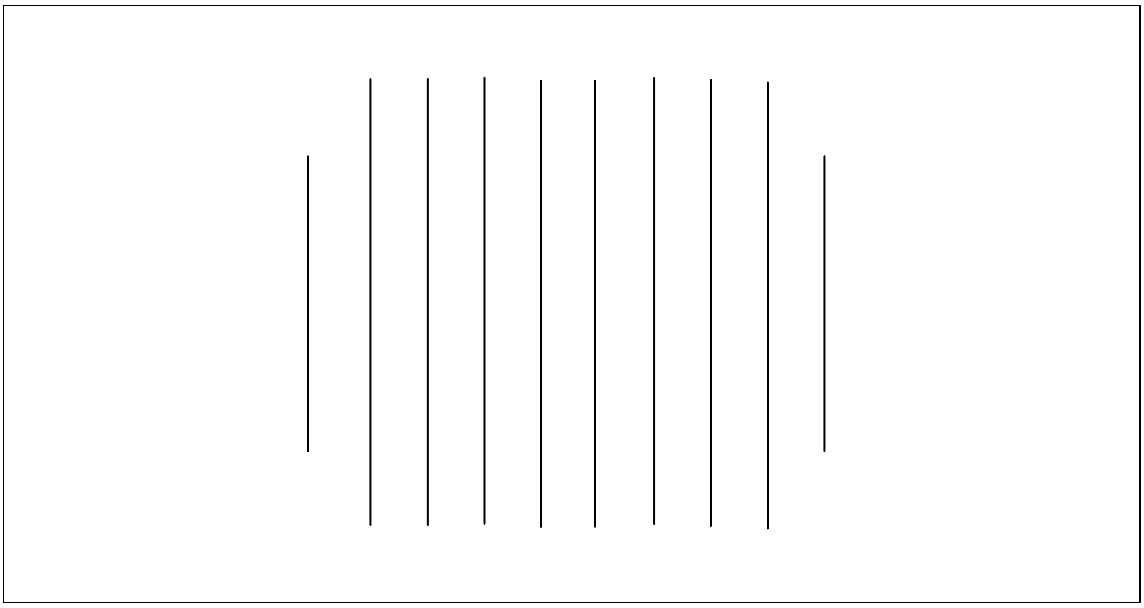

Top view

Fig. (18): Final cracking pattern for slab cast in winter with B/L=0.8

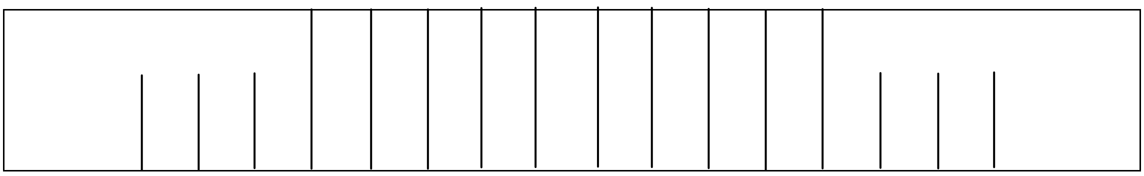

Side view of the central section along length direction

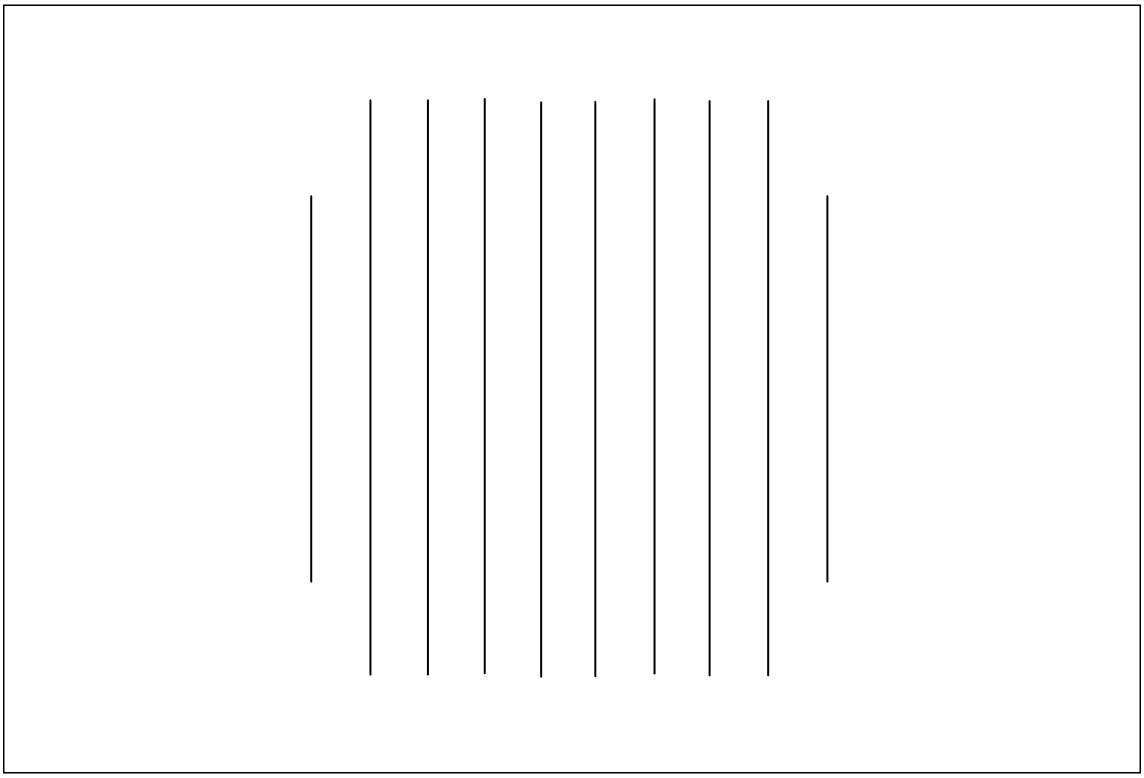

Top view

Fig. (19): Final cracking pattern for slab cast in winter with B/L=1.0

REFRENCES

ACI Committee 207, "Effect of Restraint, Volume Change, and Reinforcement on Cracking in Massive Concrete", (ACI 207.2R-95). American Concrete Institute, Detroit, 1999, 26 pp.

ACI Committee 209, "Prediction of Creep, Shrinkage, and Temperature Effects in Concrete Structures", (ACI 209R-92), (Reapproved 1997). American Concrete Institute, Detroit, 1999, 47 pp.

ANSYS 5.4 Inc., "ANSYS Theory Reference", Eighth Edition, SAS IP, Inc. 1997, Chapter 4 pp. 48-56.

Carlson, R. W., "Drying Shrinkage of Large Concrete Members" ACI Journal, Proceedings, Vol. 33, January-February 1937, pp.327-336.

Cook, R. D., Malkas, D. S., and Plesha, M. E., "Concepts and Applications of Finite Element Analysis", John Wiley and Sons Inc., Third edition, 1989, 630 pp.

Fung, Y. C., "Foundations of Solid Mechanics", Prentice-Hall Inc., Englewood Cliffs, New Jersey, 1965, 525 pp.

Holman, J. P., “Heat Transfer”, Fourth Edition, 1976, McGraw-Hill.
Kammouna, Z. M., “Development of A Mathematical Model for Creep of Concrete with Reference to Baghdad Climate”, M.Sc. Thesis, Baghdad University, College of Engineering, 2001, 90 pp.

Willam, K. J., and Warnke, E. D., “Constitutive Model for the Triaxial Behavior of Concrete”, Proceedings, International Association for Bridge and Structural Engineering, Vol. 19, ISMES, Bergamo, Italy, p. 174 (1975).

Number 3 Volume 13 September2006 Journal of Engineering

MONITORING PROCESS IN TURNING OPERATIONS FOR CRACKED MATERIAL ALLOY USING STRAIN AND VIBRATION SENSOR WITH NEURAL NETWORK CLASSIFICATION

Asst.Prof.Dr.Nabeel Kadim Abid AL-Sahib
University of Baghdad
Al-khawarizmi College of Engineering
Mechatronics Eng. Department

ABSTRACT

Surface finish and monitoring tool wear is essential for optimization of machining parameters and performing automated manufacturing systems. There is a very close relationship between tool wear and machining material parameters as surface roughness, shrinkage, cracks, hard particle ... etc. Monitoring of manufacturing processes plays a very important role to avoid dawn time of the machine, or prevent unwanted conditions such as chatter, excessive tool wear or breakage. Feature extraction and decision making is a matter of considerable interest for condition monitoring of complex phenomena with multiple sensors.

In this work, the implementation of a monitoring system utilizing simultaneous vibration and strain measurements on the tool tip is investigated for the shrinkage and crack of cast iron work piece. Machining parameters taken into consideration are cutting speed (116.5 and 136.6) m/min, feed rate (0.17 and 0.23)rev/min respectively and depth of cut (1) mm. Data from the machining processes were recorded with one piezoelectric strain sensor type (PCB 740B02) and an accelerometer type (4370), each coupled to the data acquisition card type (9111 DR). There were 22 features indicative of crack were extracted from the original signal. These include features from the time domain (mean, STD, crest factor, RMS, kurtosis, variance), frequency domains (power spectral density), time-series model coefficient (AR) and four packet features extracted from wavelet packet analysis (RMS, STD, kurtosis, crest factor).

The (2x1) self organizing map neural network was employed to identify the crack and shrinkage effect on the tool state. The program used with this process is MATLAB V.6.5. As a result of the present work, we have an SOM model can classifying the crack with minimal error.

الخلاصة:

تشغيل السطوح ومراقبة بليان أداة القطع ضرورية لتحديد الظروف المثلى لانظمة التصنيع . ان هنالك علاقة بين مراقبة بليان اداه القطع مع ظروف تشغيل سطوح المسبوكات المتشققة، الخشنة، المنكمشة والمحتوية على جسيمات صلدة وما الى . . الخ. مراقبة عمليات التصنيع تَلْعبُ دورمهم جداً لتَجَنُّب صرف وقتِ الماكنةِ، أَو يَمْنعُ شروطَ غير مرغوبةَ مثل الثرثرةِ، التاكل المفرط للاداة أوالكسرِ. إنتزاع وإتّخاذ القرارات مسألة كبيرة الاهميةِ لمراقبة الظواهر المعقّدةِ بالمحسّساتِ المتعدّدةِ.

في هذا العملِ، تطبيق نظام مراقبة يَستعملُ إهتزازاً آنياً ومقاييسَ إجهادِ على رأسِ الأداةَ لتحرّى الإنكماشِ وشَقِّ قطعةِ منِ الحديد الصلبِ. أَخذتْ معاملات التشغيل بنظر الإعتبار سرعةَ القطع (١١٦,٥ و١٣٦,٦) م/ دقيقة، نسبة تغذية (٠,١٧ و٠,٢٣) دورة /دقيقة على التوالي وعمق القطعِ (١) مليمتر. البيانات مِنْ عملياتِ التشغيل سُجّلتْ بنوعِ محسّسِ إجهادِ piezoelectric (**PCB 740B02**) ونوع معجّلِ (**4370**)، كُلّ مُزَاوَج إلى بطاقةِ جمعَ البيانات نوع(**9111 DR** **)**. كان هناك ٢٢ ميزّةَ مؤشّر على الشَقِّ إنتزعَ مِنْ الإشارةِ الأصليةِ. تتضمن ميزّات مجالِ الوقتَ (**mean, STD, crest factor, RMS, kurtosis, variance**)،

مجالات ترددِ (كثافة طيف كهربائية)، معامل الزمن النموذجي المتوالي (AR) واربع ميزّات حزم إنتزعتْ مِنْ تحليلِ حزمةِ wavelet (**RMS, STD, kurtosis, crest factor**). ان (**2x1**) يُنظّمُ شبكة عصبيةَ إستخدمتْ لتَمييز الإنكماشَ والشَقَّ على حالة أداة القطع. إنّ البرنامجَ المستخدم بهذه العمليةِ Matlab V.6.5 و كنتيجة للعملِ الحاليِ، حصلنا على نموذجُ SOM يُمْكِنُ أَنْ يُصنّفَ الشَقَّ باقل خطأ ممكنِ.

KEYWORDS :MONITORING, MEASUREMENT,WEAR,NEURAL NETWORK,CUTTING ,VIBRATION

SURVEY OF MONITORING PROCESS:

(Xiaoli etal 2000):used the wavelet transforms and fuzzy techniques are used to monitor tool breakage and wear conditions in real time according to the measured spindle and feed motor currents , respectively .**(Reuben etal 1998) :** feature extraction and decision – making was a matter of consider interest for condition monitoring of complex phenomena with multiple sensors. **(Kndili etal 2003) :** have studied the outlines of a neural networks based modular tool condition monitoring system for cutting tool wear classification . Multi layer neural network structure was used and data set has been trained off – line using back propagation algorithm, an important variation in mean, RMS, standard deviation of cutting forces and vibration can result in estimation and classification error. **(Scheffer etal 2001):** discussed the implementation of a monitoring system utilizing simultaneous vibration and strain measurement on the tool tip, was investigated for the wear manufacturing of aluminum pistons. Data from the manufacturing process was recorded with two piezoelectric strain sensors and an accelerometer, each coupled to a DSPT analyzer. A large number of features indicative of tool wear automatically extracted from different parts of the original signals (**Nadgir etal 2000):** studied the out line of a neural network based (TCMS) for cutting tool state classification. Orthogonal cutting tests were performed on H13 steel using PCBN inserts and on line cutting force data was acquired with a piezoelectric force dynamometer. Simultaneously flank wear data was measured using a tool makers microscope and along with the processed data were fed a back propagation neural network to be trained .All papers which discussed previously were used different method to measure the tool wear such as using (vibration, strain, acoustic emission and feed current signal), the steel and aluminum material was used in most papers as a work – piece with constant cutting condition. In this work are using monitoring processes to classify the cutting tool wear through using the strain and vibration signal , which measured from piezoelectric strain sensors and accelerometer respectively , after that we extract the feature from the signal to applying it into SOM neural network to have the classification of the amount tool wear . It can be divide in two parts theoretical included: (Time domain, Modeling domain, Frequency domain, Wavelet packet coefficients) from the original signals, and use it in SOM neural network. In addition classifying the cutting tool wear using SOM neural network. And experimental such as: (Machining of Cast Iron shaft with and without crack on the surface work-piece using turning machine with different cutting condition; Measuring the wear of Carbide cutting tool type(SNMG 120412) using microscope; Measuring the signal from piezoelectric strain sensor and accelerometer using Data Acquisition Card).

WEAR IDENTIFICATION AND MONITORING

A conventional method for tool wear and shrinkage appeared at the work piece identification is basically a two-step approach: First, extract features from the signals of a single sensor that is highly sensitive to tool-wear and shrinkage but insensitive to noise; then, a physical model is established to reflect the relationship between the sensor signals and the wear status. This is because a crack model based on information from a single sensor cannot adequately reflect the complexity of a cutting process. Therefore, approaches using sensor integration have been introduced in the area of crack and shrinkage monitoring, and have attracted wide interest in recent years. Cutting force measurement is one of the most commonly employed methods for on-line tool and work piece state monitoring, especially in turning because cutting force values are more sensitive to tool and work piece wear than other measurements such as vibration or acoustic emission. In recent years, intelligent control systems such as, genetic algorithm, fuzzy logic, artificial neural network and hybrid of these methods (fuzzy-neuron) are popular **(Xiaoli 2000)**. Conventional methods are mathematical model based systems, so it is difficult to take the machining parameter into account in such models. But artificial intelligence based methods are less dependent on the machine parameters.

MONITORING STAGES:

The classification of work piece and tool wear is a complex task because wear introduces very small changes in a process with a very wide dynamic range. Furthermore, it is difficult to identify whether a change in a signal is caused by wear or a change in the cutting conditions. The task of wear monitoring can be subdivided into a number of stages (Rueben 1998):

- Sensor selection and deployment.
- Generation of a set of features indicative of wear condition.
- Classification of the collected and processed information as to determine the amount of wear.

Sensors used in Monitoring Systems:

The sensors used for monitoring tool conditions can be divided into Two categories: direct and indirect. Despite their high accuracy, direct sensors are rarely used in real-time industrial applications because of their high cost and difficulty of installation also the direct measurements are not possible in many instances such as drilling and milling. Further, such measurements in most cases involve interruption of the machining process. On the other hand, indirect sensors, which are relatively economical and small, can be used for on-line crack and shrinkage detection if a certain relationship between sensor signals and tool-wear status can be established. A variety of indirect sensing methods have been applied to crack monitoring studies, including cutting force signal detection, cutting temperature detection, electrical resistance measurement, cutting vibration detection, measurement of AE (Kandilli 2003) and electrical signals like spindle motor current and power are also useful sources of information about tool states.

Wavelet Transform in Monitoring Process:

Signal processing is a very important step for (TCM). Recently, wavelet transform has provided a significant new technique in signal processing, because it offers solution in the time-frequency domain and is able to extract more information in the time domain at different frequency band. There have been many research activities in the application WT for tool condition monitoring (Scheffer 2001)

- It uses wavelet transform to decompose measured signals. Acoustic emission signal and RMS value of decomposed signals are taken as tool wear monitoring features.
- It uses wavelet transform to analyze cutting force signals and wavelet transform coefficients are taken as recognition parameters of crack.

Neural Networks in Monitoring Process:

In recent past, neural network models which employ cutting forces for estimation as well as classification of wear have been developed. The present work outlines a neural networks based modular tool condition monitoring system for crack and shrinkage classification. A multi layer neural network structure was used and data set has been trained off-line using SOM algorithm. An important variation in mean, RMS, standard deviation of cutting forces and vibration can result in estimation and classification error.

MONITORING PROCESS STAGES:

Work –Piece and Cutting Tool Materials:

Cemented carbide is composed of carbides tungsten, titanium and tantalum with some percentage of cobalt. The chemical composition of work–piece material are given in **Table** (1) **.**

Table (1) chemical composition of cast Iron work piece .

C%	Mn%	Si%	P%	S%	Cr%	Ni%	M%	Fe
3.31	0.72	3.09	0.65	0.13	0.081	0.062	0.038	balance

Cutting Tool Wear Measurement:

After switching off the turning machine the cutting tool wear measured through the microscope. The process of measuring (sensors signal and cutting tool wear) was repeated for other W.P. that have the same dimensions until the wear level reach the maximum (0.3)mm , the cutting condition of the machine were then changed , and the process was repeated . For each of the above tests, strain and vibration data were obtained in order to be used in wear classification by neural network techniques.

- ♦ Carbide tools: roughing = 0.8 mm.
- ♦ Carbide tools: finishing = 0.35 down to 0.15 mm.

Instrument Used in Monitoring Process:

Different instruments are used for different monitoring process depending on the variable to be measured. In the present work (a piezoelectric strain sensor Model 740B02 used to measure the strain at the tool holder and this gives an indication of cutting force applied to the cutting tool , signal conditioner for strain sensor is used for amplifying and analyzing signals , Accelerometer sensor is used to measure the vibration at the tool holder , The power amplifier is used to amplify the accelerometer signal , Data Acquisition Card type PCI-9111 , used for signal analysis application and process control , Microscope used in the measurement of tool wear , Interface between the instrument and the turning machine) .
The system ready to measure the data , from the turning machine as shown in **Fig** (1) .

Experimental Design of Monitoring Processes:

A set of tool wear cutting data were acquired by machining a bar of Cast Iron under a given set of cutting conditions with a coated cemented carbide tip **Table (2)**. The set of sensors used, were an accelerometer for measuring vertical vibrations, piezoelectric strain sensor on tool holder for force measurement as a strain, in order to find the amount of crack compared with the amount of strain and vibration signal. The specification of the instruments used, listed in **Table** (3)

Table (2): Experimental parameters used in the monitoring process

Components	Description
Lathe	HARRISON 15"
Work piece	Cast iron shaft (D:70mm L:270mm)
Holder type	Sandvik SDJCR 2020K11
Insert type	Carbide tips sintered square SNMG 12041 pattern TP15
Feed rate	0.078 -0.23 mm/rev
Cutting speed	105-165m/min
Depth of cut	1 mm

Table (3) Instruments used in the monitoring process

Sensor	Description	Mounting
Piezoelectric strain sensor	PCB model 740B02	On tool holder
Accelerometer	Type 4370	On tool holder
Signal conditioner	Type PCB 480E09	
Power amplifier	Type 2626	
Data acquisition card	PCI 9111DG	In computer board
Software program	Math lab V6.5	

The turning operation was carried out using (HARRISON 15”) turning machine. The experimental set-up and instrumentation are shown in **Fig (1)**. Most previous work interested in monitoring process for crack found the sampling rate at 10 KS/s enough to represent the analogue signal for cutting force. In this work the analogue signals were sampled with an Ampilicon PCI 9111DR data- acquisition board at a sample rate of 10K Hz per channel for a time period of 25.6 ms, number of samples reading through each stage are 12800 sampling pear channel. Data were acquired at intervals between (1.5~3.5) min depending on cutting conditions at which point crack was also measured, taking into account tool life inserts. The total number of tests is 2 each having different cutting conditions (to construct test and conformation sets). Each data record, of 12800 points acquired at the end of the cut, was processed to generate features used in the classification stage. Each feature vectors were extracted from time domain, wavelet domain, frequency domain, and model domain of all sensors. These features were then passed directly to the neural networks for classification (Silva 2000), with the training data coming from selected tests and the testing data used being from tests that were not used during the training phase. The cutting conditions used during the training experiment see in **Table** (4).

Table (4) Cutting conditions used in machining experiment .

Test No	Diameter of shaft (mm)	Cutting speed m/min	Feed mm/rev	Depth of cut DOC (mm)	Wear land (mm)	Number of components	Tool life for each test (min)
1	58	136.6	0.23	1	0.033-0.21	13	17
2	70	116.5	0.17	1	0.002-0.44	6	13

Test (1 and 2) with constant DOC .

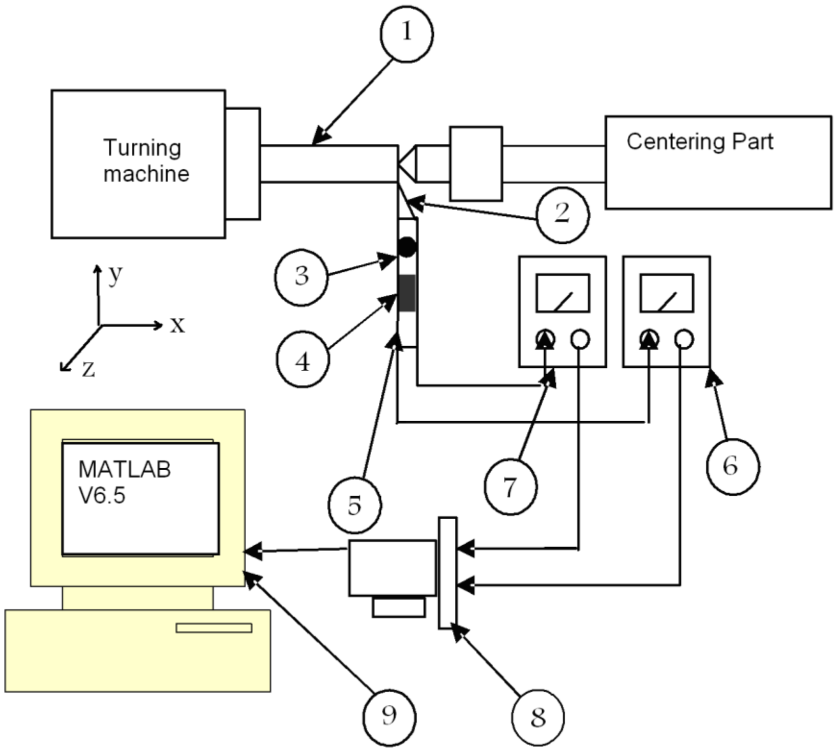

Fig (1) Experimental set-up and Instrumentation

1. Cast iron shaft with dimension (D:70 mm, L:270mm)
2. Square carbide tool
3. Accelerometer
4. Strain sensor
5. Tool holder
6. Power amplifier type 2626
7. Signal conditioner type PCB 480E02
8. DAQ card type 9111DR installed in PC board
9. PC P4 installed MATLAB program

Programming of Monitoring Process :

The flow chart of the programming process is shown in **Fig.(2).**

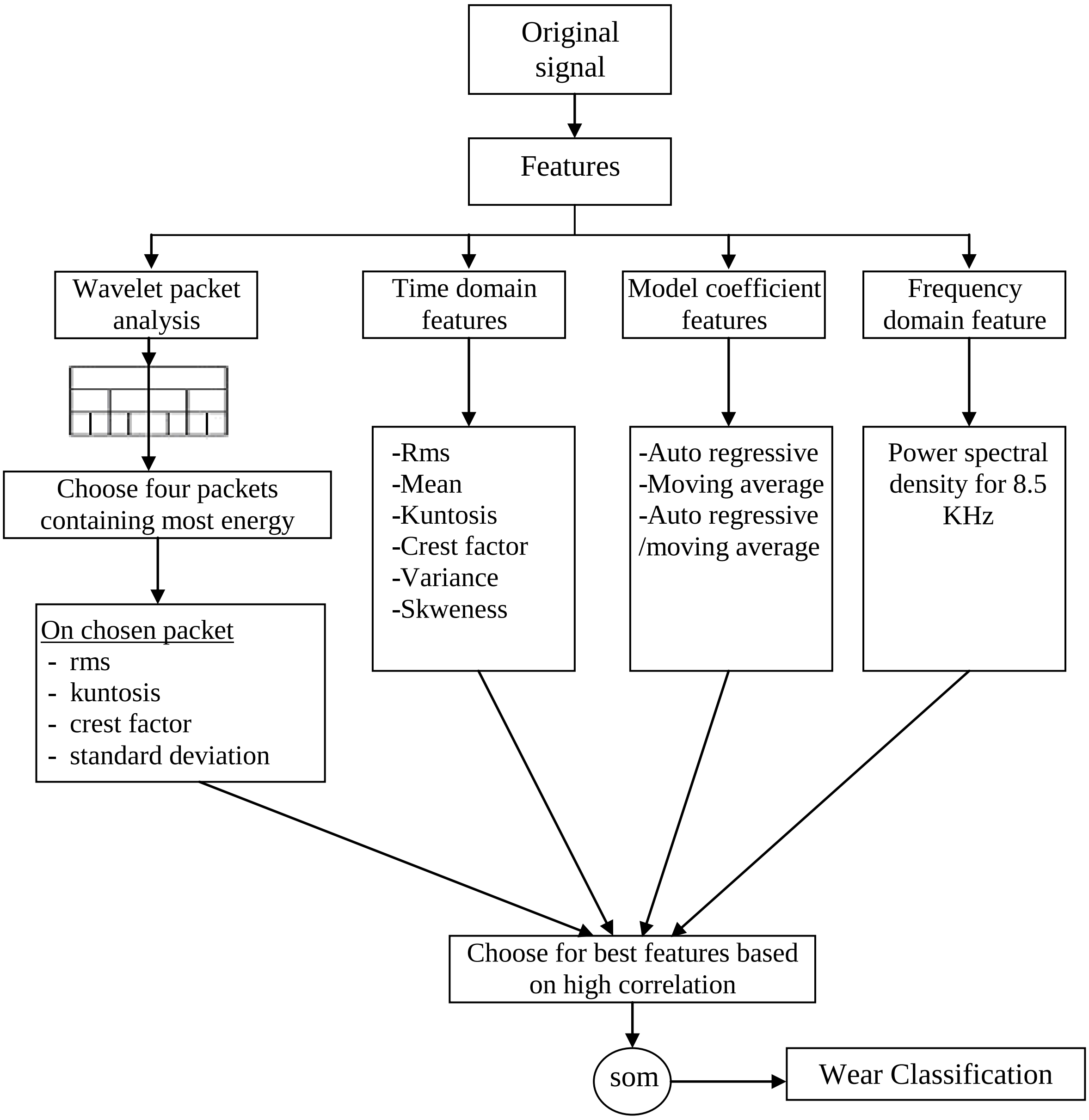

Fig (2) flow chart of the programming process .

Feature Extraction

To increase the reliability of the tool wear monitoring system, in the presented work a monitoring strategy was devised that is based on four type of feature:

- Time and modeling domain feature
- Frequency domain feature
- Wavelet packet analysis feature

The Features of the Time and Modeling Domain:

We can use some time – domain features as descriptors of crack and shrinkage **(Nadgir 2000)**, therefore, the following time-domain features were extracted from each signal: mean, rms, crest factor, standard deviation, skewness and kurtosis. A brief mathematical description of each is given as follows:

1- mean: the mean value of a function x(t) over an interval N is

$$\overline{X} = \frac{1}{N} \sum_{i=1}^{i=N} xi \qquad (1)$$

2- standard deviation (б) :

$$\sigma = \frac{1}{N} \sum_{i=1}^{i=N} [xi - \bar{x}]^2 \qquad (2)$$

3- root mean square (rms) : the rms value Xrms of a function x(t) over an interval of N is :

$$X_{rms} = \sqrt{\frac{1}{N} \sum_{i=0}^{i=N} (x_i)^2} \qquad (3)$$

4- the crest factor CF: is the ratio of the peak level(Xmax) to the RMS level (Xrms)

$$CF = \frac{\text{Xmax}}{\text{Xrms}} \qquad (4)$$

5- the skewness S : is the third statistical moment of a distribution :

$$S = \frac{1}{N\sigma^3} \sum_{i=0}^{i=N} (x_i)^3 \qquad (5)$$

6- the kurtosis K : is the fourth statistical moment of distribution :

$$K = \frac{1}{N\sigma^4} \sum_{i=0}^{i=N} (x_i)^4 \qquad (6)$$

Time-series models of the sensor signals are constructed and the model coefficients are used as features indicative of crack **(Kuo 1999, Ravindra 1997 and Obikawa 1996)**. This is because the model coefficients represent the characteristic behavior of the signal. Depending on the order of the model, a number of model coefficients can be chosen. Normally, only the first model coefficient, or sometimes the first three to four model coefficients are chosen, because they are most descriptive of the signal characteristics of interest. In this case coefficients from (AR) models were considered. A brief discussion of these models follows **(Rueben 1998).**

In a pth-order AR model for a time series x (n), where n is the discrete time index, the current value of the measurement is expressed

as a linear combination of p previous values:

x(n)= a1 x(n-1)+ a2 x(n-2)+………ap x(n-p) (7)

Where a1, a2, a3… ap are the AR coefficients. The first AR coefficient was chosen as a feature.

Frequency Domain Feature:

The most common frequency domain characteristic in the literature is the spectral energy around the first natural frequency of the tool-work piece system **(Rueben 1998)**. It was established that the fundamental natural frequency for this system lies at about 8.5 kHz. The spectral energy at 8.5 KHz was taken as a feature.

$$\psi_{xb}^2 = \int_{fl}^{fh} S_X(f)df \tag{8}$$

With $S_x(f)$ the one-sided PSD function and fl and fh the lower and upper frequencies chosen to reflect the energy in the region of interest.

Wavelet Packet Analysis Feature

The wavelet transform is a relatively new method of signal processing that has been applied to many engineering studies with great success. Fairly recent studies also proved that wavelet analysis could be utilized for monitoring of the machining process **(Jiang 1987)**. The success of the wavelet transform is generally attributed to the natural shape of the wavelet, which is more descriptive of most natural processes than the sine function used in Fourier analysis. Wavelet analysis is capable of revealing aspects of data that other signal analysis techniques miss, like trends, breakdown points, discontinuities in higher derivatives, and self-similarity. In this instance, wavelet packet analysis was used to generate features that may show consistent trends towards tool and work piece wear. Like other wavelet analysis techniques such as (DWT), wavelet packet analysis also requires the construction of a wavelet decomposition tree. Each packet in the decomposition tree contains information on the original signal in the form of wavelet coefficients. The original signal can be reconstructed using any chosen number of the packets on the tree. However, the normal practice is to choose the packets containing the most information on the original signal, and then discarding the packets containing noise or less important information. Usually, an energy-based approach is used to choose the optimal packets. The Shannon entropy formula was used, see equation (9), which is a non-normalized entropy involving the logarithm of the squared value of each signal sample or, more formally **(Obikawa 1996)**,

$$E = -\sum_i S_i^2 \log(S_i^2 \tag{9}$$

Where E is the Shannon entropy and S_i is the signal sample at instant i.

In this study, the method requires that a reliable wavelet packet analysis be established for the given signal. The reliability of the wavelet packet analysis can be investigated in a number of ways, such as assessing the cross-correlation, rms error and cross-coherence between the original signal and the reconstructed signal. A number of packets containing the most energy representative of the original signal must then be chosen. The order of the decomposition tree will determine the maximum number of representative packets that may be chosen.

Wear classification using neural network (SOM):

The self-organizing maps, developed by Kohonen **(Kohonen 1998)**, is a fairly new and effective software crack for data analysis. The SOM has been implemented successfully in numerous applications, in fields such as process analysis, machine perception, control and communication **(Surender 1994)**. The SOM implements the orderly mapping of high-dimensional data onto a regular low-dimensional grid. Thereby the SOM is able to identify hidden relationships between high-dimensional data into simple geometric relationships that can be displayed on a simple figure. The SOM can generally be described as a neutral network with self-organizing capabilities. Most neural networks require information and interaction from the user for classification. Although the SOM was intended as a data visualization tool, it can be used for classification as well. The SOM automatically arranges the data on a two-dimensional grid of neurons where similar observations are placed close to one another and dissimilar ones further away. If the classes of some of the observations are known, certain regions on the grid could be allocated for these classes. The computation of the SOM is a non-parametric, recursive regression process. The incremental-learning SOM algorithm can be described briefly as follows: Regression of an ordered set of model (initialization) vectors mi Є □□Rn into the space of observation vectors xi Є □□Rn is often made by the following processes:

$$mi(t + 1) = mi(t) + hc(x),i(x(t) – mi(t)) \qquad (10)$$

Where t is the index of the regression step, and the regression is performed recursively for each presentation of a sample of x, denoted x (t). The scalar multiplier hc(x),i is called the neighborhoods function, which causes similar observations to be placed in the same region on the map. Its first subscript c = c(x) is defined by the condition

$$\forall_{\mathrm{I},} \ \|x(t) - m_c(t)\| \leq \|x(t) - m_i(t)\| \qquad (11)$$

which means that mc (t) is the model that matches best with x(t). The neighborhoods function is often taken as the Gaussian function. Note that a batch version of algorithm exist which is computationally much faster.

RESULT AND DISCUSSIONS

Flank Wear Accursed in Machine Cutting Tool due to Crack

The sudden flank wear for tests (1) are shown in **Fig** (3). Certain features of flank wear are identified, first an extreme condition of flank wear often appears on the cutting edge at locations corresponding to the original surface of the work piece it is called (notch wear) .It is accrue because the original work surface is harder and more abrasive than the internal material due to sand particles in the surface from casting or other reason. As a consequence of the harder surface, wear is accelerated at this location. At this level of the tool wears, when the machining process continue the fracture was increased, very high noise appeared and surface roughness of the work piece became very bad **(Surender 1994)**.

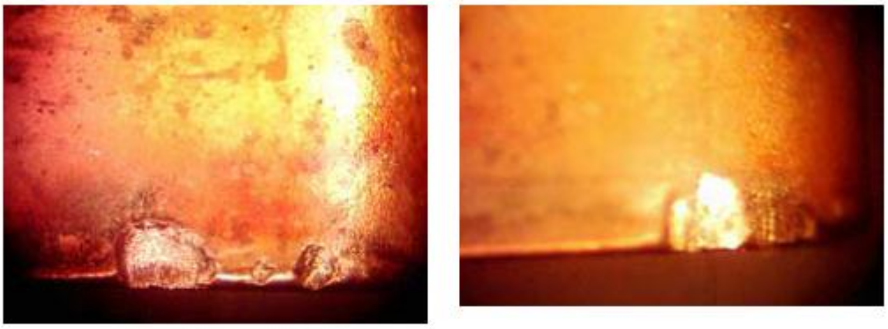

Fig (3) sudden wear at cutting tool due to presenting crack in work piece , wear land (0.33 - 0.2)mm (test1).

Effect of Cutting Condition Tool Life :-

Table (4) represent test with constant D.O.C and different cutting conditions , gave loot life of (13 , 17) min respectively . from these tests it could be seen the tool life decrease with decrease in cutting speed and feed rate . It is occur because the original work surface crack and harder particles in the surface . As a consequence of crack or hard particles , wear is accelerated at this location .

Properties of Signals in Tool Condition Monitoring:

In the metal cutting, the signal from (strain and vibration) sensor is a transient energy spontaneously released in material undergoing deformation or fracture or both. At microscopic level, signal is related to grain size ,dislocation density ,and distribution of the second-phase particles crystal-line form **(Kannatey 1982)** .The signals from (strain and vibration) sensor generator during cutting operation are non stationary and may pass a different magnitude , damping ,frequency and phase **(Stern 1971 and Du 1991)**.

Fig (4) shows the sample of signals for (strain and vibration) sensor. The signal generated from the data sample at 25600 Hz at 1 second contains 25600 data point, for both strain and vibration signal from a turning operation. The continuation of the signal is contributed for by deformation of work piece material at shear zones, the friction at tool work piece and chip –tool contact regions. In **Fig (5)** the approximately constant amplitude signal that run throughout the record, constitute the continuous part of the signals. Superimposed on the continuous part, the transient part of the signal is generated by micro-cracks of the crystal structure of work piece material, nonhomogeneity of work piece material and chip breakage. The high amplitude short –duration signals that appears in all figures are the transient parts of the signal **(Kamarthi 1997)**.

The signal generated from a machining process fundamentally depends on properties of tool and work piece materials applied stress, strain rate and material volume involved in the deformation process. In cutting process, the signal form the function between the tool and

work piece can be distinguished from the signals generated by the chip-breakage and the material deformation process at the share zones this can be shown in **Fig (5)**, where the chip-breakage generated no uniform signal while the material deformation zone make the signal be approximately stable and this can be shown clearly in the feature curves because the chip breakage make the curve flow up or down instantaneously.

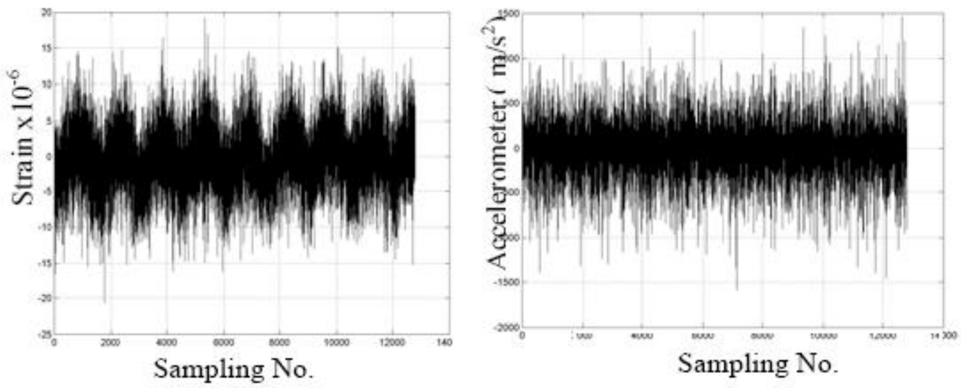

Fig (4) Samples of vibration and strain signals

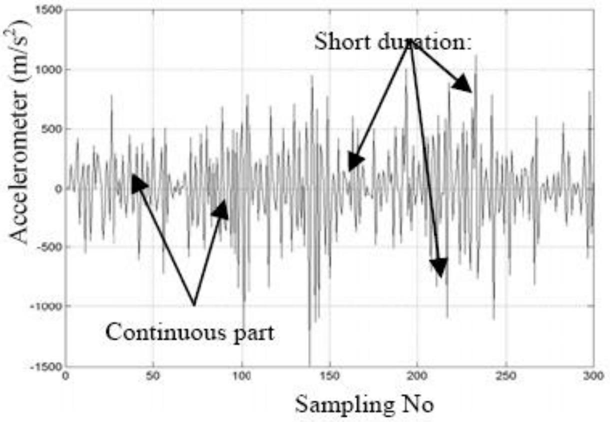

Fig (5) vibration signals for 300 sampling no.

Strain Signals Measured During the Tests and It's Effect of Crack

As the signal spectral is sensitive to tool wear and tool fracture, it is possible to use signal for tool condition monitoring, the strain signal as shown in **Fig (4)** is basically sinusoidal in nature. During the course of their propagation, they often undergo considerable changes to scattering by structural defects, multiple reflect at interface and refraction where there is a medium change along the travel path **(Kamarthi 1997)**. **Fig (6)** which show the strain signal measured for cutting tool in test 1 with cutting speed 136.6 mm/sec and feed 0.23 mm/rev when the crack appear on the work piece. Fig(6a) shown clearly that the strain signal have an greatest effect when the crack accurse , where the signal have an negative shoot at the lower frequency of the signal between (1000-3000) Hz. Fig (6b) shows the same signal when the is no crack accursed in work piece where there is no negative shoot in the strain signal. **Fig (7)** shows the power spectral density for the same which shown the signal have a high constricted at the lower frequency when the crack at the work-piece accursed. This produce an indication that when the crack appeared in the work piece the strain signal have an negative shoot indication at the lower frequency of the signal

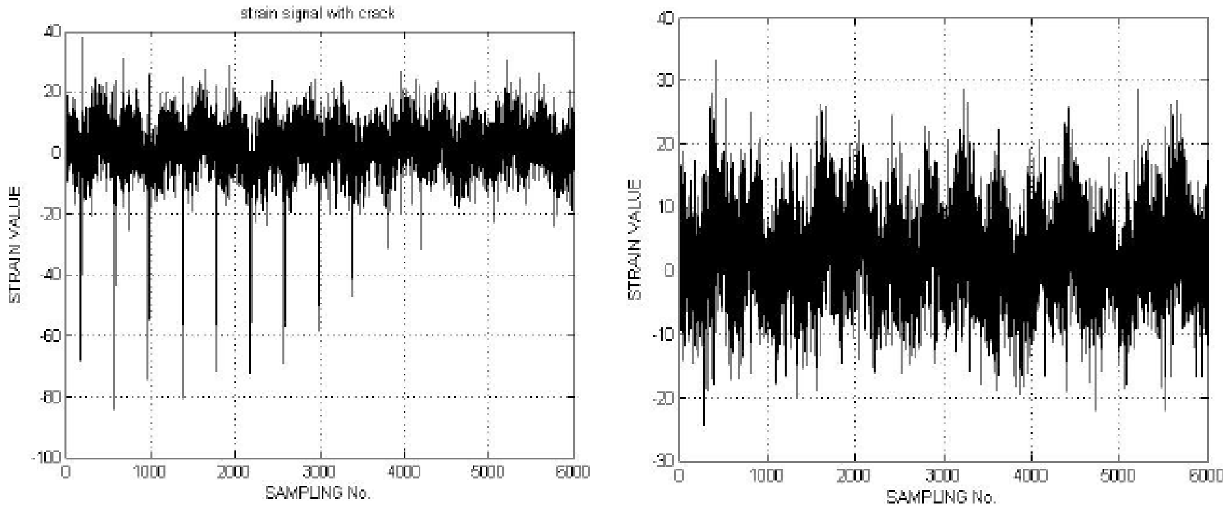

(a) (b)

Fig(6) a: strain signal with crack

b: strain signal without crack.

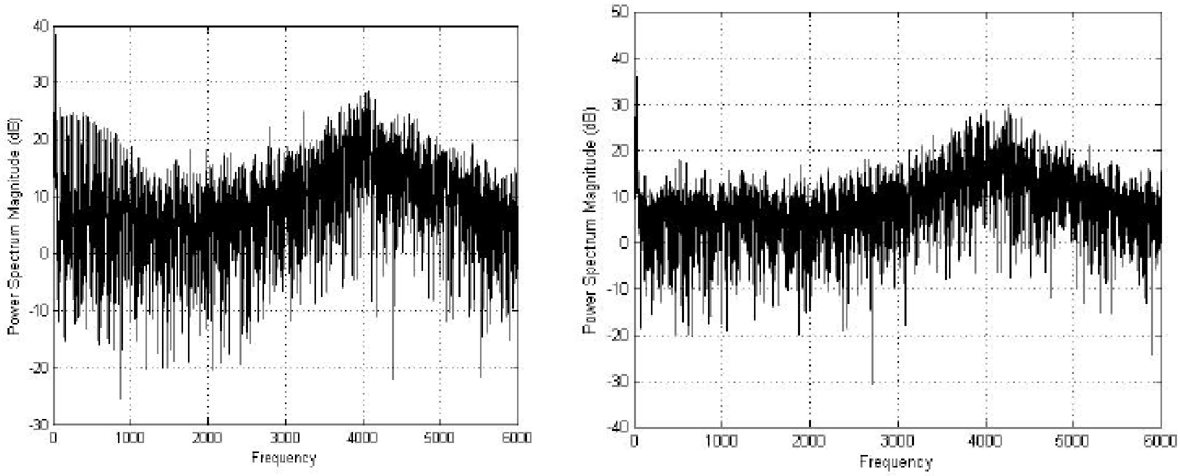

(a) (b)

Fig (7) a: PSD for strain signal with crack
b: PSD for strain signal without crack.

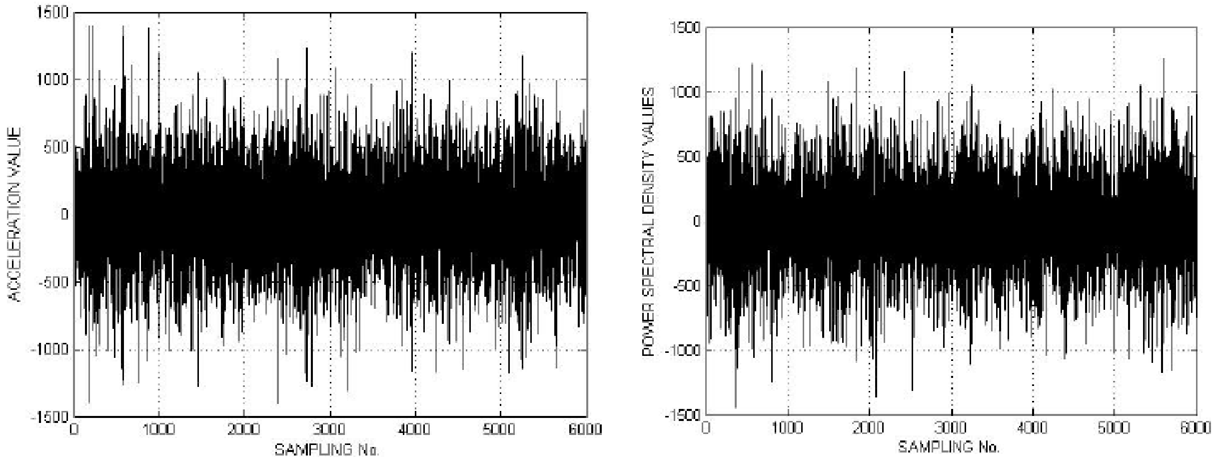

(a) (b)

Fig (8) a: vibration signal with crack
b: vibration signal without crack.

Vibration Signals Measured During the Tests and Its Effect of Crack

The vibration signal has a high effect on strain signal during the machining process. As can be show in **Fig (8a)** where the crack appear at the work piece and compare the result with **Fig (8b)** where the crack are not appear we can found there is no trend of vibration signal at the crack of the work piece, this is because the vibration signal result from many external recourses such as gear of cutting machine and other dynamic influence which make the lower frequency not sensitive at the crack in work piece. Also **Fig (9)** which shows the PSD for the vibration signal in both state not give any pure indication towered the crack.

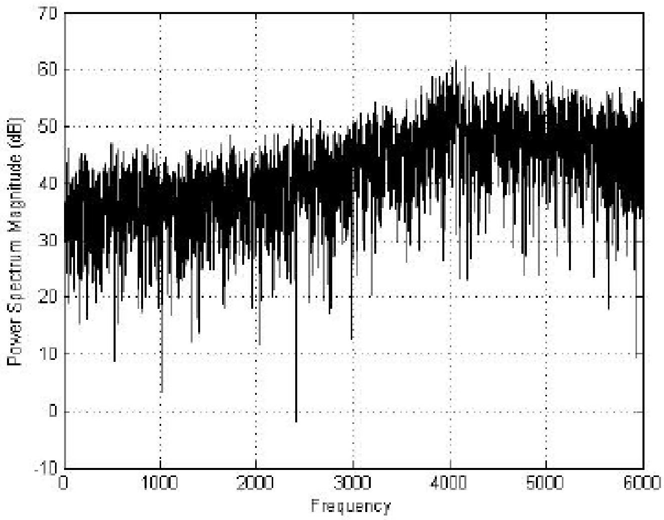

(a)

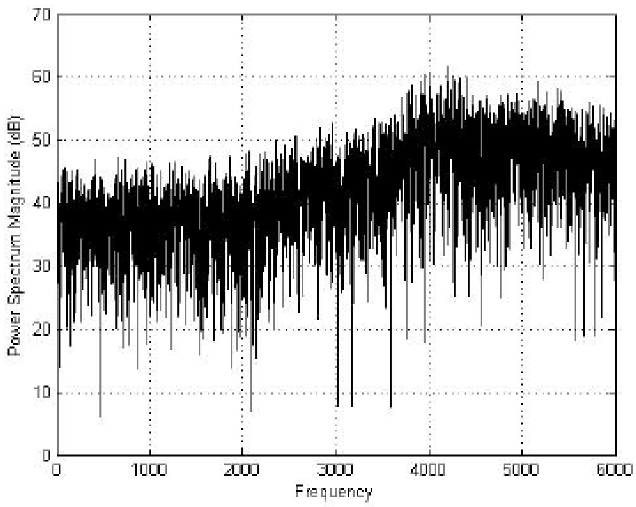

(b)

Fig (9) a: PSD for vibration signal with crack
b: PSD for vibration signal without crack.

Crack Effects at the Feature Extracted Form Measured Signal

All the feature which are extracted from the measured signals and used to recognized the effect of crack at the strain and vibration signal can be shown in **Table (5)**. When analyzing these feature it can be found that the strain feature has a greatest trend toward crack than the vibration signal. Other that there is a feature has good trend towered crack that others. The time features for strain signal such as (mean, STD, RMS) given a good indication toward crack where it's values when the crack found lower than when the crack disappear. Wavelet packet analysis feature have good indication for crack, such as wavelet packet for (STD, S, K, RMS). In wavelet packet we know it's divide the signal in lower and highest frequency and then select the lower frequency which give good indication for the signal behavior, so in this work we choose the wavelet packet (1 and 3) to represent the effect of crack in wavelet packet domain, in modeling domain feature the auto regressive have good indication towered crack where it's value where the crack happened lower than when the crack disappear. All features for strain signal have the same behavior for crack which it's value with presented the shrinkage and crack are lower than it's value when the crack disappear. For the vibration signal all the feature have lower trend toward crack where it's values with present crack approximately the same without present the crack.

Table (5) features values for strain and vibration signal measured during machining process

features	Strain signal with crack	Strain signal without crack	Vibration signal with crack	Vibration signal without crack
Mean	1.3612	51.477	2.5952	2.8035
STD	9.735	148.1	358.33	351.06
RMS	105.44	3987.4	201.02	217.16
CF	0.35845	0.16752	6.9225	5.801
S	1.0934e+013	8.4593e+013	2.2063e+007	1.1244e+008
K	4.41e+018	6.7478e+019	1.1244e+011	9.8614e+011
WS1	10.146	109.39	175.79	170.09
WS2	9.2921	178.53	475.17	466.55
WS3	13.143	123.92	127.55	129.63
WS4	5.6827	92.217	213.85	202.49
WR1	75.119	2825.5	143.29	154.36
WR2	2.242	87.388	532.37	447.43
WR3	53.92	2007	103.16	109.8
WR4	2.7417	6.0201	46.03	109.99
W1CF	0.31056	0.15768	4.744	5.3746
W2CF	14.862	8.0926	3.238	3.5868
W3CF	0.4681	0.22931	5.193	4.2721
W4CF	15.186	55.881	14.407	6.3551
WK1	2.0635e+062	9.964e+063	1.188e+062	1.3137e+064
WK2	9.9748e+069	3.6012e+065	4.1267e+062	9.5615e+062
WK3	4.1267e+062	1.4139e+064	7.2489e+067	1.866e+062
WK4	1.0767e+064	1.0638e+060	4.6772e+058	5.4921e+062
A(2)	-0.089601	0.37441	0.79146	0.80926

Self Organizing Map for Neural Network:

The selected features from the two learning data sets were used to train (2 x 1) SOM with 10000 epoches. **Figs (10-12)** show the feature of SOM neural network for test 1. The SOM layer for specific feature represent the behavior of that feature curve, there is a two specific layer for crack state. The reason why only a small number of neurons are used is because it makes classification easier (although less flexible). In this case, one neuron is used to correspond to no crack present and one neuron refers to crack presented see **Fig (13)**. When more neurons are used in the network, the regions corresponding to a certain classification become larger, and classification becomes more flexible, because when we increase the number of layer in the output the range of each feature to have a specific layer will decrease so the layer have an precise specific feature. For each of the selected features, a (2 x 1) representative SOM for test 1 can be shown in **Figs (10 - 12)**. It is important to note that although a SOM for each feature is available, the SOM is actually a single entity. A view on a selected feature is only the view in the direction of that dimension. The SOM can represent multidimensional data in this manner. This is illustrated in **Figs (10-12)**, where all the selected variables are shown on a single graph. When color coded, such a figure can display how the values of the features correspond among one another. The observations in the (testing) data set were labeled (no crack) and (crack), corresponding to the number of machined components (work piece used in machining process). The best matching units for these data were looked up on the SOM. As shown in **Fig (13)**, it is clear that neurons 1 correspond to a no crack present and neuron 2 to a rack present. The figures show a SOM layer which distributed corresponding to the best matching units of the test data. It is clear that the trajectory moves in time from the (without crack) to the (crack).

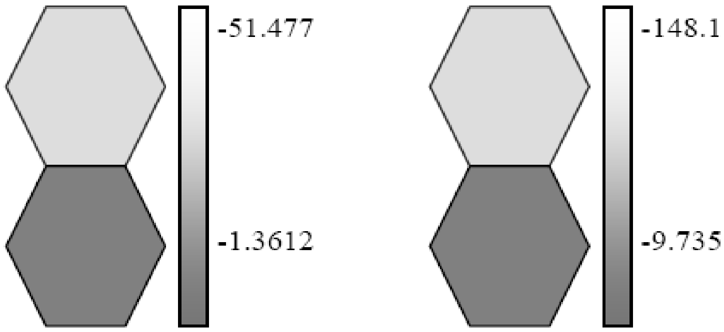

SOM for Mean SOM for standard deviation

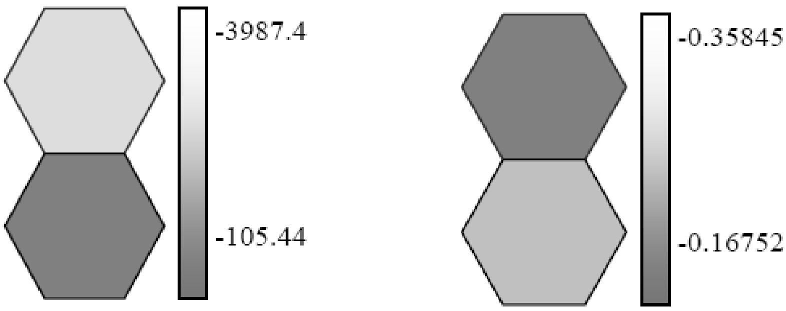

SOM for root mean square SOM for crest factor

Fig (10) SOM for time domain feature for strain signal test (1).

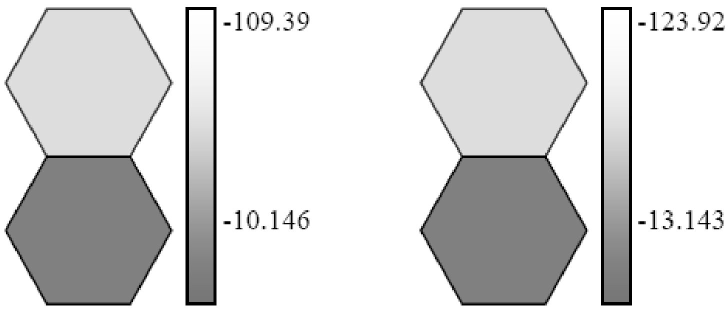

SOM for STD for Wavelet packet (1) SOM for STD for Wavelet packet (3)

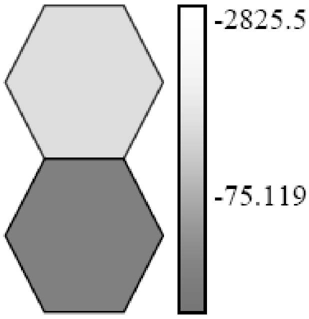

SOM for RMS for
Wavelet packet (1)

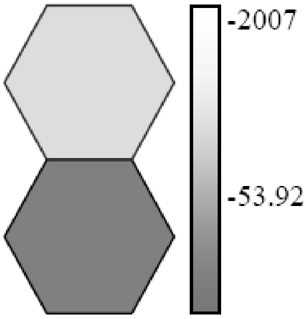

SOM for RMS for
Wavelet packet (3)

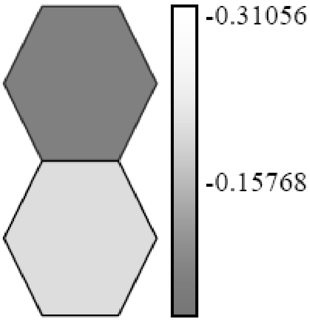

SOM for CF for
Wavelet packet (1)

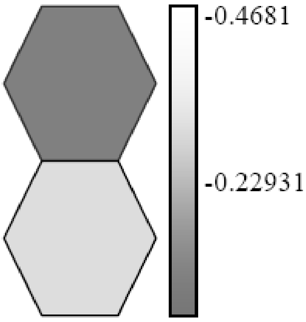

SOM for CF for
Wavelet packet (3)

Fig (11) SOM for wavelet packet analysis features for strain signal test (1).

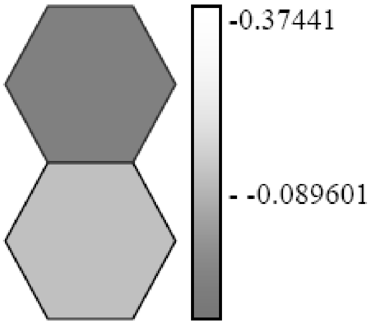

Fig (12) SOM for Auto regressive at strain signal for test (1).

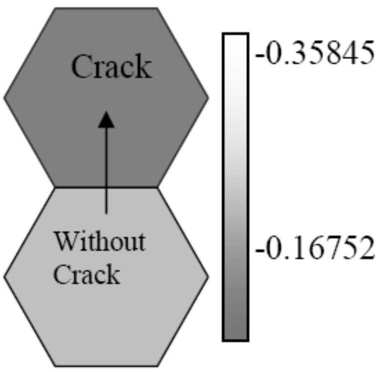

Fig (13) SOM for Crest Factor at strain signal for test (1) with label.

CONCLUSIONS

1- The monitoring system can extract and select features quickly enough to enable the manufacturer to implement an on-line monitoring system.

2- The result we showed that vibration signal has a lower trend toward crack than a strain signal during a machining process.

3- Most features give approximately a behavior toward crack, that when the crack present the features vales became lower values than when the crack not present.

4- RMS, STD, mean, PSD for 8.5 KHz, wavelet features for packet (3), it gives a better indication of tool wear than other features.

5- When using SOM neural network a best correct classification of the tool can be obtained.

6- There are a cutting condition (feed rate & cutting speed)with constant depth of cut in machining process , which give good indication result for tool life and number of work – piece (with and without crack) used.

7- A vibration signal has a high effect on strain signal during a machining process.

REFERENCES

Du R. and Yan 1991 .”time- frequency distripution of Acoustic Emission Signal for tool wear detection in turning”.

C. Y. Jiang, Y.Z. Zhang and H. J. Xu 1987 ,” In-Process monitoring of tool wear stage by the frequency band energy method.” 45-48.

S.V.Kamarthi.1997 “Flank wear estimation in turning through wavelet representation of acoustic emission signals” Departement of mechanical, indestrualand manufacturing engineering, Northeastern University.

I. Kandilli and H.Metin 2003. “development of On-Line monitoring system for tool wear in cutting operations.” International XII. Turkish Symposium on Artificial Intelligence and Neural Networks.

Kannatey A.1982.” Study of tool wear using statistical analysis of metal-cutting Acoustic Emission.” No.2 247-261

T. Kohonen 1998 Neuro computing 21, 1-6. The self-organising map.

R. J. Kuo and P. H. Cohen 1999 “Multi-sensor integration for online tool wears estimation through radial basis function networks and fuzzy neural network” .Neural Networks 12, 355-370.

A. Nadgir and Tugrul Özel. July 30-August 2, 2000, “Neural network modeling of flank wear for tool condition monitoring in orthogonal cutting of hardened steels.” International Conference on Engineering Design and Automation, Orlando, Florida, USA.

T. Obikawa, C. Kaseda, 1996 “Tool wear monitoring for optimizing cutting conditions” Journal of

Materials Processing technology 62, 374-379.

H. V. Ravindra, Y. G. Srinivasa 1997 "Acoustic emission for tool condition monitoring in metal cutting" 212, 78-84.

R. L. Rueben, R. G. Silva, , K. J. Baker and S. J. Wilcox 1998 "Tool wear monitoring of turning operations by neural network and expert system classification of a feature set generated form multiple sensors." Mechanical Systems and Signal Processing 12, 319-332

C. Scheffer , P.S.Heyns 2001 "Wear monitoring in turning operations using vibration and strain measurements" Mechanical Systems and Signal processing 1185-1202.

R. G. Silvas,2000 "The adaptability of a tool wear monitoring system under changing cutting condition" Mechanical Systems and Signal Processing . 287-298

K.Stern 1971 "Application of correlation analysis to Acoustic Emission " ASTM,Philadelphia.

Surender K. and others.1994. "production engineering design (tool design)" 179-180.

Xiaoli Li, Shiu Kit Tso 2000. "Monitoring Using Wavelet Transforms and Fuzzy Techniques" IEEE Transactions on system, man, and cybernetics Vol. 30, No. 3.

Notification:

A	cross section area of shaft.(mm2)	N	Number of sampling
Ac	alternative current.(A)	n1	Net input in neural network
A/D	analogue to digital converter	Pc	personal computer
AE	acoustic emission	PSD	power spectral density
AR	auto regressive	R	input vector
ARMA	auto regressive moving average		
ANN	adaptive neural network	RMS	Root mean square
Rn	end condition parameter	S	Skew ness function
BPNN	Back propagation neural network		
C	SOM function	SOM	Self organizing map
Cf	crest factor	SOMF	Self organizing map function
DAQ	Data Acquisition Card	T	Time (sec.)
DSPT	Digital signal processing transformer		
DWT	Discrete wavelet transform	TCM	Tool condition monitoring
F	feed rate (mm/min)		
f	frequency function	VB	Vibration signal
(n)	wavelet function	X	Mean value
h(n)	wavelet function		
ICP	Integrate circuit programming		

I.D.D	Independent Identification Distribution
K	kurtosis function
L	length shaft
MA	Moving average

NUMERICAL INVESTIGATION OF LAMINAR NATURAL CONVECTION IN RECTANGULAR ENCLOSURES OF POROUS MEDIA

Dr. Ala'a A. Mahdi
College of Eng.
Mech. Dept.
Kufa University

Ass. Prof Dr. Majid H. Majeed
College of Technology
Al Najaf
F. T. E.

Selah M. Salih
College of Eng.
Mech. Dept.
Kufa University

ABSTRACT

In this investigation, steady two-dimensional natural convective heat transfer in a rectangular porous cavity, (heated from below) with horizontal walls heated to uniform but different temperatures and adiabatic sides has been studied numerically. The numerical results of heat transfer rates are presented for porous Rayleigh numbers (Ra^*), based on width of cavity, in the range ($Ra^* \leq 500$), with layer aspect ratios (Ar), (height/width) ranging between ($0.5 \leq Ar \leq 5$). Plots of streamlines and isotherms to show the behavior of the flow and temperature distribution are presented. The current study shows that the Nusselt number is a strong function of the porous Rayleigh number, and the geometry of the cavity is represented by aspect ratios. Porous Rayleigh number has a large effect on the flow field, whereas any increase in (Ra^*) results in changing the flow pattern from unicellular to multicellular flow. Correlation equation has been obtained to show the dependence of Nusselt number on the porous Rayleigh number, and aspect ratio (Ar), as this correlation will be beneficial in design of systems of thermal insulators in the energy storage engineering applications.

الخلاصـــــــة

في هذا البحث ، تم إجراء دراسة عددية لانتقال الحرارة بالحمل الطبيعي المستقر ثنائي البعد في تجويف مسامي مستطيل الشكل، (مسخن من الأسفل) له جدران أفقية مسخنة إلى درجات حرارة منتظمة ولكن مختلفة والجوانب معزولة. تم تمثيل النتائج العددية لمعدلات انتقال الحرارة بعدد رالي المسامي (Ra^*) المحسوب على أساس عرض التجويف، في المدى ($Ra^* \leq 500$) ولنسب أبعاد (Ar) ، (الارتفاع / العرض) تمتد من ($0.5 \leq Ar \leq 5$). لقد تم عرض رسومات لخطوط الانسياب ولخطوط درجات الحرارة لوصف سلوك الجريان وتوزيع درجات الحرارة. بالإضافة ، بينت إن عدد نسلت هو دالة قوية من عدد رالي المسامي ونسبة الأبعاد. أن عدد رالي المسامي يمتلك تأثير كبير على مجال الجريان، حيث أن أي زيادة بعدد رالي المسامي (Ra^*) يسبب تغيير لشكل الجريان من جريان أحادي الخلايا الى جريان متعدد الخلايا. تم إيجاد معادلة تقريبية تبين اعتمادية عدد نسلت على عدد رالي المسامي ونسبة الأبعاد، وان هذه العلاقة يمكن الاستفادة منها في تصميم العوازل الحرارية من اجل حفظ الطاقة في التطبيقات الهندسية.

KEY WORDS: Heat Transfer, Numerical Solution, Free Convection, Rectangular Porous Medium

INTRODUCTION

Natural convection heat transfer in enclosures involves different aspects of problems. This variety of problems comes from possibly geometry characteristic of enclosures, type of fluid, nature of fluid flow, orientation of the enclosure etc. The most studies of natural convection in enclosures, based on tow-dimensional or three- dimensional parallelogram enclosure investigation, annuli and cylinders with different aspect ratio or diameters, or caliber. It's very interesting because of sensibility of natural convection phenomena from geometry. Important thing like aspect ratios of enclosures according to acceleration gravity vector, produce variety of physical situation. Also the type of fluid with influence on natural convection phenomena. If new phenomena are added like radiation, change of fluid phase, porous media, and chemical reaction and so on, have very difficult physical models often unsolvable, **(Miomir, 2001)**.

In general natural convection is one of the important modes of heat transfer. This phenomenon has been observed in numerous environmental circumstances. It occurs frequently as a result of density inversion caused by either the thermal expansion of a fluid, or the concentration gradients within a fluid system. Natural convection can also happen in a porous medium saturated with a fluid. Generally, the porous medium is a solid with voids in it. These voids are interconnected with each other so that it is possible for a fluid to penetrate the medium. There are many fields of application of flow through porous media ranging from industrial processes in factories to the movement of oil or gas in an oil field, **(Bouwer, 1978)**, and **(Raudkivi, and Callauder, 1976)**. Natural convection heat transfer in porous enclosures commonly takes place in nature, and engineering and technological applications. This phenomenon plays an important role in diverse applications including thermal insulators, storage of solar energy in underground containers, underground cable systems, heat exchangers, food industry, biomedical applications and heat transfer from nuclear fuel rod bundles in nuclear reactors, **(El Kady, 1999)**. Over the past years, more emphasis is put on natural convection in porous media due to its growing importance in engineering and geophysical areas. The analysis of the fluid flow and heat transfer for natural convection is difficult. Only a few problems have been solved analytically, many more have been solved numerically, **(Dawood, 1991)**. In particular, when air is trapped in the void space of fibrous porous media, the overall thermal conductivity of the medium is very low, consequently these emphasis is put on natural convection in porous media due to its growing importance in engineering and geophysical areas.

The present work involves a numerical study of the effect of porous Rayleigh number on laminar natural convection heat transfer in a rectangular enclosure filled with a porous medium heated from below. Also, the object of this investigation is to study the influence of geometry of enclosure represented by aspect ratios (Ar) on the behavior of fluid flow and heat transfer by free convection through a porous medium.

MATHEMATICAL FORMULATION

The problem under investigation, consists of a two-dimensional porous cavity has opposite isothermal hot and cold walls, at temperatures (T_{ho} & T_{co}), respectively, and adiabatic vertical walls. Physical model of the enclosure is represented on **Fig. (1)**. The cavity is fully filled with a porous media saturated with fluid, and all the surfaces are impermeable.

In the porous medium, Darcy's law is assumed to hold, and the fluid is assumed to be a normal Boussinesq fluid. The viscous drag and inertia terms in the governing equations are neglected, which are valid assumptions for low Darcy and particle Reynolds numbers. With these assumptions, the continuity, momentum and energy equations for steady, two-dimensional flow in an isotropic and homogeneous porous medium are

$$\frac{\partial u}{\partial x}+\frac{\partial v}{\partial y}=0 \tag{1}$$

$$u=\frac{-K}{\mu}\left(\frac{\partial P}{\partial x}\right) \tag{2}$$

$$v=\frac{-K}{\mu}\left(\frac{\partial P}{\partial y}-\rho_f g\right) \tag{3}$$

$$u\frac{\partial T}{\partial x}+v\frac{\partial T}{\partial y}=\alpha_e\left[\frac{\partial^2 T}{\partial x^2}+\frac{\partial^2 T}{\partial y^2}\right] \tag{4}$$

In the above equations, (u, v, μ, P, T) are the fluid velocity components **Fig. (1)**, the viscosity, the pressure and the temperature. The two momentum equations (2), and (3) reflect the Darcy flow model, where (K) stands for the permeability of the porous material. It is assumed that the fluid and the porous solid matrix are in local thermal equilibrium, at temperature $T(x,y)$. The thermal diffusivity (α_e)is defined as ($\alpha_e = k_e/\rho_f cp_f$) where, (k_e) is the effective thermal conductivity of fluid-saturated porous matrix composite and ($\rho_f cp_f$) is the thermal capacity of the fluid alone.

The governing equations (1)-(4) reflect also the Boussinesq approximation, where by the fluid density (ρ_f) is regarded as a constant except in the body force term of the vertical momentum Eq. (3) where it is replaced by

$$\rho_f \cong \rho_o\left[1-\beta(T-T_o)\right] \tag{5}$$

Using this approximation, and eliminating the pressure terms between eqs. (2), and (3), yields a unique momentum conservation statement,

$$\frac{\partial u}{\partial y}-\frac{\partial v}{\partial x}=-\frac{\rho_o g\beta k}{\mu}\frac{\partial T}{\partial x} \tag{6}$$

The above equations are subjected to the following boundary conditions:

Impermeable walls
$$u=0 \quad \text{at} \quad x=0,\mathrm{L}, \qquad v=0 \quad \text{at} \quad y=0,\mathrm{H}, \tag{7}$$

Isothermal horizontal walls
$$T=T_{ho} \quad \text{at} \quad y=0, \qquad T=T_{co} \quad \text{at} \quad y=\mathrm{H}, \tag{8}$$

adiabatic vertical walls $\frac{\partial T}{\partial x}=0 \quad at \quad x=0, L,$ (9)

NUMERICAL PROCEDURE

The mathematical problem formulated above was first placed in dimensionless from by defining the new dimensionless variables

$$x_* = \frac{x}{L},\ y_* = \frac{y}{L}$$

$$\psi_* = \frac{\psi}{\alpha_e},\ \theta = \frac{T - T_{co}}{T_{ho} - T_{co}} \tag{10}$$

where, (ψ) is stream function ($u=\frac{\partial \psi}{\partial y}$, $v=-\frac{\partial \psi}{\partial x}$) and ($\Delta T = T_{ho} - T_{co}$). The dimensionless forms of the momentum and energy equations are then

$$\frac{\partial^2 \psi_*}{\partial x_*^2} + \frac{\partial^2 \psi_*}{\partial y_*^2} = -Ra^*\left[\frac{\partial \theta}{\partial x_*}\right] \tag{11}$$

$$\frac{\partial \psi_*}{\partial y_*}\frac{\partial \theta}{\partial x_*} - \frac{\partial \psi_*}{\partial x_*}\frac{\partial \theta}{\partial y_*} = \frac{\partial^2 \theta}{\partial x_*^2} + \frac{\partial^2 \theta}{\partial y_*^2} \tag{12}$$

Where, (Ra^*) is porous Rayliegh number, based on width of the enclousre, and defined as:-

$$Ra^* = Da * Ra = \frac{Kg\beta L\Delta T}{\nu\alpha_e} \tag{13}$$

The corresponding dimensionless from of boundary conditions (7) – (9) is:-

$$\theta = 1,\quad \psi_* = 0 \qquad at \quad y_* = 0 \quad , for \quad 0 \le x_* \le 1$$

$$\theta = 0,\quad \psi_* = 0 \qquad at \quad y_* = Ar \quad , for \quad 0 \le x_* \le 1$$

$$\frac{\partial \theta}{\partial x_*} = 0, \psi_* = 0 \qquad at \quad x_* = 0 \quad and \quad 1 \quad , for \quad 0 \le y_* \le Ar$$

The physical quantity of interest in this problem is the average Nusselt number along the hot wall, defined by

$$Nu = \frac{Q_{conv.}}{Q_{cond.0}} \tag{14}$$

The ratio of the convective to conductive heat transfer rates and (0) indicates porous Rayleigh number ($Ra^* = 0.0$). The convective heat transfer is calculated from:-

$$Q_{conv.} = -k_e \int_0^L \left(\frac{\partial T}{\partial y}\right)_{y=0 \quad or \quad H} dx \tag{15}$$

Where as the conductive heat transfer is calculated from:

$$Q_{cond.0} = k_e L \frac{\Delta T}{H} \tag{16}$$

Thus, eq.(14) becomes

$$Nu = -Ar \int_0^1 \left(\frac{\partial \theta}{\partial y_*}\right)_{y_*=0} dx_* \tag{17}$$

Numerical method is used to compute the stream function and temperature distribution for the porous cavity. A finite-difference technique is applied to solve the governing equations. The upwind differences method is used for the transport terms in the energy equation. All other terms in the energy and momentum equations are discretized by central differencing. The successive substitution formulas derived in this way satisfy the convergence criterion and are quite stable for many circumstances, **(Najdat, 1987)**. The choice of an already-used numerical scheme was intentional, in order to be able to check the validity of the present results against published results for the no-obstruction case (l/L=0); this test is presented later in this section. The finite difference approximation of the governing equations was based on dividing the ($0 \le x_* \le 1$) interval into (m) equal segments separated by ($m+1$) nodes. Likewise, the (y_*) interval was divided into (n) segments. The numerical worl starts with postulating a certain distribution of flow and temperature in the ($x_* - y_*$) space ; in the present solution of distributions were taken as ($\Psi_*=0$) and ($\theta = y_*$), i.e. no flow and pure conduction. Based on these old fields, the momentum equation (12) is used to determine point-by-point the new (Ψ_*) field, while the energy equation (13) is used to determine the new (θ) field. The iteration process is terminated under the following condition

$$\sum_{i,j} \left|\tau^{r+1}{}_{i,j} - \tau^{r}{}_{i,j}\right| \Big/ \sum_{i,j} \tau^{r+1}{}_{i,j} \le 10^{-5} \tag{18}$$

where,(τ) stands for either (ψ_* or θ); (r) denotes the iteration step.

Before starting the computational solution, the grid independence of the results must be tested. Thus, numerical experiments have been carried out to solve a two-dimensional convection problem. The porous Rayleigh number in this test is set to be (300), while the grid size varies from (10×10) to (70×70) for different values of aspect ratio as shown **Fig.(2)**. It is found that the change in the heat flow rate for grid size of (40×40), and (50×50) is less than (0.45) percent for the whole range of aspect ratio ($0.5 \le Ar \le 5$). Therefore , the number of grid that is adopted in the present study is (40×40). The number of grid was selected as a compromise between accuracy and speed of computation.

RESULTS AND DISCUSSION

Effect of porous Rayliegh number on the temperature distribution and flow fields can be clearly seen in **Figs. (3)** to **(6)**. For ($Ra^* \to 0$) the case, heating from below at constant surface temperature, the energy is transported from hot wall to cold wall by pure conduction (i.e. $Nu = 1.0$) for saturated porous media at (Ra^*) less than its critical value. In the conduction regime, the isotherms are almost parallel to isothermal walls. The conduction mode of heat transfer continues until a critical value of Rayleigh number is reached.

For the case of ($Ar=1$), the value of (Ra_c^*) has been found to be equal to (39.5). This is in a good agreement with the value predicted from the linear theory ($Ra_c^* = 4\pi^2$). At this value the onset of convection begins because of the buoyancy effects. Thus, the flow field comprises a primary cell circulating around the entire enclosure with clockwise (this is an arbitrary direction). It may be counterclockwise, **Fig. (3)** and has a maximum value for the stream function ($\psi_{*max} = 1.95$). The small value of (ψ_{*max}) characterizes a very weak convective flow. The isotherms deviate only slightly from those of the pure conduction state. The extremum value of the stream function becomes larger as (Ra^*) increases, indicating a more effective motion, a circulatory motion is established because of the buoyancy influences. In addition, further increase in (Ra^*) results in changing the direction of the isotherms and change the flow pattern from unicellular to multicellular flow. **Fig. (4)** shows the streamlines at ($Ra^*=100$), ($Ar=1$). This flow exhibits two counter- rotating cells, each covering half of the cavity. It also indicates the flow rising slightly in the middle, turning at the top of the cavity, moving adjacent the cold wall, turning, and falling down the insulated wall. The number of cells are increased to three at ($Ra^*=300$) and then reduced to two at ($Ra^*=500$), see **Figs. (5)** , and **(6)**. The same phenomenon has been noticed by (Prasad and Kulacki, 1985).

Effect of aspect ratio on the flow pattern can be inferred with reference to **Figs. (7)** to **(10)**. It is worthwhile to note that any increase in aspect ratio delays the appearance of convective mode. The reasoning for this is as follows. As the aspect ratio increase, the isothermal walls become smaller than the insulated walls. Thus, there is a small area for convective contribution, compared to the path for flow. Also it is seen the flow change to multicellular flow at ($Ra^*=100$) for ($Ar=1$). Now, different values of aspect ratio will be taken to examine the appearance of the multicellular flow. The results of the numerical computations for streamlines and isotherms at ($Ra^*=100$) with ($Ar=0.5,1,1.5$, and 2) are plotted in **Figs. (7)** to **(10)** which show that the number of cells depends strongly on the value of aspect ratio. As depicted in this Figures, two cells appeared at ($Ar = 1$) while the number of cells reduced to one at ($Ar=1.5$). This is expected because the distance between isothermal wall at ($Ar=1$) is smaller than that of ($Ar=1.5$). Thus, the resistance to flow is lower. Also, it is interesting to note that for ($Ar>1$) and ($Ra^*=100$) the flow is still unicellular. While, the onset of convection starts at ($Ra^*=39.5$) for ($Ar=1$). It is worthwhile to note that any increase in aspect ratio delays the appearance of convective mode. **Fig.(11)** represents the relation between the maximum value of stream function (ψ_{*max}) and porous Rayleigh number compared for different values of aspect ratio (Ar). At low porous Rayleigh number ($Ra^* \leq 50$), (ψ_{*max}) seems to be invariable with aspect ratio this is due to dominance of conduction as mentioned before. At higher porous Rayleigh number or when convective becomes dominant, (ψ_{*max}) increases with increasing (Ar), since for a higher aspect ratio, the path along which the ascending flow is heated is longer, the velocity as well as the circulation (ψ_{*max}) becomes higher. It is also show that the peak value of (ψ_{*max}) depends on (Ra^*).

Figure (12) show the variation of Nusselt number versus porous Rayleigh number for aspect ratio ($Ar=1$). Porous Rayleigh numbers take values in the range ($Ra^*=50$ to 500), because of the stability of problem and program into computer. It is clear that (Nu) equal to one in the conduction regime (i.e. at $Ra^* \leq Ra_c^*$). The reason is that the viscous force is greater than the buoyancy force therefore the heat is transported by conduction as discussed previously. In general form, the value of (Nu) increases with increase (Ra^*), as shown in **Fig. (12)**. Then, (Nu) increase rapidly as (Ra^*) increases expressing the existence and increase of convective heat transfer.

The effect of aspect ratio on the Nusselt number, and porous Rayleigh numbers in range (Ra^*=100,150, 300, and 500) is depicted in **Fig. (13)**. It is noted that the aspect ratio has a great effect on the heat transfer results. For (Ra^*=150), it appears that the value of (Nu) increases with an increase in aspect ratio beyond (0.5). It reaches a maximum value of (Nu) at about (Ar=1.5). Then, the value of (Nu) decreases with an increase in aspect ratio in the case (Ar >1.5). This can be explained as follows. For large aspect ratio, the fluid encounters much more flow resistance in the y-direction due to the increased path length. The location of the maximum Nusselt number change with changing porous Rayleigh number. The above Figure also indicated that the Nusselt number is a strong function of porous Rayleigh number. For the range of (Ra^*) which is used in this investigation, the maximum (Nu) is found to be lay between aspect ratio from (0.5 to 1.5). The present result of the rate of heat is in good agreement with those reported by **(Caltagirone, 1975)**, for a porous layer heated from below and **(Chan et.al., 1970)**, for a porous layer heated from side.

Finally, correlation equation has been predicted depending on variation of porous Rayleigh number, and aspect ratio, by using least square method.

$$Nu = 0.2174\left(Ra^*\right)^{0.5256}\left(Ar\right)^{-0.4966} \tag{19}$$

The above correlation is acceptable in the range of porous Rayleigh number (0 to 500), and aspect ratio (0.5 to 5).

To ensure that this approximation correlation is usable, the correlation coefficient (R) had been obtained for each equation. The minimum value of (R) was (0.96) , that means this approximate equation are good for predicting the value of Nusselt number. **Fig. (14)** shows the comparison between predicted and numerical results. Agreement between numerical and predicted is close, although most the predicted points lie near the theoretical line.

The problem is modeled in a rectangular domain subjected to different temperature on it's horizontal sides with the left and right sides are insulated. All the analytical and numerical solutions, and experimental study show that the onset of natural convection in a porous layer starts at ($Ra^* = 4\pi^2$). The numerical solution agrees with those solutions, this is shown **Table (1)**.

Further, values of the average Nusselt number along the hot wall of the cavity at the steady-state flow for (Ra^*= 50, 100, and 200), are given in **Table (2)**. It is seen again that the present values of (Nu) are in very good agreement with that obtained by different authors, such as (Chan et al, 1970). (Burns et al, 1974), have analyzed a similar problem for different values of aspect ratio. The comparison with their results for (Ar=0.5, and 1) show agreements within (± 8 %) except the case for (Ar=1 and Ra^*=200) where the agreements is (± 4 %). (Chan et al, 1970), and experimental investigation presented by (Close, Symons, and White, 1985), presented their results in a graph and some errors might have been introduced in reading the graph. Also, as shown in the table, there are some difference between the present work and those of **(Burns et al, 1974)**, and **(Bejan and Tien, 1978)**. These differences are attributed to the finite difference approximation.

CONCLUSIONS

The problem of steady laminar natural convection in a two-dimensional, porous cavity under uniform temperature on two opposite walls while the other walls are insulated has been studied numerically. The main conclusions of the present study are:

1. For the porous enclousres that have been solved, it has been demonstrated that the Nusselt number (Nu) is a strong function of porous Rayleigh number, the value of (Nu) increases with increase (Ra^*) for same aspect ratio.

2. The heat transfer is represented by Nusselt number (Nu) as a function of the geometry represented by the aspect ratio (Ar). As the aspect ratio increase, the isothermal walls become smaller than the insulated walls. Then the value of (Nu) decreases with an increase in aspect ratio beyond (0.5) for the same porous Rayleigh number. Later, any increase in aspect ratio delays the appearance of convective mode should have been noted.

3. The effect of porous Rayleigh number has a large effect on the flow field. At low value of (Ra^*), the flow field comprises a primary cell circulating around the entire enclosure. The extremum value of the stream function becomes larger as (Ra^*) increases, indicating a more effective motion, a circulatory motion is established because of the buoyancy influences. Further, increase in (Ra^*) results in changing the flow pattern from unicellular to multicellular flow. The number of cells are increased to three at ($Ra^*=300$) and then reduced to two at ($Ra^*=500$).

4. Correlation equation (19), can be used to calculate the rate of heat transfer as a function of (Ra^*), and (Ar). As this correlation will have been benefiting in a design for systems of thermal insulators so that storage of energy in the engineering applications.

REFERENCES

Bejan, A., and Tien, C. L., "Natural Convection in a Horizontal Porous Medium Subjected to an End-to-End Temperature Difference", Journal of Heat Transfer, Vol.100, pp.191-198, 1978.

Bouwer, H., Groundwater Hydrology, McGraw-Hill Book Company, Inc.,1978.

Burns, P. J., Chow, L. C., and Tien, C. L., "Convection in Vertical Slot filled with Porous Insulation", Int. Journal of Heat Mass Transfer , Vol.20, pp. 919-926,1974.

Caltagirone , J. P., " Theroconvective Instabilities in a Horizontal Porous Layer", Journal of Fluid Mech., Vol.72, pp. 269-687, 1975.

Chan, B. K. C., Ivey, C. M., and Barry, J. M., "Natural Convection in Enclosed Porous Medium with Rectangular Boundaries", Journal of Heat Transfer , Vol.2, pp. 21-27, 1970.

Close, D. J., Symons, J. G., and White, R. F., "Convective Heat Transfer in Shallow, Gas - filled Porous Media : Experimental Investigation " , Int. Journal of Heat Mass Transfer, Vol.28, pp. 2371- 2378, 1985.

Dawood, A. S., " Steady Three-Dimensional Natural Convection in Porous Media Via The Multigrid Method " , Ph. D. Dissertation , Dept. of Mech. Eng. , Colorado State University, 1991.

El Kady, M.S., Araid, F.F., El Negiry , F.A., and Abd El Aziz, G.B., "Natural Convection Heat Transfer in an Annular Porous Medium " , 3rd Jordanian Mechanical and Industrial Engineering Conference, JMIEC, PP. 473-482, 1999.

Miomir, R., "Numerical Investigation of Laminar Natural Convection in Inclined Square Enclousres", Series:Physics, Chemistry and Technology Vol. 2, No 3, pp. 149 - 157, 2001.

Najdat Nashat Abdulla, " Laminar Flow Separation in Constructed Channel", Ph.D. Thesis, Michigan State University, 1987.

Prasad, V., and Kulacki, F. A., and Keyhani, M., "Natural Convection in Porous Medium", Journal of Fluid Mech.,Vol.150, pp. 89-119, 1985.

Raed, A., Mehdy, " Studying Two Dimensional Steady Heat Transfer by Natural Convection Through Porous Media Surrounded Isothermal Body", thesis M.sc.,University of Technology, 2002.

Raudkivi, A.J., and Callauder, R.A., Analysis of Groundwater Flow, Edward Arnold, Great Britain, 1976.

NOMENCLATURE

List of Symbols

Ar = Aspect ratio = (H/L)

C_P = Specific heat at constant pressure, $(J/kg.K)$

Da = Darcy number = (K/L^2)

g = Acceleration due to gravity, (m/s^2)

H = Height of cavity, (m)

L = Width of porous cavity, (m)

K = Permeability of porous medium, (m^2)

k_e = Effective thermal conductivity of fluid-saturated porous medium, $(W/m.K)$

Nu = Average of Nusselt number

P = Pressure, (Pa)

Q_{conv} = Convection heat transfer rate, (W)

$Q_{cond.}$ = Conduction heat transfer rate, (W)

Ra^* = Porous Rayleigh number based on width of cavity

T = Temperature, (K)

T_{co} = Temperature of cold horizontal wall, (K).

T_{ho} = Temperature of hot horizontal wall, (K).

u = Fluid velocity in x-direction, (m/s)

v = Fluid velocity in y-direction, (m/s)

x, y = Cartesian coordinates

Greek Symbols

α_e = Thermal diffusivity of porous medium, (m^2/s)

β = Thermal coefficient of volumetric expansion, (K^{-1})

ΔT = Temperature difference between isothermal surfaces = $(T_{ho} - T_{co})$, (K)

θ = Dimensionless temperature = $(T-T_{co})/(T_{ho}-T_{co})$

μ = Dynamic viscosity, $(kg/m.s)$

υ = Kinematic viscosity of fluid, (m^2/s)

ρ = Density, (kg/m^3)

ψ = Stream function, (m^2/s)

$( )_*$ = Dimensionless variables

Table (1) Comparison of the Onset of Convection in two-dimensional porous layer.

	Dawood 1991 Numerical	Caltagirone 1975 Numerical	Present work Numerical
Ra^*	39	44.41	39.5

Table (2) Nusselt number comparison for the present work with the past studies at the same boundary condition.

Ar	Ra^*	Nu					
		Numerical Study Raed 2003	Numerical Study Chan1970	Analytical and Numerical Study Burns1970.	Analytical Study Bejan and Tien 1978	Experimental Study Close, Symons, and White 1985	Present work Numerical
0.5	50	—	1.480	1.430	1.770	1.234	1.363
	100	—	2.500	2.854	2.800	2.244	2.689
1	100	1.897	2.100	2.200	2.120	—	2.289
	200	3.815	3.560	3.600	3.250	—	3.413

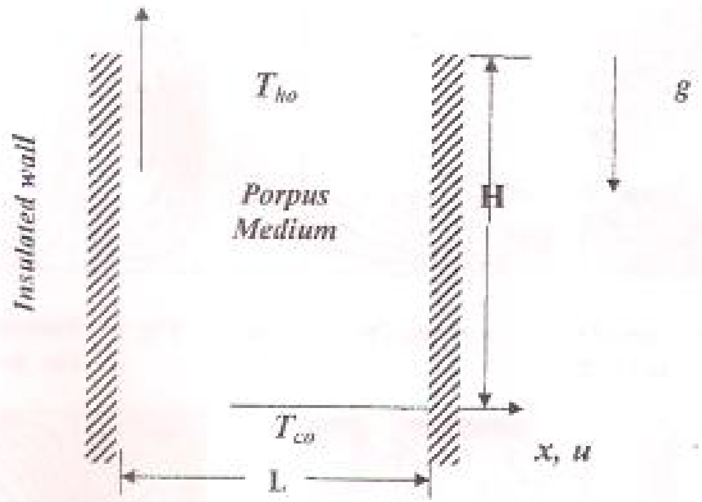

Fig.(1) Schematic diagram of the physical model and coordinate system.

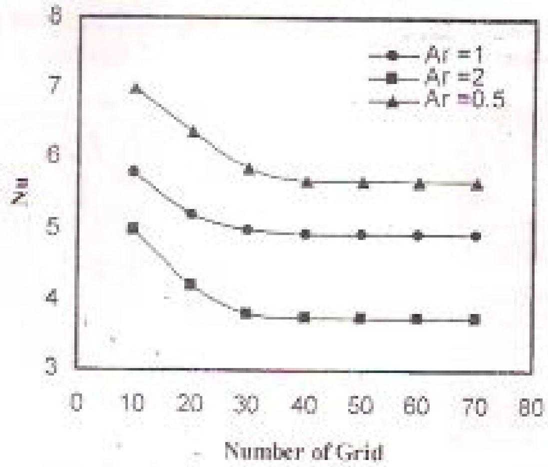

Fig.(2) Variation of Nusselt number with number of grid for different aspect ratio

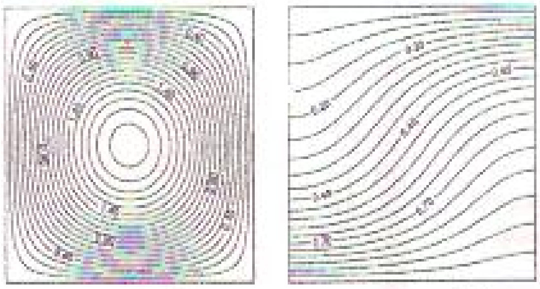

(a) (b)

Fig.(3) Pattern of (a) streamlines, (b) isotherms For $Ar=1$, $Ra^*=50$

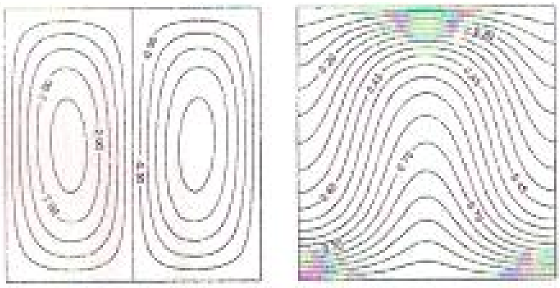

(a) (b)

Fig. (4) Pattern of (a) streamlines, (b) isotherms For $Ar=1$, $Ra^*=100$

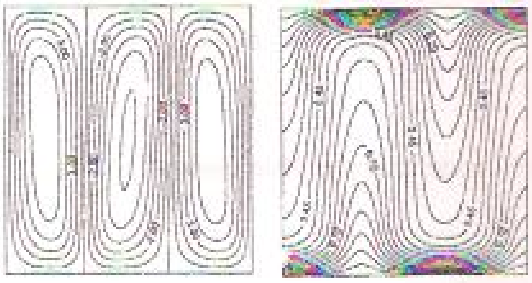

(a) (b)

Fig.(5) Pattern of (a) streamlines, (b) isotherms For $Ar=1$, $Ra^*=300$

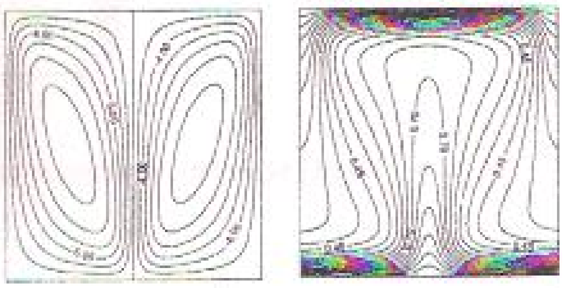

(a) (b)

Fig.(6) Pattern of (a) streamlines, (b) isotherms For $Ar=1$, $Ra^*=500$

(a)

(b)

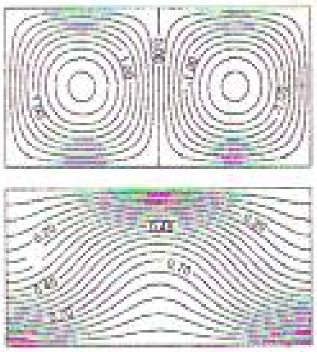

Fig. (7) Pattern of (a)streamlines, (b)isotherms For $Ar=0.5$, $Ra^*=100$

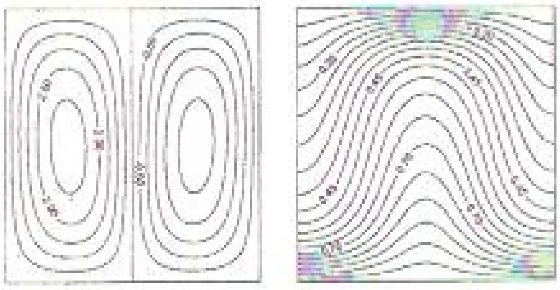

(a) (b)

Fig. (8) Pattern of (a) streamlines, (b) isotherms For $Ar=1$, $Ra^*=100$

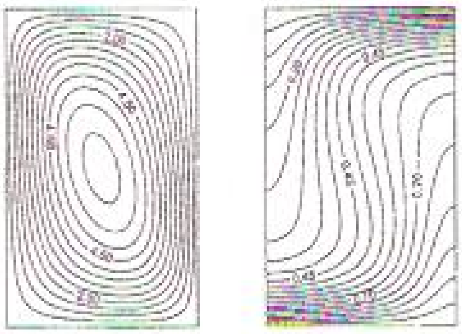

(a) (b)

Fig. (9) Pattern of (a) streamlines, (b) isotherms For $Ar=1.5, Ra^*=100$

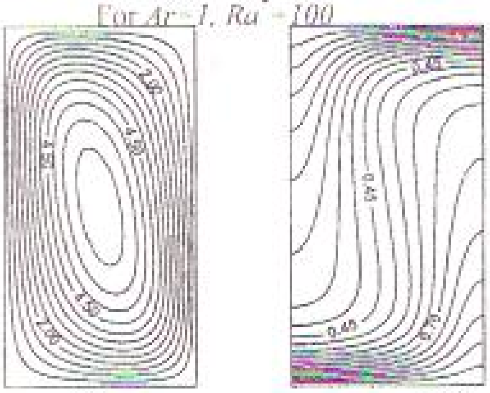

(a) (b)

Fig.(10)Pattern of (a)streamlines,(b)isotherms For $Ar=2$, $Ra^*=100$

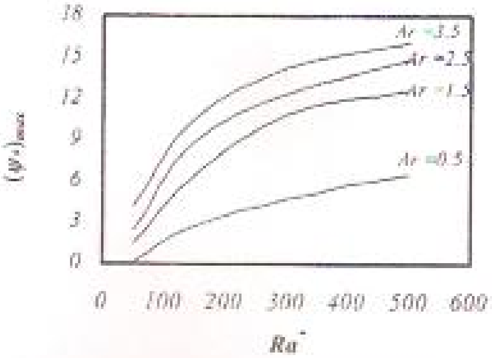

Fig.(11) Variation of maximum stream function with a porous Rayleigh number for different values of aspect ratios (Ar)

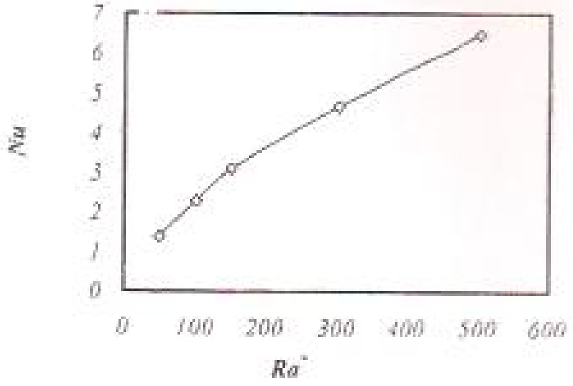

Fig.(12) Nusselt number vs. a porous Rayleigh number for Ar=1

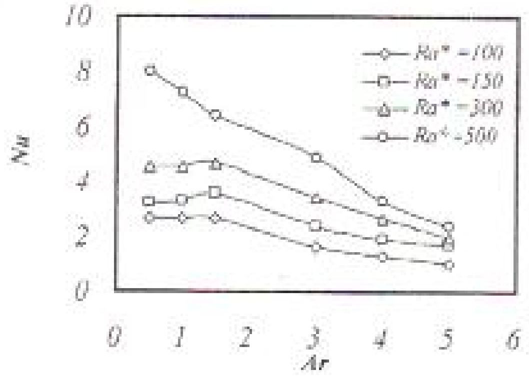

Fig.(13) Variation of Nusselt number vs.aspect ratio for different values of (Ra^*).

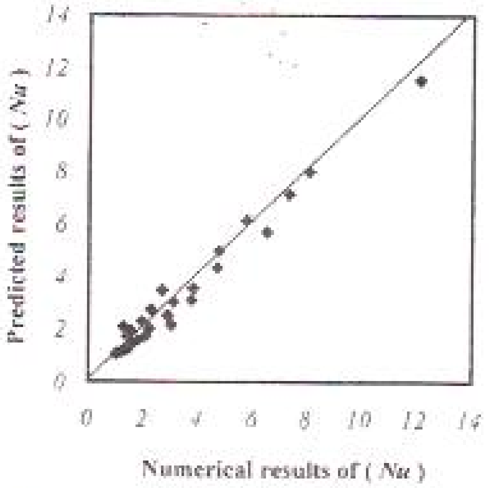

Fig. (14) Predicted vs. numerical results of heat transfer rate.